University of Stuttgart
Institute of Nuclear Technology
and Energy Systems

Thermal mixing characteristics of flows in horizontal T-junctions

A doctoral dissertation by

P. Karthick Selvam

March 2017 IKE 8-127

IKE

University of Stuttgart
Institute of Nuclear Technology
and Energy Systems

Thermal mixing characteristics of flows in horizontal T-junctions

Von der Fakultät 4 – Energie-, Verfahrens- und Biotechnik der Universität Stuttgart zur Erlangung der Würde eines Doktors der Ingenieurwissenschaften (Dr. -Ing.) genehmigte Abhandlung

Vorgelegt von

P. Karthick Selvam

aus Dharmapuri, Indien

Vorsitzender: Prof. Dr. -Ing. Andreas Kronenburg (Universität Stuttgart)
Hauptberichter: Prof. Dr. -Ing. habil. Eckart Laurien (Universität Stuttgart)
Mitberichter: Prof. Dr. -Ing. Horst-Michael Prasser (ETH Zürich)

Tag der Einreichung: 11 November 2016
Tag der mündlichen Prüfung: 29 März 2017

ISSN-Nr. : 0173-6892

Institut für Kernenergetik und Energiesysteme der Universität Stuttgart
März 2017

ACKNOWLEDGEMENTS

I would like to firstly thank my Doktorvater Prof. Eckart Laurien for giving me a chance to work on the topic investigated in this study. His guidance and encouragement provided me the motivation to stay the course, especially during challenging times. I am also thankful to Dr. Rudi Kulenovic who facilitated my integration and subsequent development at the institute.

Dr. -Ing. Mario Kuschewski and David Klören – my predecessors from whom I inherited this work for my doctoral study – are sincerely acknowledged by the author. They took me under their wings and shared with me their accumulated knowledge for which I am always indebted. Their mentoring enabled me to stand on their shoulders and approach my work from a completely different perspective for which I do not have words to thank. But for the day-to-day interactions and frequent discussions with them, this work would not have been possible.

I am greatly thankful to all my fellow colleagues and the staff with whom I had the opportunity to spend my time here at the Institute of Nuclear Technology and Energy Systems (IKE). Special thanks to my students, Patrick Buchwald and Patrick Gauder from whom I had the opportunity to learn more about my work from a fresh perspective which made it possible to move my work forward. Technicians from the Materials testing institute (MPA), namely, Hermann Huber and Thomas Pfeiffer are gratefully acknowledged by the author for their invaluable contributions in setting up the measurements.

The author is also thankful to the High Performance Computing Center Stuttgart (HLRS) for the generous computational hours offered which made possible the work presented here. It was a great learning experience to work together with Dr. sc. John Kickhofel and Prof. Horst-Michael Prasser from the Laboratory of Nuclear Energy Systems (LKE), ETH Zürich during our joint experimental studies which improved my understanding of the flow dynamics within pipes.

Finally, I would like to sincerely acknowledge the scholarship awarded by the German Academic Exchange Service (DAAD) for the entire duration of my doctoral studies.

This work is dedicated to my beloved parents Panneer Selvam and Vijayalakshmi.

"Water does not resist. Water flows.
When you plunge your hand into it, all you feel is a caress.
Water is not a solid wall, it will not stop you.
But water always goes where it wants to go, and nothing in the end can stand against it.
Water is patient. Dripping water wears away a stone. Remember that, my child.
Remember you are half water. If you can't go through an obstacle, go around it. Water does."

- Margaret Atwood, The Penelopiad

CONTENTS

	Acknowledgements	III
	Abstract	VII
	Zusammenfassung	IX
	Nomenclature	XI
1	Introduction	1
	1.1 Motivation	1
	1.2 Literature Review	8
	1.3 Aim of the present study	23
2	Experimental setup	25
	2.1 Instrumentation	27
	2.2 System start-up, heating, and cooling	29
3	Numerical approach	32
	3.1 Background	32
	3.2 Large-eddy simulation (LES)	34
	3.2.1 Filtered governing equations	35
	3.2.2 Subgrid-scale modeling	36
	3.2.3 Near-wall flow modeling	37
	3.3 Computational mesh	37
	3.4 Assessment of mesh resolution	39
	3.4.1 y-plus ($\boldsymbol{y}^+$) value estimation	39
	3.4.2 Non-dimensional grid size ($\Delta\boldsymbol{x}^+$, $\Delta\boldsymbol{y}^+$, $\Delta\boldsymbol{z}^+$) estimation	39
	3.4.3 Energy scale (L_R) and Taylor micro-scale (λ) estimation	40
	3.5 Initial and boundary conditions	41
4	Results	43

4.1 Mixing behavior of flows at ΔT = 60 °C – 180 °C 45
4.1.1 Velocity field in the mixing region 46
4.1.2 Thermal field in the mixing region 51
4.1.3 Flow penetration in the main and branch pipes 54
4.1.4 Near-wall mean temperature distribution 58
4.1.5 Temperature fluctuations 61
4.1.6 Frequency analysis of temperature fluctuations 69
4.2 Mixing behavior of flows at ΔT = 233 °C 73
4.2.1 Turbulent Penetration and Pipe Bending 74
4.2.2 Near-wall mean and RMS temperature distribution 76
4.2.3 Frequency Spectrum Analysis 78
4.3 Mixing behavior of flows at increased branch flow velocities 80
4.3.1 Qualitative analysis of the mixing region 80
4.3.2 Quantitative analysis 90
4.3.2.1 Mean temperature distribution 90
4.3.2.2 Temperature fluctuation distribution 92
4.3.2.3 Frequency spectrum of temperature fluctuations 98
Summary and Outlook 101
Bibliography 103
Appendix 118

ABSTRACT

Thermal striping induced fatigue cracking incidents in the vicinity of a T-junction – where coolant streams at different temperatures mix together intensively – has been reported in several Nuclear Power Plants (NPPs) and is considered a challenge to the safe operation of NPPs. The complex underlying turbulent flow behavior following the T-junction makes it difficult to monitor the extent of fatigue damage employing the surface thermocouple instrumentation. While there are isolated guidelines issued by regulatory bodies on how to approach the issue, no general consensus exists internationally regarding the fatigue assessment approach induced by such incidents.

The existing literature predominantly contains T-junction mixing experiments where the temperature difference (ΔT) between the fluids is lower in relation to the ΔTs experienced in NPPs. Experiments carried out at realistic ΔT between the fluids, on the other hand, lack detailed numerical studies analyzing the different aspects of the flow mixing behavior. This work deals with the coupled experimental and numerical studies of flow mixing occurring in a horizontal T-junction piping from a thermal-hydraulic standpoint. The chosen range of temperature difference (ΔT) between the mixing fluids lie between 60 °C and 240 °C which is highly representative of operating temperatures encountered in an NPP. Experiments have been conducted at the horizontally aligned Fluid-Structure Interaction (FSI) test loop at the University of Stuttgart using deionized water as the working fluid. Numerical studies were performed using the large-eddy simulation (LES) turbulence model to capture the T-junction mixing flow behavior in greater detail using the ANSYS CFX solver.

The observed mixing behavior could be summarized as follows: Thermally stratified flow behavior is observed in all the investigated cases with (i) an oscillating flow at lower ΔT (< 140 °C) between the fluids and (ii) a stably stratified flow at higher ΔT (> 140 °C) where buoyant forces significantly come into play. Hot flow penetration into the cold branch and vice versa occurs at higher ΔT (> 140 °C) resulting in the partial mixing of fluids even before they converge at the T-junction. Results from the study reveal that significant thermal gradients exist near the stratification layer, a potential region of high amplitude thermal fluctuations (a factor in thermal fatigue analysis). Frequency analyses of thermal fluctuations using the power spectral density (PSD) method highlight the absence of any

specific dominant frequency (spectral peak) in the thermal fatigue relevant frequency range of 0.1 – 10 Hz. Comparison of measurement data and LES predictions exhibits very good agreement with one another highlighting the utility of LES as a useful tool in nuclear safety based research.

In addition, LES calculations to analyze the flow mixing scenario at inflow conditions that could not be presently realized at the FSI test facility (e.g. higher branch velocity) were also performed in the present study. With rise in branch velocities, the flow nature changes from an unstably stratified flow to a completely mixed flow at lower ΔT (< 140 °C) between the fluids. At higher ΔT (> 140 °C) between the fluids, a transition from a stably stratified flow to an unstably stratified flow is observed.

ZUSAMMENFASSUNG

Thermisch induzierte Ermüdungsrissereignisse in der Nähe einer T-Stück Rohrverbindung – wo sich Kühlmittelströme unterschiedlicher Temperaturen intensiv miteinander vermischen – sind für mehrere Kernkraftwerke bekannt geworden und werden als technisch relevante Herausforderung bezüglich des sicheren Betriebs von Kernkraftwerken betrachtet. Das zugrunde liegende komplexe turbulente Strömungsverhalten nach dem T-Stück erschwert die Erfassung des Ermüdungsschadensausmaßes anhand üblich eingesetzter Messtechnik mit Oberflächenthermoelementen. Obwohl es einzelne, von Kontrollbehörden herausgegebene Richtlinien gibt, wie diese Problemstellung zu behandeln ist, besteht international kein allgemeiner Konsens hinsichtlich der Erfassungs- und Beurteilungsmethodik der Materialermüdung, die durch solche Ereignisse verursacht wird.

Die verfügbare Literatur beinhaltet hauptsächlich Untersuchungen zu Vermischungsexperimenten an T-Stück Rohrverbindungen, die mit einem vergleichsweise kleineren Temperaturunterschied (ΔT) zwischen den Fluidströmen als den zu erwartenden ΔTs in Kernkraftwerken durchgeführt wurden. Andererseits fehlen für Experimente mit einem realitätsnahen ΔT der Fluidströme detaillierte numerische Untersuchungen, die die verschiedenen Aspekte des Strömungsvermischungsverhaltens analysieren. Die vorliegende Arbeit befasst sich daher unter einem thermohydraulischen Gesichtspunkt mit gemeinsam verbundenen experimentellen und numerischen Untersuchungen zur Strömungsvermischung in einer horizontalen T-Stück Rohrverbindung. Der gewählte Temperaturdifferenzbereich (ΔT) für die Fluidströme liegt hierbei zwischen 60 °C und 240 °C, der äußerst repräsentativ in Bezug auf die in Kernkraftwerken vorzufindenden Betriebstemperaturen ist. Die Experimente wurden an dem horizontal ausgerichteten Strömung-Struktur-Wechselwirkung-Versuchskreislauf (Fluid-Structure-Interaction, FSI) an der Universität Stuttgart mit deionisiertem Wasser als Arbeitsmittel durchgeführt. Die numerischen Untersuchungen erfolgten unter Anwendung der Grobstruktur-Turbulenzmodellierung (Large-Eddy Simulation, LES), um das Strömungsvermischungsverhalten in der T-Stück Rohrverbindung unter Verwendung des ANSYS CFX Solvers mit einem erhöhten Detaillierungsgrad zu erfassen.

Das beobachtete Mischungsverhalten kann wie folgt zusammengefasst werden: Ein thermisch geschichtetes Strömungsverhalten ist in allen untersuchten Fällen bei (i) einer oszillierenden Strömung mit kleinerem ΔT (< 140 °C) der Fluidströme und bei (ii) einer stabil geschichteten Strömung mit größerem ΔT (> 140 °C), in der Auftriebskräfte signifikant zum Tragen kommen, beobachtbar. Ein Eindringen der heißen Strömung in den kalten Nebenstrang des T-Stücks und umgekehrt entsteht bei höherem ΔT (> 140 °C) und erzeugt eine Teilvermischung der Fluide noch bevor sie im T-Stück zusammenströmen. Die Ergebnisse der Untersuchung zeigen, dass beachtliche thermische Gradienten in Nähe der Schichtungsschicht bestehen, ein potenzielles Gebiet für hohe Temperaturfluktuationsamplituden (ein Faktor in der Analyse thermischer Materialermüdung). Frequenzuntersuchungen der thermischen Fluktuationen unter Anwendung der Methode der spektralen Leistungsdichte (Power Spectral Density, PSD) erbringen, dass keine spezifische dominante Frequenz (Frequenzmaximum) im für die thermische Materialermüdung relevanten Frequenzbereich von 0,1 – 10 Hz vorhanden ist. Der Vergleich zwischen Messergebnissen und LES Vorhersagen weist eine sehr gute beiderseitige Übereinstimmung nach, die die Anwendbarkeit der LES als zweckdienliches Werkzeug für die nukleare Sicherheitsforschung aufzeigt.

Zusätzlich wurden in vorliegender Arbeit LES Rechnungen durchgeführt, um die Strömungsvermischung für Einströmbedingungen zu analysieren, die zur Zeit am FSI-Versuchskreislauf nicht realisiert werden können (z. B. höhere Nebenstranggeschwindigkeit). Bei kleinem ΔT (< 140 °C) zwischen den Fluiden verändert sich mit Zunahme der Strömungsgeschwindigkeiten im Nebenstrang die Strömungsstruktur von einer instabilen Schichtenströmung zu einer vollständig vermischten Strömung. Bei einem höheren ΔT (> 140 °C) zwischen den Fluidströmen wird ein Übergang von einer stabilen Schichtenströmung zu einer instabilen Schichtenströmung beobachtet.

NOMENCLATURE

LATIN LETTERS

D	Pipe diameter, m
f	Source term
g	Acceleration due to gravity, m s^{-2}
h	Specific enthalpy, J kg^{-1}
N	Number of sampled data points
P	Pressure, bar
t	Time, s
T	Temperature, °C
u	Velocity, m s^{-1}
x, y, z	Cartesian coordinates

GREEK LETTERS

σ_{ij}	Stress tensor due to molecular viscosity, N m^{-2}
τ_{ij}	Residual stress tensor, N m^{-2}
Δ	Difference / Grid Size
θ	Angular position, °
k	Turbulent kinetic energy, m^2 s^{-2}
δ	Kronecker delta
ε	Rate of dissipation of turbulent kinetic energy, m^2 s^{-3}
λ	Thermal conductivity (W m^{-1} K^{-1}) / Taylor microscale (mm)
μ	Dynamic viscosity, N s m^{-2}
ν	Kinematic viscosity, m^2 s^{-1}

ρ	Density, kg m^{-3}

NON-DIMENSIONAL PARAMETERS

$\overline{T^*}$	Normalized mean temperature
$\overline{u^*}$	Normalized mean fluid velocity
M_R	Momentum ratio
T^*	Normalized instantaneous temperature
T^*_{rms}	Normalized root mean square temperature
u^*	Normalized instantaneous fluid velocity
u^*_{rms}	Normalized root mean square fluid velocity
$\Delta x_i{}^+$	Non-dimensional grid spacing
Pr	Prandtl number
Re	Reynolds number
Ri	Richardson number
y^+	Distance of the first node from the wall expressed in wall units

SUPERSCRIPT/SUBSCRIPT

m	Main pipe
b	Branch pipe
t	Turbulent
ref	Reference
i, j, k	Tensor indices
mix	Mixing
eff	Effective

ABBREVIATIONS

BMBF	Federal Ministry of Education and Research, Germany
BWR	Boiling Water Reactor
CFD	Computational Fluid Dynamics
CV	Control Volume
CVP	Counter-rotating Vortex Pair
DNS	Direct Numerical Simulation
EPRI	Electric Power Research Institute
FAMOS	Fatigue Monitoring System
FEM	Finite Element Method
FFT	Fast Fourier Transform
FSI	Fluid Structure Interaction
FVM	Finite Volume Method
HCTF	High Cycle Thermal Fatigue
HSV	Horseshoe Vortex
IAEA	International Atomic Energy Agency
IEA	International Energy Agency
IKE	Institute of Nuclear Technology and Energy Systems
KTA	Nuclear Safety Standards Commission
LES	Large Eddy Simulation
LKE	Laboratory of Nuclear Energy Systems
LMFBR	Liquid Metal Fast Breeder Reactor
LWR	Light Water Reactor
MPA	Materials Testing Institute

NEA	Nuclear Energy Agency
NPP	Nuclear Power Plant
NRC	Nuclear Regulatory Commission
OECD	Organization for Economic Co-operation and Development
PSD	Power Spectral Density
PWR	Pressurized Water Reactor
RANS	Reynolds Average Navier-Stokes
RHRS	Residual Heat Removal System
rms	Root Mean Square
SGS	Sub-grid Scale
SST	Shear Stress Transport
WALE	Wall-Adapting Local Eddy-Viscosity
WMS	Wire Mesh Sensor

„Nothing is softer or more flexible than water,
yet nothing can resist it "

- Lao Tzu

1 INTRODUCTION

1.1 Motivation

Consistent, reliable supply of electricity is the foundation and a key driver of economic, technological and social growth in any country. The world energy outlook 2015 special report on energy and climate change [152] from the International Energy Agency (IEA) estimates the total worldwide electricity generation in 2030 to be 30,620 terawatt-hours (TWh), a 32 % increase from the 23,234 TWh generated in 2013. In the midst of such a lofty outlook, there is a growing consensus regarding the need to substantially reduce the greenhouse gas emissions due to power generation. Base load power generation supplying round-the-clock electricity throughout the year – the foundation of the modern electrical grid – comes from two primary fuel sources: coal and nuclear. Coal-based electricity generation is set to be significantly curbed over the coming years as part of the clean energy initiative adopted by many countries around the world. On the other hand, nuclear-based electricity generation is set to become an important part of the energy mix in many countries over the next decade. The latest data from the International Atomic Energy Agency (IAEA) point to the fact that there are 441 nuclear power reactors currently in operation worldwide generating nearly 383 GW electrical power output [48, 94]. 67 reactors are presently under construction, 172 reactors are either ordered or planned and a further 337 reactors are proposed worldwide [153]. Thus the trend clearly points towards significant expansion in the global nuclear capacity over the next decade due to the low-carbon, low-cost base load electricity produced in a nuclear power plant.

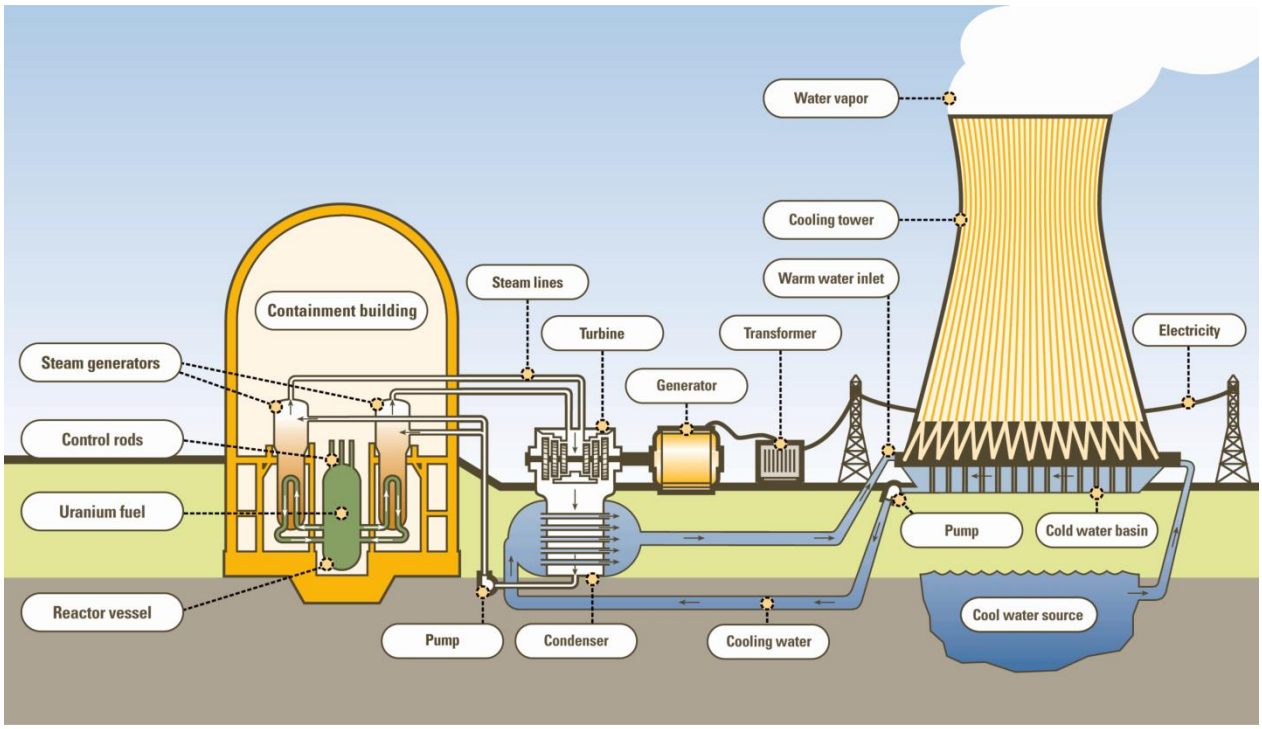

Fig. 1 Simplified illustration of a Nuclear Power Plant, Pressurized Water Reactor [95]

Table 1: Types of nuclear power plants worldwide (Source: IAEA [94])

Reactor type	Fuel	Coolant	Moderator	#
Pressurized Water Reactor (PWR)	Enriched UO_2	Water	Water	282
Boiling Water Reactor (BWR)	Enriched UO_2	Water	Water	78
Pressurized Heavy Water Reactor 'CANDU' (PHWR)	Natural UO_2	Heavy water	Heavy water	49
Gas-cooled Reactor (AGR & Magnox)	Natural U (metal), enriched UO_2	CO_2	Graphite	14
Light Water Graphite Reactor (RBMK & EGP)	Enriched UO_2	Water	Graphite	15
Fast Neutron Reactor (FBR)	PuO_2 and UO_2	Liquid sodium	none	3
Total number of reactors				441

A nuclear power plant (NPP) is basically a thermal power station where heat is generated by splitting the atoms (nuclear fission) of fuel elements (typically, enriched UO_2) in the

nuclear reactor. The generated heat is absorbed by the surrounding coolant (e.g. water) to produce steam which then drives a steam turbine connected to an electrical generator to produce electricity (see Fig. 1). A vast majority of the commercial nuclear reactors (> 80 %) currently in operation worldwide are light water reactors (LWRs) using ordinary (light) water as the coolant. LWRs are further classified as pressurized water reactors and boiling water reactors. A classification of the different types of NPPs currently in operation is summarized in Table 1.

Piping systems perform the essential function of facilitating coolant transport within an NPP. Being a vast infrastructure, an extensive network of piping serving different purposes are available within an NPP. Ensuring the integrity and functional capability of piping systems throughout their service life are important for the safe operation of an NPP. The quality and the properties of the piping are initially controlled during the design and manufacturing stage. It may change during its service life due to the operating conditions (e.g. ≈ 290 °C, 155 bar in the reactor core of a PWR [151]) to which it is exposed. Additionally, the quality of the piping is also influenced by new knowledge and experience acquired during the operation of the power plant along with other technical and scientific progress. These changes are collectively indicated by the term 'ageing'. There are six identified ageing mechanisms that tend to reduce the working life of components in an NPP, namely, thermal fatigue, vibrational fatigue, thermal ageing, primary water stress corrosion cracking, boric acid corrosion and atmospheric corrosion [47]. This work is primarily focused on thermal fatigue induced piping degradation.

Thermal loading imposed on the piping structure by the underlying fluid flow results in some of the unexpected material degradation and failure reported in nuclear power plants (NPPs). Thermal fatigue was identified as a challenge to the nuclear safety during the early operation of NPPs during the 1970s and 1980s when new loading conditions (e.g. thermal stratification, vortex penetration in tees, dead leg and valve leaks) that were not considered during the design stage resulted in fatigue cracks at different locations during the operation [1]. Research efforts were subsequently made to understand these issues by the nuclear community. The regulatory agencies – based on the findings – issued guidelines to the utility operators to put in place practical systems capable of identifying and safeguarding the components from such occurrences at the earliest possible time. For example, the

nuclear regulatory commission (NRC) in the United States issued Bulletin 88-08 and subsequent guidelines establishing Licensee actions ensuring appropriate degradation management [137, 138, 139, 140, 141, and 142]. The German nuclear safety standards commission (KTA) mandated the use of additional measuring equipment including the installation of long-term temperature measuring devices in order to obtain comprehensive information about the real loading experienced by the components during operation. Since thermal fatigue is a highly local phenomenon, knowledge of both the local geometry of components and their loading conditions are required. Thus, the German nuclear rule KTA 3201.4 [69] mandated the use of local monitoring systems to tackle this issue. Excerpts from this rule detailing local monitoring measures are given below.

"9.2 Monitoring of loadings

9.2.1 Monitoring of quasi-static mechanical and thermal loadings

(1) It shall be ensured that temporal and local temperature changes relevant to fatigue are monitored by a sufficiently dense net of measuring points of the standard instrumentation. When selecting the measuring points the effects of the mode of operation (little mass flows, indifferent pressure conditions, switching operations, temperature differentials) and the design (pipeline installation, isolating function of valves) shall be taken into account.

(2) Where thermal stratification is expected to occur, the temperature measuring points shall be located such that all relevant loading variables across the pipe cross-section and axially to the pipe run can be measured."

The nuclear industry responded by developing monitoring systems to address the issue of thermal degradation induced fatigue in piping components. An example would be the in-service fatigue monitoring system (FAMOS) developed by Siemens – KWU (Kraftwerk Union) during the 1980s. The monitoring strategy employed by FAMOS and its application in the German NPPs are discussed in Golembiewski and Miksch [38]. Similar fatigue monitoring systems used in commercial NPPs include the FatiguePro [109] developed by the Electric Power Research Institute (EPRI) in the United States, Operating Transients Monitoring System (OTMS) and Fatiguemeter [8] developed in France, K-FAMS developed in Korea [154], Westinghouse thermal event monitoring system (WESTEMS™) by the

Westinghouse Electric company [143, 149] and the more recent fatigue monitoring system integrated (FAMOSi) developed by AREVA [1].

Data from the earlier application of fatigue monitoring systems, to everyone's surprise, showed that the transients observed during the operation are significantly different from what was envisioned during the design stage. This provided further impetus for enhanced monitoring of the plant operation using additional instrumentation at different locations in order to obtain the most recent information about the thermal loading in the structure. The data served an additional purpose in assessing changes in the structural thermal loading behavior in response to changes in the operating conditions of the plant (e.g. during plant startup and shutdown). Thus fatigue analyses were performed based on operational data obtained after years of monitoring with lower fatigue damage factors than what was used during the design stage with more conservative assumptions [104]. This process naturally resulted in the early detection and possible prevention of components being exposed to potentially damaging thermal loads. An example would be the redesigning of the feedwater sparger of the steam generator in a German NPP to minimize the stresses brought about by cyclically occurring stratification transients [1]. Also, the development of predictive models during the mid-1990s contributed to the decline of through-wall thermal fatigue cracking events [84]. Thus the common thermal fatigue issues caused by clearly identifiable thermal loadings on the structure appeared to be well understood over the years. Monitoring them could also be adequately performed using the existing plant instrumentation systems.

But incidents reported in recent years highlight the occurrence of thermal fatigue in structures caused by low-amplitude thermal loading that could not be monitored using conventional plant instrumentation systems. Predominantly caused by mixing between flows at significant temperature differences (ΔTs), the issue is still being widely investigated and no consensus exists internationally on assessing the fatigue damage caused by such thermal mixing events.

The above-mentioned mixing between flows at significant ΔT is technically denoted by the term 'Thermal Striping'. In essence, thermal striping is defined as the random thermal fluctuations caused by the incomplete mixing of coolant streams at different temperatures. The mixing of fluids induces thermal fluctuations on the surface of the structure and causes

surface strains. Material fatigue may occur when the amplitude and number of strain cycles are sufficiently high [145]. Understanding the mixing characteristics of the flow is important in tackling the reported occurrences of high-cycle thermal fluctuation induced cracking in the structure.

A well-known example is the T-junction (also called 'mixing tee') piping where the coolant streams at significant ΔT mix together intensively. The mixing causes significant thermal stresses on the inner surface of the structure. Damage is typically initiated as a network of surface cracks. Depending on the material properties, the component geometry and the thermal loading in the structure, the cracks (i) may remain at the surface or (ii) propagate and arrest at a certain depth or (iii) propagate to form a through-wall crack [98]. The evolution of these cracks over time and the subsequent failure in the structural integrity of the piping results in the phenomenon of high-cycle thermal fatigue (HCTF). As opposed to common thermal fatigue issues arising due to thermal stratification, vortex penetration in tees, dead leg and valve leaks where the underlying flow behavior could be reasonably identified using instrumentation, thermal striping induced fatigue poses several distinct challenges in performing structural integrity assessment [100]. They are:

(i) The inherent difficulty in determining local thermal loads since the underlying flow behavior is complex. Also, monitoring using thermocouple instrumentation is inadequate due to the delayed response of the sensors. Thus piping integrity evaluations mainly rely on estimations and boundary conditions that might lead to either too conservative or non-conservative results [50].

(ii) Availability of appropriate high-cycle fatigue data.

(iii) Fatigue damage assessment process for variable loading histories.

Another important challenge is the multi-disciplinary nature of the thermal loading and the associated damage involving three complementary scientific disciplines: (i) Thermal-hydraulic field, (ii) Thermo-mechanical field, and (iii) Materials science [32]. Thus any effort to understand the issue of HCTF caused by thermal striping should involve a multi-disciplinary strategy.

Piping prone to HCTF damage are identified in the residual heat removal system (RHRS), surge and spray lines, emergency core cooling systems, several branch lines and nozzles

(charging line, safety injection lines etc.). Schematic of a T-junction piping in the RHRS is shown in Fig. 2. Shown in Table 2 is a brief list of T-junction related thermal fatigue incidents reported in the Network for Evaluation of Structural Components – Thermal Fatigue report [24].

Table 2. Operational damage cases in T-junctions. Source: NESC-TF database [24]

ID	Location	Load type	Event	ΔT (°C)
3	BWR mixing tee	Cold water from leaking pump	Stratification	210
4	BWR mixing tee	Not known	Stratification/ Turbulence	280
5	BWR pipe mixing tee with inner sleeve	Intermittent inlet of cold water	Turbulence	90, intermittently 200
6	BWR mixing tee	Turbulent mixing under normal conditions	Turbulence	64, intermittently 170
13	BWR pipe mixing tee with inner sleeve	Possibly untight sealing	Instability	90
15	PWR mixing tee with elbow	Turbulent mixing, operational	Turbulence or large scale instability	160
16	PWR mixing tee	Valve leakage	Stratification	230
17	PWR mixing tee	Valve leakage	Turbulence or stratification	180
18-31	PWR mixing tees	Operational	Turbulence	80 and larger
32	BWR straight pipe after mixing tee	Valve leakage	Stratification	200
33	PWR elbow (Civaux 1)	Operational	Large scale instability directly after turbulent mixing in a tee	80 and larger
35	PWR elbow near tee (Tihange 2)	Leakage	Stratification	270

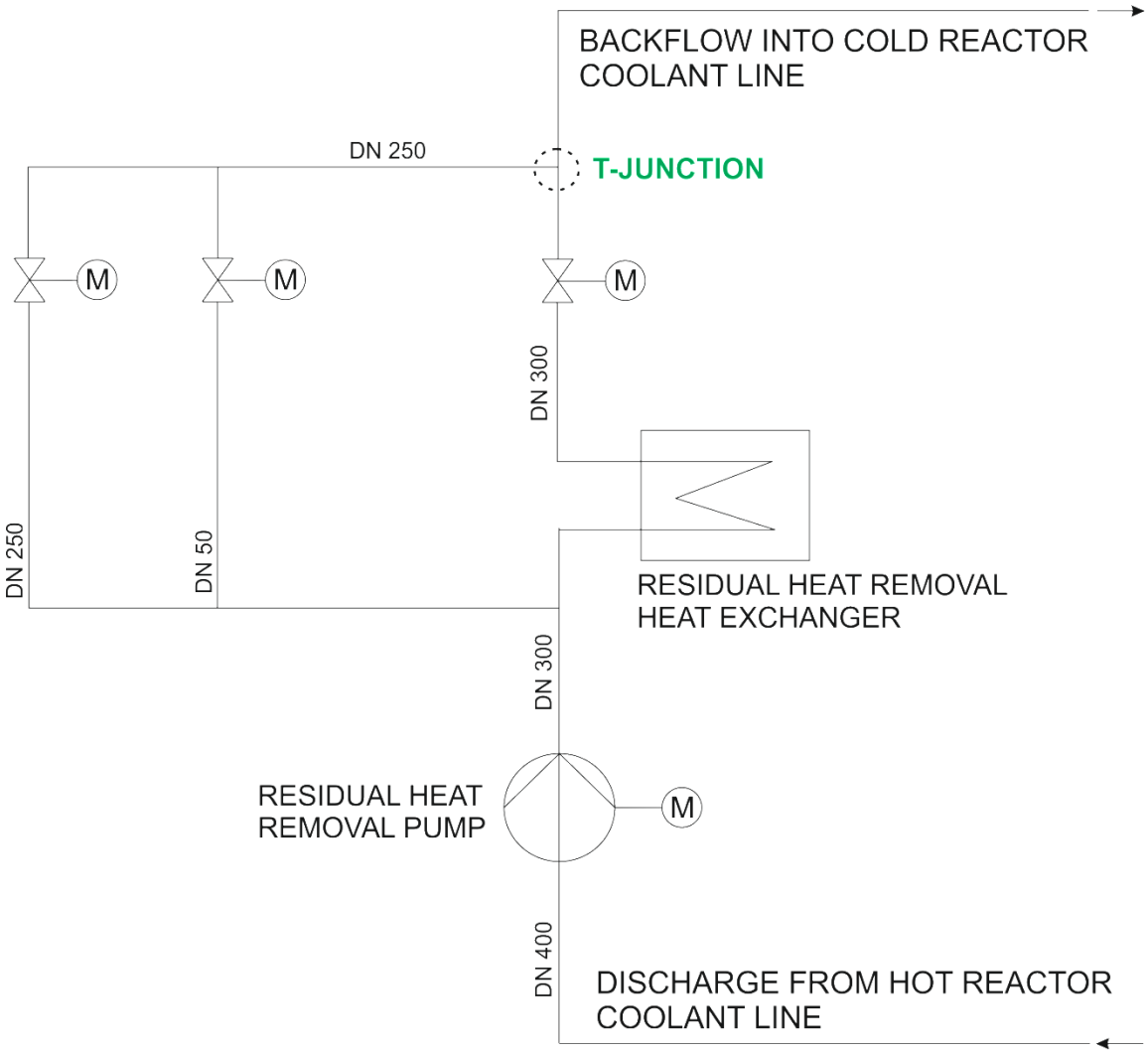

Fig. 2 Schematic of T-junction piping in the RHRS [39]

1.2 Literature Review

Investigations related to thermal striping induced fatigue events were initially investigated in the context of liquid metal fast breeder reactors (LMFBRs) [15, 77, 134, and 145] due to the thermal properties of the liquid sodium coolant (thermal conductivity and thermal diffusivity of liquid sodium are nearly 100 and 400 times that of water). A sodium leak detected near the secondary circuit T-junction (ΔT = 90 °C) of the French Phénix reactor (see Fig. 3(a)) formed the basis of a coordinated research project (CRP) organized by the IAEA during 1996 – 1999 [46]. Eleven participating institutes from around the world contributed to this project whereby numerical codes developed for thermohydraulic and

thermomechanical analyses were applied to studying thermal mixing behavior and its effect on the piping structure of the Phénix T-junction.

Thermal fatigue evaluation of tubes and plates subjected to temperature fluctuations in the context of thermal mixing in LMFBRs were performed under the cooperative framework of the French Atomic Energy and Alternative Energies Commission (CEA) and the Japan Nuclear Cycle Development Institute (JNC) using the FAENA (ΔT = 158 – 268 °C) and TIFFSS (ΔT = 240 °C) sodium facilities [79]. Other experimental investigations to study thermal mixing of sodium coolant in LMFBRs include the GEVEJET and NAJET test facilities (see Fig. 3(b, c)) [135].

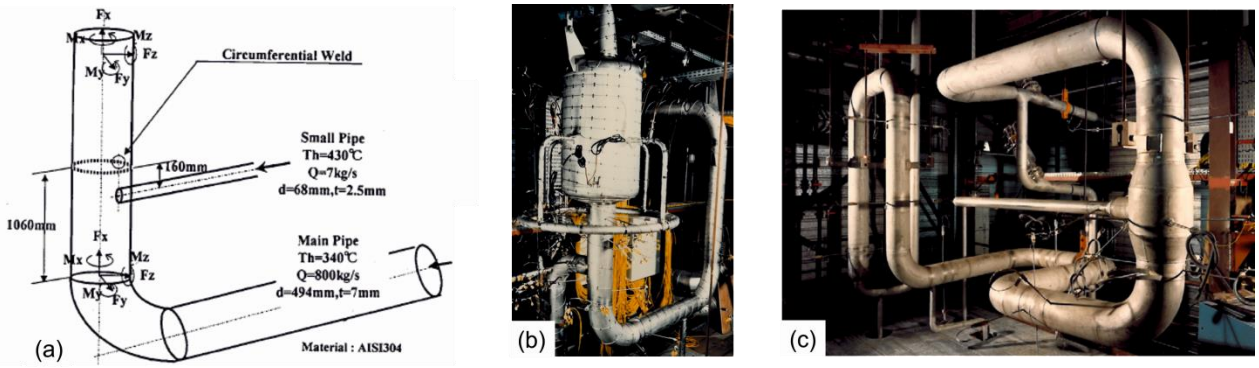

Fig. 3 Phénix T-junction [46] (a), GEVEJET (b) and NAJET (c) sodium test facilities [135]

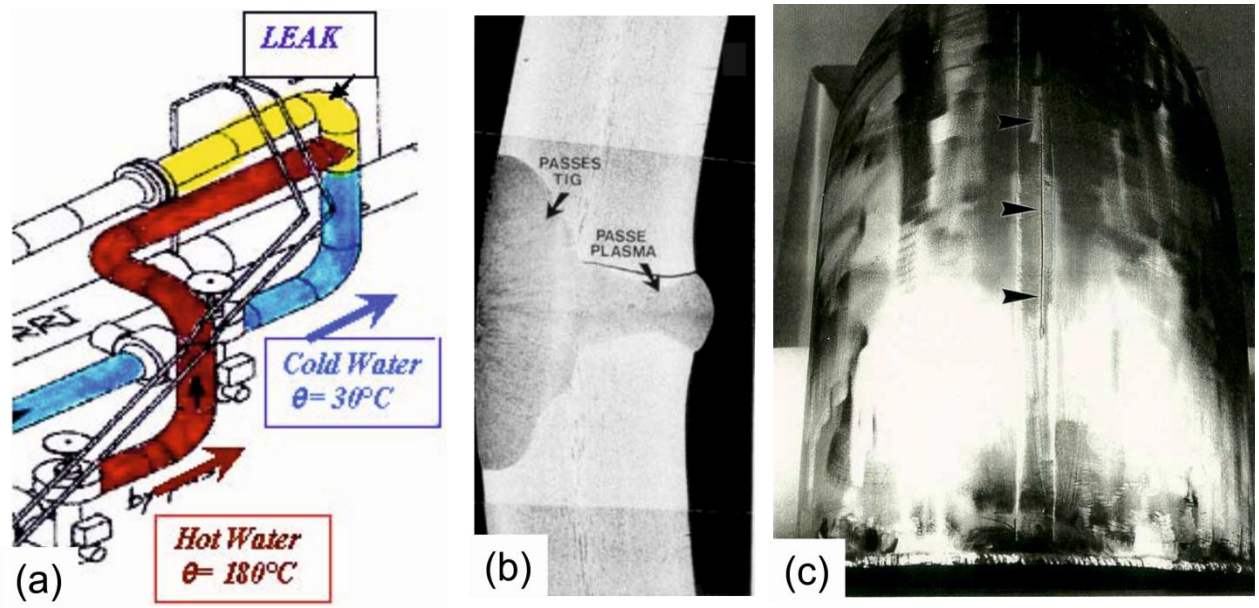

Fig. 4 Civaux T-junction [26] (a), its through-wall crack [26] (b) and longitudinal crack [25] (c)

Following the leakage incident in the French NPP Civaux-I on May 12, 1998 (see Fig. 4), research efforts of the nuclear community were then directed towards understanding high-

cycle fatigue issues in light water reactor components. The incident took place in the vicinity of a T-junction piping in the RHRS where hot and cold coolant streams (ΔT = 150 °C) mixed together intensively. A through-wall crack and a host of part-wall cracks developed in the elbow section following the T-junction within 1500 hours of operation. The outer and inner surface lengths of the through-wall crack were 180 mm and 350 mm, respectively [30]. Metallurgical examinations concluded that the origin of this degradation phenomenon was brought about by thermal fatigue [16, 31]. HCTF issues in T-junctions in the context of the Civaux incident became an important topic of discussion in the subsequent international conferences [31, 112, and 113].

Fig. 5 FATHER [26] (a) and FATHERINO [14] (b, c) T-junction test facilities

In the aftermath of this incident, several national level research and development (R&D) programs to understand this phenomenon were initiated. In France, all the RHRS mixing zones were replaced with manufacturing improvements following the Civaux incident. Also, an endurance thermal fatigue test named FATHER [18, 26, and 32] where flow mixing in a T-junction piping with geometry and inflow conditions (velocity, ΔT) similar to the Civaux NPP T-junction (see Fig. 5(a)) was performed. The test lasted 300 hours and more than 50 thermal fatigue cracks (observed mainly on geometrical discontinuities like weld toes or grinding striations) with depths ranging from 100 to 1000 μm were detected in the mock-up. In addition, the CEA conducted another experiment called FATHERINO [14] with two T-junction mock-ups (ΔT = 75 °C) – one to investigate and select the zones of high-temperature fluctuation ('the skin of fluid' mock-up, see Fig. 5(b)) and the other for applying advanced instrumentation to assess fluctuating temperature, thermal flux and heat transfer coefficient ('the stainless steel' mock-up, see Fig. 5(c)).

The European Commission has also supported research efforts in this area through the project on thermal fatigue evaluation of piping system Tee-connections (THERFAT) [85].

This was mainly initiated to advance the reliability and the accuracy of thermal fatigue load determination with the aim of providing a practical methodology in managing thermal fatigue risks. Another European project involving both the utilities and the R&D organizations to produce a consensus methodology for assessing HCTF with a special focus on T-junctions in LWRs was organized by the Network for Evaluation of Structural Components (NESC) [24] which is coordinated by the European Commission's Joint Research Centre (Project: EUR 22763 EN). The primary objectives of this project are (i) the creation of a service and mock-up investigations based database, and (ii) the development of a European level procedure for assessing thermal fatigue that reflects the multi-disciplinary nature of the phenomenon. The Japanese Society of Mechanical Engineers (JSME) conducted investigations of their own and issued guidelines on dealing with HCTF [52]. In the United States, the EPRI's Materials Reliability Project (MRP) was used as a platform to address utilities regarding thermal fatigue issues in T-junction piping components [29]. The German initiative, sponsored by the Federal Ministry of Education and Research (BMBF), resulted in the commissioning of a Fluid-Structure Interaction (FSI) T-junction facility at the University of Stuttgart to investigate the various facets of the flow mixing processes at ΔT between fluids up to 240 °C [73, 74, and 116].

Several other thermal striping experimental investigations – carried out over a wide range of ΔT between the mixing fluids – are reported in existing literature, of which a selected few are described below.

Water experiments in a T-junction (named WATLON, ΔT = 15 °C) with upstream elbow was performed by Ogawa et al. (2005) [97]. Based on the momentum ratio (M_R) formulation, flow patterns emerging from the branch jet were classified as (i) wall jet, (ii) deflecting jet, and (iii) impinging jet (see Fig. 6 (a, b, c)). In case of wall jet flows, temperature fluctuation intensity was observed to be larger in a T-junction with upstream elbow than without it.

$$M_R = \frac{4 * \rho_m * (D_m * D_b) * {U_m}^2}{\rho_b * \left(\pi * {D_b}^2\right) * {U_b}^2} \quad (1)$$

where ρ, D and U represent the density, inner diameter and velocity of the fluids, respectively. Suffixes m and b denote the fluids flowing in the main and branch pipes, respectively. A similar study in a vertical T-junction was performed by Hosseini et al. (2008) [43] to classify branch jet induced flow pattern – based on momentum ratio (M_R) –

as (i) Wall jet, (ii) Reattached jet, (iii) Turn jet, and (iv) Impinging jet (see Fig. 6 (d, e, f, g)). Turn jet flow was identified as the optimum flow condition to reduce near-wall thermal fluctuations in the mixing zone.

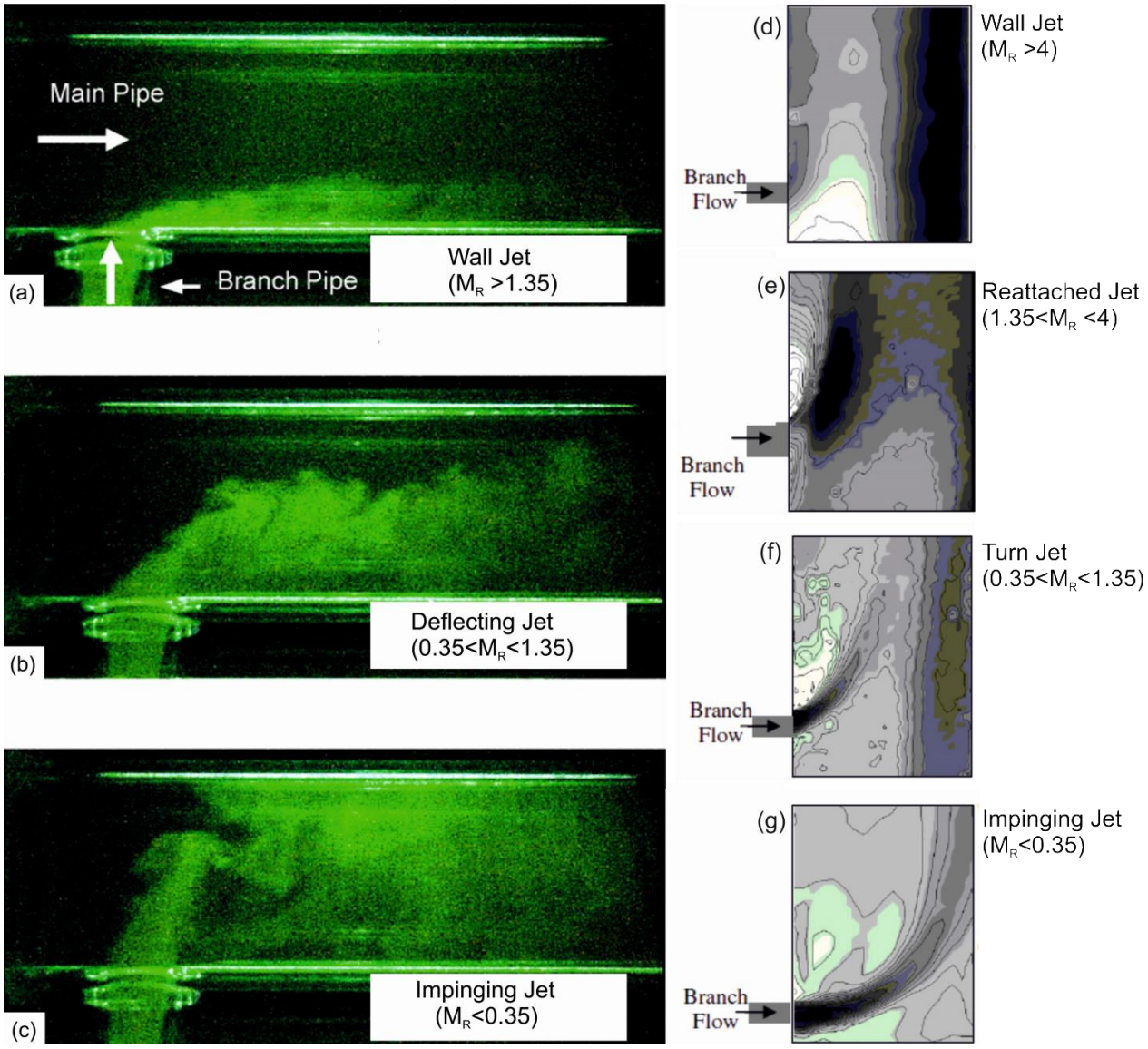

Fig. 6 Classification of turbulent jets in a vertical T-junction based on (a, b, c) Ogawa et al. (2005) [97], (d, e, f, g) Hosseini et al. (2008) [43]

Thermal mixing experiments were performed in a vertical T-junction piping (ΔT = 15 °C, see Fig. 7(a)) at the Älvkarleby lab of Vattenfall research and development. Near-wall temperature data from thermocouples, inlet velocity profiles measured using laser Doppler velocimetry were collected during the experiments and later served as the basis of an international computational fluid dynamics (CFD) benchmarking exercise [131] organized

by the OECD/NEA. Additionally, single point laser-induced fluorescence technique was also used to collect concentration data at isothermal mixing conditions.

A similar project (ΔT = 15 °C, [4]) involving pan-European participation from the research institutes and the industry is called MOTHER (Modelling T-junction Heat Transfer, see Fig. 7(b)). Experiments using two different geometries – T-junction with a sharp corner and round corner – were performed for the purpose of conducting a benchmarking exercise similar to Vattenfall experiments [131] to improve the thermal fatigue predictive capabilities using CFD.

Fig. 7 Vattenfall [131] (a), MOTHER [4] (b) and EXTREME [17] (c) T-junction test facilities

Thermal mixing behavior of coolant streams (ΔT = 70 °C, see Fig. 7(c)) at various flow rates in the main and branch pipes were performed by Chen et al. (2014) [17] at the EXTREME (Experiments with T-junction on rapid and emergent mixing effects) test facility. It was observed that the occurrence of reverse flow (which may produce cracks in pipes) took place in measurements where the branch velocity is much higher than the main flow velocity.

Kuschewski et al. (2014) [74] performed a range of measurements in a horizontal 90° T-junction (FSI test facility) with ΔT between fluids from 30 – 130 °C. Different aspects of the flow, viz, buoyancy effects, thermal stratification of flows, recirculation, and backflow observed under the investigated inflow conditions were discussed in the study.

Isothermal flow mixing experiments employing alternative techniques to obtain flow field information in the mixing zone have also been performed in existing literature and is discussed below.

Kuschewski et al. (2013) [73] applied a novel image-based measurement technique called the near-wall light emitting diode induced fluorescence (NWLED-IF) to study isothermal mixing of flows at the IKE cold test facility (see Fig. 8(a)). A density difference between fluids – equivalent to ΔT of 106 °C – was established by mixing sugar in the branch flow.

Spatially resolved flow field information in the mixing region were captured in the midst of high-density differences and results from this study indicated that the positioning of thermocouples in practical installations can have a significant effect on the observed local root mean square (RMS) temperature fluctuation amplitudes.

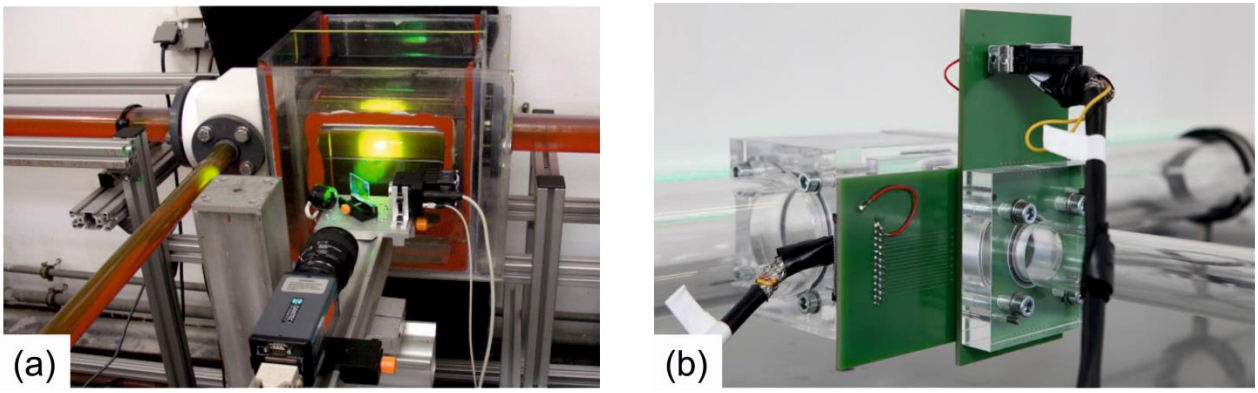

Fig. 8 IKE (a) and LKE [59] (b) isothermal T-junction test facilities

Similar isothermal mixing experiments at the LKE T-junction test facility at ETH Zürich involved the application of wire mesh sensors (WMSs) which exploited the difference in electrical conductivity between the participating fluids to characterize the turbulent mixing in the vicinity of T-junction. Walker et al. (2009) [147] performed mixing experiments in a T-junction using the wire-mesh sensor (Fig. 8(b)). The main and branch pipes are supplied with water having different electrical conductivities. The transient structures of the transport scalar downstream of T-junction were characterized, and a two-point correlation of the signal in the axial direction and within the cross-section was performed, providing a database for CFD validation.

A list of T-junction mixing experiments conducted over the past two decades has been summarized in Table 3. In addition to the T-junction mock-up based investigations discussed above, thermal fatigue tests on specimens being subjected to alternate heating and cooling effects are also available in literature and a list of such tests are summarized in Table 4.

Aside from investigations related to the T-junction mixing of flows over a wide range of temperature differences, experiments investigating different methods to reduce thermal fluctuations in the mixing zone of T-junctions have also been performed in the existing literature.

Table 3. T-junction mixing studies performed over the past two decades

Name of the test facility	Pipe material	Fluid, Temperature, Inner diameter		Velocity ratio (u_m/u_b)	References	
		Main Pipe	Branch Pipe		Experiment	CFD
Phénix LMFR T-junction	Stainless steel (AISI 304)	Sodium, 340 °C, 494 mm	Sodium, 430 °C, 68 mm	2.2	[46]	[9, 46]
Hitachi and Toshiba tests	Acrylic	Water, 20 – 60 °C, 100 mm	Water, 20 – 56.5 °C, 100 mm	0.2 – 6.05	[58, 64]	[45, 78]
FATHER	Stainless steel (AISI 304L)	Water, 204 °C, 152.4 mm	Water, 44 °C, 152.4 mm	1	[12, 18, 19, 20, 26]	[32, 101]
FATHERINO	Brass and Stainless steel (304L)	Water, 80 °C, 54 mm	Water, 5 °C, 54 mm	3	[14, 24]	[71]
WATLON	Acrylic resin	Water, 48 °C, 150 mm	Water, 33 °C, 50 mm	0.2 – 3	[54, 97]	[54, 90]
Vattenfall	Plexiglas®	Water, 19 °C, 140 mm	Water, 36 °C, 100 mm	1.32	[131]	[10, 49, 70, 91, 136, 150]
EXTREME	Stainless steel	Water, 90 °C, 208 mm	Water, 20 °C, 21 mm	0.13 – 0.22	[17]	[80]
IKE cold test rig	PVC	Water, 20 °C, 71 mm	Sugar water, 20 °C, 35.5 mm	0.3 – 1	[73]	[66, 67]
LKE T-junction	Acrylic glass	Tap water, room temperature, 50 mm	Deionized water, room temperature, 50 mm	0.6 – 400	[63, 147, 155, 156]	[33, 146]
FSI	Stainless steel	Water, 142 °C, 71.8 mm	Water, 25 °C, 38.9 mm	1.4	[74,116]	[65,116]
T-Cubic	Stainless steel	Water, 25.7 °C, 150 mm	Water, 59.8 °C, 50 mm	1.5	[86, 88]	[87]
MOTHER	Stainless steel	Water, 30 °C, 54 mm	Water, 15 °C, 54 mm	1	[4]	[44]
Ulchin based tests	Stainless steel	Water, 177 °C, ≈ 243 mm	Water, 60 °C, ≈ 243 mm	0.5	[50]	[50]

Suzuki et al. (2005) [133] conducted T-junction mixing experiments using a countermeasure structure nicknamed 'Elephant Nose' with the objective of reducing thermal fluctuations in the flow. It consists of a smaller bore elbow from the branch pipe leading up to the run pipe (see Fig. 9). As the branch fluid is discharged in parallel with the main flow, the shear force between them results in enhanced mixing of fluids and the high thermal fluctuation regions are located farther downstream of T-junction. Data from experiments have shown that thermal fluctuations are highly attenuated by using the countermeasure structure than without it.

Table 4. Specimen based thermal fatigue tests performed in literature

Test name	Specimen material	Test conditions		References	
		Fluid	Temperature	Experiments	Numerical
INTHERPOL	Stainless steel (304L)	Water	ΔT = 120 – 140 °C	[22, 23, 24, 132]	[22, 23, 132]
FAT3D	Stainless steel (316L)	Water	Hot: 650 °C Cold: 17 – 20 °C	[3, 21, 24]	[21]
JRC Cyclic down-shock	Stainless steel (316L)	Water	Hot: 300 – 550 °C Cold: Ambient	[3, 24, 98, 99, 100]	[98, 99, 100]
SPLASH	Stainless steel (304L)	Water-Air mixture	ΔT = 125 – 200 °C	[3, 24, 40]	[40]
FAENA	Stainless steel (316L(N))	Sodium	ΔT = 158 – 268 °C	[79]	[79]
TIFFSS	Stainless steel (316(FR))	Sodium	ΔT = 240 °C	[79]	[79]
SPECTRA	Stainless steel (304SS)	Sodium	Hot: 650 °C Cold: 250 °C	[55]	-

Gao et al. (2015) [36] performed similar experiments (ΔT = 17 °C) using a branch distributor (see Fig. 9) to weaken thermal fluctuations in the T-junction mixing zone. Numerical calculations were also performed using the large-eddy simulation (LES) turbulence model. Results have shown that that the inclusion of branch distributor moves

the mixing region to the middle of the pipe reducing thermal fluctuations at the internal wall surface. This also makes the mixing process more efficient as opposed to a T-junction without a branch distributor.

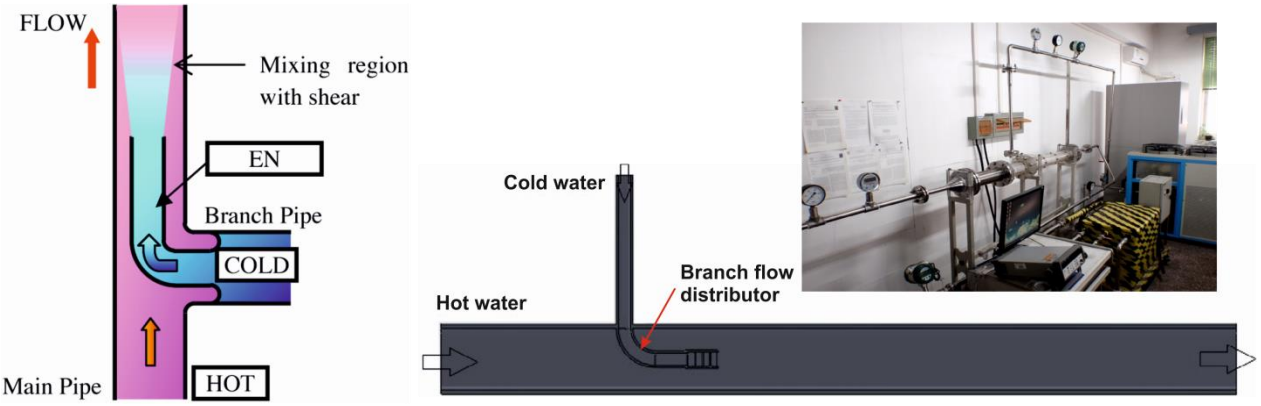

Fig. 9 Weakening thermal fluctuations using Elephant Nose (EN) [133] (left) and branch distributor [36] (right)

Wang et al. (2014) [148] performed T-junction flow mixing experiments (ΔT = 7.5 – 20 °C) with a porous medium composed of stainless steel spherical particles. Influence of (i) flow ratio in the main and branch duct and (ii) ΔT between fluids on thermal fluctuations were analyzed in this study. The distribution of hot and cold fluids in the mixing zone was observed to depend on flow ratio which had an effect on thermal fluctuations. But the ΔT between fluids was found to have a limited impact on thermal fluctuations.

Aside from the above mentioned investigations, discussions at forums such as the *International Conference on Fatigue of Reactor Components* [25, 112, and 113] involving experts, utility operators and regulators are a rich source of information about the numerous other investigations that were conducted to study and address various thermal fatigue related issues.

Advances in high-performance computing over the past two decades enabled CFD investigations of T-junction flows in much greater detail than was deemed possible before. CFD has complemented experiments in providing reliable information and description of the flow field at locations that are otherwise inaccessible using instrumentation. One of the earlier applications of CFD codes to study the flow behavior in a T-junction (ΔT = 90 °C) was done in the case of the French Phénix LMFBR [46]. The trend gained rapid momentum

following the Civaux leakage incident in 1998. Best practice guidelines and code assessments [82, 126, 127, 128, and 129] are periodically updated by the CFD community to reflect the new knowledge gained through experience. Few of the numerical studies investigated in literature dealing with T-junction mixing is discussed below.

Hu and Kazimi (2006) [45] performed LES studies of T-junction mixing (ΔT = 31 – 40 °C) based on thermal striping experiments performed by a Japanese working group aimed to help the Japan Society of Mechanical Engineers (JSME) establish guidelines for high-cycle fatigue. Mean and fluctuating temperatures predicted by LES showed good agreement with experimental data.

Westin et al. (2008) [150] performed numerical studies of T-junction mixing (ΔT = 15 °C) using both LES and Detached Eddy Simulation ($k-\omega$ based Shear Stress Transport (SST) model) turbulence models. Two boundary conditions were studied: (i) without inlet perturbations and (ii) with inlet perturbations to understand their influence on flow mixing behavior. The strong large-scale instabilities in the mixing region are seen to be triggered independent of the applied inlet perturbations. LES and measurement data exhibited good agreement with one another.

Odemark et al. (2009) [96] performed experimental and numerical studies of turbulent mixing in a T-junction for three different flow ratios. Velocity and temperature data predicted by the LESs are compared with experimental results and a good agreement is obtained between them. The sensitivity of the different inlet velocity profiles on temperature fluctuations downstream of the T-junction is studied and is seen to have very little effect on the results.

Kamide et al. (2009) [54] performed numerical analyses of the WATLON experiments (ΔT = 15 °C) using the finite difference method based AQUA code to analyze the temperature and velocity fields in the mixing zone downstream of the T-junction. Quantitative comparison of data showed numerical predictions exhibiting close correlation with the measurement data.

Lee et al. (2009) [78] performed LES analyses of temperature fluctuations in a mixing tee for four investigated test cases (ΔT = 31 – 35 °C) along with the corresponding structural response analysis. Two factors were highlighted to be the dominant factors causing thermal fatigue failure in T-junctions: (i) temperature difference between the mixing fluids (ΔT) and

(ii) enhanced heat transfer coefficient due to turbulent mixing. LES predictions exhibited reasonable agreement with measurement data.

Kuhn et al. (2010) [71] studied the FATHERINO experiments (ΔT = 75 °C) numerically using LES. The influence of subgrid-scale (SGS) models on LES predictions was analyzed using the classical Smagorinsky model and dynamic procedure. Results from the dynamic procedure exhibited good agreement with measurement data.

The idea of utilizing the predictive qualities of various CFD codes to analyzing turbulent T-junction flow mixing resulted in the blind CFD benchmarking exercise organized by OECD/NEA based on the Vattenfall experiments [130, 131]. A total of 29 participants took part in this exercise and 19 used the LES turbulence model to study the mixing behavior. Results showed LES predictions exhibiting close agreement with the measurement data as it occupied at least the first 8 positions of the rankings in terms of degree of correspondence to velocity, temperature, and spectral data. Reynolds Average Navier-Stokes (RANS) based approach fell short in its predictive capabilities of near-wall temperature fluctuations, an important factor in HCTF analysis.

Walker et al. (2010) [146] performed steady state CFD calculations of T-junction mixing based on adiabatic experiments at the LKE T-junction facility. Three turbulence models were employed: $k-\varepsilon$ model, $k-\omega$ based SST model and the baseline Reynolds Stress Model (BSL-RSM). Turbulent mixing and turbulent momentum transport downstream of the T-junction were seen to be underestimated by all three models. Better results were obtained with increase in model coefficient in the $k-\varepsilon$ model, resulting in improved concentration and velocity profiles.

Frank et al. (2010) [33] numerically studied isothermal and thermal mixing (ΔT = 15 °C) experiments in a T-junction using RANS [SST, BSL-RSM], Unsteady RANS and scale-resolving [Scale Adaptive Simulation (SAS) with SST model (SAS-SST)] turbulence models. Turbulent mixing phenomenon in isothermal test case predicted by the RANS models exhibited good agreement with measurement data. But results obtained from scale-resolving simulations based on thermal mixing experiments were seen to be unsatisfactory in terms of obtained accuracy in comparison with measurement data in spite of thermal striping and large-scale turbulence structure development being qualitatively well reproduced by the simulations.

Naik-Nimbalkar et al. (2010) [89] performed cross flow thermal mixing experiments (ΔT = 15 °C) in a T-junction and three-dimensional steady state simulations were subsequently performed using the k-ε turbulence model along with a temperature variance transport equation to analyze temperature fluctuations. The predicted mean temperature and velocity fields along with temperature fluctuations were consistent with the trend exhibited by measurement data.

Jayaraju et al. (2010) [49] analyzed the suitability of wall-functions in predicting thermal fluctuations caused by turbulent mixing of flows in a T-junction using the LES turbulence model. Reynolds number scaling was performed and the numerical results obtained using wall-function approach showed good agreement with the wall-resolved approach in predicting the mean velocity and temperature field. But the near-wall velocity and temperature fluctuations were consistently under-estimated by the wall-function approach.

Hannink and Blom (2011) [41] performed a numerical investigation of turbulent mixing of hot and cold fluids in a T-junction by linking two numerical models, namely, coupled CFD-FEM model and a sinusoidal model. LES was used for CFD modeling. A comparison of temperature fluctuations and stress intensity fluctuations obtained from both models are found to be in good agreement with each other.

Ndombo and Howard (2011) [91] performed LES analysis of T-junction mixing of fluids using the dynamic Smagorinsky model. Turbulent inlet conditions were applied using Synthetic Eddy Method. The addition of turbulence at the inlet had an effect on the near-wall flow in terms of variation in the near-wall temperature fluctuations and temperature-velocity correlation.

Höhne (2014) [42] performed numerical studies based on the Vattenfall T-junction experiment. The computational results showed that RANS (k-ω SST model) based simulations fail to predict a realistic mixing between the fluids. LES predicted the velocity field and mean temperatures with good accuracy. Spectral peaks are found in the range of 3 – 5 Hz in both the numerical and experimental data.

Galpin and Simoneau (2011) [35] carried out LES studies investigating the thermal mixing of fluids in a T-junction and compared the numerical results with measurement data. Two sub-grid scale models, namely, the Smagorinsky model and the structure-function model,

are used to study the sensitivity of the sub-grid scale closure. Results from the structure-function model were in better agreement with the measurement data.

Table 5. List of CFD calculations to investigate T-junction mixing over the past two decades

Investigated test facility	CFD Solver	Turbulence model	Subgrid-scale model	No. of nodes	Reference
Phénix LMFR T-junction	Trio-VF, AQUA, DINUS-3, Star-CD etc.	LES, pseudo-DNS, DNS, RANS	Selective structure function	up to 0.4 million	[9, 46]
Hitachi and Toshiba tests	FLUENT	LES	RNG, Smagorinsky-Lilly	1.3 million	[45, 78]
FATHER	CAST3M, Trio_U, Code Saturne	RANS, LES	-	0.54 million	[32, 101]
FATHERINO	FLUENT	LES	Smagorinsky-Lilly	2 million	[71]
WATLON	CFX	DES	-	1.3 million	[54, 90]
Vattenfall	FLUENT, CFX, OpenFOAM, Star-CCM+, etc.	LES, SAS-SST, DES-SST, ILES, V2F, RNG, etc.	WALE, Dynamic Smagorinsky, Spectral damping, Dynamic kinetic energy, Vreman, etc.	0.28 – 70.5 million	[131]
EXTREME	FLUENT	Standard $k-\varepsilon$, Realizable $k-\varepsilon$, SST $k-\omega$; V2F	-	2.35 million	[80]
IKE cold test rig	FLUENT	LES	Dynamic Smagorinsky	≈ 5 million	[66, 67]
LKE T-junction	CFX	URANS	-	0.44 – 7.8 million	[33, 146]
FSI	CFX	LES	WALE	7 million	[65,116]
T-Cubic	CFX	DES	-	1.73 million	[87]
MOTHER	Code_Saturne 2.0	Implicit-LES	Dissipation of numerical scheme deals with small-scales	9.12 million	[44]
Ulchin based tests	CFX	SST $k-\omega$	-	0.54 million	[50]

Kloeren and Laurien (2011) [65] performed two LESs of thermal mixing in a T-junction (ΔT = 100 °C) using the adiabatic boundary condition and the conjugate heat transfer boundary condition. The mixing region was characterized by a wavy flow movement and stable stratification. Temperature fluctuations in the near-wall region were smaller when using the conjugate heat transfer approach.

Ayhan and Sökmen (2012) [10] studied turbulent mixing in a T-junction (ΔT = 15 °C) using the RANS ($k-\varepsilon$ model) and the LES turbulence models to estimate the frequency of near-wall velocity and temperature fluctuations in the mixing region. LES results, even with a coarse mesh, exhibited good agreement with experimental results. On the other hand, RANS computations, either steady or unsteady, failed to reliably predict measurement data. A list of numerical studies on T-junction mixing at different ΔT performed over the last two decades is summarized in Table 5.

The review of existing literature discussed above point to a clear lack of experimental T-junction mock-up studies at ΔT > 100 °C. The available literature predominantly contains T-junction mixing studies at ΔT < 100 °C (see Fig. 10). Only a handful of literature (e.g. FATHER [18]) are publicly available dealing with ΔT > 100 ºC between mixing fluids. That being said, problems related to the operational safety in the new and the ageing NPPs caused by thermal striping induced fatigue related incidents are critically important to be overlooked. In a Phenomena Identification and Ranking Table (PIRT) study [125], thermal fatigue was ranked moderately high among the list of single phase nuclear reactor safety-related issues. In an OCED/NEA organized pipe failure data exchange project (OPDE) [81], over 3700 piping failure related events were analyzed and cataloged. Of these, over 128 thermal fatigue-related events (non-through wall crack/wall thinning, leak) were recorded along with 3 cases of structural failure. International Atomic Energy Agency (IAEA) has also identified thermal fatigue as one of the six ageing mechanisms that tend to reduce the working life of components in an NPP [47]. Such information highlight the need for detailed fluid mixing investigations to be performed close to the power plant conditions to gain valuable information about potential factors causing and accelerating piping degradation induced fatigue in NPPs.

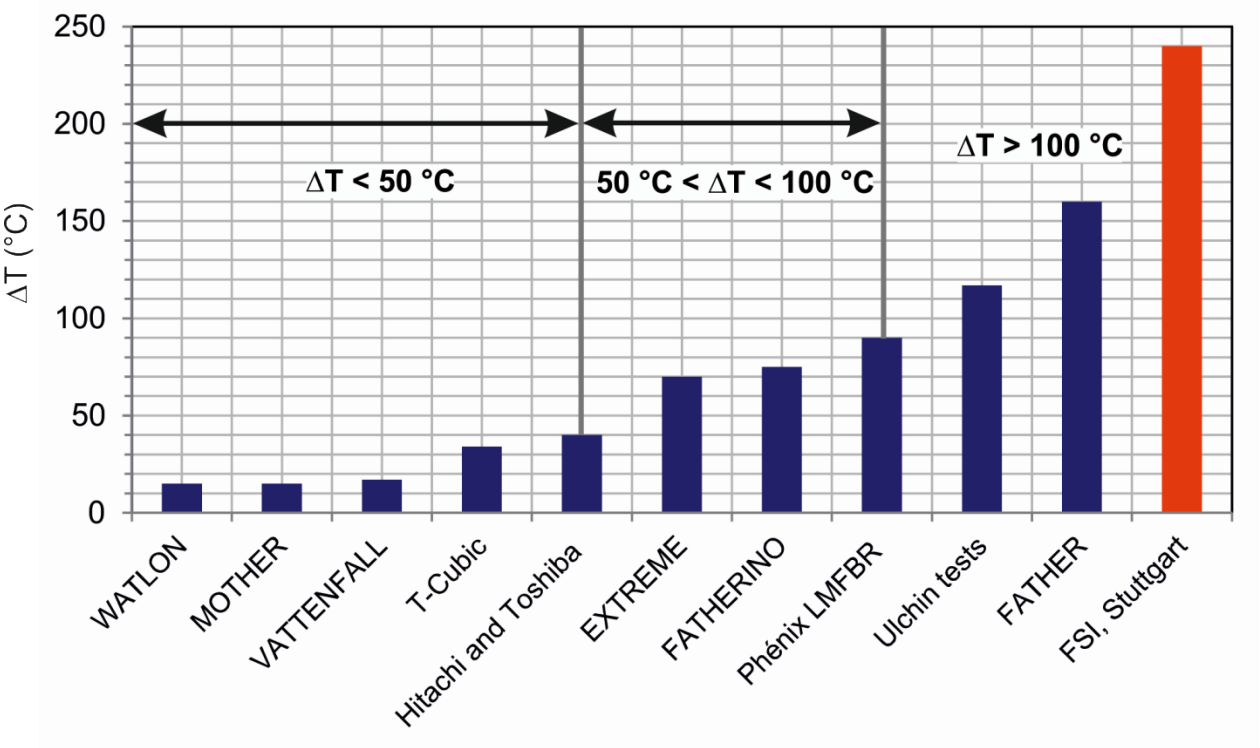

Fig. 10 Comparison of ΔT between fluids across T-junction studies in literature

In addition, complementary numerical investigations using high-fidelity CFD models at ΔT > 100 °C will broaden the understanding of the flow field dynamics and the combined experimental and numerical database will serve a much realistic input for the next stage of thermomechanical analysis that might subsequently lead to a better assessment of the fatigue usage factors and thermal stresses induced in the structure caused by the fluid temperature fluctuations.

1.3 Aim of the present study

With a clear picture regarding the current status of the existing literature, the aim of this work could be summarized as follows:

- Conducting experimental studies at the FSI test loop in the ΔT range of 60 – 240 °C to understand and describe the fluid mixing behavior in the context of high cycle thermal fatigue in horizontal T-junctions.
- Performing numerical calculations to study the turbulent flow mixing behavior in greater detail. The investigated ΔT range is 60 – 180 °C and the calculations are done using the large-eddy simulation (LES) turbulence model.

- LES predictions of critical parameters that serve as inputs to thermal fatigue analyses like near-wall mean temperature, temperature fluctuations and the frequency spectrum of thermal fluctuations will be validated against experimental data.
- Performing additional LES calculations to study the changes in the flow mixing behavior caused by higher mass flow rates in the branch pipe. This exercise is specifically done as turbulent inflow conditions could not be experimentally realized in the branch flow currently (for reasons explained in section 2.2) leading to various degrees of incomplete fluid mixing at all the investigated ΔT levels. This aspect of utilizing LES to study 'beyond design operating conditions' answers the currently unanswered question of 'What happens to the fluid mixing behavior at the FSI test loop at higher mass flow rates in the branch pipe ?'

„The true method of knowledge is experiment"

William Blake

2

EXPERIMENTAL SETUP

In view of the shortcomings discussed previously regarding fewer flow mixing studies at higher inflow temperatures, an experimental T-junction facility called the Fluid-Structure Interaction (FSI) test loop was commissioned at the Materials Testing Institute (MPA), University of Stuttgart in 2011 under the framework of network research project titled "Thermal Fatigue – Basics of the system, outflow and material characteristics of piping under thermal fatigue" funded by the German Federal Ministry of Education and Research (BMBF) [73, 116].

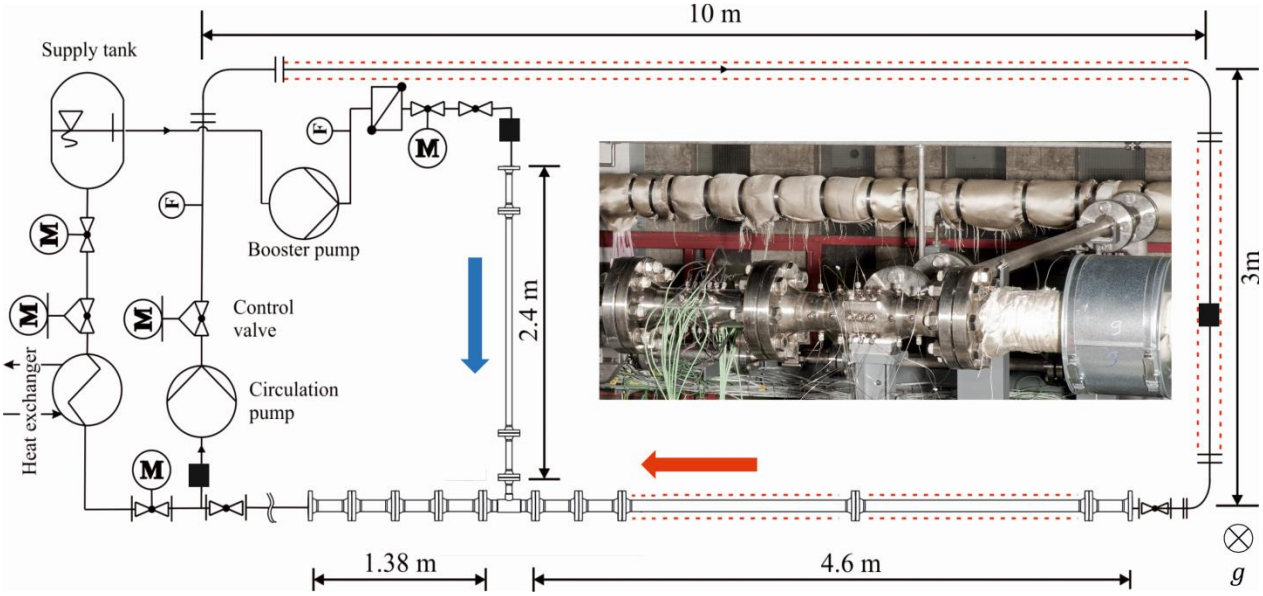

Fig. 11 Schematic of the FSI test facility and close-up view of the T-junction (red arrow – hot fluid, blue arrow – cold fluid, black square – pressure sensor)

The schematic and the close-up view of the FSI T-junction loop is shown in Fig. 11. Designed as a closed loop test facility, the FSI setup comprises a three stage membrane booster pump (Fig. 12(a)) and a circulation pump (Fig. 12(b)) to keep the fluid circulating. The booster pump is also used to pressurize the fluid. A mobile ion-exchanger unit is used to convert the input tap water into deionized water with electrical conductivity ranging from 2 – 5 μS/cm. This deionized water is used as the working fluid for the flow mixing experiments and is stored in a supply tank with a capacity of nearly 700 liters. Excluding the volume of water contained in the pipes during measurements (at least 150 liters), the remaining capacity of the supply tank is adequate to manage the water requirements of the facility during the flow mixing measurements.

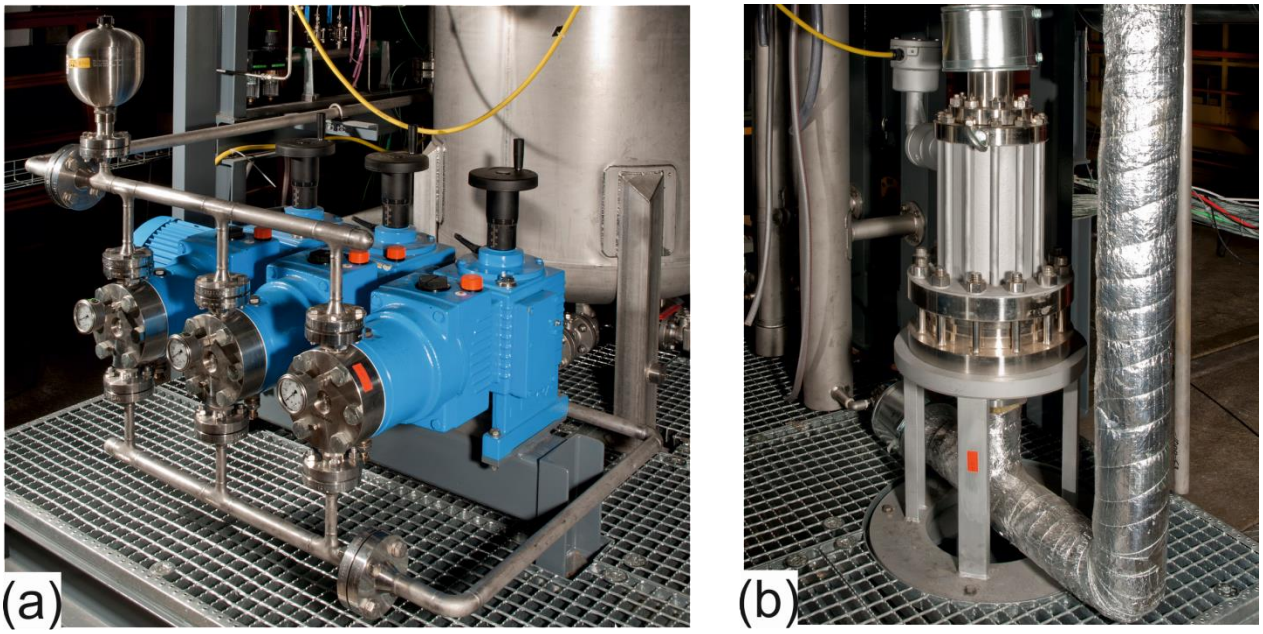

Fig. 12 Booster pump (a) and circulation pump (b) used in the FSI test facility

The main and the branch pipelines have inner diameters of 71.8 mm (D) and 38.9 mm (d), respectively. The T-junction vicinity is surrounded by different interchangeable modules (see Fig. 11) connected together by means of male-female faced flanges. This modular arrangement offers the flexibility to apply different instrumentation or measurement techniques (e.g. thermocouples, wire mesh sensors, particle image velocimetry, near-wall light emitting diode induced fluorescence and so on) to characterize the flow field.

The T-junction is forged and made of austenitic stainless steel 1.4550 (X6 CrNiNb 18-10) with sharp edges and reduced carbon content in accordance with the German Nuclear

Safety Standards Commission [68]. The piping material in the vicinity of the T-junction (both upstream and downstream regions) is made of austenitic stainless steel 1.4404 (X2-CrNiMo 17-12-2). Upstream of the T-junction, there is a straight pipe section extending for more than 60 diameters in the main and branch pipes, respectively. Flow straighteners are used at the beginning of the straight pipe sections to reduce any secondary flow effects stemming from the upstream elbows.

2.1 Instrumentation

Information about the near and in-wall temperature distribution in the mixing zone is important to ascertain the nature of the flow mixing behavior at different inflow conditions. A separate module containing thermocouples was fabricated to achieve this objective as shown in Fig. 13. Thermocouples are soldered into clamp cones of high-pressure compression connectors in the thermocouple module and are placed along the horizontal axis at three successive positions located 5, 5.5 and 6 diameters downstream from the center of the T-junction. Eight thermocouples are placed along the circumference at each axial position (24 thermocouples in total) in the mixing zone.

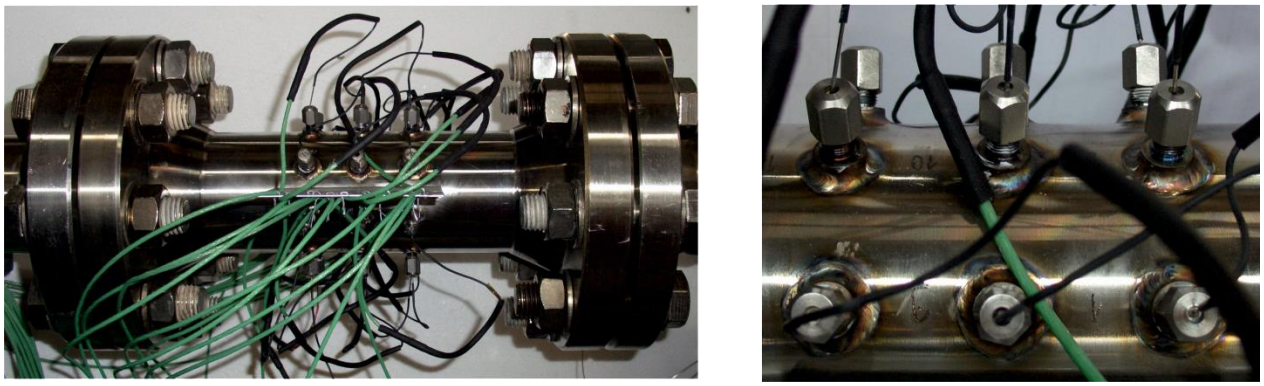

Fig. 13 Thermocouple module (left), its close-up view (right)

Of these 24 thermocouples, 16 are placed 2 mm in the flow (henceforth called ‘in-flow’ thermocouples) and the remaining 8 thermocouples are positioned in the structure at a distance of 0.15 mm from the inner wall surface (henceforth called ‘in-structure’ thermocouples). The axial position and the angular arrangement of thermocouples are depicted in Fig. 14. K-type ungrounded and shielded thermocouples, having a diameter of 0.25 mm, are installed in the thermocouple module (see Fig. 15). Data acquisition systems sample the temperature data from the thermocouples at a frequency of 100 Hz. Thermocouple diameter is chosen to be smaller in order to minimize its thermal capacity.

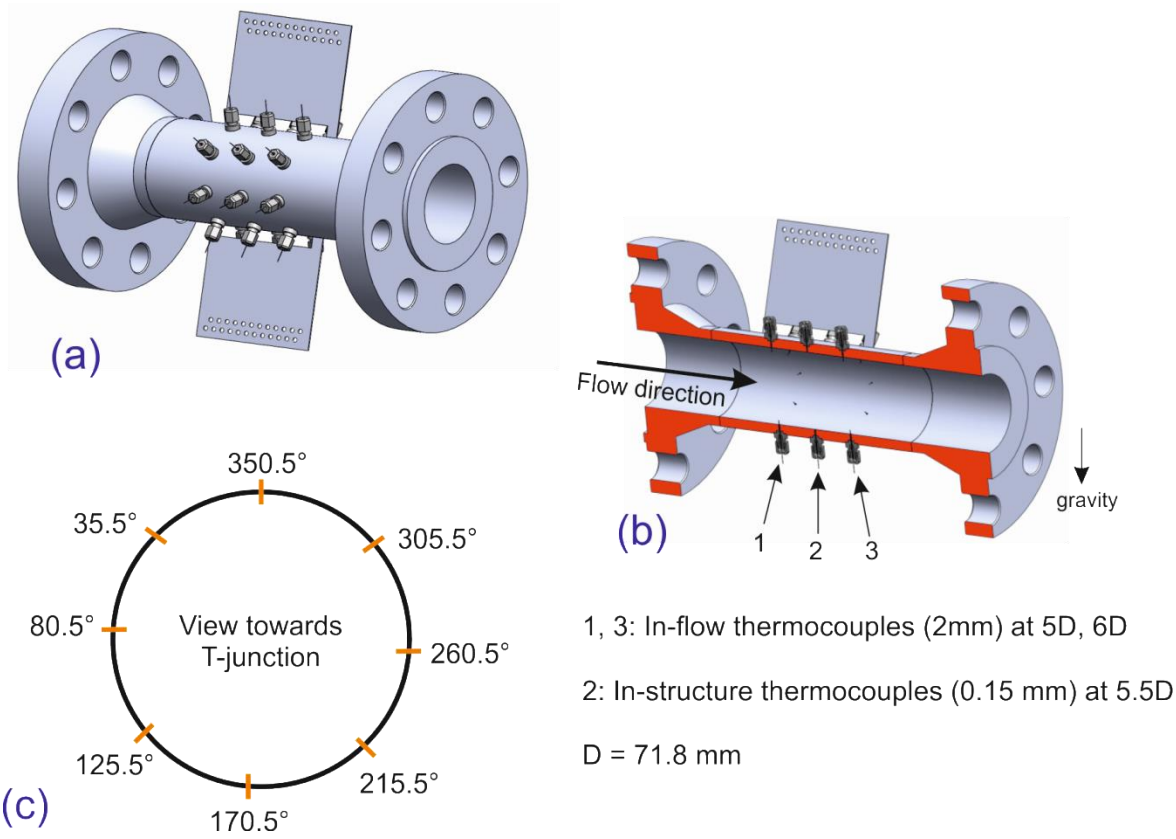

Fig. 14 Thermocouple module and its sectional view (a, b). Angular positions of thermocouples along the circumference (c)

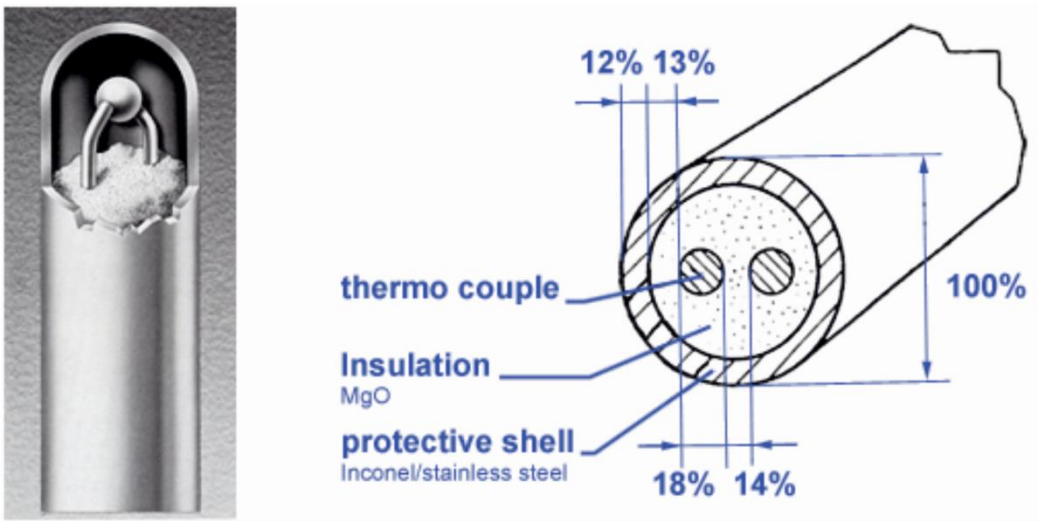

Fig. 15 View of the sheathed ungrounded thermocouple [27]

Extensive analyses have been previously carried out to decide on the size of the thermocouple used in the thermocouple module. The influence of thermocouple on the

flow, its dynamic and attenuation characteristics have been previously studied in detail by Kuschewski (2015) [72].

Apart from thermocouple module in the mixing zone, in-structure (0.25 mm diameter, 100 Hz, 2 mm into the structure) and surface thermocouple instrumentation (1 mm diameter, 30 Hz frequency) are placed upstream of the T-junction in both the main and branch pipes to characterize the upstream flow behavior with rise in ΔT between the fluids or with changes to the inflow velocity of fluids.

The pressure in the system is continuously monitored using three pressure transmitters in the FSI test loop. Their positions are indicated by the black colored squares shown in Fig. 11. Two Coriolis mass flow meters are used in the main and branch pipes to measure the flow rates of fluids. The accuracy of the instrumentation used in the FSI test loop is detailed in Table 6.

Table 6. Instrumentation used in the FSI test facility

Device	Measurement range	Accuracy
Thermocouple [27]	- 200 °C to +1150 °C	Max [< 1.5 °C or 0.4 % of Temperature]
Mass flow meter [28]	up to 1 kg/s	± 0.2 % of the mass flow rate
Pressure sensor [115]	0 – 100 bar	± 0.3 % of the upper range value

The following section describes the start-up procedure used to initiate fluid mixing experiments along with the fluid heating procedure used in the FSI test loop.

2.2 System start-up, fluid heating, and cooling

Firstly, the piping system is filled with deionized water using the following procedure: The Booster pump is switched on and deionized water from the supply tank flows continuously through the branch pipe (see Fig. 11), reaches the T-junction and the entire test loop is filled within 10 – 15 minutes. Fluid pressure is then slowly increased and air in the system is subsequently vented out manually using the venting outlets installed in the facility. The circulation pump is then switched on enabling continuous flow of water in the main pipe. Heating the fluid flowing through the main pipe is the next step is and is accomplished using heating mats made from ceramic pad elements (Fig. 16) attached to the outer surface of the

pipe. A total of 8 heating mats are attached along the length of the main pipe section and are controlled using the proportional-integral-derivative controllers (PIDs) to achieve the desired temperature level on the outer pipe surface. In general, fluid flow inside the main pipe is sequentially heated at the rate of 40 °C/hour. The heating mats are powered using three separate heat treatment units [111] as shown in Fig. 16 with each unit having an output power of 84 kW.

Fig. 16 Heating mat (top left), its arrangement on the pipe surface (top right), and the powering heat treatment units (bottom)

Since the FSI setup has a closed loop design, part of the mixed flow during measurements (at a higher temperature than the cold fluid) downstream of the T-junction is diverted to a heat exchanger unit where the fluid temperature is brought down to about 18 – 20 °C and fed back again into the supply tank. This ensures that the volumetric capacity of the cold deionized water in the supply tank is always maintained within an acceptable limit to allow for continuous operation of the FSI test loop. The remaining part of the mixed flow simply keeps circulating within the main pipe and is reheated to the required temperature level as it flows through regions covered by heating mats. Thus the hot and cold fluid temperatures are maintained at their respective levels using heating mats and the heat exchanger unit, respectively. In terms of thermal mixing, the FSI test facility is designed to operate at a

maximum ΔT between the fluids of nearly 240 °C and the system pressure during such measurements could be as high as 75 bar.

Reynolds number (Re) calculations are used to categorize the pipe flows as laminar (Re < 2300), transitional (2300 < Re < 4000) or turbulent (Re > 4000) [105]. It is defined using the formula

$$Re = uD/\nu \quad (2)$$

where u is fluid velocity, D the pipe diameter and ν the kinematic viscosity of the fluid flowing through the pipe. Based on this formulation, turbulent fluid flow conditions could be easily achieved in the main pipe ($Re_m > 20000$) due to the maximum operational mass flow rate of 1 kg/s offered by the circulation pump. On the other hand, transitional flow is the maximum achievable flow condition in the branch pipe ($Re_b = 3200 – 3600$) due to the fact that the booster pump used in the branch pipe could not be operated beyond the mass flow rate limit of 0.1 kg/s. Such large Reynolds number differences between the main and branch pipes have clear consequences on the flow mixing behavior as discussed later in the results section.

„All models are wrong, but some models are useful"

-George P.E. Box

3

NUMERICAL APPROACH

3.1 Background

The turbulent mixing of fluids produces a wide range of flow scales in the vicinity of the T-junction. The turbulence could be considered to be composed of eddies of different sizes. Eddies of the largest size could be comparable with the diameter of the pipe. The idea of energy cascade within eddies was put forth by Richardson [110] and excerpts explaining this idea [105] is as follows:

"Richardson's notion is that the large eddies are unstable and break up, transferring their energy to somewhat smaller eddies. These smaller eddies undergo a similar break-up process, and transfer their energy to yet smaller eddies. This energy cascade – in which energy is transferred to successively smaller and smaller eddies – continues until the Reynolds number is sufficiently small that the eddy motion is stable, and molecular viscosity is effective in dissipating the kinetic energy. Richardson (1922) succinctly summarized the matter thus:

Big Whorls have little whorls,
Which feed on their velocity;
And little whorls have lesser whorls,
And so on to viscosity
(in the molecular sense)."

Fig. 17 depicts the energy cascade process involving eddies of different sizes. This classification is done on the basis of Kolmogorov's second similarity hypothesis explained in Pope (2000) [105]. Most of the energy is contained in the larger eddies and is denoted by

the term 'energy-containing range'. This energy is dissipated by the viscous action at the smallest scales (also called 'Kolmogorov scales') and is denoted by the term 'dissipation range'. There is an intermediate range where flow scales are smaller than the energy-containing range but considerably larger than the dissipation range called the 'inertial subrange'. As the name implies, motions in this range are determined by the inertial effects and the viscous effects are negligible.

Kolmogorov's hypothesis of local isotropy states that "At sufficiently high Reynolds number, the small-scale turbulent motions are statistically isotropic". This means that while the large eddies are anisotropic and affected by the boundary conditions of the flow, such directional biases of the large eddies are lost in the energy cascade process by which energy is transferred to successively smaller and smaller eddies.

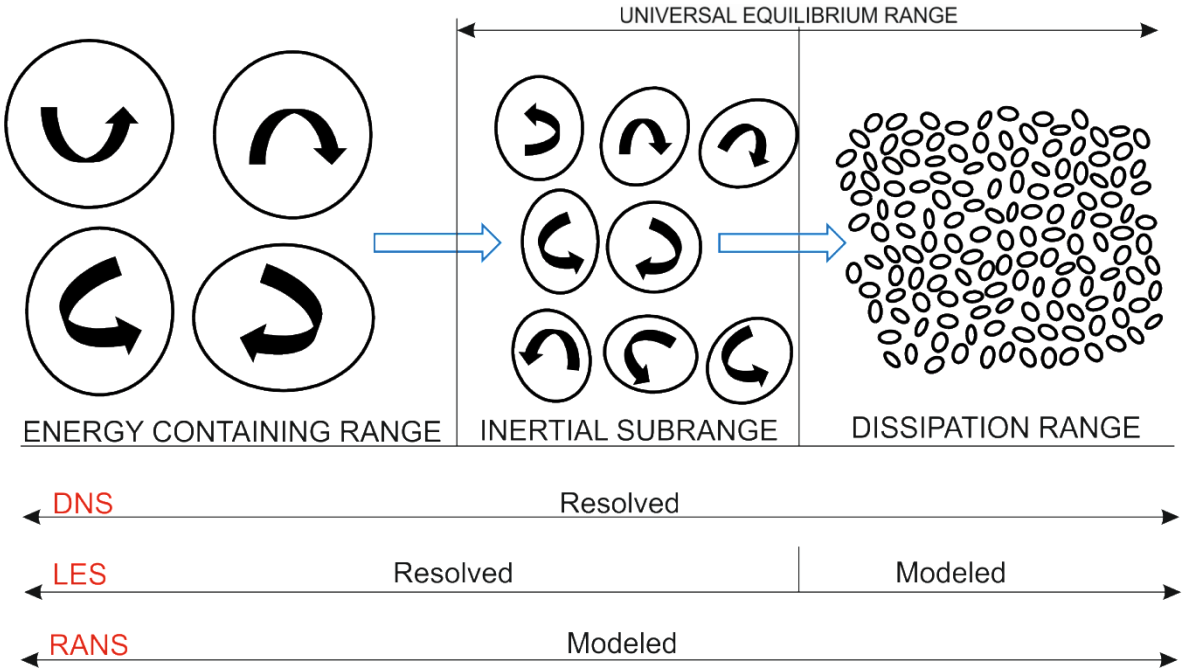

Fig. 17 Simplified illustration of the energy cascade process involving different flow scales and the capability of the numerical turbulence models to resolve them

As a result, the statistics of the small-scale motions are in a sense universal and is similar in every high Reynolds number turbulent flow. The timescales of such small eddies are so small in comparison with the large eddies that they can quickly adapt to maintain a dynamic equilibrium with the energy transfer rate imposed by the large eddies [105].

The attempt to numerically investigate and resolve the different scales of motion in a turbulent flow gave rise to three broadly classified CFD approaches that are commonly used today, namely, (i) Direct numerical simulation (DNS), (ii) Large-eddy simulation (LES), and (iii) Reynolds-averaged Navier-Stokes (RANS) approach.

DNS approach resolves the entire spectrum of flow scales ranging from the largest eddies to the smallest eddies (see Fig. 17). The conservation equations (mass, momentum, and energy) are solved directly, making the solution highly accurate but computationally very expensive. This method is not feasible for analyzing flows involving high Reynolds numbers for the foreseeable future barring any breakthroughs in high-performance computing. The opposite is the RANS based approach where the conservation equations are time-averaged instead of solving for directly making it computationally affordable. This method is predominantly used everywhere including industrial applications where the mean flow field information is mainly desired. Nonetheless, it falls short in its predictions of fluctuating components since the equations are time-averaged making it the least accurate method. LES, motivated by the limitations of the DNS and the RANS based approaches, incorporates both the traits whereby the large eddies which are geometry dependent are solved for directly (as in DNS) and the small eddies which are statistically isotropic and universal are modeled (similar to RANS). Computationally, it is less expensive than DNS but more accurate than RANS making it the suitable choice for studying the complex flow phenomenon like the T-junction mixing.

3.2 Large-eddy simulation (LES)

This study makes use of the LES method to numerically study T-junction mixing flows involving high ΔT between the fluids. ANSYS CFX solver is used to perform the LES calculations. The basic concept behind this approach involves the separate treatment of large eddies (which are geometry dependent) and the small eddies (which are considered isotropic).

Governing equations for LES are derived by applying a filtering process to the time-dependent conservation equations. By this process, a governing variable (φ) is split into a filtered component ($\bar{\varphi}$) and a residual component (φ'). So the filtering process effectively separates eddies with sizes smaller than the grid spacing used in the numerical calculations [114]. Such smaller eddies are accounted for using the sub-grid scale (SGS) modeling

approach while the filtered component – being three dimensional and time dependent – represents the motion of large eddies.

3.2.1 Filtered governing equations

The filtered equations of mass and momentum conservation are as follows [6]

$$\frac{\partial \rho}{\partial t} + \frac{\partial (\rho \bar{u}_i)}{\partial x_i} = 0 \tag{3}$$

$$\frac{\partial (\rho \bar{u}_i)}{\partial t} + \frac{\partial}{\partial x_j}\left(\rho \bar{u}_i \bar{u}_j\right) = -\frac{\partial \bar{p}}{\partial x_i} + \frac{\partial \sigma_{ij}}{\partial x_j} - \frac{\partial \tau_{ij}}{\partial x_j} + f_i \tag{4}$$

where $\bar{u}$ and $\bar{p}$ represent the filtered component of velocity and pressure. i, j, k are the tensor indices while τ_{ij} is the subgrid-scale shear stress tensor, f_i is the source term accounting for buoyancy effects and is defined as

$$f_i = g(\rho - \rho_{ref}) \tag{5}$$

where g is the acceleration due to gravity, ρ_{ref} is the reference density, usually taken to be the average density of mixing fluids. The density difference $(\rho - \rho_{ref})$ is evaluated directly during the calculations.

σ_{ij} is the stress tensor due to molecular viscosity (μ) and is defined as

$$\sigma_{ij} = \mu\left[\frac{\partial \bar{u}_i}{\partial x_j} + \frac{\partial \bar{u}_j}{\partial x_i}\right] - \frac{2}{3}\mu \frac{\partial \bar{u}_k}{\partial x_k}\delta_{ij} \tag{6}$$

The conservation of energy equation is defined as

$$\frac{\partial (\rho \bar{h})}{\partial t} + \frac{\partial}{\partial x_j}\left(\rho \bar{h} \bar{u}_j\right) = \frac{\partial}{\partial x_j}\left(\lambda_{\text{eff}} \frac{\partial \bar{T}}{\partial x_j}\right) \tag{7}$$

where $\bar{h}$ and $\bar{T}$ represent filtered enthalpy and temperature, λ_{eff} represents an effective coefficient which includes both molecular conduction and SGS contribution and is defined as

$$\lambda_{\text{eff}} = \lambda + \frac{\mu_t c_p}{Pr_t} \tag{8}$$

where λ is thermal conductivity, c_p is specific heat capacity at constant pressure, μ_t is turbulent eddy viscosity and Pr_t is subgrid-scale turbulent Prandtl number.

3.2.2 Subgrid-scale modeling

Subgrid-scale (SGS) stresses resulting from the filtering operation are unknown and require modeling. Eddy viscosity modeling approach is used in ANSYS CFX for SGS modeling, which presumes a linear relation between the SGS stress tensor and the filtered rate of strain tensor. It is defined as

$$\left(\tau_{ij} - \frac{1}{3}\tau_{kk}\delta_{ij}\right) = -2\mu_t \bar{S}_{ij} \tag{9}$$

where μ_t is the eddy viscosity to be modeled. $\bar{S}_{ij}$ is the rate of strain tensor for the resolved scale and is given by

$$\bar{S}_{ij} = \frac{1}{2}\left[\frac{\partial \bar{u}_i}{\partial x_j} + \frac{\partial \bar{u}_j}{\partial x_i}\right] \tag{10}$$

The SGS eddy viscosity is modeled using the Wall-Adapting Local Eddy-Viscosity (WALE) model. The generic form of eddy-viscosity model could be written as

$$\nu_t = (C_m \Delta)^2 \, \overline{OP}\,(x,t) \tag{11}$$

where C_m is the model constant, Δ the sub-grid characteristic length scale and $\overline{OP}\,(x,t)$ is "*an operator in space and time, homogenous to a frequency, and defined from the resolved fields*" [93]. The operator $\overline{OP}\,(x,t)$ used in the WALE model is defined based on the following properties as defined in Nicoud and Ducros (1999) [93]: (i) it should be invariant to any coordinate translation or rotation, (ii) it could be easily accessed in any kind of computational grid, (iii) it is a function of both the strain and rotation rates, (iv) it goes to zero at the wall so that neither damping function nor dynamic procedure are needed to reproduce the effect of no-slip condition. Thus the WALE model is based on a tensor invariant and reproduces appropriate scaling at the wall. It is defined as

$$\nu_t = (C_w \Delta)^2 \frac{\left(S_{ij}^d \, S_{ij}^d\right)^{3/2}}{\left(\bar{S}_{ij} \, \bar{S}_{ij}\right)^{5/2} + \left(S_{ij}^d \, S_{ij}^d\right)^{5/4}} \tag{12}$$

$C_w = 0.5$ is the WALE model constant, S_{ij}^d denotes the traceless part of the square of the velocity gradient tensor ($\bar{g}_{ij}$) and both are defined as follows

$$S_{ij}^d = \frac{1}{2}\left(\bar{g}_{ij}^2 + \bar{g}_{ji}^2\right) - \frac{1}{3}\delta_{ij}\bar{g}_{kk}^2 \tag{13}$$

$$\bar{g}_{ij} = \frac{\partial \bar{u}_i}{\partial x_j} \tag{14}$$

3.2.3 Near-wall flow modeling

Strong gradients of flow variables exist near the wall due to the no-slip condition. In addition, molecular viscosity plays a significant role in the transport of momentum and heat inside the boundary layer. The above mentioned flow phenomenon should be realistically reproduced in a numerical model in order to obtain the best possible results. Near-wall modeling in ANSYS CFX is based on two approaches:

(i) The **wall function method** which imposes empirical formulas near the wall without resolving the boundary layer. This method is an extension of the method described in Launder and Spalding (1974) [76].

(ii) The **Low Reynolds number (low-Re)** method which resolves the details of the boundary layer using very small mesh length scales in the direction normal to the wall. Here, the Reynolds number refers to the turbulent Reynolds number in the near-wall region. Unlike the wall function method, computations in the low-Re method are extended through the viscosity affected regions near the wall.

LES turbulence model in ANSYS CFX utilizes the **automatic wall treatment** method which allows for a gradual switch between the wall function method and the low-Re method as the mesh resolution becomes higher near the wall. Similar to the velocity boundary layer, the thermal boundary layer in the near-wall region is modeled using the **thermal law-of-the-wall function** of Kader (1981) [53]. Further details are elaborately described in ANSYS CFX modeling and theory guide [5, 6].

3.3 Computational mesh

Two different upstream lengths (see Fig. 18) have been selected for the present study to perform the numerical T-junction mixing calculations: Hot inflow length – 4D or 15D; Cold inflow length – 5d or 10d; Mixing zone length – 20D. The decision to use two different upstream domain lengths was based on the observation of cold flow penetration into the main pipe and hot flow into the branch pipe occurring over longer distances at higher ΔT (> 140 °C) during the measurements.

Thus the computational domain with a shorter upstream length is used to study flow mixing experiments involving very little or moderate distance upstream flow penetration.

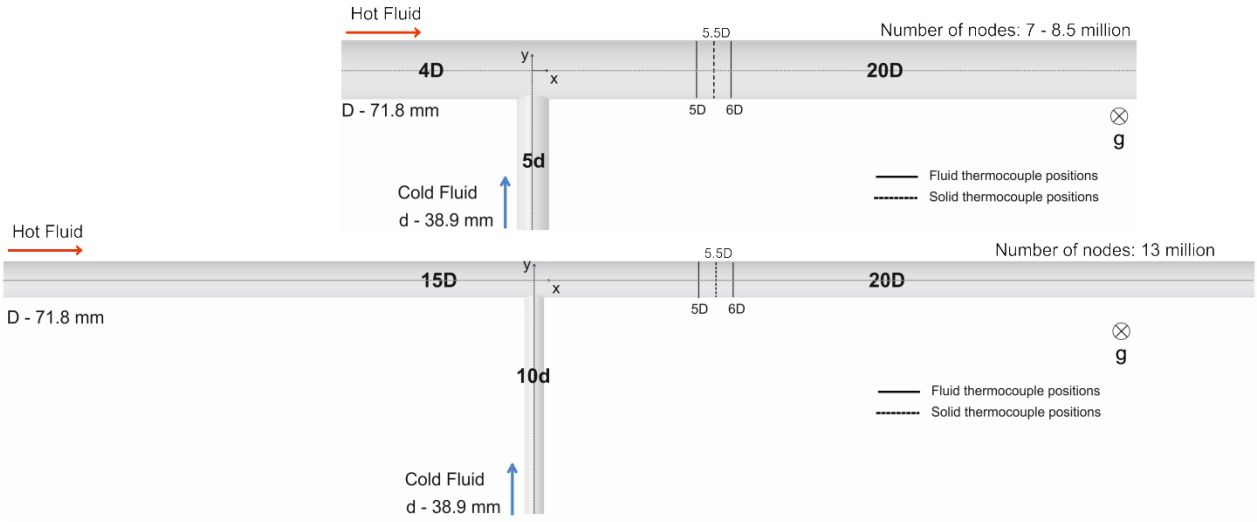

Fig. 18 FSI T-junction geometry having shorter upstream length (top) and longer upstream length (bottom) used for LES calculations

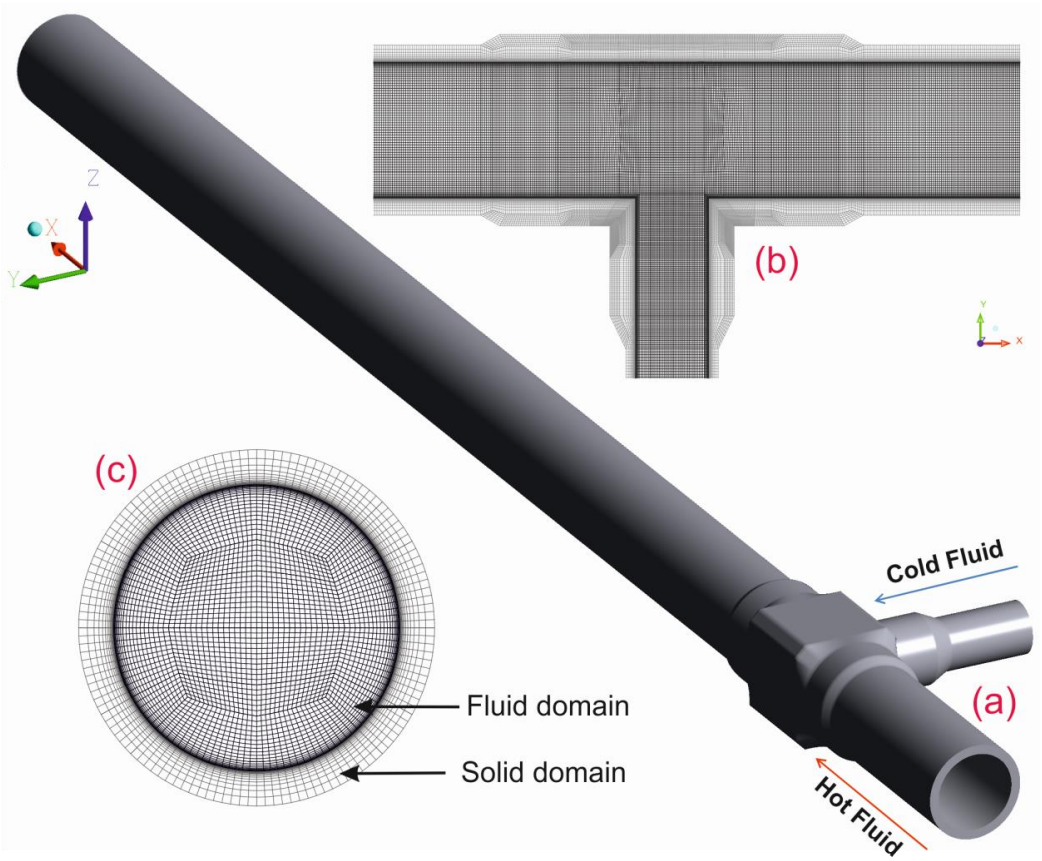

Fig. 19 View of computational domain (a), mesh at the T-junction (b), and cross-sectional mesh (c)

On the other hand, the computational domain with a longer upstream length is used to study flow mixing experiments where the measurement data indicated a longer distance upstream flow penetration in both the main and the branch pipe, respectively.

3.4 Assessment of mesh resolution

It is essential to ensure adequate resolution of the numerical mesh in order to expect LES results of good accuracy. Standard methods are established in literature to assess the appropriate mesh size based on the inflow conditions. They are (i) y-plus (y^+) value estimation, (ii) assessment of non-dimensional grid size (Δx^+, Δy^+, Δz^+), and (iii) energy length scale (L_R) and Taylor micro-scale (λ) based estimation. Each method is briefly discussed below.

3.4.1 y-plus (y^+) value estimation

This non-dimensional parameter – representing the distance of the first node from the wall measured in wall units – is used to assess the near-wall mesh resolution. It is defined as follows:

$$y^+ \equiv (y * u_\tau)/\nu \tag{15}$$

where y is the distance of the nearest node from the wall, u_τ the friction velocity and ν the kinematic viscosity. Near-wall regions are categorized on the basis of y^+ values as follows [45, 105]:

- Viscous stress dominated laminar sublayer is defined as $y^+ < 5$;
- The buffer layer, a transition region between viscosity dominated and turbulence dominated regions, is defined as $y^+ < 30$;
- The contribution of viscosity to wall shear stress diminishes beyond $y^+ > 50$ through y = 0.05D.

The distance of the nearest node from the wall used in this study ranges between 0.025 and 0.04 mm, which corresponds to $0 < y^+ < 3$ throughout the computational domain with the exception at the T-junction where the highest y-plus values are registered ($5 < y^+ < 9$) in all the LES cases.

3.4.2 Non-dimensional grid size (Δx^+, Δy^+, Δz^+) estimation

The method formulated by Piomelli (2001) [103] to calculate the non-dimensional grid spacing ($\Delta {x_i}^+$) is defined as follows

$$\Delta x_i{}^+ = (\Delta x_i * u_\tau)/\nu \quad (16)$$

where u_τ is friction velocity, ν the kinematic viscosity and the tensor index i represents grid spacing along the x, y, z directions. A range of values were suggested in his study to ensure that the numerical mesh is adequately resolved along all the three directions. A comparison of $\Delta x_i{}^+$ values used in the present study and the recommended range of values in literature are shown in Table 7.

Table 7. Non-dimensional grid spacing comparison in the present study and literature

Parameter	Present study	Piomelli (2001) [103]
Δx^+	16 – 29	50 – 150
$*\Delta z^+$	9 – 15	15 – 40

* $\Delta y^+ = \Delta z^+$ in the present study

3.4.3 Energy length scale (L_R) and Taylor micro-scale (λ) estimation

This method was formulated by Addad et al. (2008) [2] involving a precursor RANS simulation to calculate L_R and λ, which are defined as follows:

$$\lambda = \sqrt{10k\nu/\varepsilon} \quad (17)$$

$$L_R = k^{3/2}/\varepsilon \quad (18)$$

where k is the turbulent kinetic energy, ε is the turbulent dissipation rate and ν the kinematic viscosity. The following condition is then applied to arrive at an optimum value of average mesh size (Δ):

$$\Delta = \max(\lambda, L_R/10) \quad (19)$$

λ and $L_R/10$ values obtained from the precursor RANS simulations are in the range 1.26 – 1.54 mm and 1.6 – 2.2 mm, respectively. The meshes used for LES calculations have an average cell size of 1.1 – 1.2 mm which satisfies the aforementioned criteria.

Thus the numerical meshes are evaluated against the three criterion mentioned above, and having satisfied it, are used to performing the T-junction flow mixing calculations in the present study.

3.5 Initial and boundary conditions

Separate single pipe simulations – based on the method proposed by Hu and Kazimi (2006) [45] – were initially performed to obtain fully developed velocity profiles for both the main and branch pipes. Measurement data from the surface thermocouple instrumentation upstream of the T-junction have indicated a slight thermal stratification behavior within the hot flow in all the investigated cases as illustrated in Fig. 20. This phenomenon is implemented at the hot inlet as a boundary condition using the 'initialize profile data' functionality in ANSYS CFX.

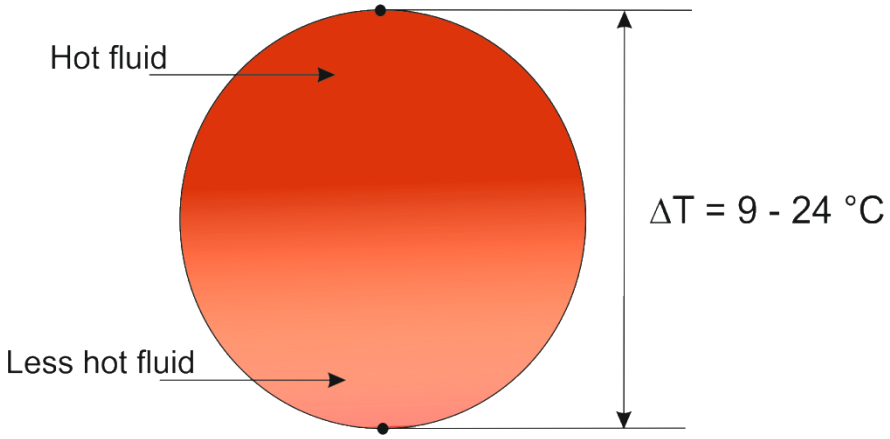

Fig. 20 Thermal stratification within the hot flow

Room temperature values (see Table 8) are used at the cold inlet. A zero-averaged static pressure boundary condition has been used at the outlet. Conjugate heat transfer is applied at the fluid-solid interface region to account for the heat transfer between the fluid and structure. No slip boundary condition with automatic wall treatment is used at the inner wall. Adiabatic heat transfer boundary condition is applied at the outer wall region. The physical properties of water (e.g. density and viscosity) vary with temperature. This variation is implemented in all the LES calculations using the IAPWS library function [144] in ANSYS CFX.

Addition of synthetic vortices at the inlets to generate a realistic turbulent flow was a method proposed by Sergent (2002) [124] and formulated by Mathey et al. (2006) [83]. This method has been used previously in LES calculations with inflow conditions obtained from one of the FSI test measurements to check for any differences between the LES results with and without synthetic vortices at the inlets [37]. The exercise showed very little

differences in analyzing relevant quantities like the mean and fluctuating quantities of temperature and velocity confirming the fact that the main generation of turbulence in T-junction flows is caused by the mixing of fluids. Thus all the LES cases presented here contain no perturbation of flow whatsoever at the inlets.

With all the boundary conditions mentioned above, steady state simulations of T-junction fluid mixing are performed using the $k-\omega$ SST turbulence model in the next step. LES cases are finally initialized using the previously converged solution from the steady state simulations. This method of initializing LES based on steady state simulation result is a standard best practice guideline recommended by ANSYS (2015) [7]. A description of this method is depicted below in Fig. 21.

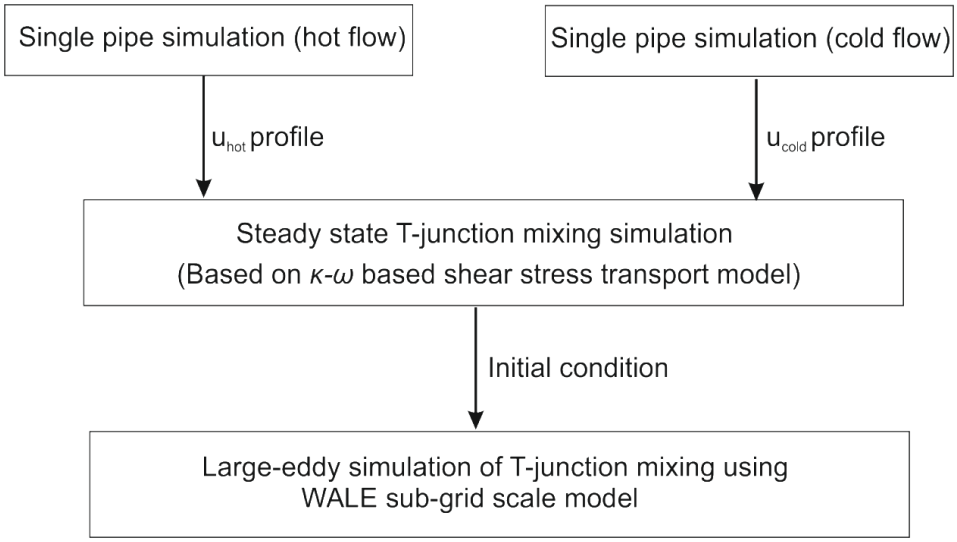

Fig. 21 Flowchart of the numerical approach used in the present study

A second order high-resolution scheme is used for the spatial discretization of the mass and energy conservation equations while a second order central differencing scheme in used for discretizing the momentum equation. Second order backward Euler method is used for temporal discretization in the present study. More details on the element based finite-volume method along with the spatial and temporal discretization schemes used in this study are described in the section A.1.

Time step (Δt) for all the LES cases is chosen to be 0.2 ms, which keeps the Courant number less than unity in each coefficient loop iteration. The total physical time simulated is 30 – 35 seconds and the last 20 – 22 seconds of data, being statistically steady, are used to analyze the turbulent statistics.

4

RESULTS

Each case shall be identified using the ΔT between fluids while explaining the flow characteristics in the mixing region for the sake of clarity and clear understanding. Unless otherwise stated, all the temperature and velocity data are normalized. The formulation used for normalization is given below.

The instantaneous fluid temperature (T) is normalized using the formula:

$$T^* = \frac{T - T_b}{\Delta T} \tag{20}$$

where $\Delta T = T_m - T_b$ is the temperature difference between the mixing fluids. The terms T_m and T_b denote fluid temperatures in the main and branch pipes, respectively.

The normalized mean temperature is defined as:

$$\overline{T^*} = \frac{1}{N}\sum_{i=1}^{N} T^* \tag{21}$$

Normalized temperature fluctuation intensity is defined using the root mean square (RMS) formulation as follows:

$$T^*_{rms} = \sqrt{\frac{1}{N}\sum_{i=1}^{N}(T^* - \overline{T^*})^2} \tag{22}$$

where N represents the number of sampled data points.

The instantaneous fluid velocity (u) is normalized using the formula:

$$u^* = \frac{u}{u_{mix}} \tag{23}$$

where $u_{mix} = \sqrt{u_m^2 + u_b^2}$ is the mixing velocity of the fluids with u_m and u_b being the inflow velocities in the main and branch pipes, respectively. The normalized mean velocity is defined as:

$$\overline{u^*} = \frac{1}{N}\sum_{i=1}^{N} u^* \tag{24}$$

Normalized temperature fluctuation intensity is defined using the root mean square (RMS) formulation as follows:

$$u^*_{rms} = \sqrt{\frac{1}{N}\sum_{i=1}^{N}(u^* - \overline{u^*})^2} \tag{25}$$

Also, most of the figures discussed below contain red and blue arrows upstream of the T-junction representing the hot and cold inflows. Additionally, the main and the branch flows in the figures are identified by their mass flow rates rather than velocities. The results presented in this study are discussed in three separate parts as follows:

(i) Mixing behavior of flows at ΔT = 60 °C – 180 °C

The mass flow rate in the main and the branch pipes are fixed at 0.4 kg/s and 0.1 kg/s, respectively. Hot inflow temperature is increased gradually yielding ΔT amplitude between the fluids in the range of 60 – 180 °C. Flow field characteristics are initially analyzed followed by quantitative analysis and comparison of measurements and LES data. For the aforementioned ΔT range between the fluids, measurements have also been performed at different mass flow rates in the main pipe of 0.3 kg/s and 0.5 kg/s while the branch flow rate is maintained at 0.1 kg/s. These results are discussed in the Appendix section A.2.

(ii) Mixing behavior of flows at ΔT = 233 °C

This measurement is a special case scenario whereby the FSI test facility is taken to its highest operating temperature resulting in the ΔT amplitude between fluids of 233 °C. No LES calculation is performed for this case, the reasons for which shall be described when elaborately discussing the results. The mass flow rate in the main and branch pipes for this measurement are set at 0.4 kg/s and 0.1 kg/s, respectively.

(iii) Mixing behavior of flows at increased branch flow velocities

The main limitation of the FSI facility is the maximum mass flow rate of the branch pipe (0.1 kg/s) being inadequate to cause complete turbulent mixing of flows. So it was decided to perform LES analyses where the branch flow rates were doubled and tripled to 0.2 kg/s and 0.3 kg/s, respectively while maintaining a flow rate in the main pipe of 0.4 kg/s. The ΔT amplitude between the fluids were 65 °C and 143 °C, respectively. Results of the flow mixing at elevated branch flow rates offers valuable insights into the flow behavior that could be expected when the FSI test loop is upgraded to operate at such branch flow rates.

4.1 Mixing behavior of flows at ΔT = 60 °C – 180 °C

Table 8 contains the inflow conditions at the main pipe and the branch pipe for the measurements performed with ΔT between the fluids in the range of 60 – 180 °C.

Table 8: Inflow conditions at the FSI test facility

Case #	ΔT (°C)	T_m* (°C)	$\dot{m}_m$ (kg/s)	u_m (m/s)	T_b* (°C)	$\dot{m}_b$ (kg/s)	u_b (m/s)	u_{mix} (m/s)
1	65	85	0.4	0.101	20	0.1	0.084	0.132
2	107	128	0.4	0.105	21	0.1	0.084	0.135
3	126	147	0.4	0.107	21	0.1	0.084	0.136
4	143	165	0.4	0.109	22	0.1	0.084	0.138
5	159	181	0.4	0.112	22	0.1	0.084	0.14
6	178	201	0.4	0.115	23	0.1	0.084	0.142
Pressure – 30 to 70 bar								

* suffixes m and b denote the main and the branch pipe, respectively

Table 9 shows the non-dimensional parameters calculated for the inflow conditions in Table 8 such as relative density ($\Delta\rho/\bar{\rho}$), Reynolds number in the main and branch pipes (Re_m, Re_b), Richardson number (Ri), and Viscosity ratio (μ_m/μ_b).

Table 9: Non-dimensional parameters for inflow conditions in Table 8

Case #	ΔT (°C)	$\Delta\rho/\bar{\rho}$ (in %)	Re_m	Re_b	Ri	Re_m/Re_b (R)	μ_m/μ_b
1	65	3	21200	3200	1.2	6.6	0.33
2	107	6.5	33160	3300	2.5	10.1	0.22
3	126	8.5	38950	3340	3.2	11.6	0.185
4	143	10.3	43920	3540	3.8	12.4	0.174
5	159	12.4	48850	3500	4.4	13.9	0.155
6	178	15	54060	3500	5.2	15.4	0.14

4.1.1 Velocity field in the mixing region

Figs. 22 and 23 show the instantaneous and the mean velocity distribution at the T-junction for all the investigated cases. Cold flow (Re_b = 3200 – 3600) from the branch pipe enters the main pipe and travels a short distance before being turned towards the downstream direction by the high Reynolds number hot flow.

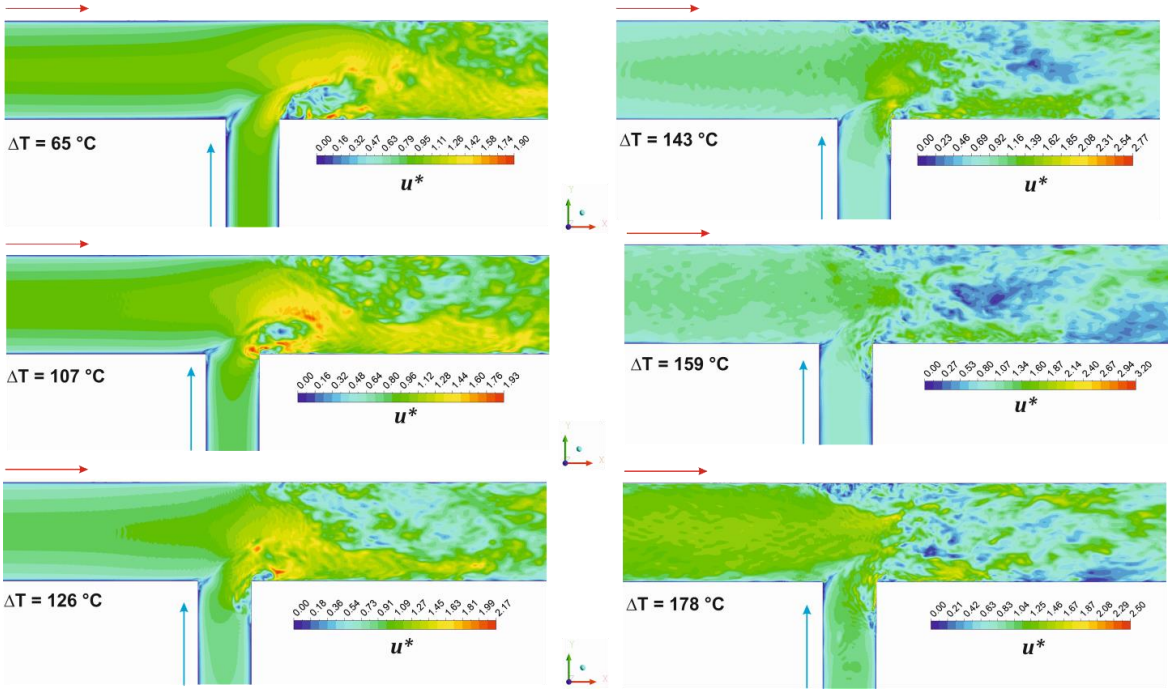

Fig. 22 Instantaneous velocity field (t = 30s) at the T-junction mid-plane (x-y axis)

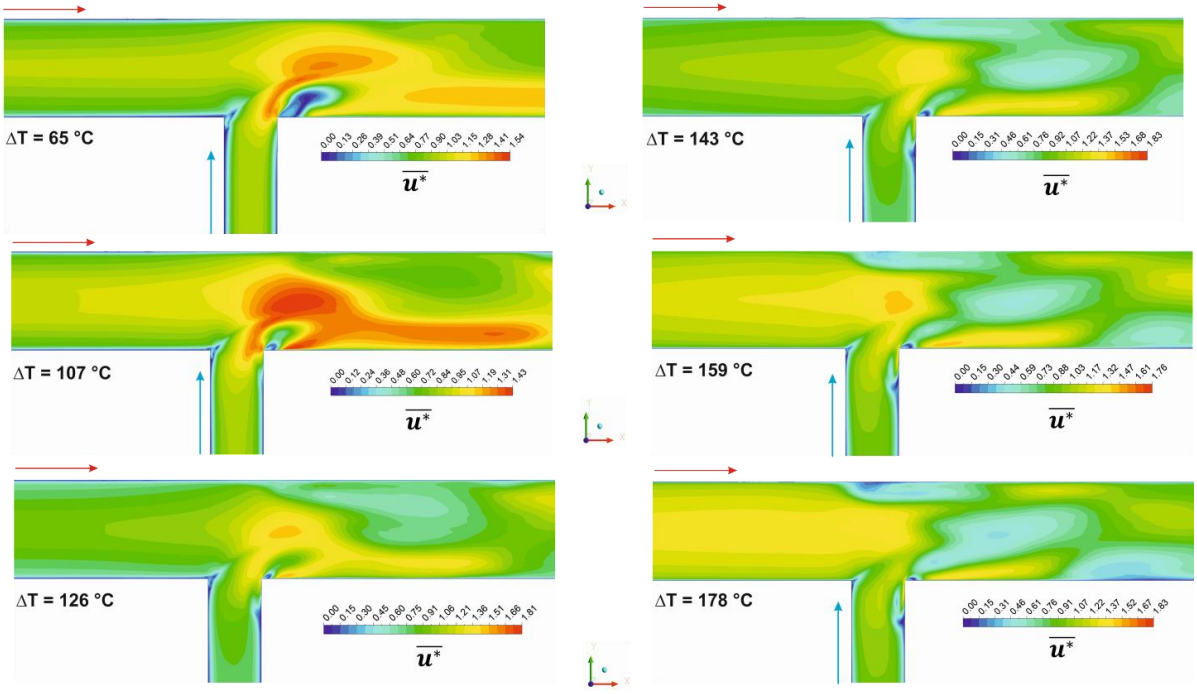

Fig. 23 Mean velocity field at the T-junction mid-plane (x-y axis)

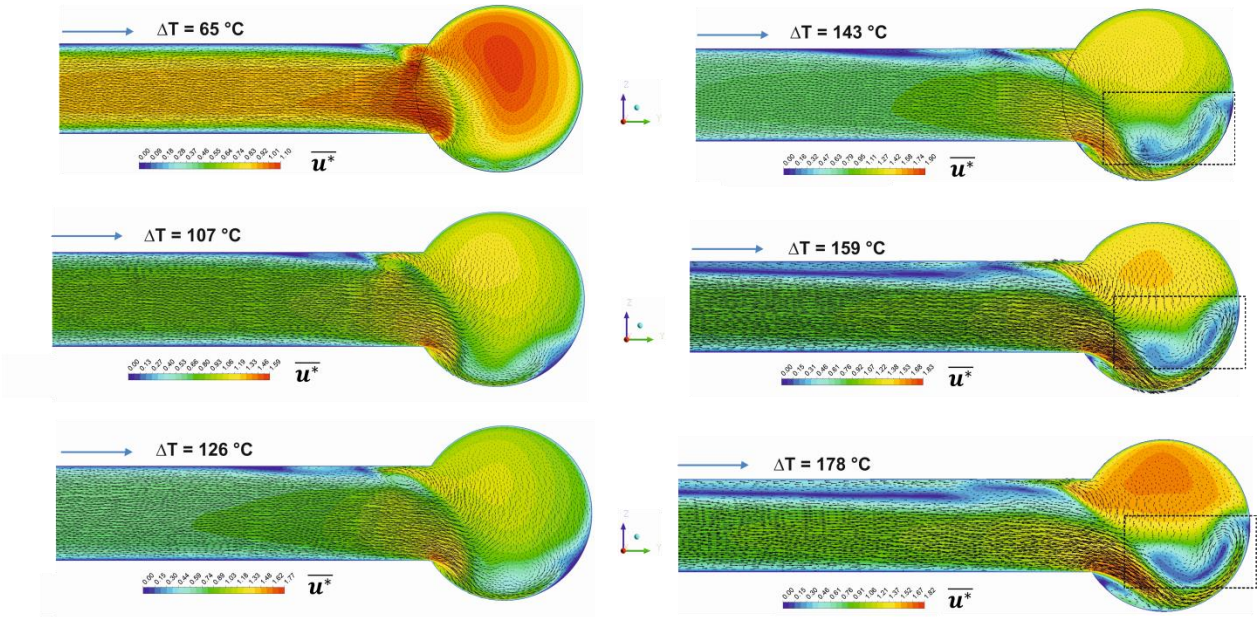

Fig. 24 Mean velocity field illustrating the entry of the cold fluid into the main pipe (view oriented towards T-junction)

The entry of the cold flow into the main pipe results in flow separation and recirculation zones being established in the vicinity of the sharp edges at the T-junction. Also, the flow mixing is incomplete in all the cases due to the low Reynolds number cold flow coming from the branch pipe. Highest $\overline{u^*}$ is usually observed at the mixing interface of hot and cold flows

till ΔTs up to 140 °C (cases 1, 2, and 3). Beyond this point, the relative density ($\Delta\rho/\bar{\rho}$) between the fluids become considerably higher (see Table 9) such that there is increased penetration of hot flow into the cold branch and vice versa. Also, the cold flow clearly sinks to the bottom of the pipe instead of moving straight ahead at ΔT > 140 °C (see Fig. 24). The sunken cold flow then interacts with the already pre-mixed hot flow at the bottom of the T-junction (caused by the partial penetration of the cold flow upstream of the main pipe) which is indicated by the dotted squares in Fig. 24. This phenomenon results in pockets of low velocity zones being established in the downstream region (see Figs. 22 and 23). The turbulent penetration behavior of the flows with rising ΔTs is discussed in detail in section 4.1.3.

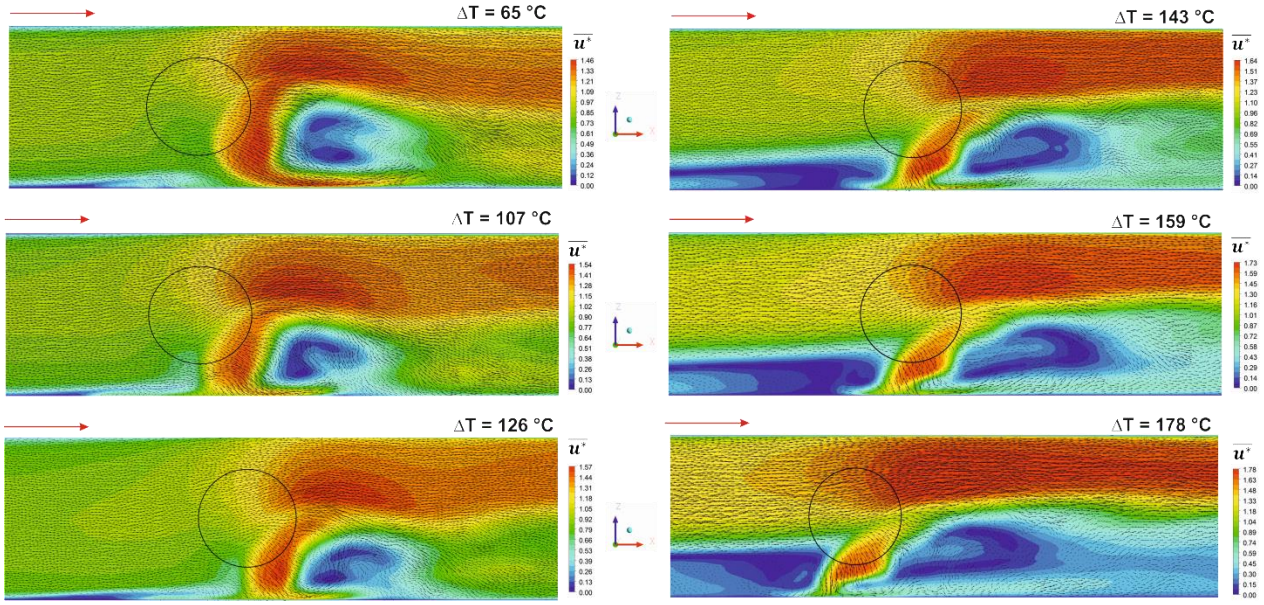

Fig. 25 Counter-rotating vortex pair (CVP) following the T-junction (y = -15 mm) at different ΔT between fluids (dark circle indicates branch pipe opening)

The entry of the cold flow into the T-junction results in certain coherent structures in the flow caused by the interaction between the mixing fluids in the near field of the T-junction. Fig. 25 shows the average velocity field as viewed from the branch pipe located 15 mm away (y = -15 mm) from the center of the T-junction. At ΔT < 140 °C (cases 1, 2, and 3), the entry of cold fluid into the main pipe results in the hot fluid skirting around and shearing the cold fluid along its upper and lower interfaces to form a recirculation zone with two counter-rotating eddies. The formation of this structure – also termed counter-rotating vortex pair (CVP) – in the context of cross-flow mixing has been previously discussed in

Blanchard et al. (1999) [13], Fric and Roshko (1994) [34] and is consistent with similar observations made during the T-junction flow mixing investigations by Kamide et al. (2009) [54]. The momentum of the cold fluid on the main flow is responsible for the generation of this vortex pair structure.

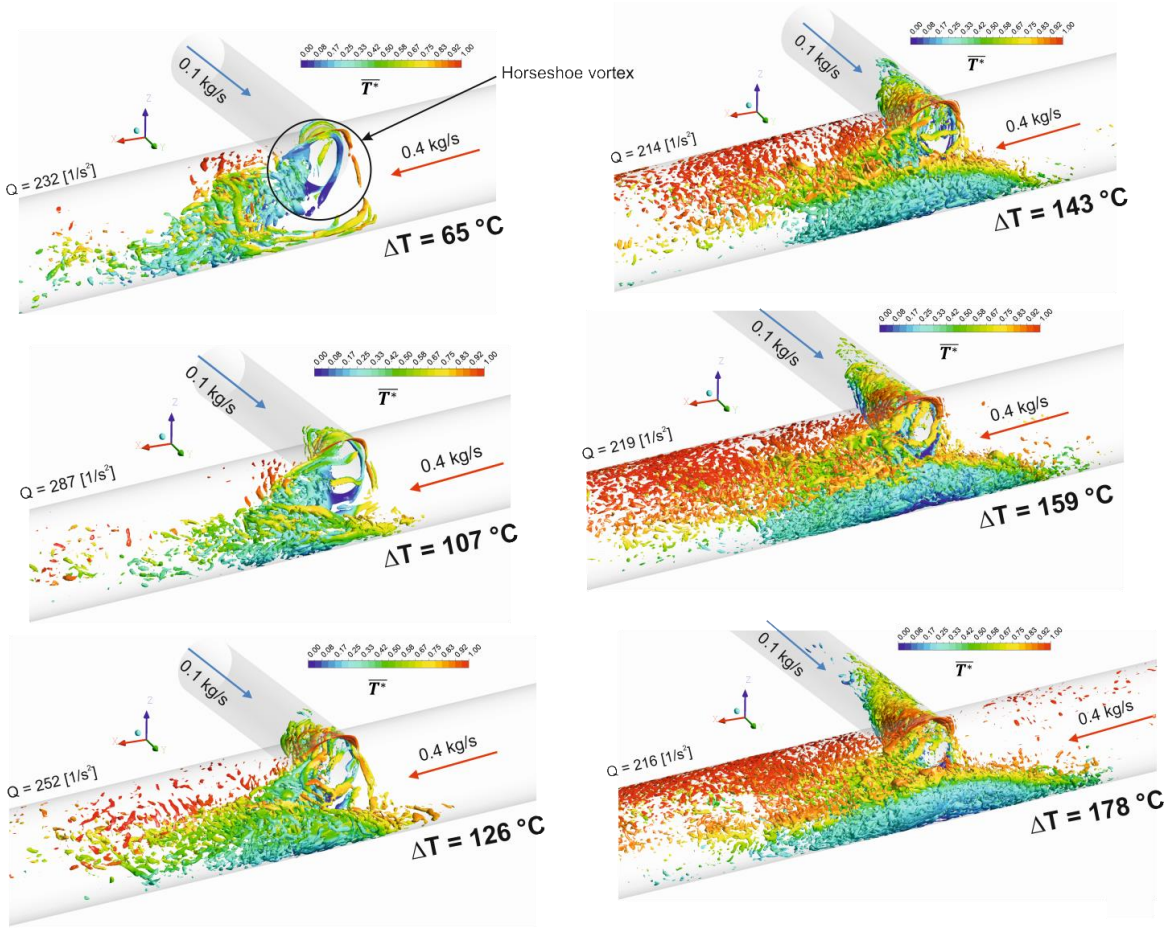

Fig. 26 Vortical structures in the vicinity of the T-junction

At ΔT > 140 °C (cases 4, 5, and 6), the cold flow simply sinks down into the bottom of the main pipe (see Fig. 24) altering the shape of the vortical structure. The flow stabilizes very quickly at these ΔT levels (explained in section 4.1.2) and changes the structure of the vortex pair significantly causing it to stretch considerably along the axial direction of the flow. Additionally, the partial turbulent penetration of cold flow upstream of the T-junction at ΔT > 140 °C could also be clearly observed in Fig. 25. Since all the inflow parameters are kept constant with the exception of ΔT between the fluids (see Table 8), the variations in eddy structures between the studied cases could be correlated with the ΔT induced changes in the flow mixing behavior downstream of the T-junction.

Distribution of the vortical structures in the flow can be analyzed using the Q-criterion which is defined in Ndombo and Howard (2011) [91] as follows

$$Q = \frac{1}{4}\left[\left(\frac{\partial \bar{u}_i}{\partial x_j} + \frac{\partial \bar{u}_j}{\partial x_i}\right)^2 - \left(\frac{\partial \bar{u}_i}{\partial x_j} - \frac{\partial \bar{u}_j}{\partial x_i}\right)^2\right] \quad (26)$$

Fig. 26 depicts the evolution of the vortical structures with mean temperature contours. The shape of the vortex structure at the cold flow outlet at ΔT = 65 °C is of particular interest. It is primarily formed due to the boundary layer separation induced by the adverse pressure gradients as the cold flow approaches the T-junction. The vortex structure has the shape of a horseshoe and henceforth called 'Horseshoe Vortex (HSV)'. The legs of the HSV extend for a certain distance along the downstream direction. These structures could have an influence on the flow properties (e.g. local heat transfer) at the T-junction. Each subsequent rise in ΔT between fluids makes this structure less obvious and gives rise to increasing number of small-scale structures in the flow. This effect could be attributed to the increasing Reynolds number in the main pipe (see Table 8) brought about by the rising hot inflow temperatures.

At ΔT > 140 °C, the vortical structures are also observed upstream of the T-junction in both the main and branch pipes caused by the partial penetration of the hot and cold fluids into the branch and main pipes, respectively. Thus Fig. 26 highlights the ΔT induced transition from a clearly visible HSV structure at ΔT < 100 °C (case 1) to that of less obvious HSV structure at 100 °C < ΔT < 140 °C (cases 2, 3) followed by numerous small-scale structures along the downstream and upstream directions at ΔT > 140 °C (cases 4, 5, and 6). Buoyancy effects, triggered by the density difference between the fluids, are identified as the primary factor in causing this transition in the shape of the vortical structures.

Evolution of the mean velocity field in the mixing zone at different cross-sectional positions is illustrated in Fig. 27. Velocity near the upper region is observed to be higher in all the investigated cases due to the unmixed hot fluid flow. Since buoyancy tends to dampen any extreme oscillations, the rise in ΔT between the fluids subjects the mixing region to shorter oscillations occurring over smaller distances (at ΔT > 140 °C) as opposed to longer distance flow oscillations observed at ΔT < 140 °C caused by strong forced convection effects. Besides, partial upstream flow penetration observed in the main and branch pipes at ΔT >

140 °C considerably slows down the mean fluid velocity in the lower region of the pipe as shown in the LES predictions in Fig. 27.

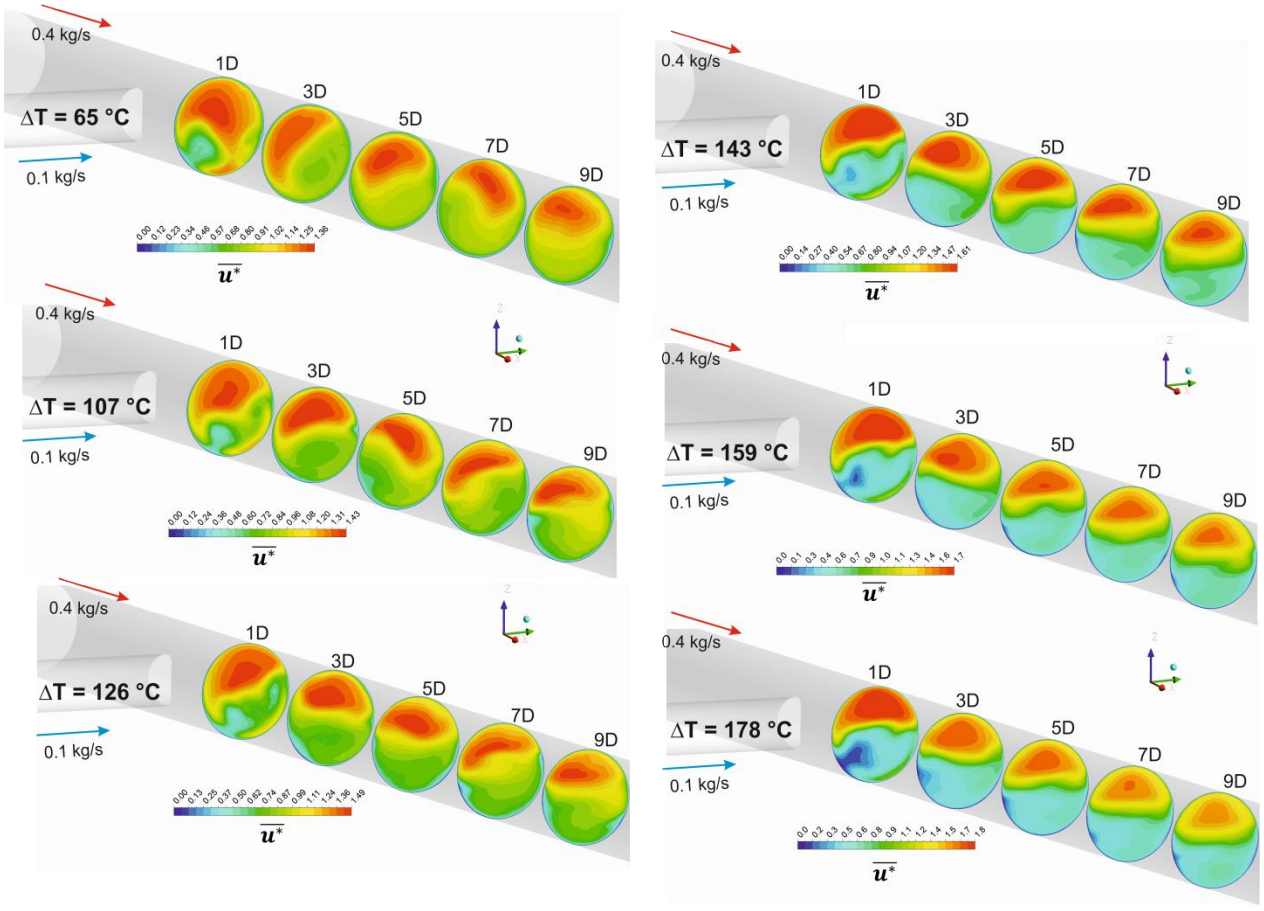

Fig. 27 Mean velocities along different cross-sections downstream of the T-junction

4.1.2 Thermal field in the mixing region

Mean temperature ($\overline{T^*}$) field along the axial flow direction is shown in Fig. 28. As explained earlier, flow mixing in all the cases is incomplete resulting in a thermally stratified flow in the mixing zone. The nature of the thermally stratified flow is directly related to the ΔT amplitude between the fluids as all other inflow parameters are kept constant. Mixing between the hot and cold flows at ΔT < 140 °C produces oscillations occurring over relatively longer distances following the T-junction. Such oscillations are identified by the alternating contours over relatively longer distances following the T-junction as illustrated in Fig. 28 and are induced by considerable forced convective effects in the flow. Rise in ΔT between the fluids reduces the oscillation distance as buoyancy forces rein the oscillations

brought about by the mixing between the flows. At ΔT > 140 °C, this effect becomes more profound and the flow stabilizes very quickly as indicated by the $\overline{T^*}$ contours in Fig. 28.

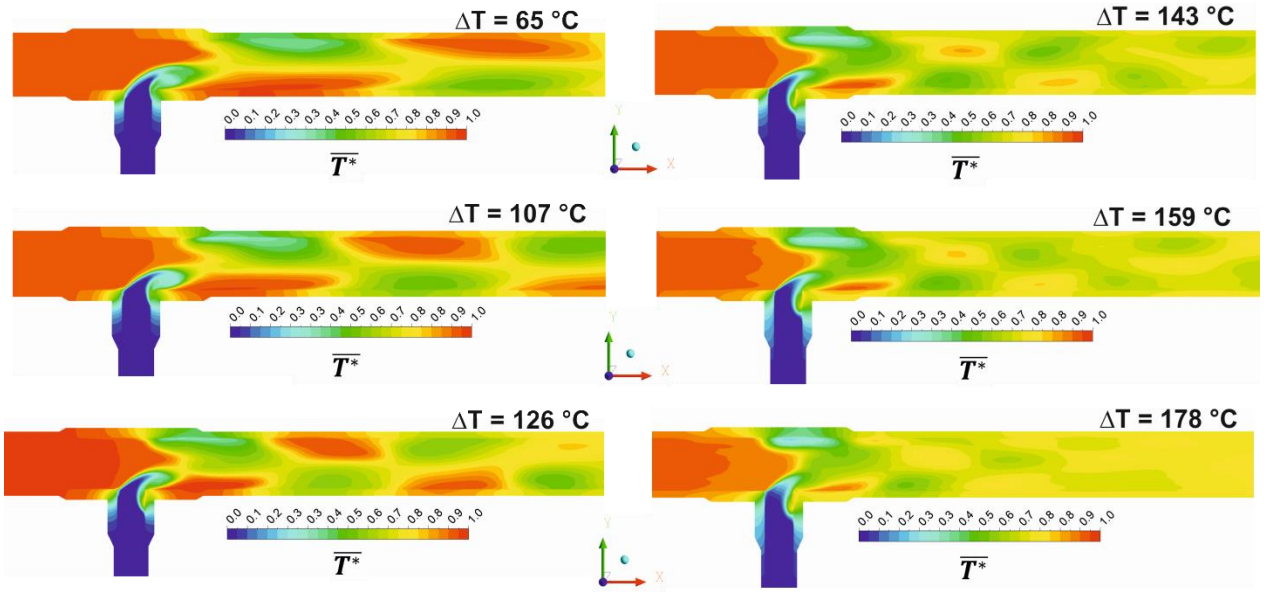

Fig. 28 Mean temperature field at the T-junction along the streamwise direction

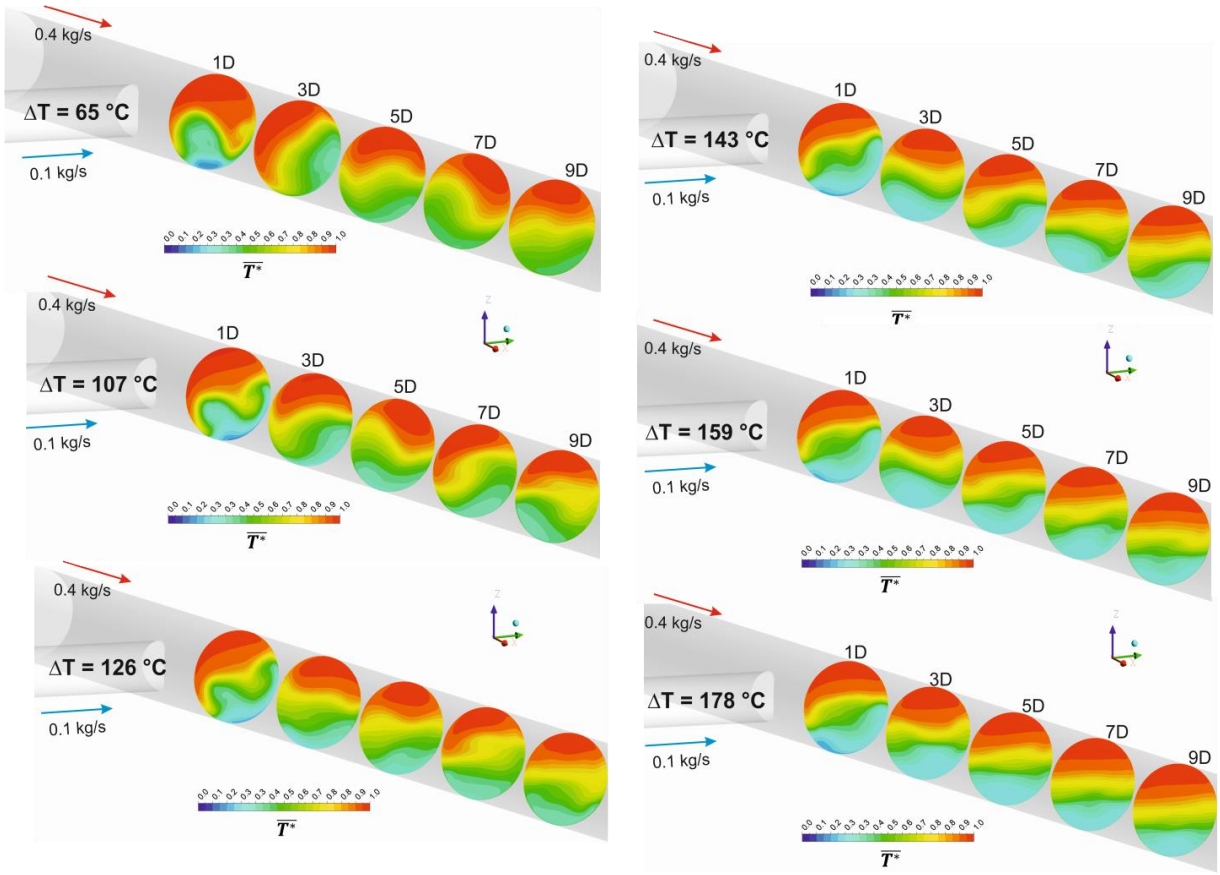

Fig. 29 Mean temperature field along the cross-sectional direction

The evolution of the thermally stratified flow is even more clearly illustrated in Fig. 29 which shows the cross-sectional $\overline{T^*}$ distribution at various locations in the mixing region. Three distinct regions are identified in all the investigated cases, namely, (i) hot fluid region near the top that remains largely unmixed, (ii) mixed flow region near the bottom, and (iii) a stratified layer at the interface between these two regions where high thermal gradients are observed (see Fig. 30).

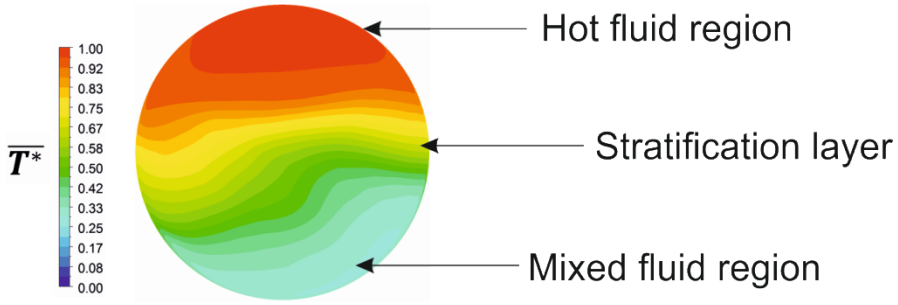

Fig. 30 Illustration of three distinct regions observed in the mixed flow

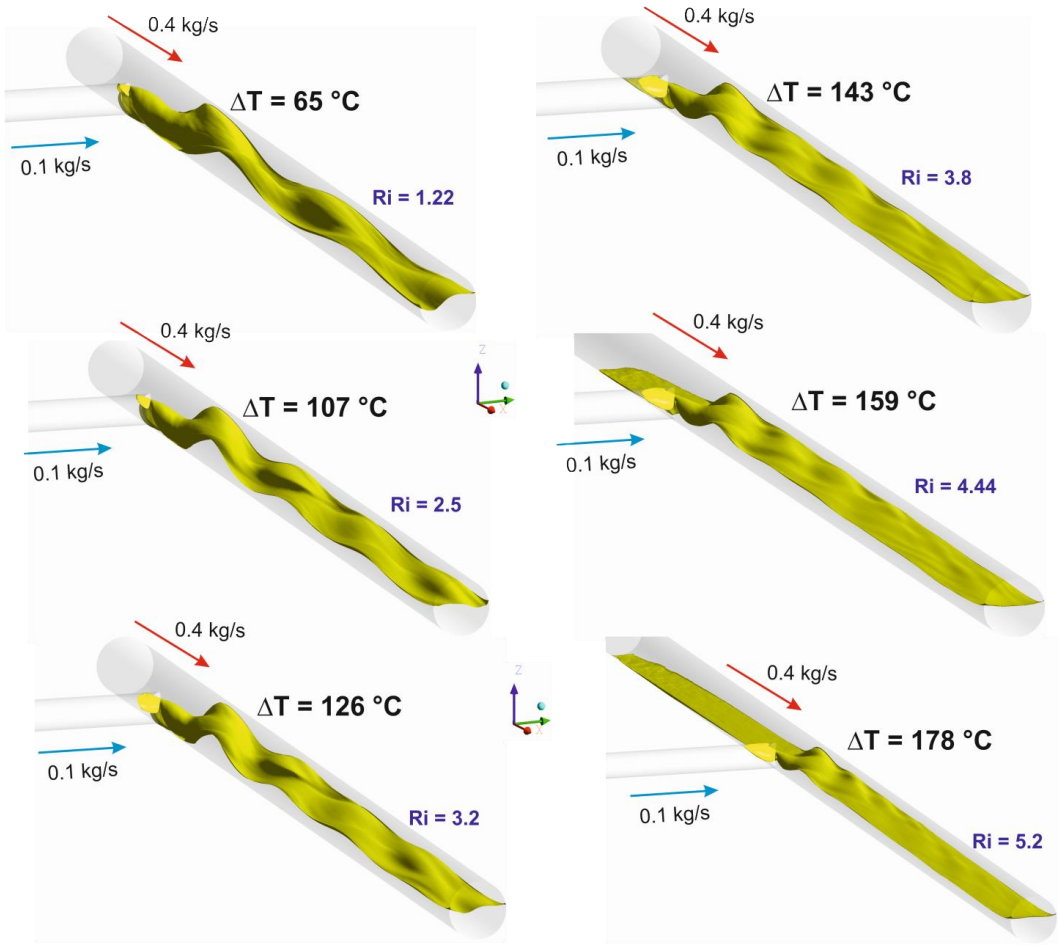

Fig. 31 Isosurfaces of mean temperature ($\overline{T^*}$ = 0.75); Ri – Richardson number

Previously explained flow behavior in the mixing region shown in Figs. 28, 29 and 30 could be more clearly illustrated using the mean temperature isosurfaces shown in Fig. 31 which highlights the evolution of the flow at different ΔT levels. Flow oscillations at ΔT < 140 °C resemble a wavy flow pattern exhibiting declining wave amplitudes as the flow progresses in the mixing zone. With ΔT >140 °C, stable stratification ensues and each subsequent rise within this ΔT range results in more stably stratified flow along with increasing flow penetration of the cold flow upstream of the T-junction in the main pipe. The evaluation of the Richardson number (Ri) in the mixing region serves as a suitable indicator in quantifying buoyancy effects for the considered inflow conditions in this study. It is defined as follows:

$$Ri = g\Delta\rho D/\bar{\rho}u_{mix}^2 \qquad (27)$$

where g is the acceleration due to gravity, $\Delta\rho/\bar{\rho}$ is the relative density, D the pipe diameter in the mixed flow region and u_{mix} is the mixing velocity of fluids. A low Ri (Ri < 1) is indicative of significant forced convection effects in the flow whereas a higher Ri (Ri > 1) would suggest significant buoyant forces acting on the flow. The rise in buoyancy effects in the flow is quantified by the rise in Richardson number (see Fig. 31) with each increase in ΔT between the fluids.

4.1.3 Flow penetration in the main and branch pipes

With the inflow rates in the main and branch pipes remaining constant during the course of the measurements, the rise in ΔT between the fluids enable partial penetration of the hot flow into the upper part of the branch pipe (due to its lower density) and the cold flow into the bottom of the main pipe (due to its higher density) upstream of the T-junction. This behavior is seen to rapidly accelerate at ΔT > 140 °C (cases 4, 5, and 6) in both the main and the branch pipes. Data from thermocouples placed upstream of the T-junction inside the solid (2 mm from the inner wall) confirmed the existence of this phenomenon while LES calculations predicted the probable distance of penetration.

Fig. 32 shows the normalized instantaneous temperature data from a thermocouple located at the top of the branch pipe (2 mm in the structure) at different ΔT between fluids. It is clearly seen that the temperature remains close to the cold flow temperature at the lowest ΔT of 65 °C (case 1). Each subsequent rise in ΔT contributes to rising density differences between the flows which further facilitates the penetration of the less dense hot flow into

the branch pipe. This scenario reaches its peak at the highest ΔT of 178 °C (case 6) with T^* > 0.7 indicating substantial hot flow penetration.

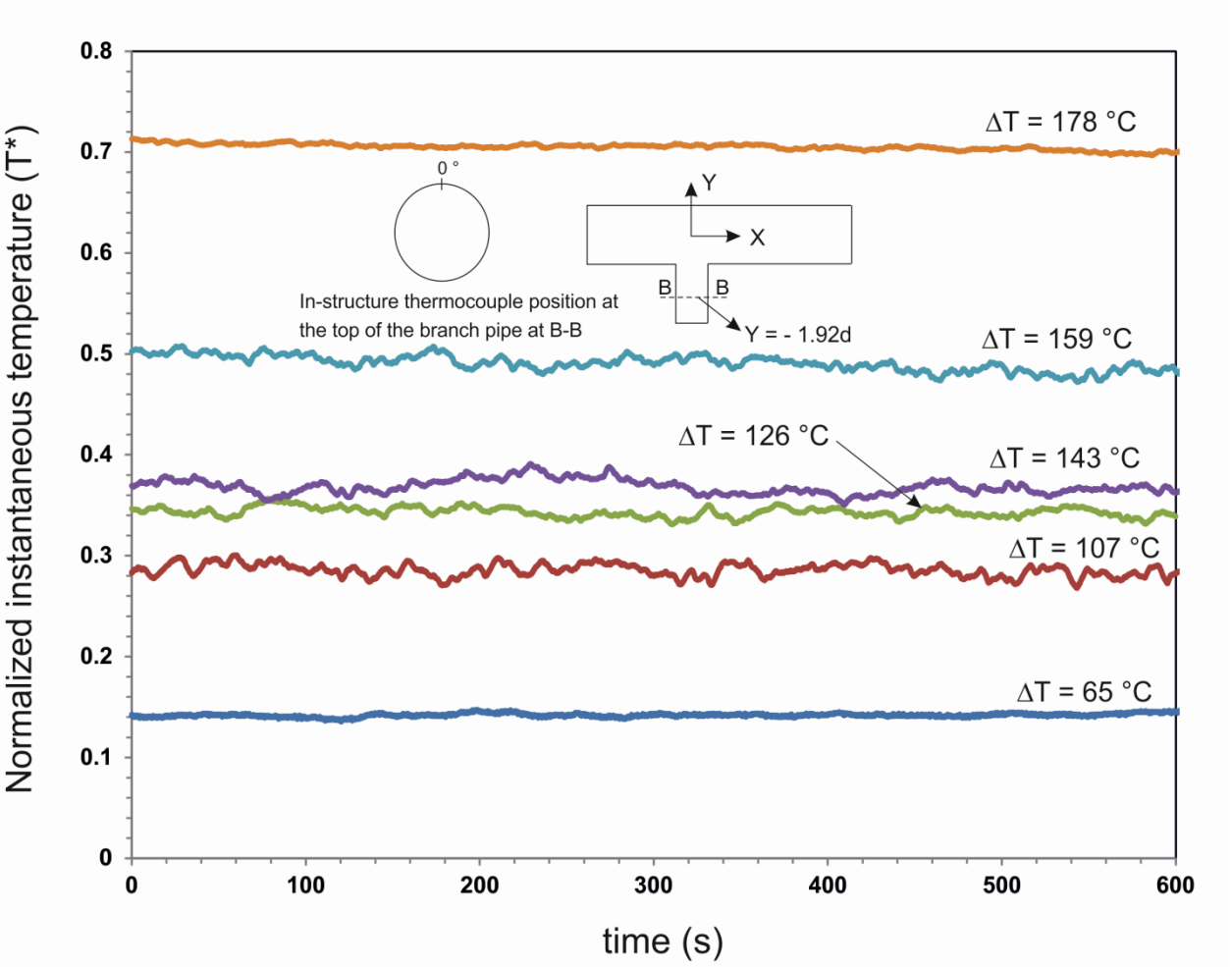

Fig. 32 Instantaneous temperature data (at y = -1.92d, θ = 0 °) from the in-surface thermocouples showing the hot fluid penetration into the branch pipe with rising ΔT

The same is seen from the LES predictions shown in Fig. 33 depicting the hot flow penetration into the branch pipe and the results are truly surprising. For a near three-fold rise in ΔT from 65 °C (case 1) to 178 °C (case 6), the penetration distance of the hot flow into the branch pipe rises by more than six times from 67 mm (in case 1) to 427 mm (in case 6). The T-junction piping also begins to bend at ΔT > 150 °C [116] which aids this process even further. The consequence of the partial flow penetration is that part of the cold flow near the top is now already mixed with the hot fluid and this certainly contributes to lowering the mean temperature ($\overline{T^*}$) magnitude of fluids in the downstream region with rise in ΔT between the fluids.

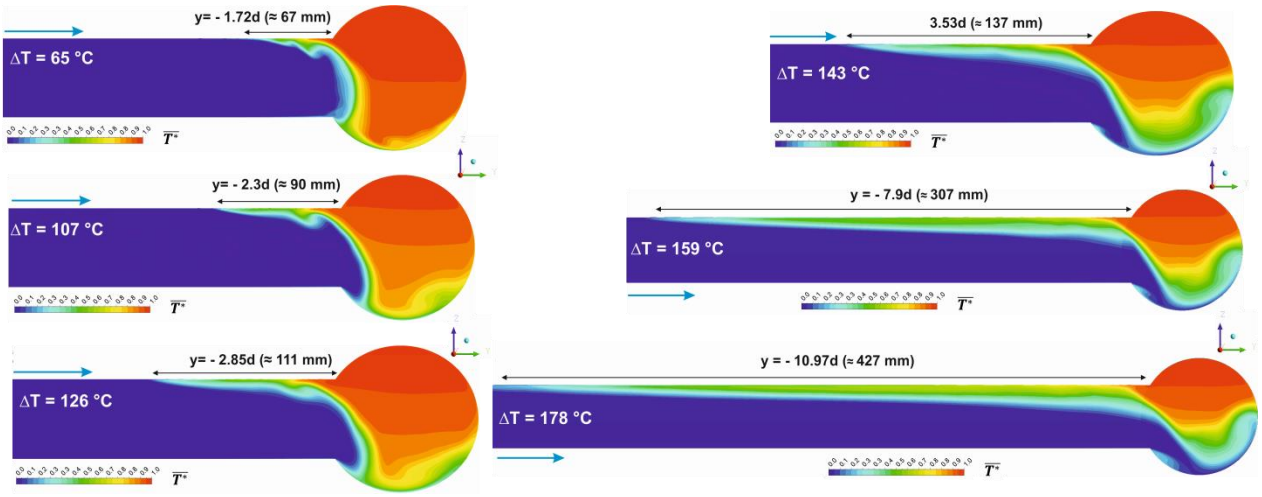

Fig. 33 Turbulent penetration of hot flow into branch pipe

Fig. 34 shows the normalized instantaneous temperature data from a thermocouple located at the bottom of the main pipe (2 mm in the structure) during investigations performed at different ΔT between the fluids. A different trend is seen here in the main pipe where the cold flow doesn't penetrate the thermocouple location until ΔT = 126 °C (case 3) which could be the result of a higher Reynolds number hot flow preventing the cold flow from traveling farther upstream into the main pipe. This scenario is seen to abruptly change in case 4 (ΔT = 143 °C) where there is a significant decline in the temperature magnitudes indicating the onset of cold flow penetration beyond that location. Each subsequent rise in ΔT causes the cold flow to penetrate even farther into the main pipe. The same is also predicted by the LES calculations depicting the cold flow penetration into the main pipe with rising ΔT illustrated in Fig. 35. The distance of penetration by the cold flow is seen to be even greater than the extent of the hot flow penetration into the branch pipe. For a near three-fold rise in ΔT from 65 °C (case 1) to 178 °C (case 6), the penetration distance of cold flow into the main pipe rises by more than 27 times from nearly 40 mm (in case 1) to greater than 1077 mm (in case 6).

It goes without saying that more mixing occurs upstream of T-junction in the main pipe with rising ΔT between the fluids which significantly brings down $\overline{T^*}$ amplitude near the lower part of the pipe in the mixing zone. Since the mass flow rates are fixed in each case, the primary cause of the partial penetration of hot and cold flows into the branch and main pipes is the density difference that arises in the flow with each uptick in ΔT between the fluids.

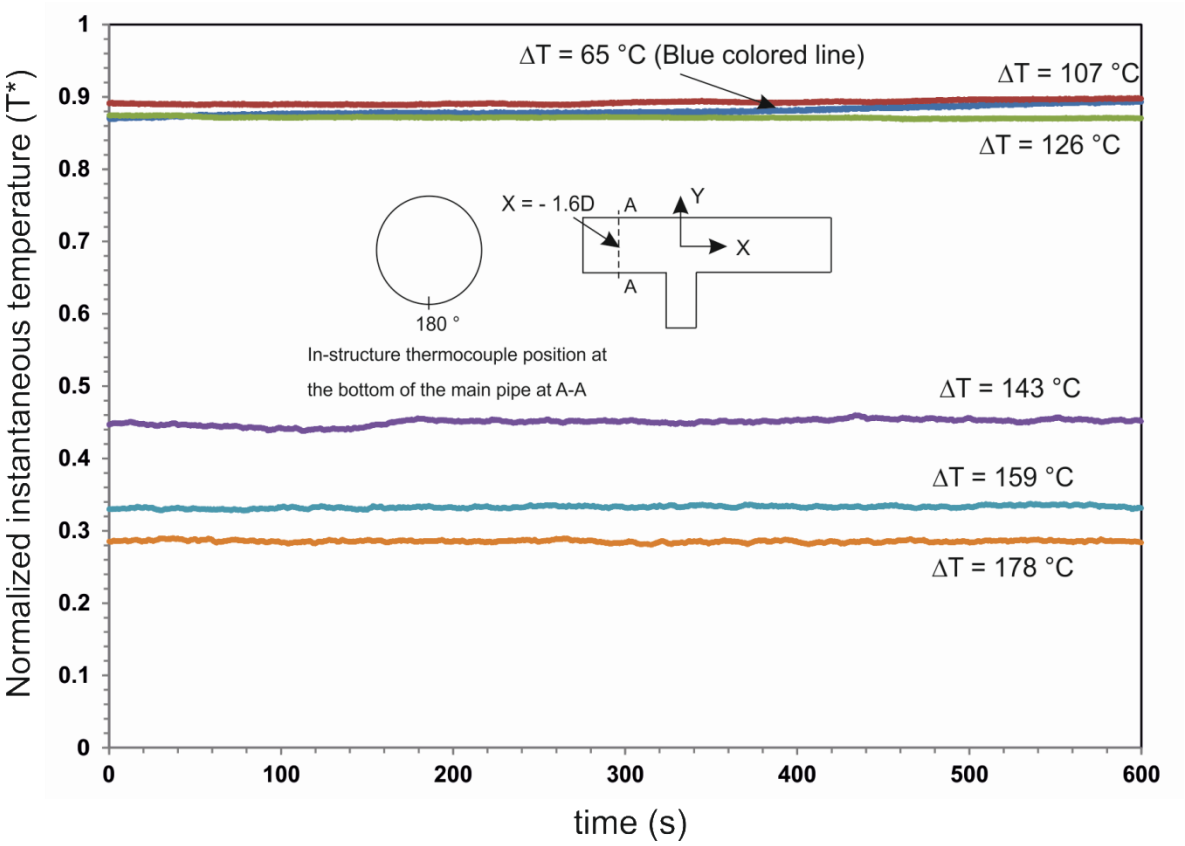

Fig. 34 Instantaneous temperature data (at x = -1.6D, θ = 180 °) from the in-surface thermocouples revealing the cold fluid penetration into main pipe with rising ΔT

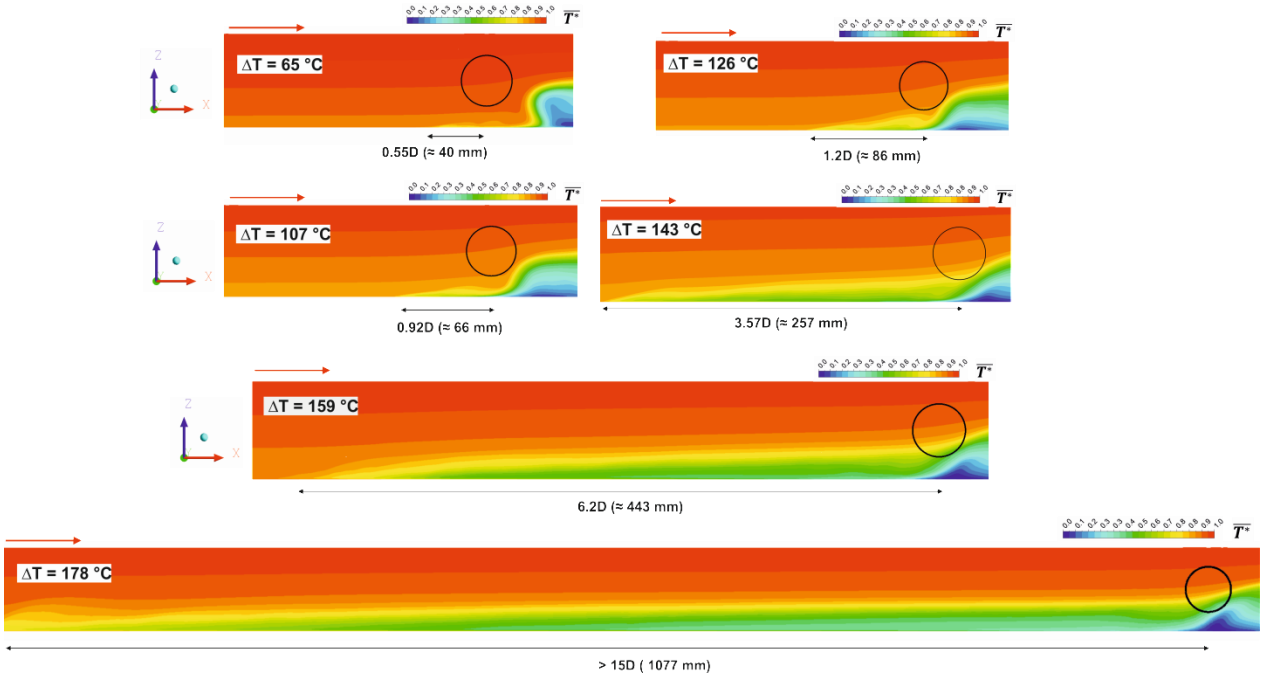

Fig. 35 Turbulent penetration of cold flow into the main pipe

4.1.4 Near-wall mean temperature distribution

Fig. 36 shows the near-wall mean temperature ($\overline{T^*}$) data obtained from the circumferential thermocouples during the measurements and the corresponding LES predictions. A common feature observed in all the investigated cases is the repeated occurrence of higher $\overline{T^*}$ amplitudes near the upper region (angular positions with $\overline{T^*}$ > 0.9). This confirms the earlier LES predictions that the flow remains largely unmixed near the top due to the low branch velocity.

Lowest $\overline{T^*}$ amplitudes are seen near the bottom of the pipe where intense fluid mixing occurs. Comparison of lowest $\overline{T^*}$ amplitudes (marked by dotted lines in Fig. 36) across all the cases portray a declining trend in $\overline{T^*}$ with rising ΔT between the fluids. The reasons could be as follows: (i) at ΔT < 140 °C, the lateral momentum of the cold flow takes a while integrating itself into the main pipe. Since the relative density between the fluids is lower, it takes a certain distance for the mixed flows to settle and actively mix with each other. This has the effect of producing relatively higher $\overline{T^*}$ amplitudes at the investigated thermocouple positions (x = 5D, 5.5D, and 6D) at ΔT < 140 °C. (ii) at ΔT > 140 °C, the relative density between the fluids are sufficiently high that the cold flow easily sinks to the bottom of the main pipe on reaching the T-junction. Besides, partial penetration of flows in the upstream direction at these ΔT levels already bring pre-mixed flows to the T-junction resulting in a sharp drop in $\overline{T^*}$ amplitudes at the investigated thermocouple positions.

The stratified interface between the hot and cold layers of the flow, important in the context of its high thermal gradients, could be probably identified by the significant jumps in $\overline{T^*}$ between the circumferential thermocouple positions. In all the investigated cases, this interface is found to invariably occur between θ = 80.5 ° and 125.5 ° on left-wall side and θ = 215.5 ° and 260.5 ° on the right-wall side.

Difference in mean temperature ($\Delta\overline{T^*}$) amplitude between the top (θ = 350.5 °) and the bottom (θ = 170.5 °) of the pipe (see Fig. 37) has a maximum value in each case as follows: 0.60 (39.5 °C) in case 1, 0.64 (70 °C) in case 2, 0.68 (88.6 °C) in case 3, 0.74 (105.6 °C) in case 4, 0.79 in case 5 (131 °C) and 0.82 in case 6 (155.7 °C). This parameter is important in the context of thermally stratified flows as bending moments and local stresses could be induced in the structure [75] when strong temperature differences occur between the top and the bottom of the pipes.

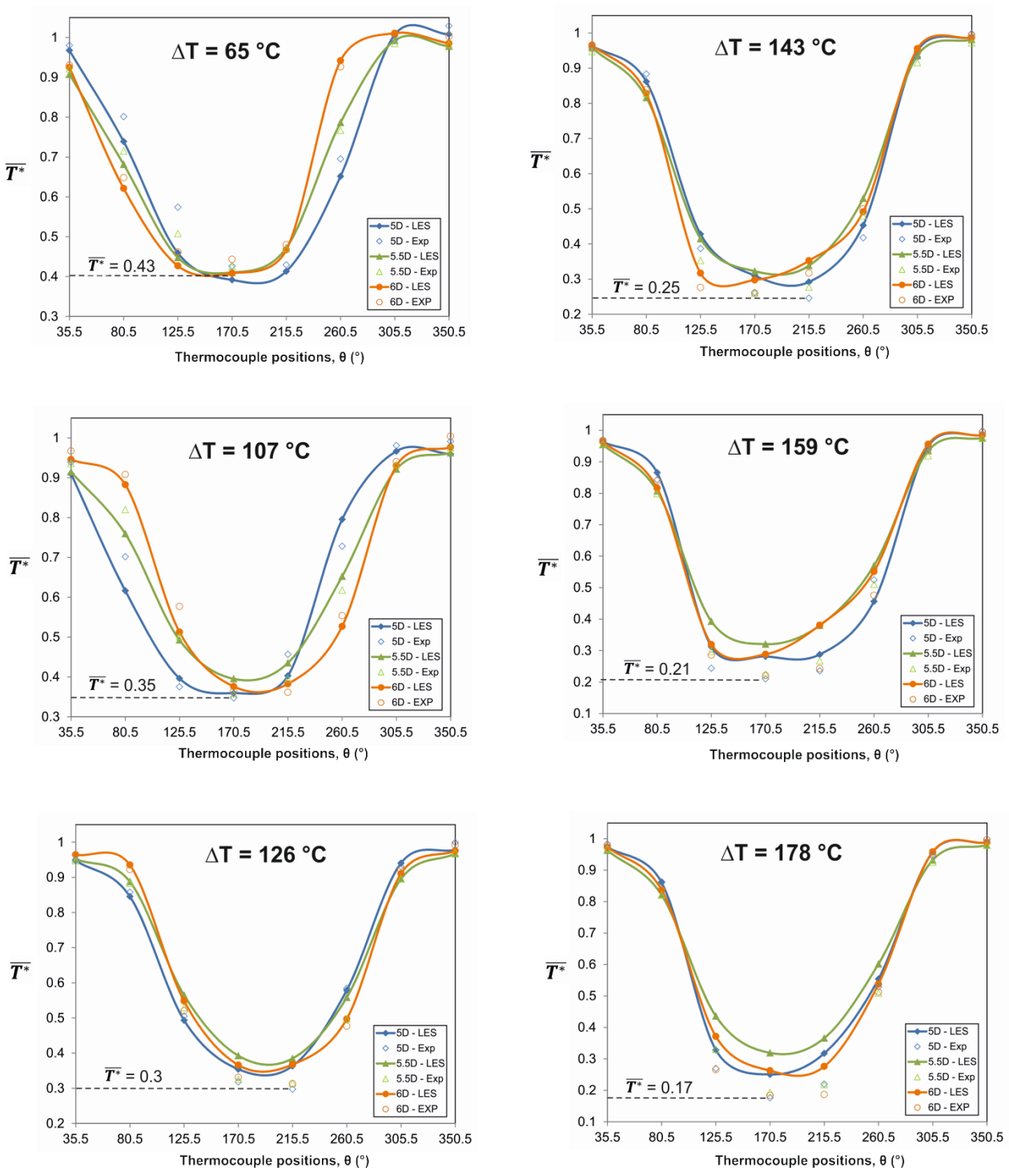

Fig. 36 Mean temperature ($\overline{T^*}$) distribution along the angular thermocouple positions. Lowest $\overline{T^*}$ values are indicated by the dotted lines

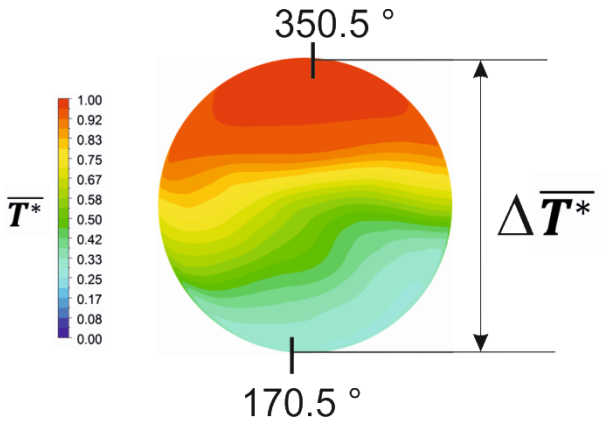

Fig. 37 Illustration of $\Delta\overline{T^*}$ between the top and bottom thermocouple positions

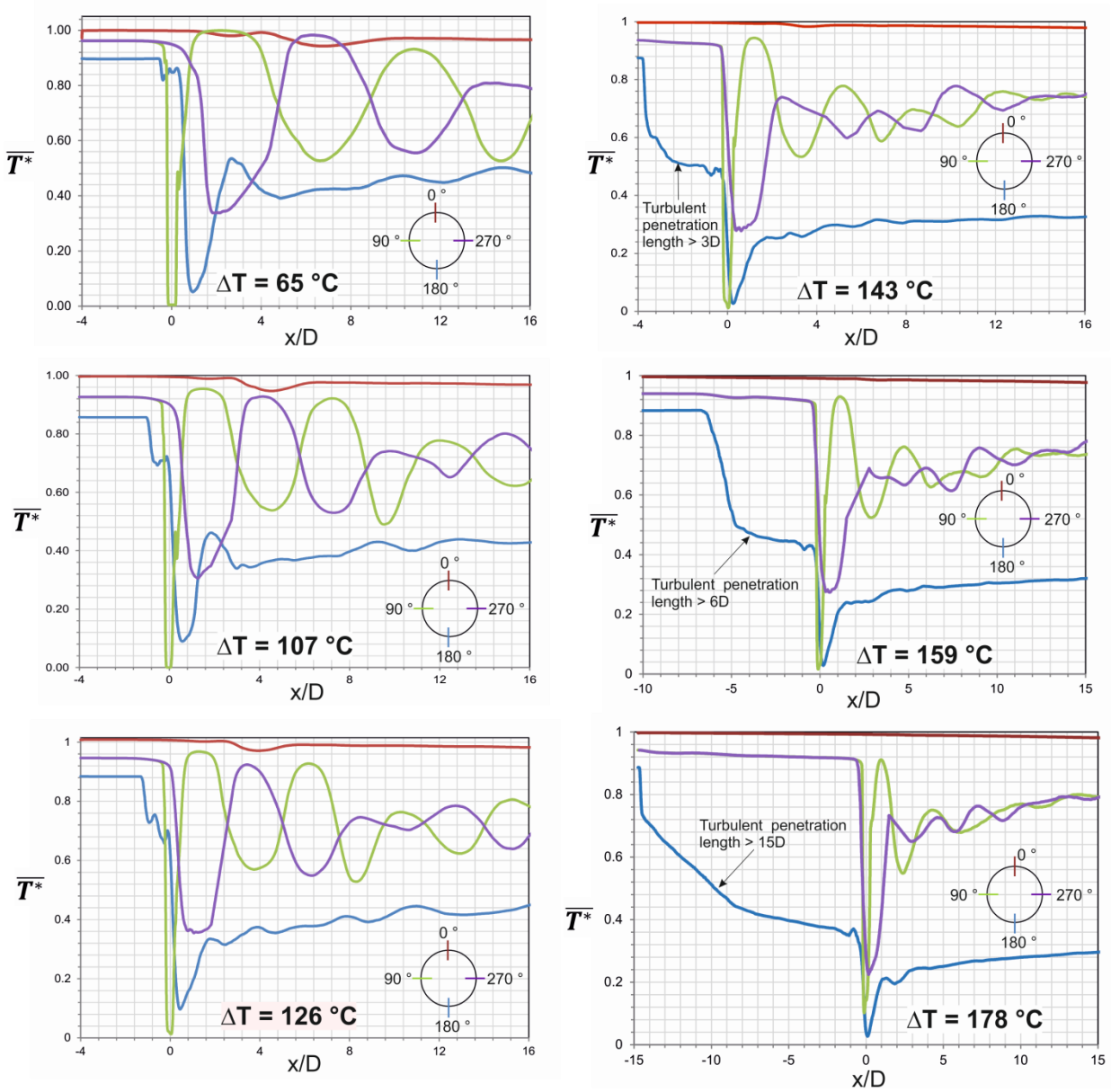

Fig. 38 Axial $\overline{T^*}$ distribution along the angular positions, θ = 0°, 90°, 180° and 270°

Visual observations during the measurements indicated no such event in cases 1, 2 and 3 (ΔT < 140 °C) while a slight non-negligible bending of the structure was observed beginning in case 4 (ΔT = 143 °C). From this point onwards, the bending effect became more clearly visible with each subsequent increase in ΔT in cases 5 and 6. $\overline{T^*}$ predictions by LES calculations closely match with the measurement data.

All the characteristics of the mixed flow described so far, namely, (a) high $\overline{T^*}$ near the top, (b) low $\overline{T^*}$ near the bottom, (c) oscillating flow near the side-wall regions and (d) turbulent penetration of cold flow into the main pipe at higher ΔTs can be explained in a single graph as shown in Fig. 38. In particular, the attenuation of the oscillation distance and the corresponding peak-to-peak $\overline{T^*}$ amplitudes in the side-wall regions (θ = 90 ° and 270 °) are particularly striking and highlights the damping caused by the buoyancy effects in response to rising ΔT between the fluids. Also shown in this figure is the extent of cold flow penetration distance with rise in ΔT which reaches its maximum at the highest ΔT of 178 °C (case 6) where the cold flow has penetrated beyond the 15D (1.077 m) distance limit used in the LES computation.

4.1.5 Temperature fluctuations

Temperature fluctuations (T^*_{rms}) in the near-wall region is a leading indicator in HCTF analyses [131]. The turbulence that arises in the flow as a result of the fluid mixing process produces random thermal fluctuations that tend to manifest in the structure in the form of thermal stresses. The T^*_{rms} amplitude in the near-wall region has a direct bearing on the thermal stress induced in the structure. But before analyzing T^*_{rms} in the near-wall region, it is useful to observe the T^*_{rms} distribution in the flow along the different planes to have an idea of the impact of the fluid mixing in creating such fluctuations.

Fig. 39 shows the T^*_{rms} distribution at the T-junction along the streamwise direction. Highest T^*_{rms} amplitudes in the flow are observed at the leading mixing interface (which is thin in all the cases due to the weak cold flow) between the hot and cold fluid flows. It ranges anywhere between 29 – 39 % of ΔT (ΔT in this context refers to individual ΔTs in each case) in all the investigated cases. It is quite useful to see the evolution of T-junction mixing at different ΔTs between the fluids by comparing the white colored squares in Fig. 39 among the investigated cases. Cold flow from the branch pipe in case 1 (ΔT = 65 °C) is

deflected by the oncoming hot flow and the mixing process ensues after a certain distance. The area near the white colored square remains unaffected. With subsequent rise in ΔT, the mixing between flows occurs sooner as buoyancy facilitates a much easier integration of the cold flow into the main pipe. This is confirmed by the mixed flow regions moving closer towards the white square. With significant cold flow penetration coming into play at ΔT > 140 °C, the premixed flow in the main pipe is easily pushed towards the opposite wall of the T-junction by the cold flow as it enters the main pipe. Thus the T^*_{rms} distribution at the T-junction changes in response to the rising ΔTs between the fluids.

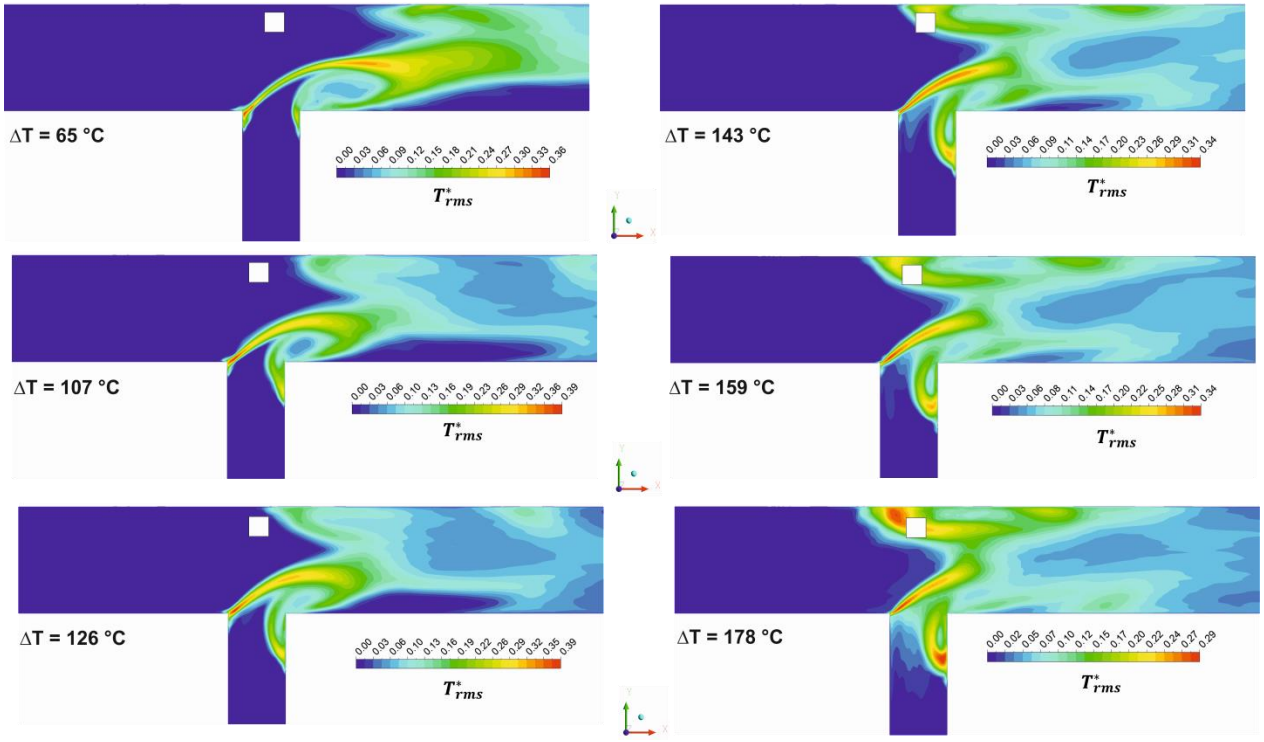

Fig. 39 Temperature fluctuations ($\boldsymbol{T^*_{rms}}$) at the T-junction along the streamwise direction

Downstream flow T^*_{rms} distribution at different cross-sections is shown in Fig. 40. There is a drop in the downstream T^*_{rms} amplitudes in comparison with the amplitudes at the T-junction and it continues to decline as the flow progresses farther away from the T-junction. The reason for this being the reduction in the turbulent mixing intensity (which is highest at the T-junction) between the fluids as the flow progresses downstream which brings down the T^*_{rms} amplitudes. Similar to the mean flow field shown in Fig. 30, cross-sectional thermal fluctuation field could be characterized by three distinct regions as shown in Fig. 41. Lowest T^*_{rms} amplitudes are observed close to the top where no fluid mixing occurs. Slightly higher

T^*_{rms} amplitudes are observed along the bottom of the pipe where complete mixing of fluids occurs. But the highest T^*_{rms} amplitudes, pointed above as one of the factor in HCTF analyses, occurs along the stratification layer where T^*_{rms} amplitudes in all the investigated cases range from 22 – 36 % of ΔT (refers to individual ΔT in each case).

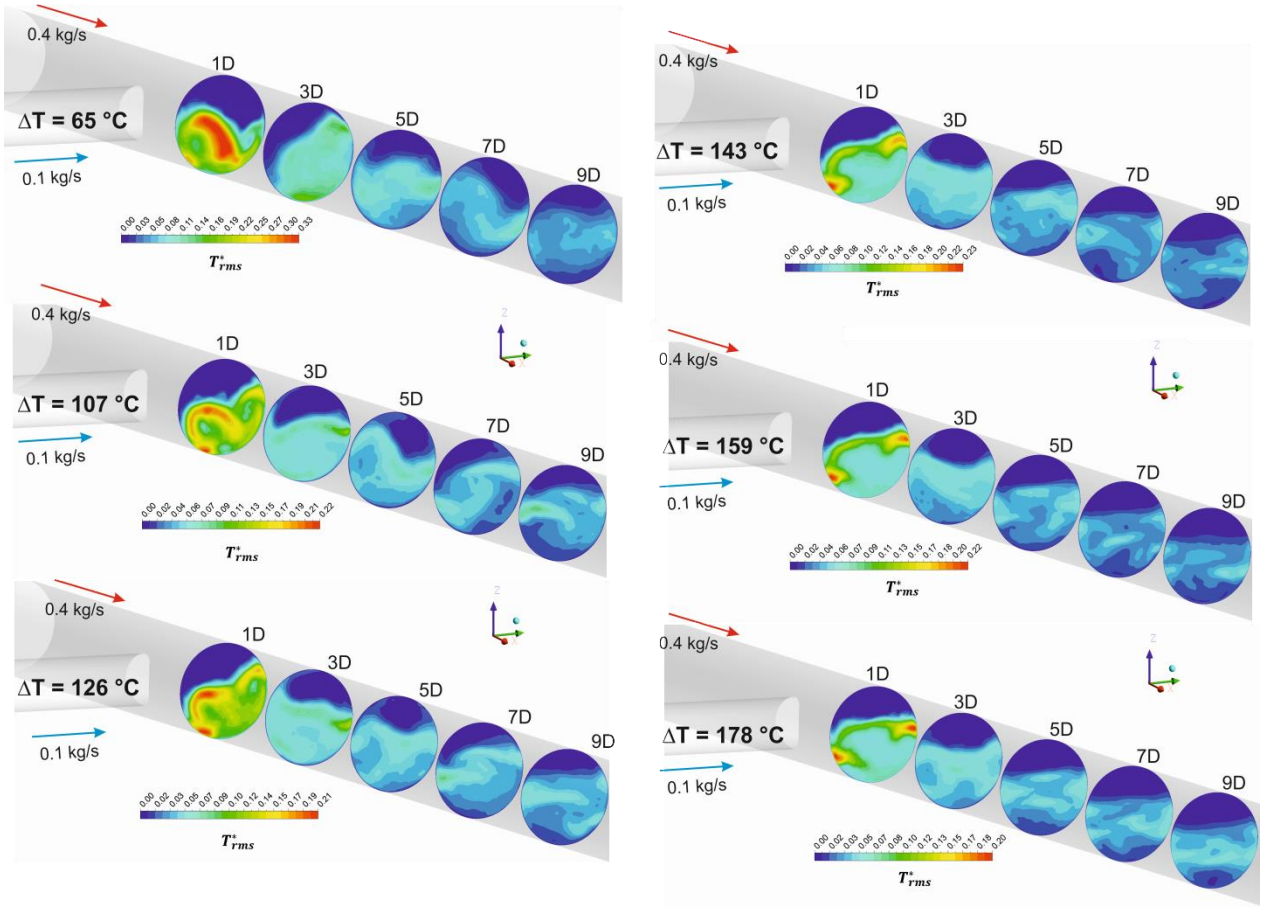

Fig. 40 Cross-sectional thermal fluctuations predicted by LES

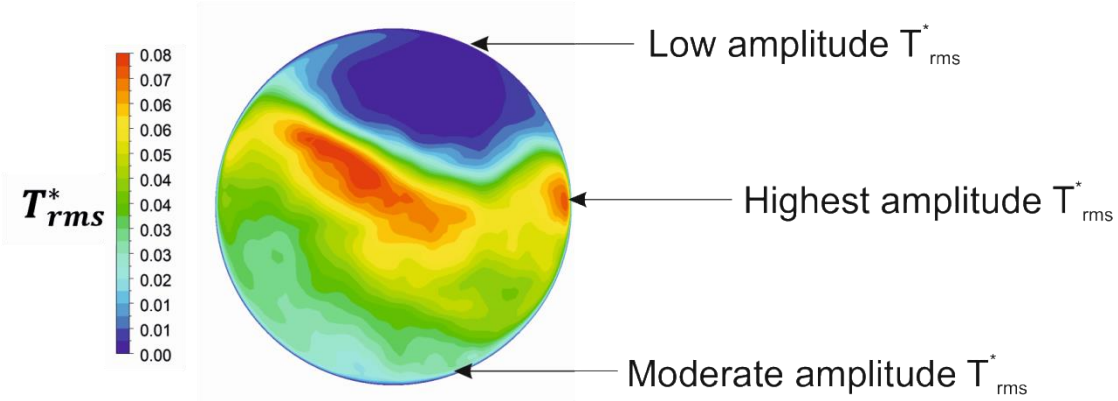

Fig. 41 Illustration of three distinct thermal fluctuation regions observed in the mixed flow

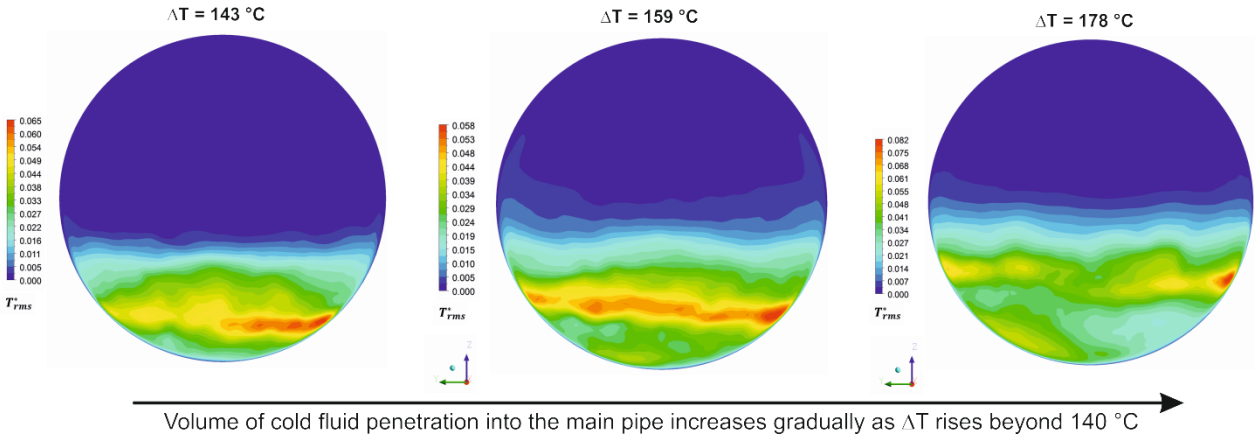

Fig. 42 Thermal fluctuations in the main pipe (x = -1.6D) caused by cold flow penetration (view oriented towards the T-junction)

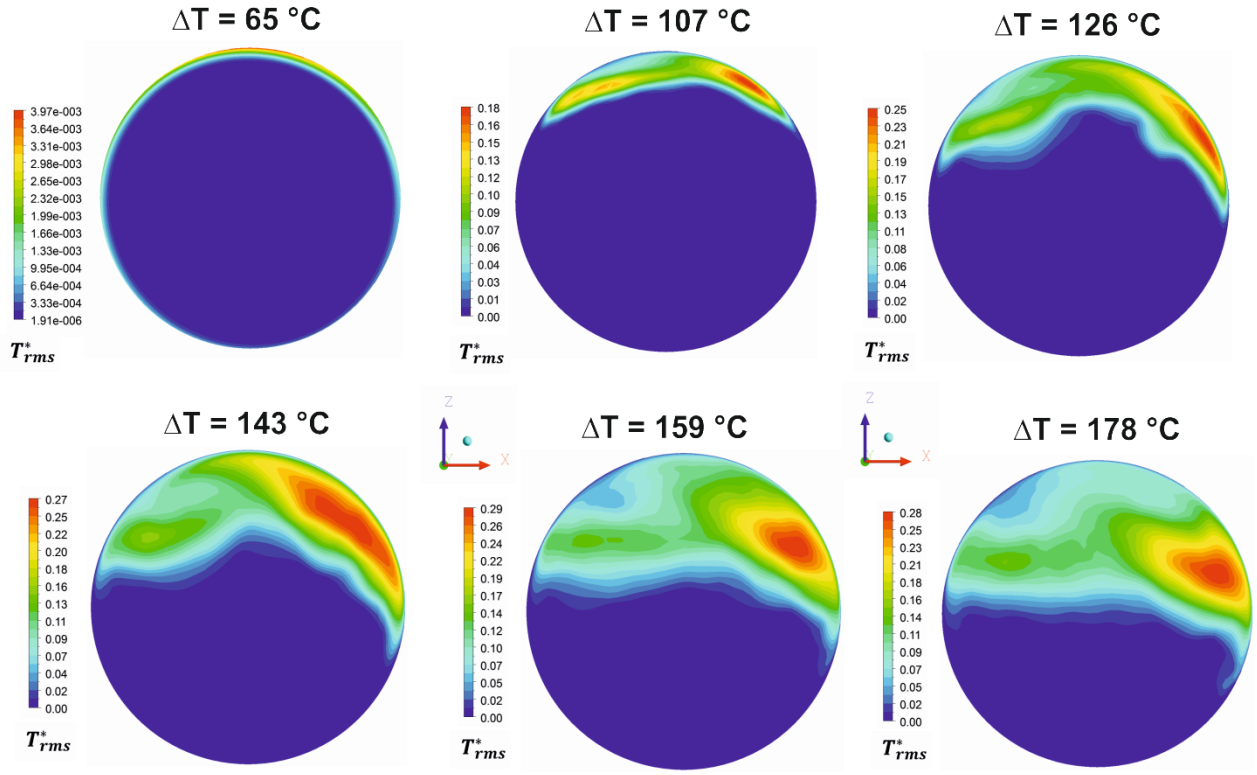

Fig. 43 Thermal fluctuations in the branch pipe (y = -1.92d mm) caused by hot flow penetration (view oriented towards the T-junction)

Fig. 42 shows the T^*_{rms} distribution along the cross-section upstream of the T-junction in the main pipe (x = -1.6D). Rise in ΔT between the fluids did not result in cold flow penetration till 140 °C. Beyond this ΔT, a substantial amount of cold flow penetrated the monitoring region at x = -1.6D that results in thermal fluctuations within the penetrated region. The

predicted T^*_{rms} amplitudes range from 0.6 – 0.8 % of ΔT. Another observation is the rising volume of occupied by the penetrated cold flow in response to rising ΔT between the fluids. Thus a thermally stratified flow is formed even before the hot flow reaches the T-junction. Especially at ΔT = 178 °C (case 6), half the cross-sectional region is occupied by penetrated flow resulting in substantial mixing of flows upstream of the T-junction.

Similarly Fig. 43 depicts the T^*_{rms} distribution upstream of the T-junction in the branch pipe (y = -1.92d). Starting from case 1 (ΔT = 65 °C) the hot flow penetrates the monitoring region in the branch pipe and volume of hot flow steadily rises with increase in ΔT between the fluids. At the highest ΔT of 178 °C (case 6) the upper-half of the branch pipe is penetrated by the hot fluid resulting in substantial T^*_{rms} amplitudes being generated within this mixing region. Highest T^*_{rms} amplitudes in the branch pipe region as predicted by the LES calculations lie in the range of 0.4 – 29 % of ΔT. This flow penetration could also be seen at the cold flow outlet in Fig. 39.

Distribution of thermal fluctuations at the in-flow and in-structure thermocouple positions and the corresponding LES predictions are shown in Fig. 44. The common features exhibited in all the investigated cases could be summarized as follows: (i) two peak T^*_{rms} amplitudes (located near the stratification layer) are identified at each of the axial thermocouple location (x = 5D, 5.5D, 6D), and (ii) a strong attenuation of thermal fluctuation inside the solid region in relation to the fluid region.

Fluctuation amplitudes are the lowest at thermocouple positions representing the upper part of the flow (any combination of θ = 35.5 °, 305.5 ° and 350.5 ° depending on the case under investigation) and such lowest T^*_{rms} amplitudes in all the investigated cases range from 0.13 – 0.5 % of ΔT between the fluids. As explained earlier, thermocouples close to the stratification layer recorded the hightest T^*_{rms} amplitudes. A case-by-case peak T^*_{rms} amplitudes on both the side-wall regions recorded by the in-flow thermocouples are shown below in Table 10. Also, the peak T^*_{rms} amplitude recorded by the in-structure thermocouples are also given in Table 10. With the exception of a few positions, LES results exhibited reasonable agreement with the measurement data obtained from thermocouples. Drop in peak T^*_{rms} amplitudes within the fluid region with increase in ΔT between fluids confirms the buoyancy induced dampening of the flow oscillations. Data also shows that the

peak T^*_{rms} in the solid occurs near the stratification layer. The extent of the drop in T^*_{rms} amplitudes inside the solid in comparison with the fluid T^*_{rms} amplitudes is significantly higher given the magnitude of the attenuation (see Table 10).

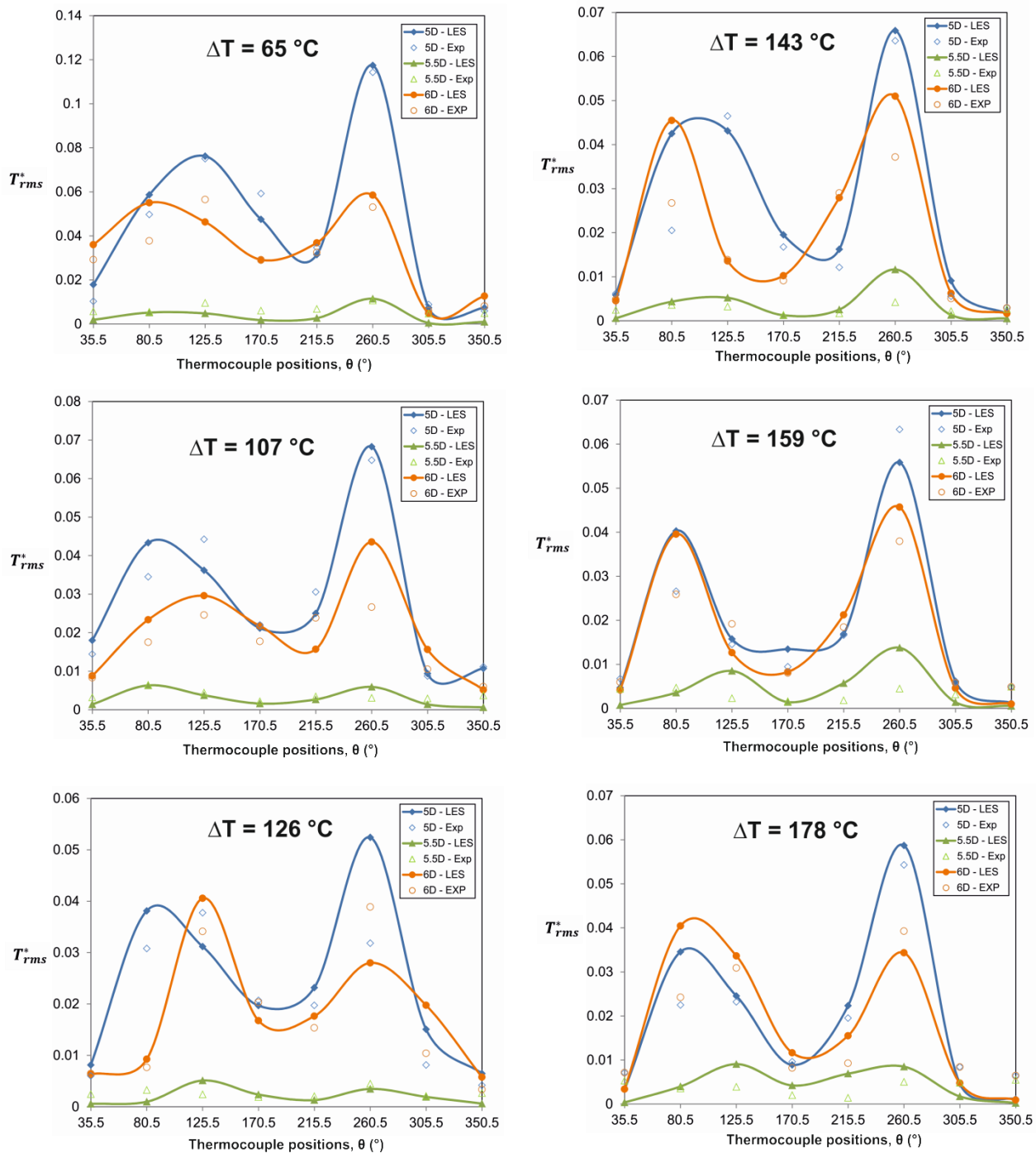

Fig. 44 Distribution of thermal fluctuations (T^*_{rms}) at near-wall thermocouples for all the investigated cases

Close to at least 90 % drop in T^*_{rms} amplitudes are observed in the solid in all the investigated cases without exception. The effect of thermal inertia in dampening the fluctuations emanating from the fluid as it gets transmitted to the structure could be clearly observed from the above mentioned numbers.

Table 10. Fluid and solid thermal fluctuations as recorded from the measurements

ΔT (°C)	Peak T^*_{rms} (as % of ΔT) along the		T^*_{rms} (as % of ΔT) inside solid	
	Left wall region	Right wall region	Peak amplitude	Attenuation from peak fluid level
65	7.5 (θ = 125.5 °)	11.4 (θ = 260.5 °)	1.1 (θ = 260.5 °)	90 %
107	4.4 (θ = 125.5 °)	6.5 (θ = 260.5 °)	0.64 (θ = 80.5 °)	90 %
126	3.7 (θ = 125.5 °)	3.8 (θ = 260.5 °)	0.4 (θ = 260.5 °)	≈ 90 %
143	4.6 (θ = 125.5 °)	6.4 (θ = 260.5 °)	0.42 (θ = 260.5 °)	≈ 93 %
159	2.6 (θ = 80.5 °)	6.3 (θ = 260.5 °)	0.47 (θ = 80.5 °)	≈ 93 %
178	2.3 (θ = 125.5 °)	5.4 (θ = 260.5 °)	0.5 (θ = 260.5 °)	91 %

Fluid temperature fluctuations along the near-wall region (2 mm into the flow) predicted by LES along the four corners of the cross-section are shown in Fig. 45. T^*_{rms} amplitudes near the top (θ = 0 °) in all the cases remain below 1.5 % of ΔT (attributed to no fluid mixing at the top) throughout the computational domain. There is a spike in T^*_{rms} amplitudes in all the cases to more than 27 % of ΔT at θ = 90 ° as the cold flow enters the T-junction. The amplitudes subsequently decline and then exhibit repeated rise and fall as the flow oscillates in the mixing zone. A similar pattern is also observed on the other end of the wall at θ = 270 ° where flow oscillations result in the rise and fall of T^*_{rms} amplitudes along the mixing region. Such flow oscillations induced rise and fall of T^*_{rms} amplitudes in the side-wall region (θ = 90 °, 270 °) is greatly diminished as ΔT rises beyond 140 °C (cases 4, 5 ,6) due to buoynacy induced damping effects in the mixing region. The bottom region (θ = 180 °) gives a clear indication on the effects of rising ΔT between flows. Cold flow penetration upstream of the main pipe results in rising T^*_{rms} amplitudes and this is limited to within a

distance of two diameters (x/D = -2) up to ΔT < 140 °C (cases 1, 2, 3). Further increase in ΔT causes a transition resulting in the cold flow penetration to occur over much longer distances upstream of T-junction. This distance continually increases with ΔT to finally beyond x/D = -15 at the highest ΔT of 178 °C (case 6). The penetration distance is also enhanced by the bending of the structure caused by higher ΔT between the top and the bottom of the pipe as a result of the thermally stratified flow observed in all the cases. This makes it easier for the cold flow to travel longer distances at higher ΔT between the fluids.

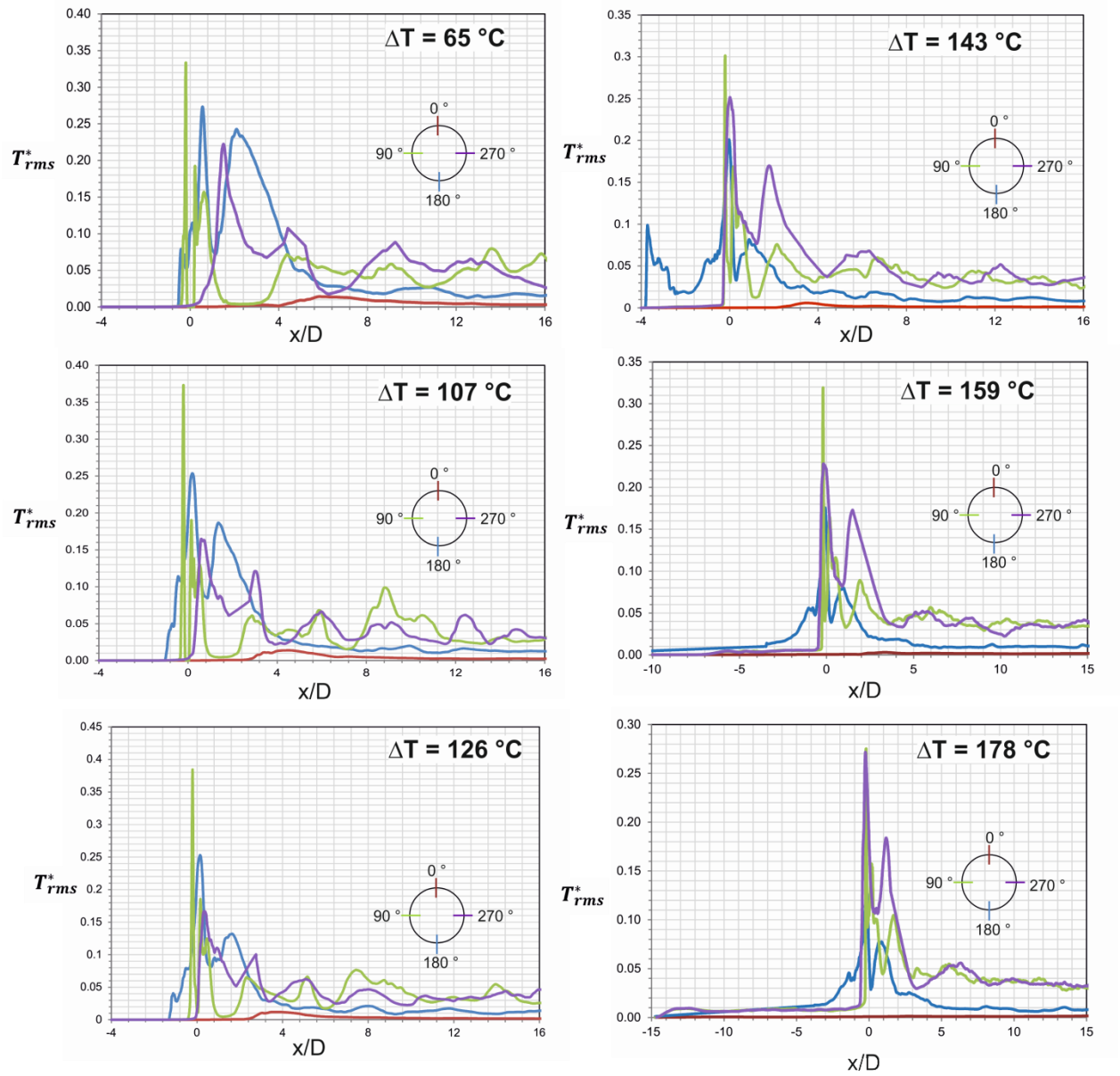

Fig. 45 LES predictions of fluid T^*_{rms} (2 mm in the flow) at θ = 0 °, 90 °, 180 ° and 270 °

While thermocouple instrumentation is placed beginning at x = 5D, LES predictions shown in Fig. 45 indicate the occurrence of much higher amplitude T^*_{rms} before 5 diameters downstream of the T-junction. This is a valuable insight whereby additional thermocouple instrumentation could now be placed much closer to the T-junction in the near-wall region which might reveal additional information that has gone unnoticed during previous measurements due to the non availability of thermocouples in the vicinity of the T-junction.

4.1.6 Frequency analysis of temperature fluctuations

Since it has been established that near-wall thermal fluctuations induce cyclical thermal stresses in the structure, it becomes important to study the frequency content of such fluctuations which might lead to much needed information about the energy distribution of the eddies as a function of frequency. The application of Fast Fourier Transform (FFT) method on a time domain signal $f(t)$ and the subsequent squaring its absolute magnitude provides the power spectral density (PSD) of thermal fluctuations which is defined as follows [63]

$$PSD = \left|\hat{f}(\omega)\right|^2 = \left|\int_0^{t/n} \bar{f}(t) e^{-i\omega t} dt\right|^2 \tag{28}$$

where t is the duration of the raw time signal and $\bar{f}(t)$ is the n-times ensemble averaged signal.

It has been established in the literature that there are attenuation factors in the process of fluid thermal fluctuations converting to thermal stresses in the structure [56, 57] that could be correlated with the fluctuation frequency (see Fig. 46). At high frequencies, fluid thermal fluctuations are transferred to the structure with attenuation due to heat transfer loss related to the heat transfer coefficient resulting in low amplitude thermal stresses. On the other hand, low-frequency thermal fluctuations result in thermal diffusivity homogenizing the structural temperature, failing to once again induce high amplitude thermal stresses. Intermediate frequency fluctuations may have the potential to induce high amplitude thermal stresses in the structure. On the basis of Civaux-I NPP leakage incident analysis, Chapuliot et al. (2005) [16] estimated such critical frequencies of thermal fluctuations responsible for possible thermal fatigue damage in the T-junction piping to be in the range of 0.1 – 10 Hz. The Vattenfall T-junction benchmark exercise report [131] additionally

suggested the presence of a dominant frequency (spectral peak) of fluctuations in the 0.1 – 10 Hz frequency range that might indicate the occurrence of high thermal stresses in the structure.

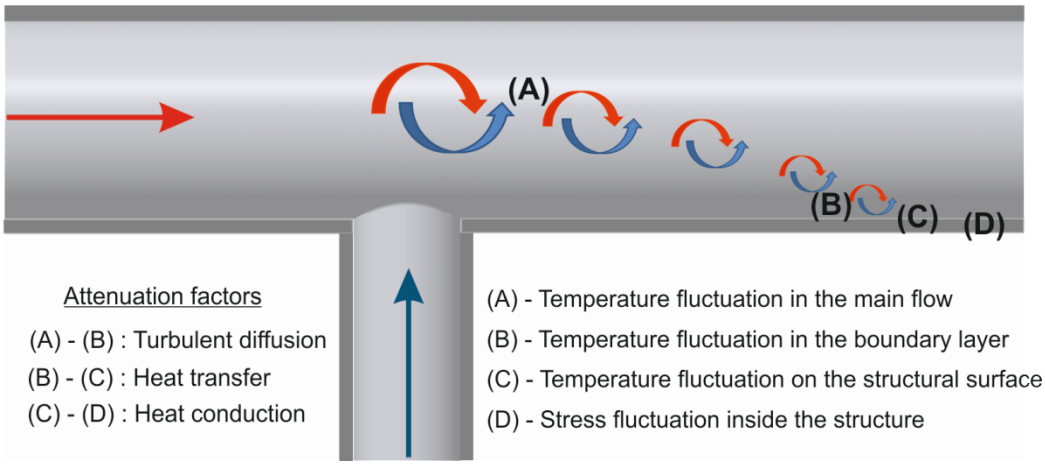

Fig. 46 Turbulent mixing and the attenuation mechanism of thermal fluctuations [56]

Thus the primary objective of power spectral density (PSD) analyses in this section is to look for thermal fluctuations exhibiting spectral peak (if any) in the 0.1 – 10 Hz range. The secondary objective is to compare the LES spectra with that of measurement spectra. Fig. 47 shows the normalized PSD of the peak amplitude thermal fluctuations within the fluid domain.

The shape of the spectra illustrates the cascading phenomenon where energy is successively transferred from the larger eddies (low frequency) to the smaller eddies (high frequency) in the flow. Power content of temperature fluctuations remains fairly stable (nearly 1 [-/Hz] in all the cases) until the frequency of 1 Hz. Beyond this, a waterfall-type drop in the power content of fluctuations is noticed. At 10 Hz the power content of fluctuations has already dropped by several orders of magnitude (indicated in Fig. 47) from where it was within the frequency range of 0.1 – 1 Hz. No distinct peak in the power content of fluctuations was observed in the 0.1 – 10 Hz range indicating that the relevance for thermal fatigue is not obvious from the in-flow thermocouple data.

Further drop in the power content of temperature fluctuations is observed beyond 10 Hz as seen from the measurement data (which is correctly followed by the LES predictions). The PSD of fluid fluctuations also follows the -5/3 slope based on the Kolmogorov spectrum

[105] in the inertial sub-range, a region between the energy containing eddy range and the dissipation range in the energy spectrum (see Fig. 17).

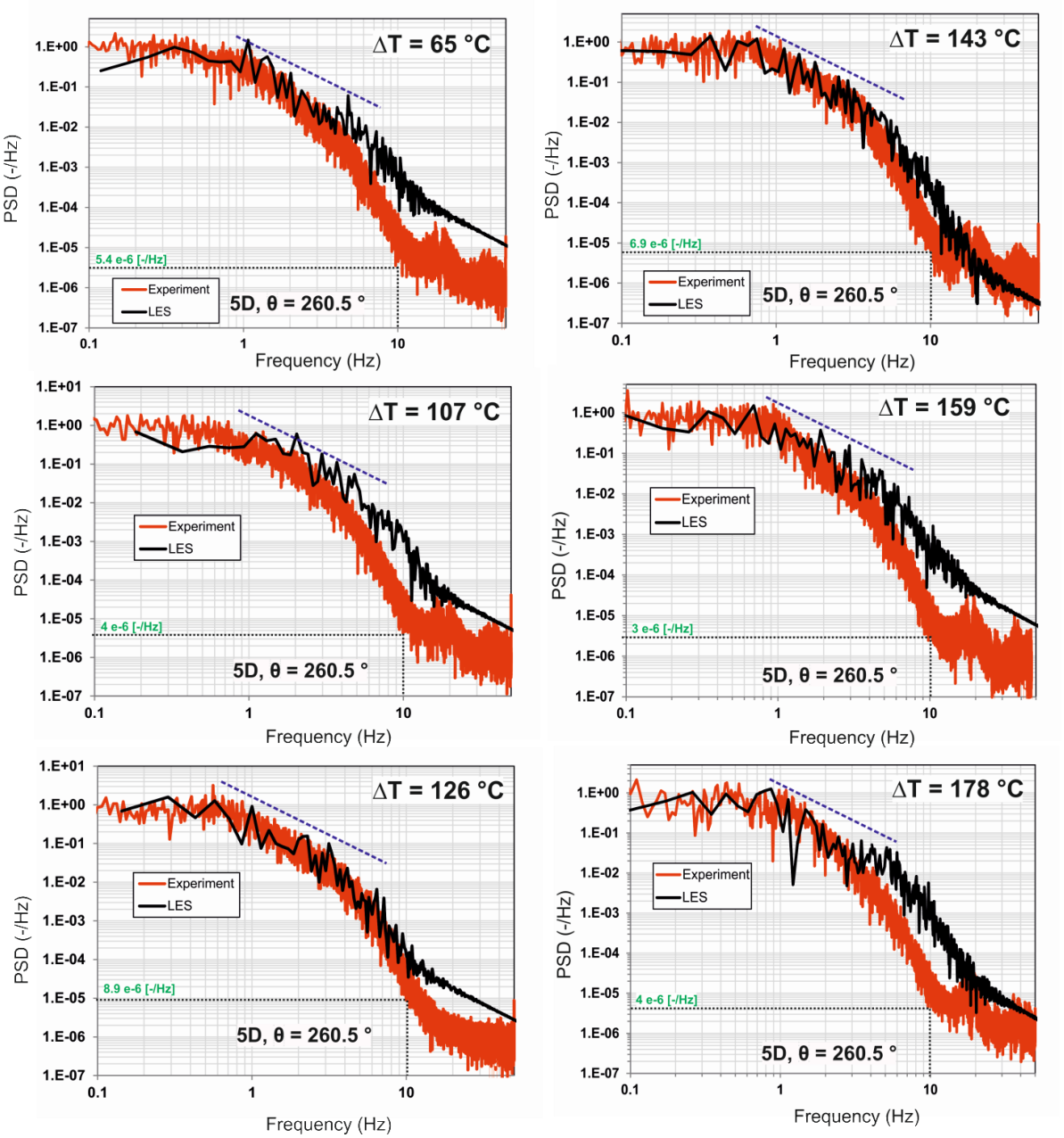

Fig. 47 PSD of peak fluid thermal fluctuations. Dotted lines show the -5/3 trend line in the inertial sub-range of the power spectrum

A different trend unfolds when analyzing the PSD of thermal fluctuations inside the solid as shown in Fig. 48. Unlike the fluid, the energy content of thermal fluctuations inside the solid is not concentrated within in a particular frequency range. The decline in the energy of thermal fluctuations with frequency is nearly linear from 0.1 till 10 Hz. Within this interval

the power content of solid thermal fluctuations are comparatively lower than the fluid fluctuations discussed in Fig. 47. Beyond 10 Hz, the PSD amplitudes within solid tend to stabilize and have higher magnitudes than the fluid PSD amplitudes.

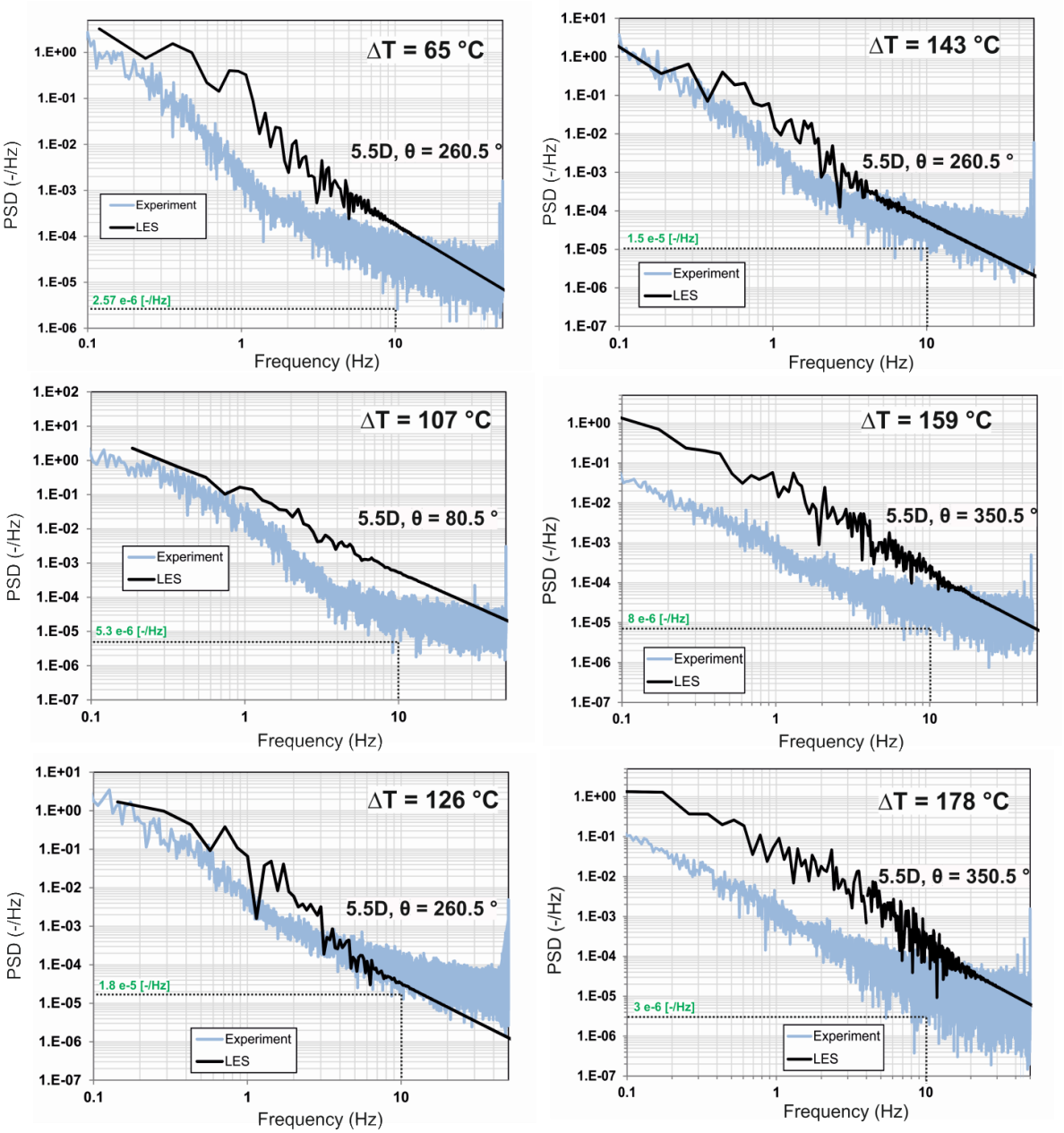

Fig. 48 PSD of peak solid thermal fluctuation in all the investigated cases

This completes the first part of the results section where flow behavior at ΔT between the mixing fluids in 60 – 180 °C range is discussed at constant main and branch flow rates of 0.4 kg/s and 0.1 kg/s, respectively. Changes in the flow mixing behavior caused by variation of the main flow rates are illustrated in the section A.2 of the appendix.

4.2 Mixing behavior of flows at ΔT = 233 °C

It has been established in the previous section that the thermally stratified flow in the mixing region becomes increasingly stable with rising ΔT between the fluids. An auxiliary effect is a rise in the flow penetration distance of hot fluid into the branch pipe and vice versa triggered by the rising density differences between the fluids and the low Reynolds number of the cold fluid coming from the branch pipe. With this understanding, it was decided to perform a single experiment in which the FSI test facility was taken to its highest operable fluid temperature to observe the mixing nature of the flow in the vicinity of the T-junction. The inflow conditions related to this experiment are shown in Table 10.

Table 11. Case 7 – Inflow conditions for experiments at ΔT = 233 °C

Parameters	Main pipe	Branch pipe
Temperature (°C)	257	24
Mass flow rate (kg/s)	0.4	0.1
Velocity (m/s)	0.13	0.084
Density (kg m^{-3})	775	999
Dynamic viscosity (Pa s)	9.95 e-5	9.13e-4
Reynolds number (Re)	71324	3580
u_{mix} (m/s)	0.153	
Ri	7.6	
Relative density ($\Delta\rho/\bar{\rho}$)	25.2 %	
Relative viscosity ($\Delta\mu/\bar{\mu}$)	160.7 %	
Pressure	70 bar	

Turbulent hot fluid flowing in the main pipe (257 °C, Re_m = 71324) combines with the transitional cold fluid flowing through the branch pipe (24 °C, Re_b = 3580) at the T-junction. Assessment of non-dimensional parameters in Table 11 points to the highest possible buoyancy effects to be expected in the flow. For example, the Richardson number is calculated to be 7.6, nearly 50 % higher than in case 6 (ΔT = 178 °C) discussed in the

previous section. Similarly, relative density ($\Delta\rho/\bar{\rho}$) is estimated to be 25.2 %, about 70 % higher than the values estimated in case 6 (ΔT = 178 °C). More importantly, the relative viscosity is estimated to be nearly 161 % indicating the highest viscosity differences among the participant hot and cold coolant streams.

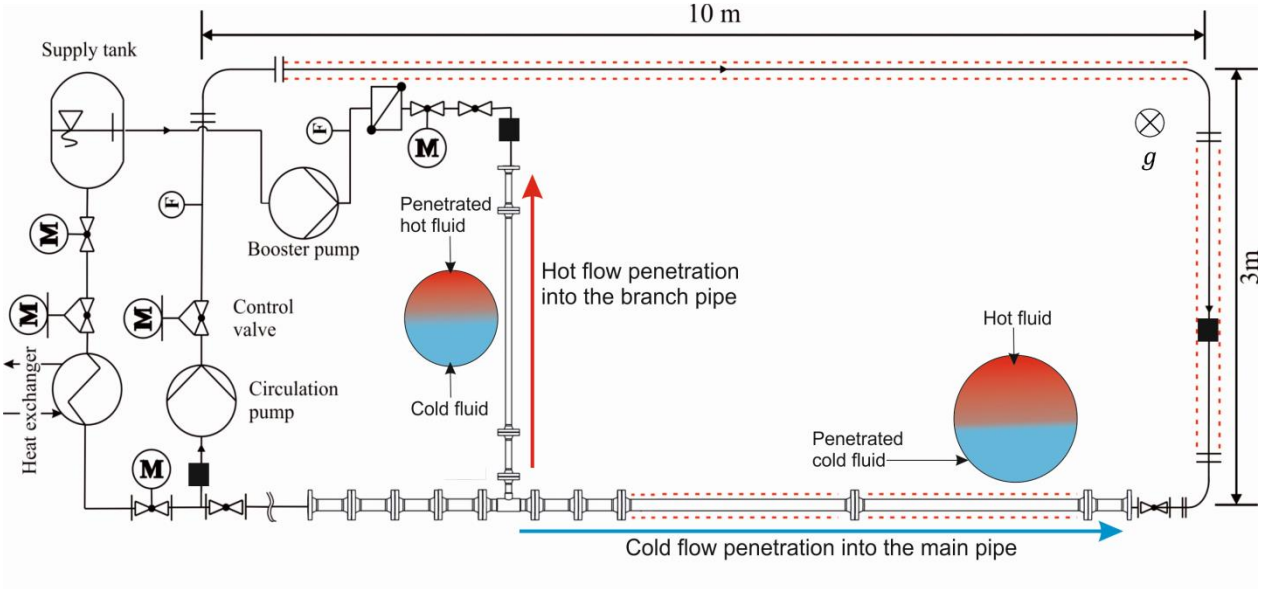

Fig. 49 FSI T-junction schematic illustrating the extent of suspected flow penetration

4.2.1 Turbulent Penetration and Pipe Bending

Two things that were often cited in the previous section is (i) the increase in the extent of cold and hot flow penetration into the main and branch pipes, respectively with rising ΔT between the fluids, and (ii) bending of pipes that could be clearly observed beyond ΔT = 150 °C. The highest ΔT in the present case of 233 °C between the fluids resulted in the culmination of both the above effects causing the highest extent of flow penetration in addition to the highest bending effect observed at the FSI test loop.

Fig. 49 depicts the assumed extent of flow penetration in both the main and branch pipes during the measurements. The highest relative density between fluids could result in the cold flow easily sinking to the bottom of the T-junction with one part flowing in the upstream direction and another in the downstream direction. Thermocouples placed in the structure in the main and branch pipes close to the T-junction reveal the stark temperature difference between the top and bottom pipe regions as illustrated in Fig. 50. Temperature differences of nearly 175 °C were recorded in both the main and branch pipe top-bottom thermocouple pairs leading to strong expansion effects near the top of the pipe (due to hot

fluid) and compression effects that could be induced at the bottom of the pipe (due to cold fluid). This automatically induces strong bending moments in the pipe structure. Previous numerical studies performed in 2012 indicated that possibility of the piping lift-up with the T-junction as its vertex [116]. That prediction is confirmed through the current experiment where thermally stratified flows are observed in all the directions (due to flow penetration in the upstream directions and due to mixing in the downstream direction).

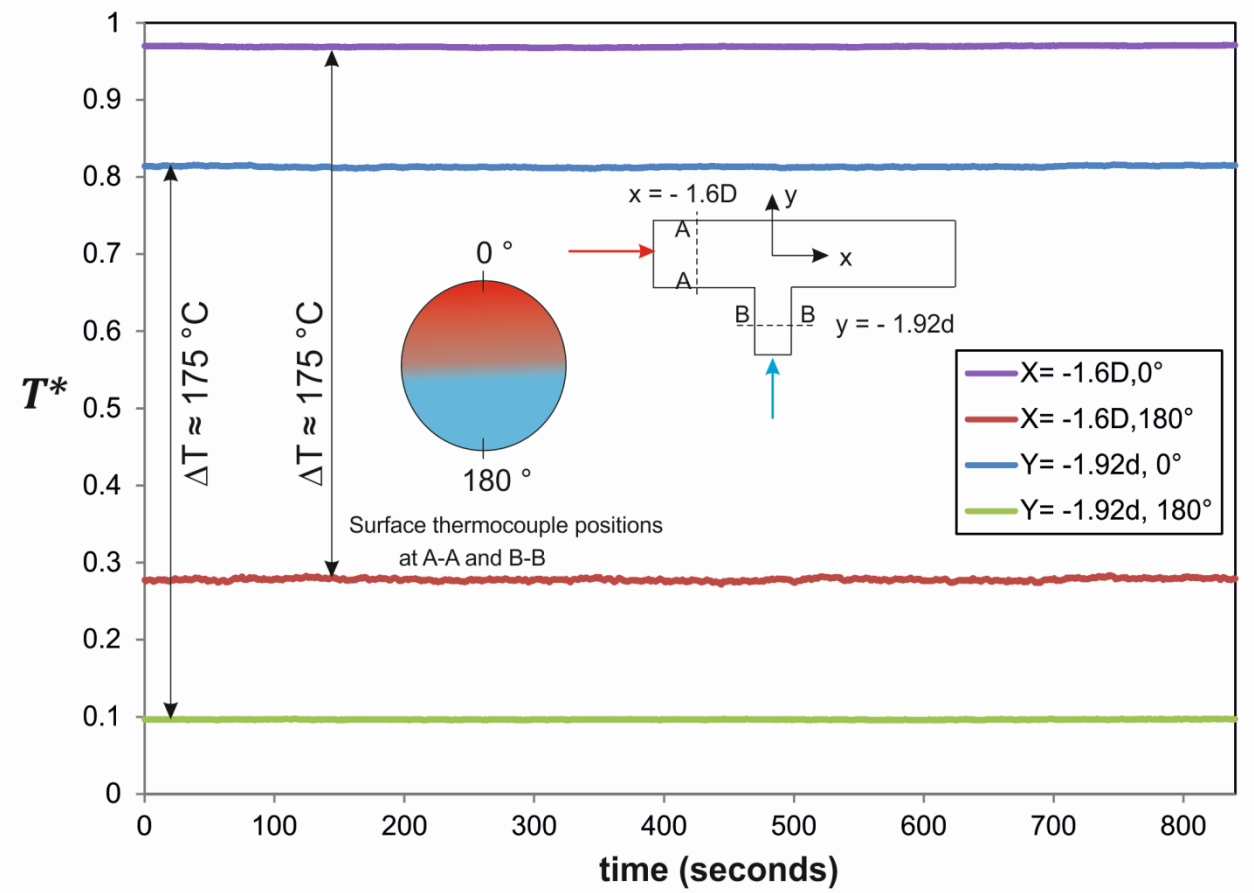

Fig. 50 Temporal evolution of in-structure temperatures in the main and branch pipes

There is a strong possibility that the hot fluid might have traveled all the way up to the beginning of the straight section of the branch pipe (nearly 2.4 m long) partly aided by the pipe bending effects which exacerbates the situation. There is no empirical evidence confirming this effect due to the fact that surface thermocouples were not placed that far upstream in the branch pipe.

On the other hand, there is an even greater possibility that the cold flow might have penetrated and traveled all the way till the beginning of the straight section of the main pipe (nearly 4.6 m long) also aided partly by the pipe bending effects. There is empirical evidence

of this phenomenon from the surface thermocouple instrumentation (see Fig. 51) primarily placed to monitor the heating mat temperatures. A temperature difference of greater than 60 °C within the top-bottom region of the hot flow close to 3 meters upstream of the T-junction confirms the cold flow penetration beyond this distance.

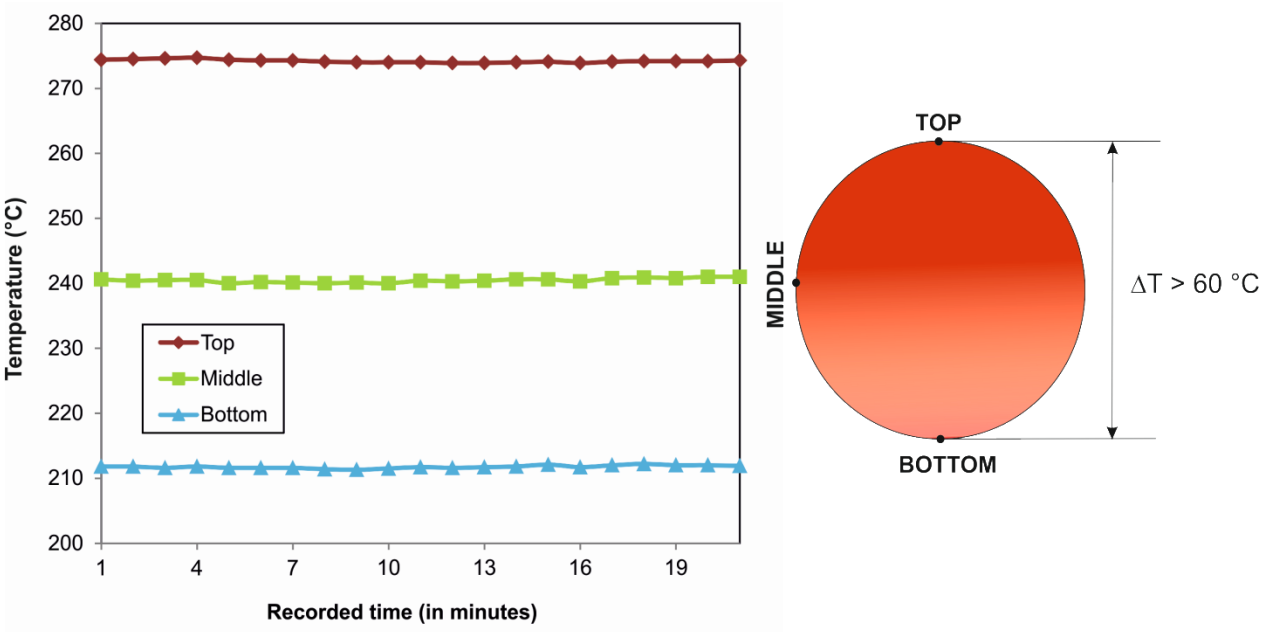

Fig. 51 Cold flow penetration in the main pipe (2.92 m upstream of T-junction) as recorded by surface thermocouple instrumentation

As a result of the flow penetration upstream of the T-junction and the stable thermal stratification in the downstream region, the piping structure is seen to lift up from its rest position with the T-junction as the vertex, described in the literature as 'banana effect' [92]. Excerpts detailing such a phenomenon involving thermal stratification are as follows:

"If the velocity of the medium in a pipe flow is small, temperature stratification may occur in horizontal pipe sections which might superimpose a significant contribution to global bending stresses ("banana effect") and fatigue"

Visual observations indicate that the T-junction might have lifted up by nearly 80 mm from its rest position as shown in the photographs in Fig. 52.

4.2.2 Near-wall mean and RMS temperature distribution

With arguably the most predictable flow behavior downstream of the T-junction in the FSI facility, the stark buoyancy effect keeps the flow in the mixing region very stable by

dampening flow oscillations quickly and this is illustrated by the mean temperature data shown in Fig. 53.

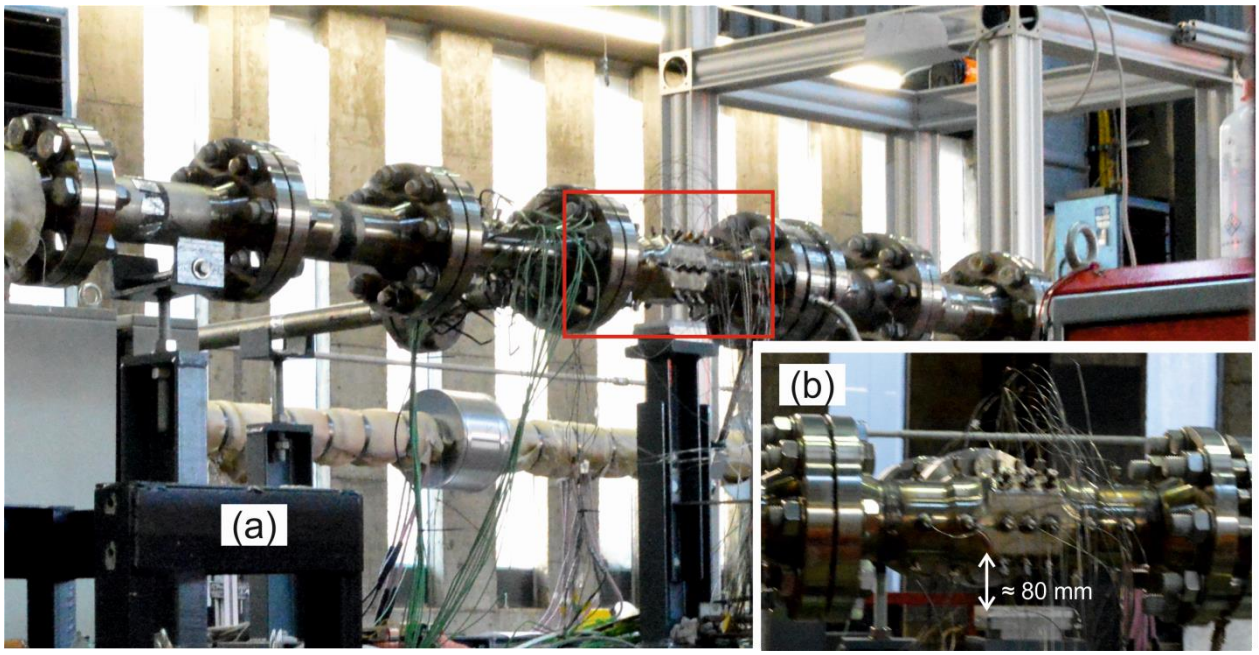

Fig. 52 Bent T-junction piping [marked in red] (a), its close-up view (b) at ΔT = 233 °C

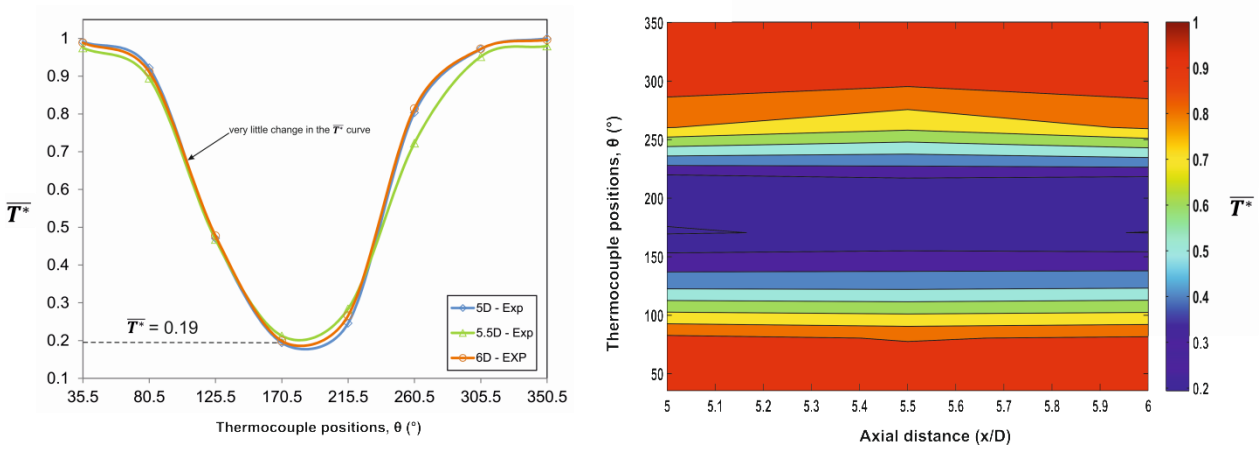

Fig. 53 $\overline{T^*}$ distribution (left) and $\overline{T^*}$ contour (right) at angular thermocouple positions

Nearly no change is observed in the $\overline{T^*}$ profile at all the axial locations (x = 5D, 5.5D and 6D) indicating a stably stratified flow that settles quickly following the initial mixing at the T-junction. Highest and lowest $\overline{T^*}$ values are observed near the upper (θ = 35.5 °, 80.5 °, 305.5 ° and 350.5 °) and lower (θ = 170.5 °) regions, respectively. It goes without saying that the very low temperatures at the bottom of the pipe in the mixing region is influenced by the pre-mixing that occurs upstream of the T-junction due to cold flow penetration in the main pipe described earlier. The stratified interface is found to occur between θ = 80.5 ° and

125.5 ° on the left-wall side and between θ = 215.5 ° and 260.5 ° on the right-wall side as denoted by the significant changes in $\overline{T^*}$ between these angular positions. Difference in mean temperature ($\Delta\overline{T^*}$) amplitude between the top (θ = 350.5 °) and bottom (θ = 170.5 °) of the pipe has the highest magnitude of 0.81 corresponding to a temperature amplitude of nearly 189 °C. This extremely high thermal gradient existing between the top and the bottom of the pipe induces the sharp bending effects discussed above.

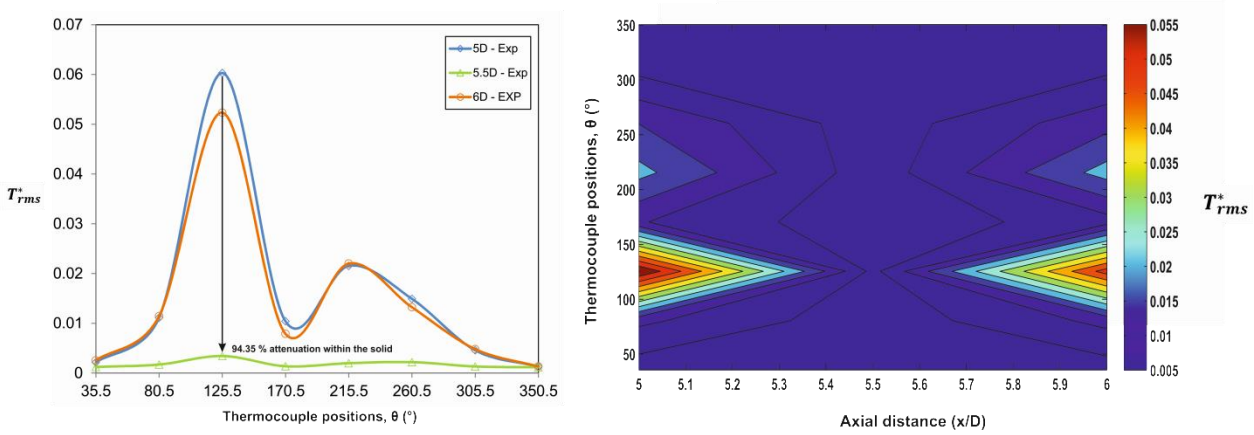

Fig. 54 $\boldsymbol{T^*_{rms}}$ distribution (left) and $\boldsymbol{T^*_{rms}}$ contour (right) at angular thermocouple positions

In-flow and in-structure temperature fluctuations (T^*_{rms}) as recorded by the 24 thermocouples in the mixing region are shown in Fig. 54. Typical of a stably stratified flow, the T^*_{rms} curves are similar at x = 5D and 6D albeit with a slight reduction in T^*_{rms} amplitude at a few angular positions. Peak T^*_{rms} amplitude of 0.06 (14 °C) occurs at θ = 125.5 ° while the lowest T^*_{rms} amplitudes occur near the top region (θ = 350.5 °) with an amplitude of 0.0013 (0.3 °C). When analyzing T^*_{rms} amplitudes inside the structure, the peak occurs at θ = 125.5 ° (similar to fluid) with an amplitude of 0.0034 (0.8 °C), a 94.35 % attenuation from the peak amplitude recorded by the in-flow thermocouple at a similar angular position at x = 5D.

4.2.3 Frequency Spectrum Analysis

Power spectral density (PSD) of peak in-flow and in-structure thermal fluctuations is illustrated below in Fig. 55. Unlike in cases 1 till 6 discussed in the previous section, a general peak at a frequency of 1.4 Hz could be observed from the in-flow thermal fluctuation data. Beyond this peak, fluctuation energies are seen to sharply decline with frequency. PSD of solid thermal fluctuations doesn't exhibit any peak while at the same time

the energy decline with frequency inside the solid is gradual in comparison with the relevant data from the fluid. Beyond 7 Hz, a change in trend is observed where the energy of solid thermal fluctuations becomes higher than that of the fluid.

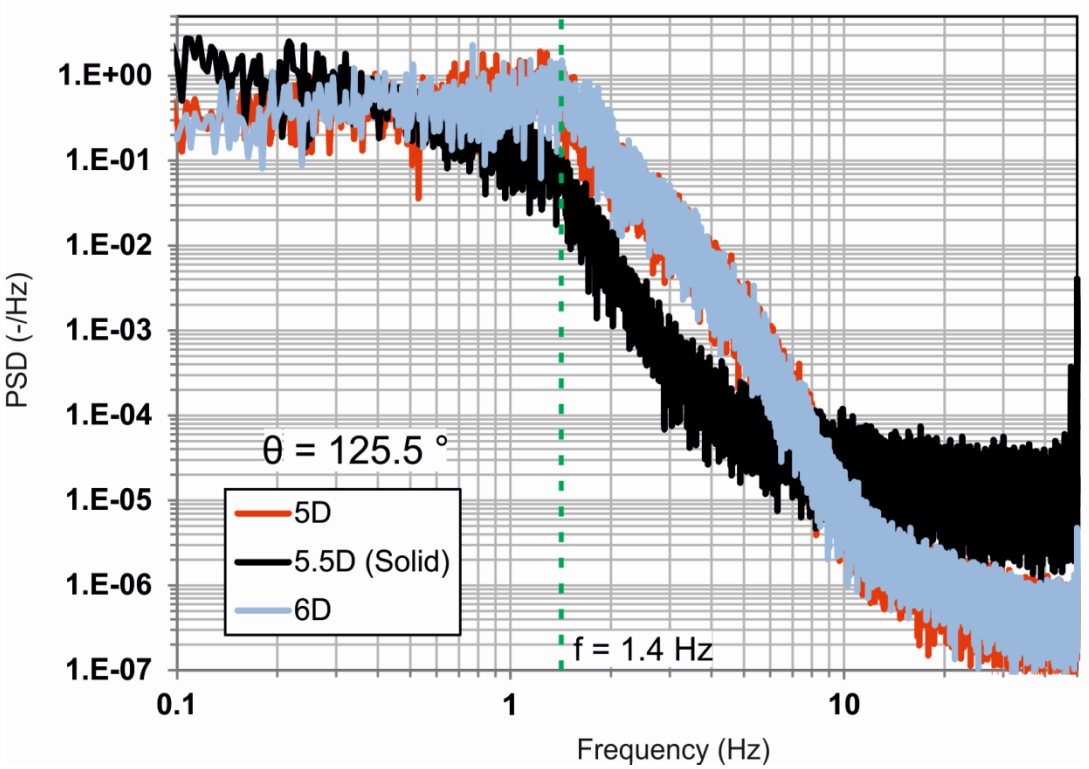

Fig. 55 PSD of temperature fluctuations at the in-flow and in-structure thermocouple positions

While the currently investigated ΔT of 233 °C induces considerable bending stresses in the structure which in turn induces flow penetration over longer distances upstream of the main and branch pipes, it is still not obvious if fatigue cracks could be initiated due to the mixing of flows under these inflow conditions. The previous numerical study carried out in 2012 [116] at an even higher ΔT of 260 °C also highlighted this fact. LES investigation for the present experiment has not been performed due to the deformation of the T-junction observed during measurements.

The next obvious advancement at the FSI test loop is the investigation of T-junction mixing at higher flow rates in the branch pipe which might shed more light into the flow mixing processes under turbulent inflow conditions (presently not the case due to low branch flow rate). While the experimental capability to do such measurements is currently in development at the moment, a precursor numerical study performed using LES could provide a valuable glimpse into the flow mixing phenomenon at higher branch flow rates.

4.3 Mixing behavior of flows at increased branch flow velocities

The obvious question that arises during the course of analyzing flow mixing at increasing ΔT between flows in section 4.1 is

"How is the mixing behavior affected/What happens to the mixing behavior when there is an increase in branch flow rates ?"

Table 12: Inflow conditions for increased branch flow studies

Case #	ΔT (°C)	T_m* (°C)	$\dot{m}_m$ (kg/s)	u_m (m/s)	T_b* (°C)	$\dot{m}_b$ (kg/s)	u_b (m/s)	u_{mix} (m/s)
1	65	85	0.4	0.101	20	0.1	0.084	0.132
1a		85	0.4	0.101	20	0.2	0.168	0.196
1b		85	0.4	0.101	20	0.3	0.252	0.272
4	143	165	0.4	0.109	22	0.1	0.084	0.138
4a		165	0.4	0.109	22	0.2	0.168	0.2
4b		165	0.4	0.109	22	0.3	0.252	0.275

* suffixes m and b denote main and branch pipes, respectively

As discussed before, the main limitation of the FSI test facility is its maximum operational branch flow rate ($\dot{m}_b$) of 0.1 kg/s is not turbulent enough to cause considerable mixing between the fluids. To analyze this issue numerically, it was decided to perform LES calculations to analyze flow mixing characteristics at increased branch flow rates while the flow rates in the main pipe were kept constant at 0.4 kg/s. Inflow conditions of cases 1 and 4, representative of lower and higher ΔTs, were chosen from section 4.1 for this exercise. Branch flow rates were increased to 0.2 kg/s and 0.3 kg/s, respectively. Results from the original cases 1 and 4 are also included here so as to easily compare and understand the effects of the rise in branch flow rates on the flow mixing dynamics in the vicinity of the T-junction. Details of the inflow conditions are shown in Table 12.

4.3.1 Qualitative analysis of the mixing region

The entry of the cold flow into the main pipe at high branch flow rates produces some distinct unsteady structures, namely, the shear layer vortices. Fig. 56 shows the

instantaneous temperature field at the T-junction. The leading edge of the cold flow as it enters the main pipe produces shear layer vortical structures that dominate the initial portion of the transverse cold flow. ΔT between flows (which affects relative density) and the velocity of the cold flow plays a clear role in the formation of these structures which could not be discerned at high ΔT (e.g. in cases 4, 4a, and 4b) in the present study. Similar comparable structures in literature observed through flow visualization studies in a crossflow-jet mixing scenario are also shown in Fig. 56.

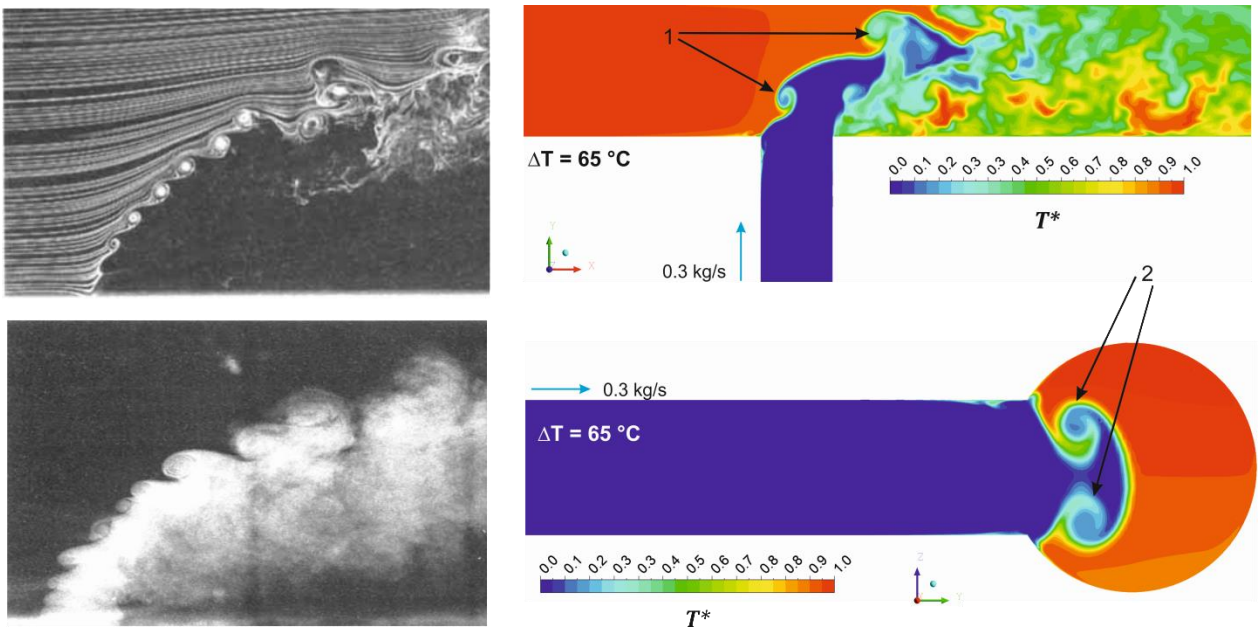

Fig. 56 Shear layer vortices (marked 1 and 2) resulting from the Kelvin-Helmholtz instability of the annular shear observed during crossflow mixing in literature ([34], left). Similar structures predicted by LES at higher branch velocities (right, at t = 35 s)

Fig. 57 shows the average velocity field as viewed from the branch pipe located 15 mm away (y = - 15 mm) from the center of T-junction. At ΔT = 65 °C (cases 1, 1a, 1b), increase in $\dot{m}_b$ clearly causes an axial shift in the CVP structure moving it closer to the branch pipe opening (indicated as dark circle in Fig. 57). There is also a vertical shift observed in the CVP structure moving it from the bottom of the pipe due to the strong branch flow. Increase in the lateral momentum of the cold flow causes considerable increase in the size of the CVP downstream of the T-junction as forced convection effects become higher with a rise in $\dot{m}_b$. At the other end of the spectrum at ΔT = 143 °C (cases 4, 4a, 4b), things evolve in a much different manner. High buoyancy combined with low $\dot{m}_b$ of 0.1 kg/s (case 4) causes (i) upstream penetration of part of the cold flow and (ii) high relative density causes the cold

flow to drop down to the bottom as it enters the T-junction changing the shape of the CVP structure. Increase in $\dot{m}_b$ (cases 4a, 4b) certainly results in the mixed flow overcoming the above mentioned characteristics to a great degree while at the same time exhibiting an axial and vertical shift of the CVP structure (similar to cases 1a and 1b) with rising $\dot{m}_b$.

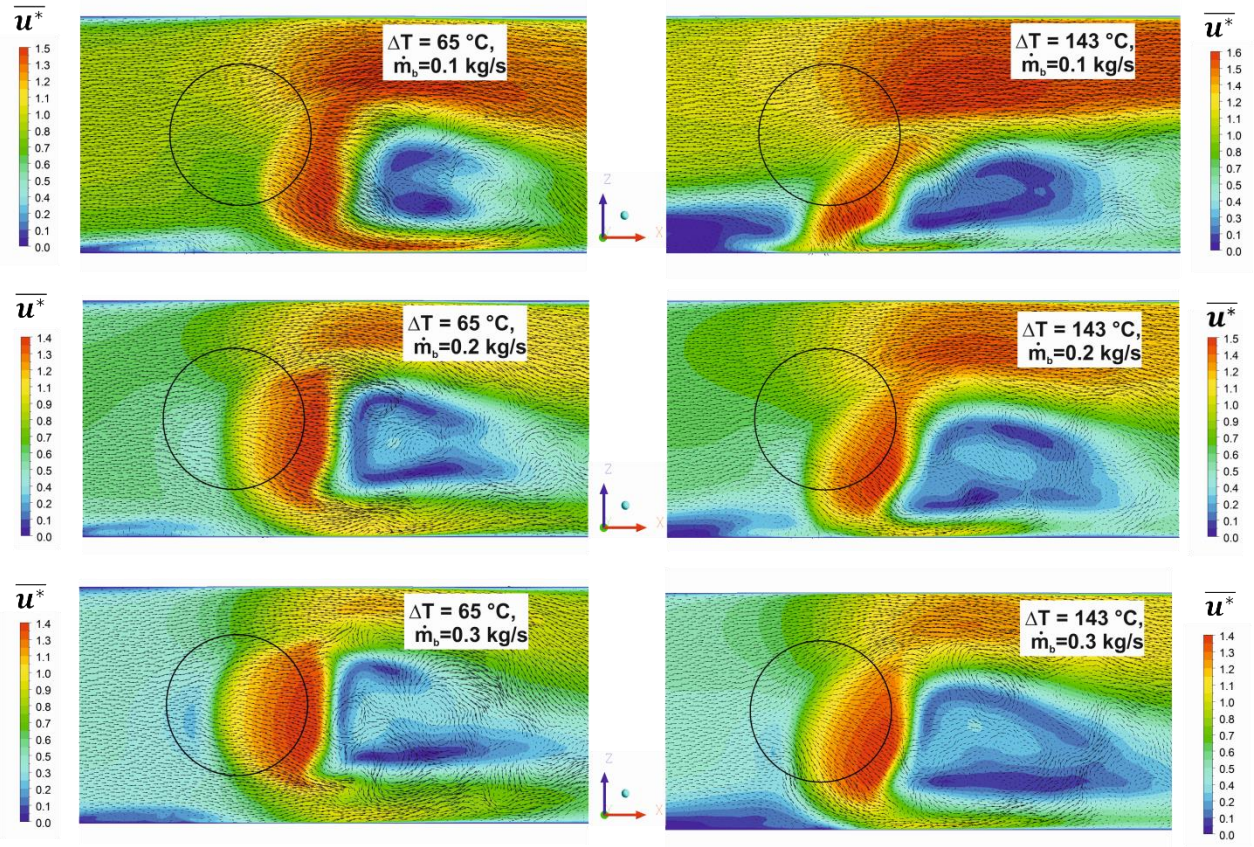

Fig. 57 Velocity field in the x-z plane (at y = - 15 mm) with in-plane velocity vectors. The dark circle indicates branch pipe opening

Fig. 58 depicts the evolution of the vortical structures (Q-criterion analysis with mean temperature contours) at ΔT = 65 °C with rising $\dot{m}_b$. As explained before, the horseshoe vortex structure observed at the cold flow outlet is primarily formed due to the boundary layer separation induced by the adverse pressure gradients as the cold flow approaches the T-junction. The legs of the HSV extend for a certain distance along the downstream direction and are clearly visible in case 1. The nature of this structure is highly influenced by the inflow conditions of the fluids arriving at the T-junction. Each rise in $\dot{m}_b$ produces strong HSV structures that tend to persist farther into the downstream region that could be attributed to the increased local heat transfer between flows in cases 1a and 1b could be attributed to these vortical structures.

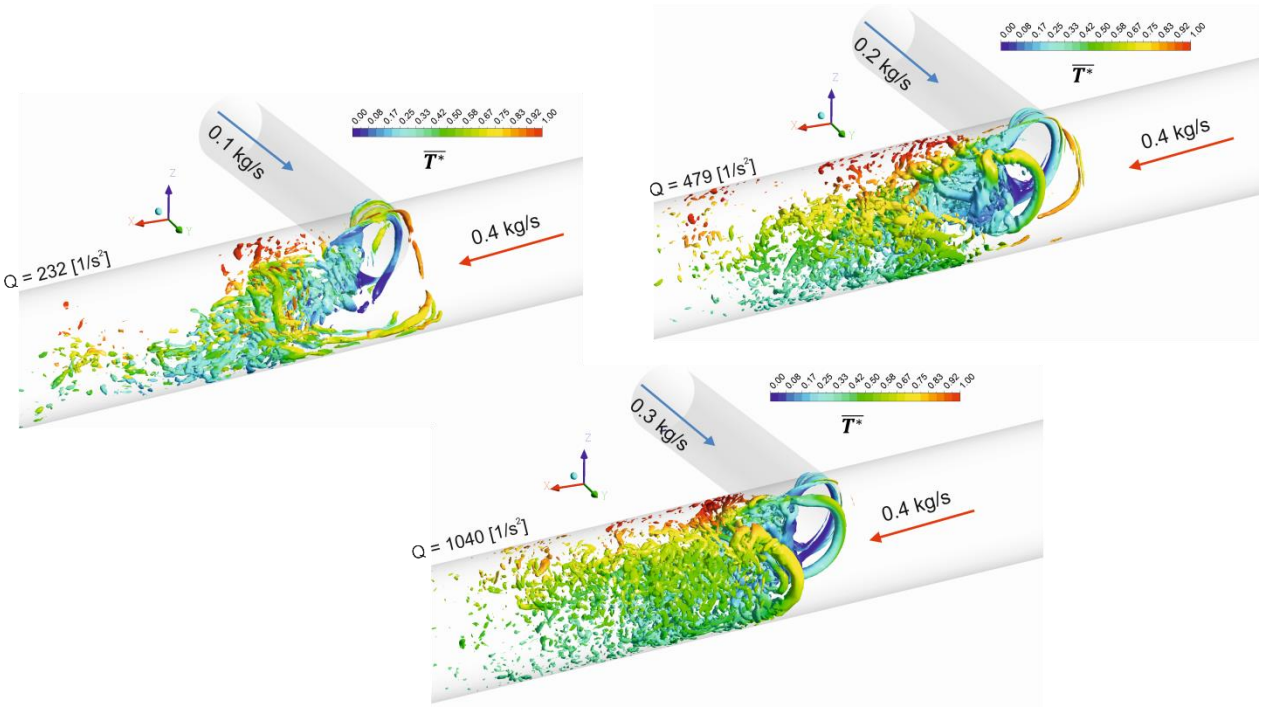

Fig. 58 Vortical structures in the T-junction at ΔT = 65 °C with rising branch flow rates

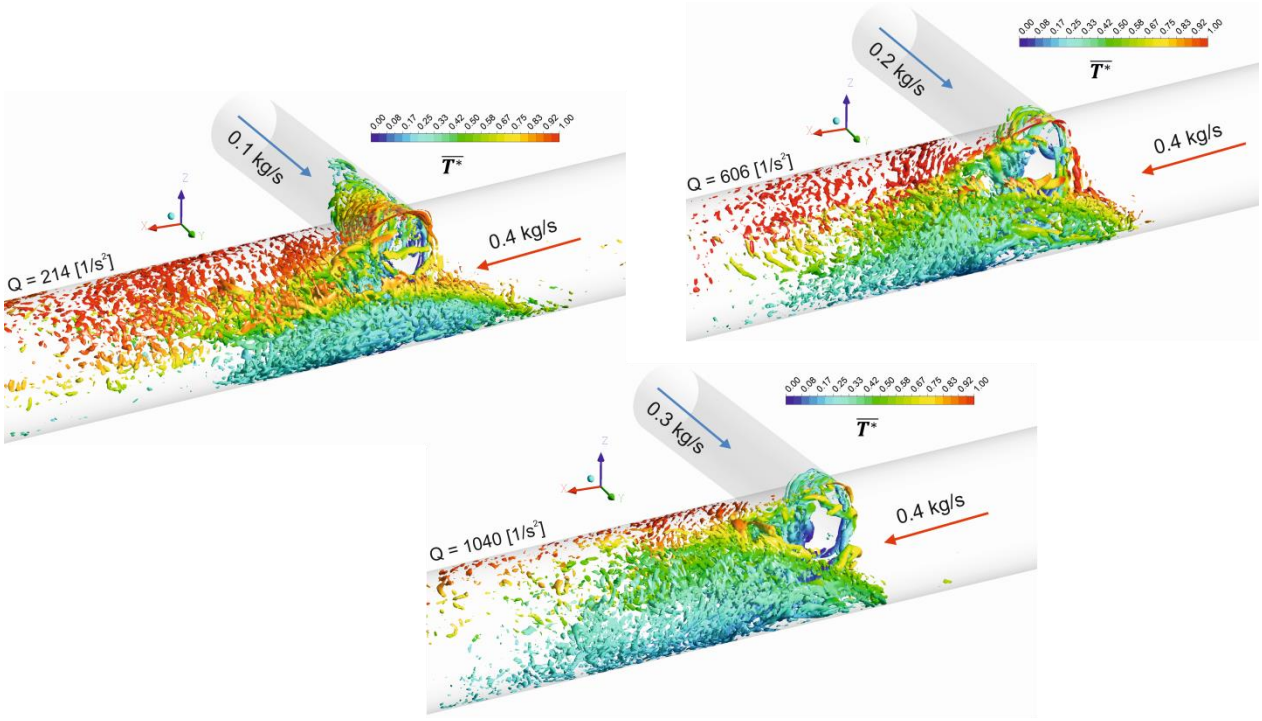

Fig. 59 Vortical structures at the T-junction at ΔT = 143 °C

Similar evolution of the vortical structures at ΔT = 143 °C with rising $\dot{m}_b$ is shown in Fig. 59. Upstream penetration of part of the hot fluid into branch pipe and vice versa in case 4 does

not result in any distinct HSV structure, but it produces multiple small-scale structures extending along the upstream and downstream directions. Elevated cold flow rates contribute to reversing this situation resulting in more mixing near the upper part of the pipe as seen from the $\overline{T^*}$ distribution of the structures. Nonetheless, no distinct vortical structures (like the HSV) are observed at the T-junction in cases 4a and 4b.

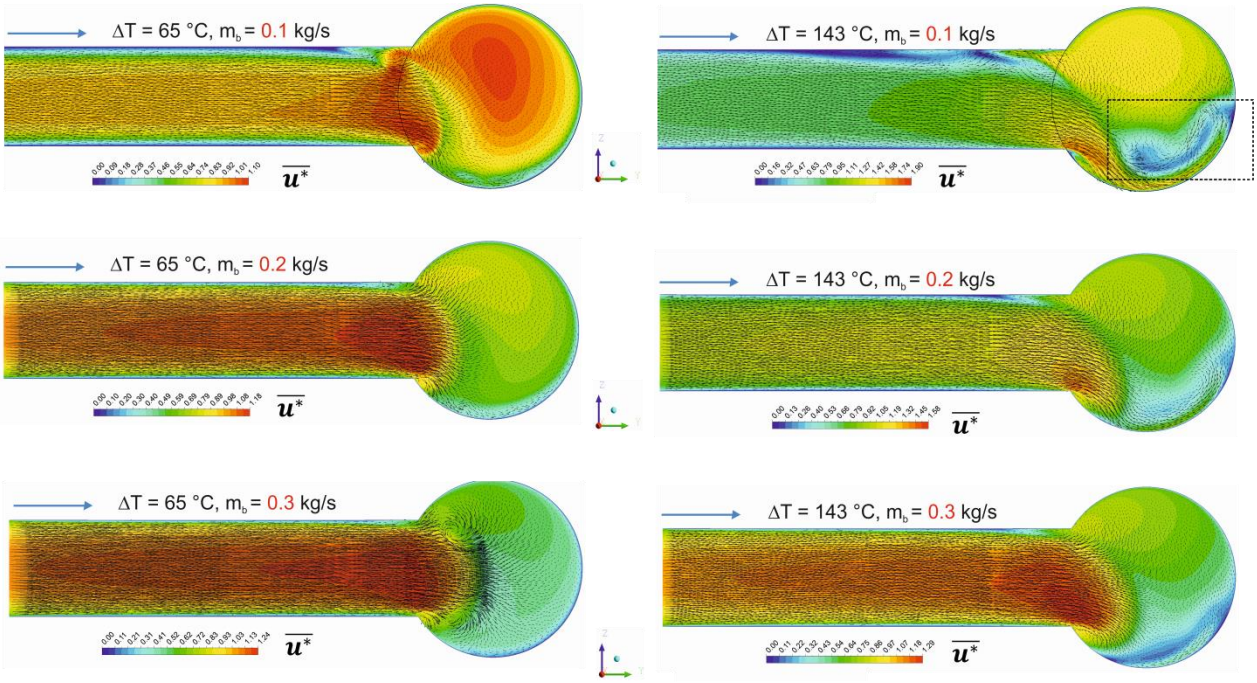

Fig. 60 Mean velocity field at the T-junction along the y-z axis

The nature of the cold flow entry into the T-junction could be a factor in the formation of these structures. At ΔT = 65 °C, the relative density is lower (≈ 3 %) which enables the cold flow to push farther into the T-junction with rising $\dot{m}_b$ (see Fig. 60) resulting in the formation of the HSV structure. At ΔT = 143 °C, the relative density has nearly tripled (≈ 10 %) causing the cold flow to sink to the bottom of the main pipe (case 4) which results in such structures not being produced. Increase in $\dot{m}_b$ (cases 4b, 4c) results in the cold flow trying to overcome the tendency to sink into the main pipe and could be a reason why no distinct HSV structures are formed at ΔT = 143 °C despite an increase in $\dot{m}_b$.

Fig. 61 shows the mean temperature distribution at the T-junction along the streamwise direction. Rise in $\dot{m}_b$ clearly results in the cold flow pushing farther into the main pipe causing complete mixing (at ΔT = 65 °C) or enhanced mixing resulting in higher oscillations of flow in the downstream region (at ΔT = 143 °C).

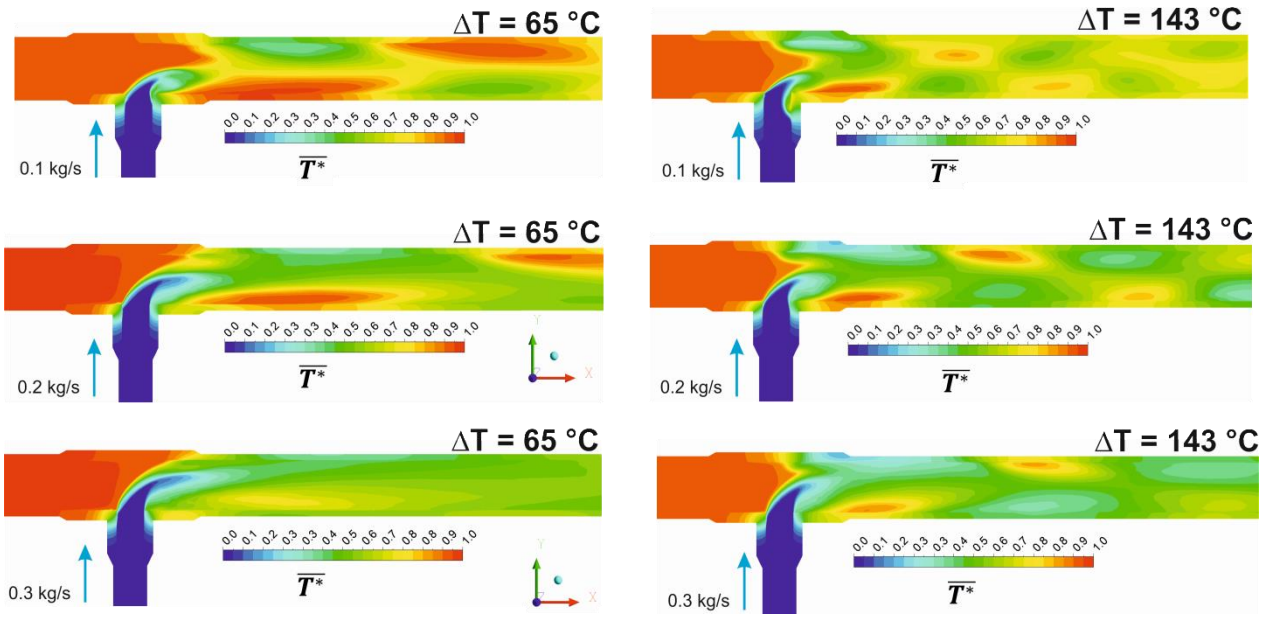

Fig. 61 Mean temperature field at the T-junction along the streamwise (x-y axis) direction

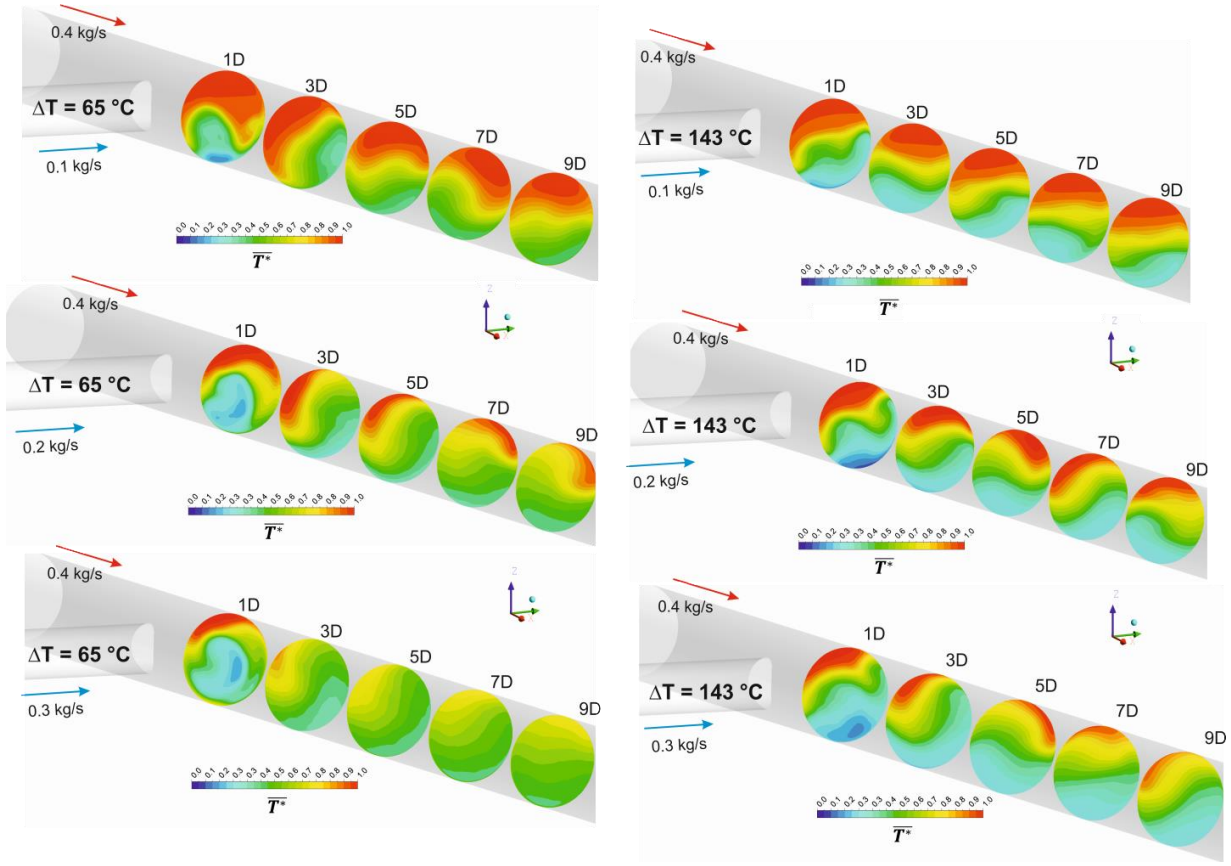

Fig. 62 Mean temperature field along the downstream cross-sectional (y-z axis) locations

This is even more clearly illustrated in Fig. 62 showing the cross-sectional $\overline{T^*}$ distribution at various locations in the mixing zone. The transition from an unstably stratified flow to a

completely mixed flow is clearly seen at ΔT = 65 °C while a similar transition from a stably stratified flow to an unstably stratified flow is seen at ΔT = 143 °C. The general observation that could be made is that increased forced convection effects brought about by rise in $\dot{m}_b$ are devoted to enhancing the turbulent mixing between flows at lower ΔT of 65 °C (cases 1, 1a, 1b). Since buoyancy becomes an important factor at higher ΔT between flows, any increase in forced convection effects caused by rising $\dot{m}_b$ is clearly devoted to overcoming the significant buoyancy effects in the flow as seen at ΔT = 143 °C (cases 4, 4a, 4b).

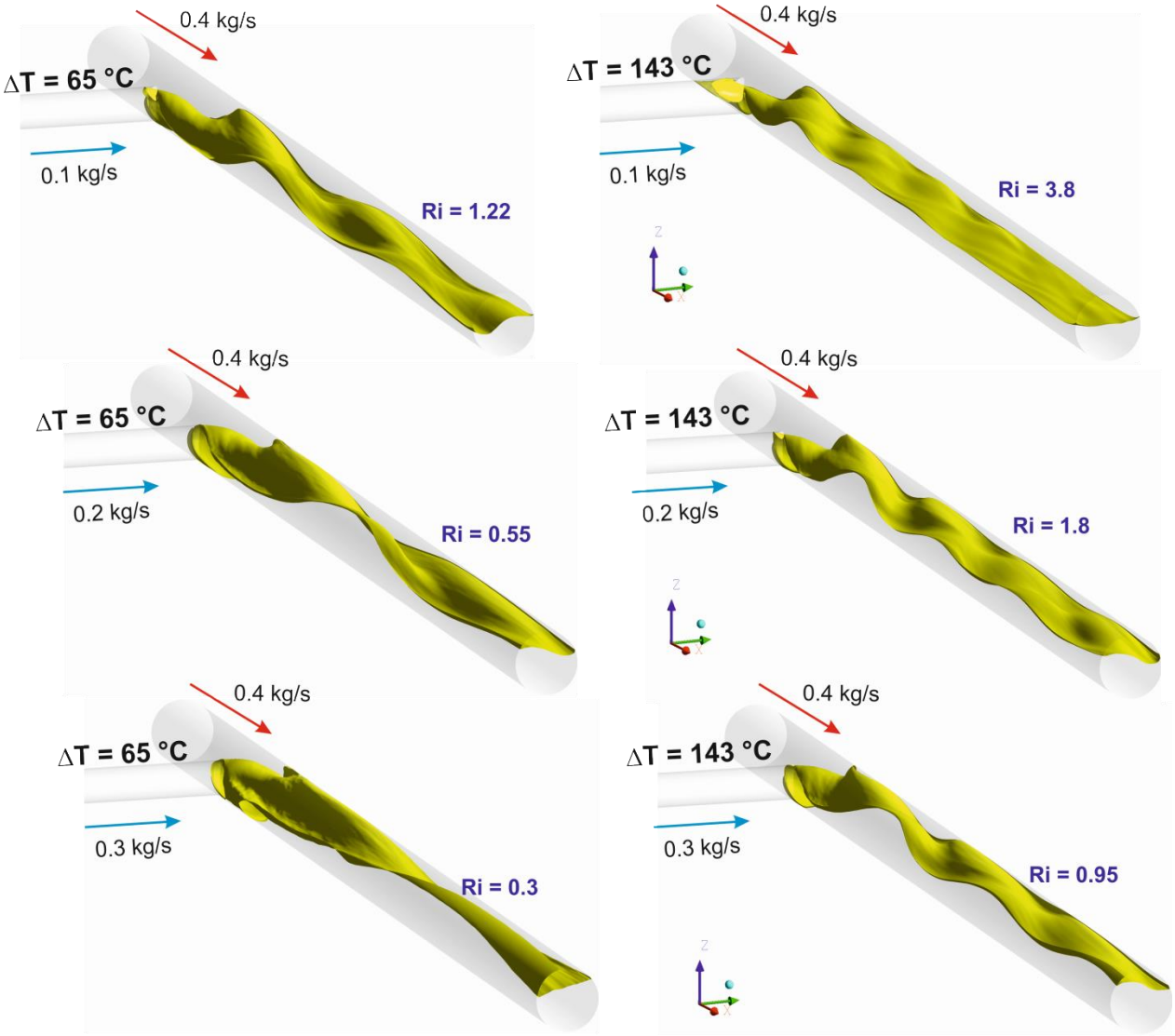

Fig. 63 Mean temperature isosurfaces at $\overline{T^*}$ = 0.75

Quantifying the influence of buoyancy or forced convection effects in the flow could be done using the Richardson number (Ri) calculations which have already been defined in section 4.1. Changes influenced by the rise in $\dot{m}_b$ to the flow mixing behavior are very clearly

illustrated using the mean temperature isosurfaces shown in Fig. 63. An oscillating wavy flow occurring over longer distances is observed at ΔT = 65 °C while a stably stratified flow becoming a unstably stratified flow with an oscillating wavy flow pattern is seen at ΔT = 143 °C.

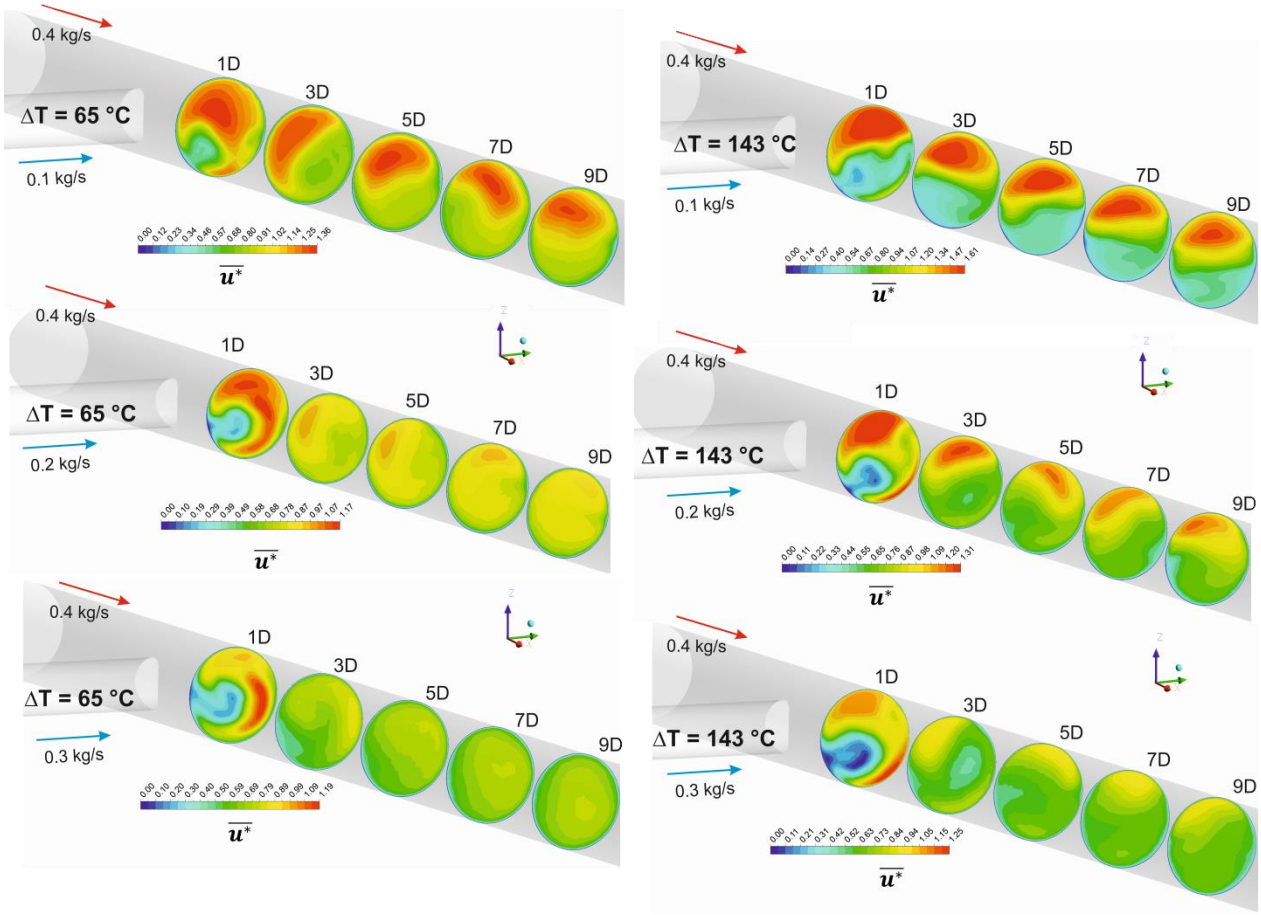

Fig. 64 Mean velocity field along various downstream cross-sectional (y-z axis) locations

The mean velocity field at various cross-sectional positions downstream of the T-junction for all the investigated cases is shown in Fig. 64. Velocity near the top is clearly higher at the lowest $\dot{m}_b$ of 0.1 kg/s as the hot flow travels unmixed at both ΔT levels of 65 °C and 143 °C, respectively. A rise in $\dot{m}_b$ enables enhanced mixing which greatly brings down the velocity near the top at ΔT = 65 °C as reflected in the vertical mean velocity profile shown in Fig. 65 which becomes nearly symmetric with the rise in $\dot{m}_b$. On the other hand, a rise in $\dot{m}_b$ is still insufficient to cause complete mixing between the flows at ΔT = 143 °C for reasons described above in Figs. 61, 62 and 63. This causes the highest mean velocity of flows to be concentrated near the upper region and the shape of the mean velocity profile in Fig. 65 confirms this trend.

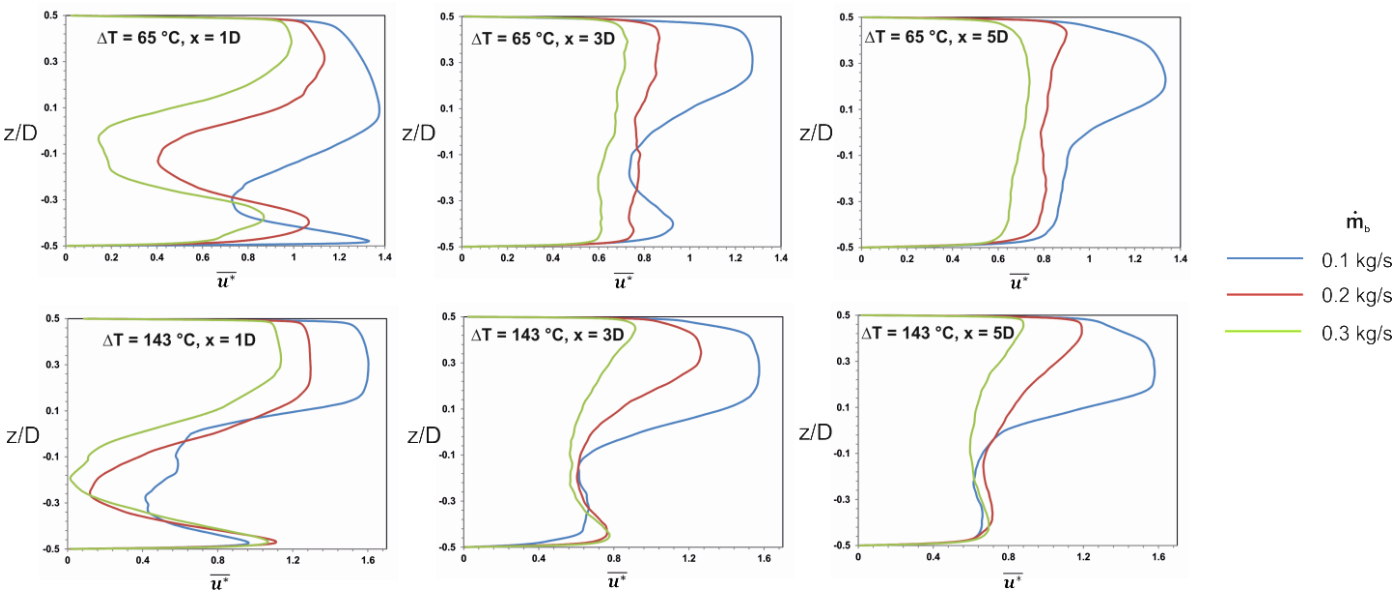

Fig. 65 Mean velocity along the vertical direction (z-axis) at downstream positions

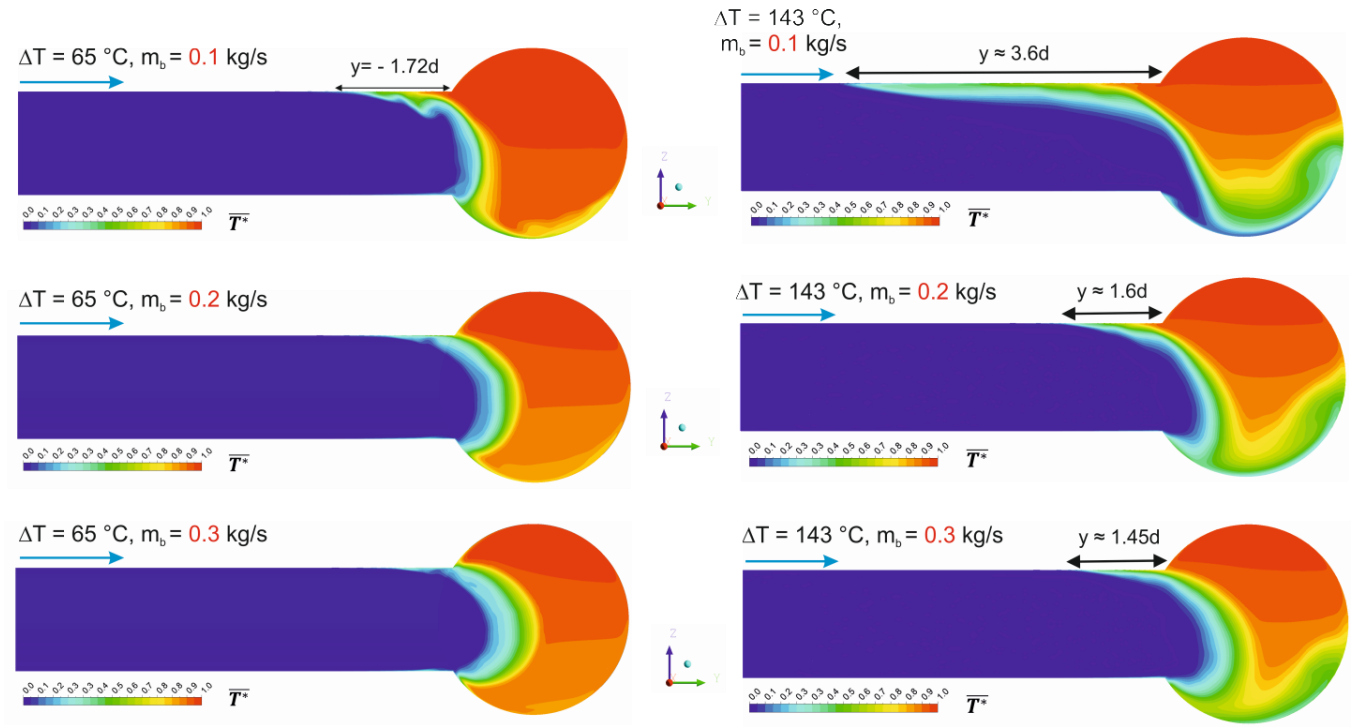

Fig. 66 Mean temperature field at the T-junction along the y-z axis

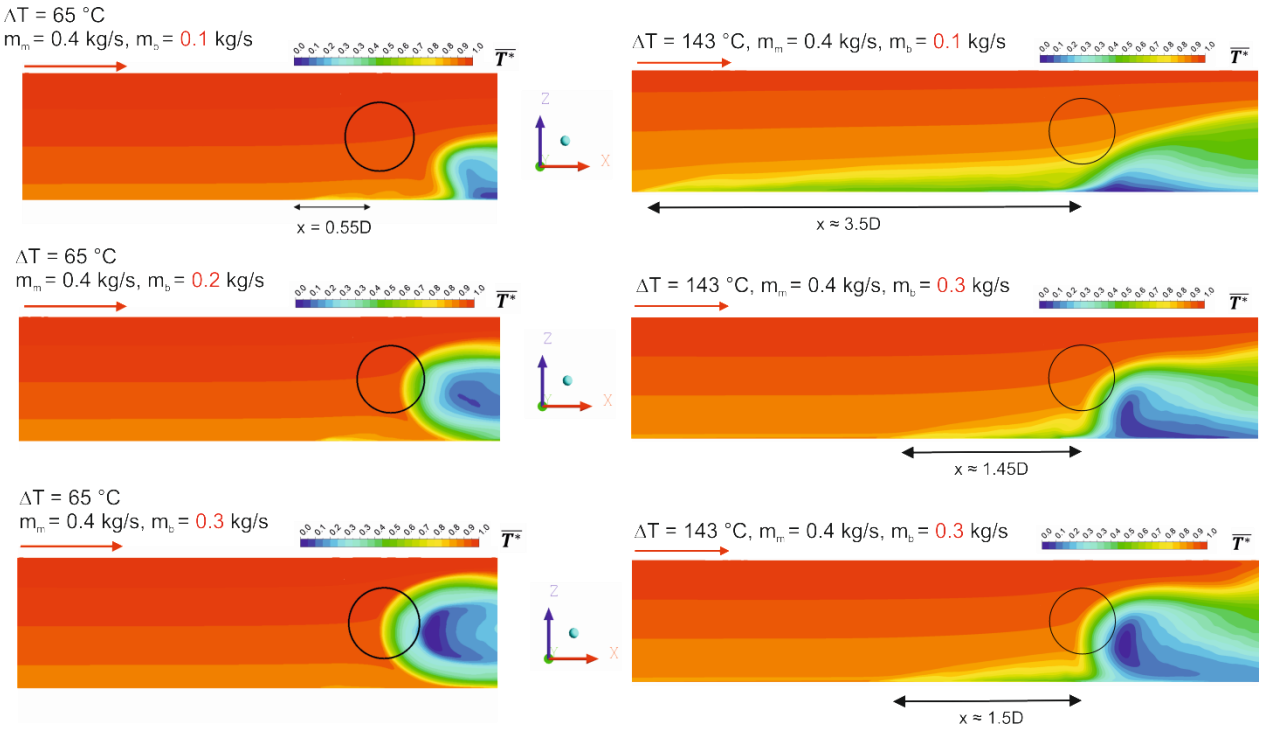

Fig. 67 Mean temperature field along the axial flow direction (x-z axis)

The density and inflow rate differences between the hot and cold flows sets up the stage for partial penetration of hot flow into the branch pipe and cold flow into the main pipe. It has been elaborately discussed in section 4.1 where it was established that the distance of penetration is influenced by ΔT between the fluids since all other inflow parameters are kept constant. Rise in $\dot{m}_b$ at ΔT = 65 °C (cases 1a, 1b) results in nearly negligible penetration of hot flow into the branch pipe (see Fig. 66) while at the same time there is a reduced penetration of cold flow into the main pipe (see Fig. 67).

The same could not be observed with rising $\dot{m}_b$ at ΔT = 143 °C (cases 4a, 4b). Firstly, there is a great degree of cold flow penetration over longer distance at $\dot{m}_b$ = 0.1 kg/s (case 4) caused by dominant buoyancy forces in the flow. Thus rise in $\dot{m}_b$ contributes to reducing the extent of cold flow penetration although it is not completely accomplished. Hot flow penetration into the branch pipe is reduced by more than 50 % from 3.6d (case 4) to 1.45d (case 4b) as shown in Fig. 66. Similarly, there is more than 50 % reduction in penetration distance of cold flow into the main pipe from 3.5D (case 4) to 1.5D (case 4b) as illustrated in Fig. 67.

4.3.2 Quantitative analysis

4.3.2.1 Mean temperature distribution

Fig. 68 shows the near-wall mean temperatures ($\overline{T^*}$) as predicted by LES with rising cold flow velocity in the branch pipe. At ΔT = 65 °C, the rise in branch flow rate to 0.2 kg/s (case 1a) is accompanied by a drop in $\overline{T^*}$ at certain angular positions (at θ = 260.5 ° and 305.5 °, for example) while a further increase in branch flow rate to 0.3 kg/s (case 1b) results in an overall reduction in $\overline{T^*}$ across several angular positions (especially near the top at θ = 35.5 ° and 350.5 °) highlighting the turbulent mixing induced temperature changes in the flow brought about by higher $\dot{m}_b$. Difference in mean temperature ($\Delta\overline{T^*}$) amplitude between the top (θ = 350.5 °) and bottom (θ = 170.5 °) of the pipe is also decreased by more than 28 % to 0.43 (28 °C) in case 1b from 0.6 (39.5 °C) in case 1.

At ΔT = 143 °C, the rise in $\dot{m}_b$ to 0.2 kg/s (case 4a) causes a change in $\overline{T^*}$ values at similar angular positions between different axial locations (x = 5D, 5.5D and 6D). Further rise in $\dot{m}_b$ to 0.3 kg/s (case 4b) results in enhanced oscillation in the flow as seen from the drop in $\overline{T^*}$ value at θ = 35.5 ° while at the adjacent positions the $\overline{T^*}$ value resembles that of unmixed hot flow at θ = 305.5 ° and 350.5 °. Difference in mean temperature ($\Delta\overline{T^*}$) amplitude between the top (θ = 350.5 °) and bottom (θ = 170.5 °) of the pipe is decreased by around 10 % to 0.67 (96 °C) in case 4b from 0.74 (105.6 °C) in case 4. Thus the data clearly shows that a rise in $\dot{m}_b$ at higher ΔT (cases 4a and 4b) reduces buoyancy effects in the flow which occurs at lower $\dot{m}_b$ (case 4).

A snapshot view of the change in the nature of the flow brought about by rising $\dot{m}_b$ in all the analyzed cases is illustrated in Fig. 69. Increasing branch velocity at ΔT = 65 °C (cases 1, 1a and 1b) changes the flow nature from unstably stratified (case 1) to a completely mixed flow (case 1b) exhibiting flow oscillations over a longer distance and a sharp reduction in $\overline{T^*}$ is observed at the top (θ = 90 °). At the same time, rising branch velocities induce more oscillations and reduction in buoyancy at ΔT = 143 °C (cases 4, 4a and 4b). Although inadequate to cause complete mixing of flows, the increased branch velocity is sufficient to cause oscillations near the top (θ = 90 °) where the $\overline{T^*}$ values begin to cyclically change over the length of the investigated domain. Cold flow penetration distance into the main pipe is also substantially decreased in cases 4a and 4b in comparison with case 4.

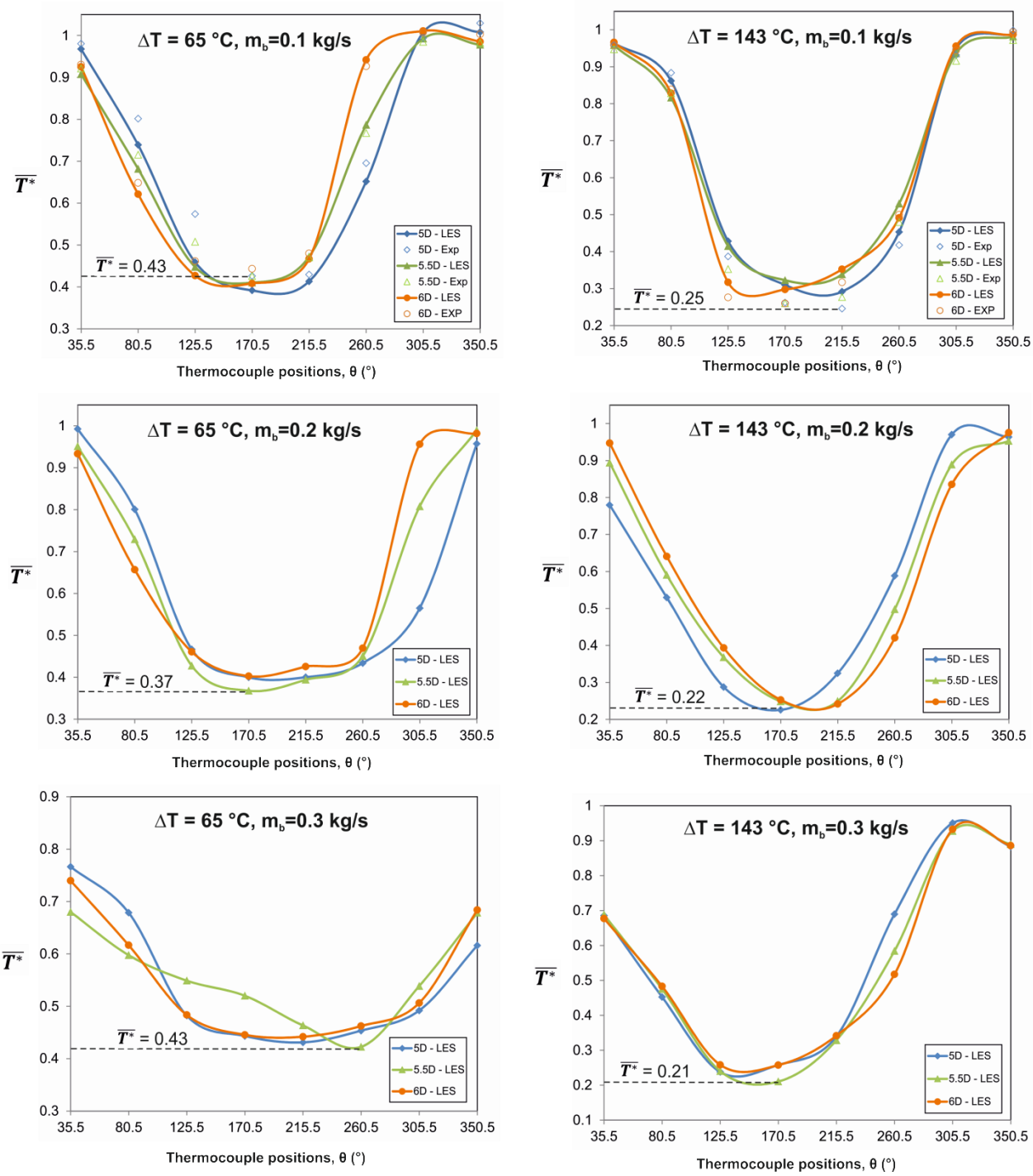

Fig. 68 Mean temperature ($\overline{T^*}$) distribution along the angular thermocouple positions, lowest $\overline{T^*}$ values are indicated by the dotted lines

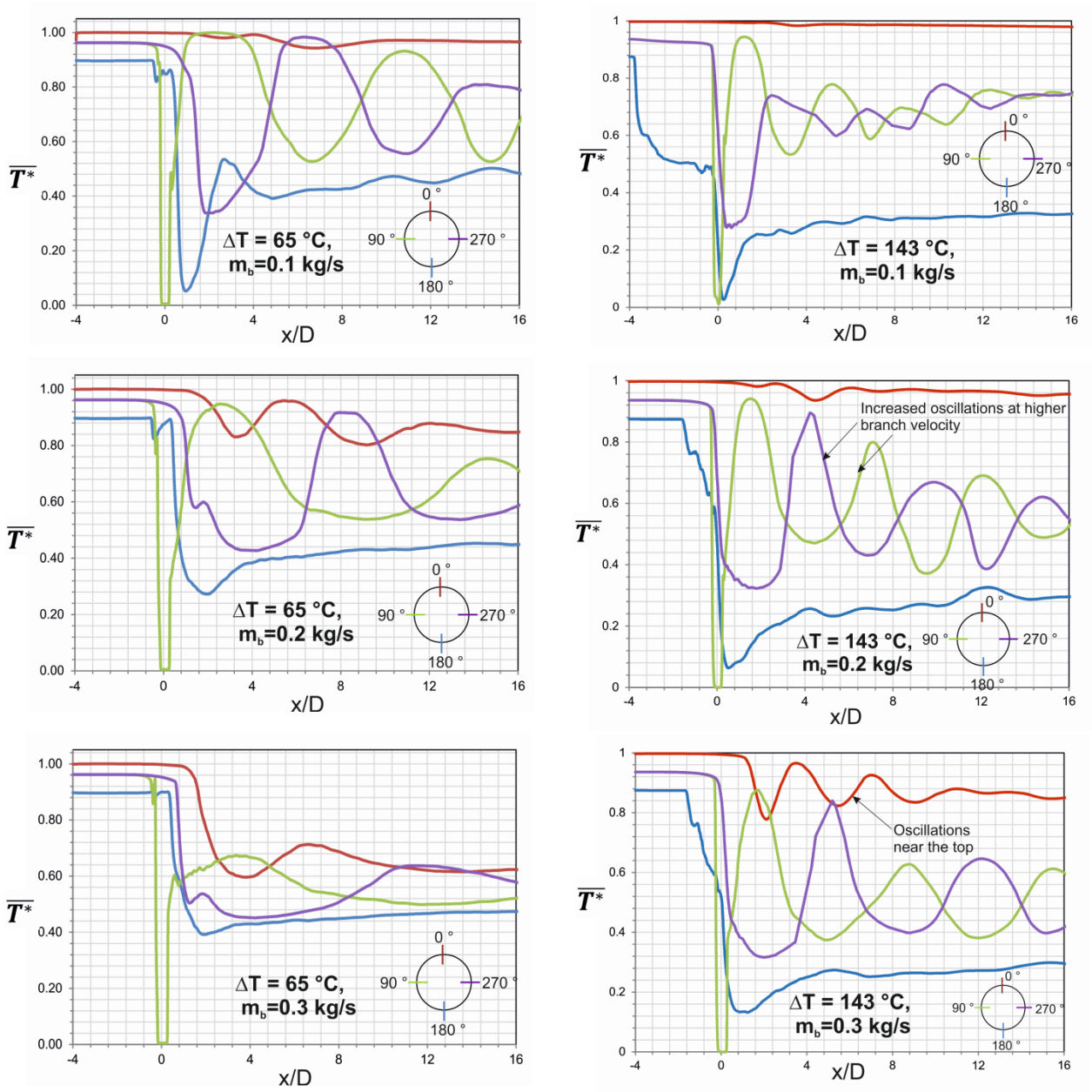

Fig. 69 Axial $\overline{T^*}$ distribution along the angular positions, θ = 0°, 90°, 180° and 270°

4.3.2.2 Temperature fluctuation distribution

Fig. 70 shows the T^*_{rms} distribution at the T-junction along the streamwise direction. At ΔT = 65 °C, the weaker branch flow is easily deflected by the hot flow in case 1. The interface of the hot-cold fluid region is also very thin. These characteristics change with rise in branch flow rates (cases 1a and 1b) where the turbulent cold flow is now able to travel farther into the main pipe and reaches the opposite wall at the highest branch flow rate of 0.3 kg/s (case

1b). Besides, the hot-cold fluid interface is also seen to broaden with rising branch flow rates and is the principal location of highest T^*_{rms} amplitudes at the T-junction.

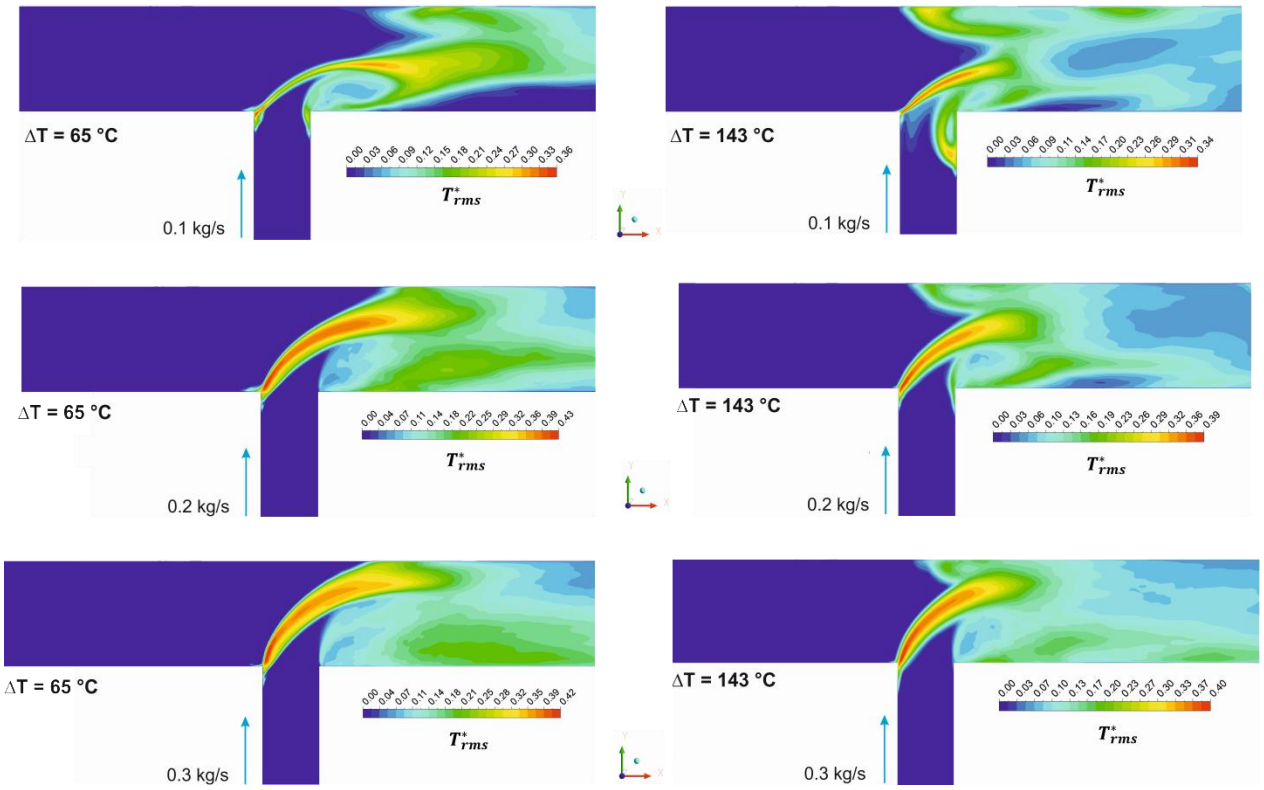

Fig. 70 Temperature fluctuations ($\boldsymbol{T^*_{rms}}$) at the T-junction along the streamwise direction

Peak T^*_{rms} amplitudes range between 36 – 43 % of ΔT (ΔT in this context refers to individual ΔT in each case) in the investigated cases 1, 1a and 1b. At ΔT = 143 °C, the prevailing issue at the lowest branch flow rate (case 4) is the significant intrusion of cold flow upstream of the main pipe and hot flow in the branch pipe. Rise in branch flow rates (cases 4a, 4b) increases the thickness of the hot-cold fluid interface, a focal point of peak T^*_{rms} amplitudes (about 34 – 40 % of ΔT). Also, cold flow is able to travel farther into the main pipe close to the opposite wall at the T-junction indicating the significant forced convection effects in play.

The cross-sectional distribution of thermal fluctuations downstream of the T-junction is illustrated in Fig. 71. Observations on the effect of increased branch flow rates at ΔT = 65 °C is summarized as follows: While it has already been established that an unstably stratified flow occurs in case 1, a doubling of $\dot{m}_b$ (to 0.2 kg/s) causes increased mixing between fluids. High amplitude T^*_{rms} are seen to shift towards the inner mixing interface between fluids

quite different from the stratified interface observed in case 1. Lowest T^*_{rms} values are still observed close to the top indicating that the mixing is still incomplete. This scenario is completely changed as the branch flow rate is increased to its highest level (0.3 kg/s in case 1b) where complete turbulent mixing of flows occur and distinct flow patterns that were ascertained in cases 1 and 1a (like unstable stratification) does not occur here. Similar observations on the effect of increased branch flow rates at ΔT = 143 °C is summarized as follows: Mixing area increases and more high amplitude T^*_{rms} zones in the flow are identified in case 4a [$\dot{m}_b$ – 0.2 kg/s] in comparison with case 4. Flow oscillations result in slightly unstable stratification with lowest T^*_{rms} values observed near the top. A subsequent rise in branch flow rate to 0.3 kg/s [case 4b] enhances and intensifies the mixing effects observed in case 4a and the unmixed area is seen to be reduced even further. Highest T^*_{rms} amplitudes for all the cases at ΔT = 143 °C lie in the vicinity of the stratification layer.

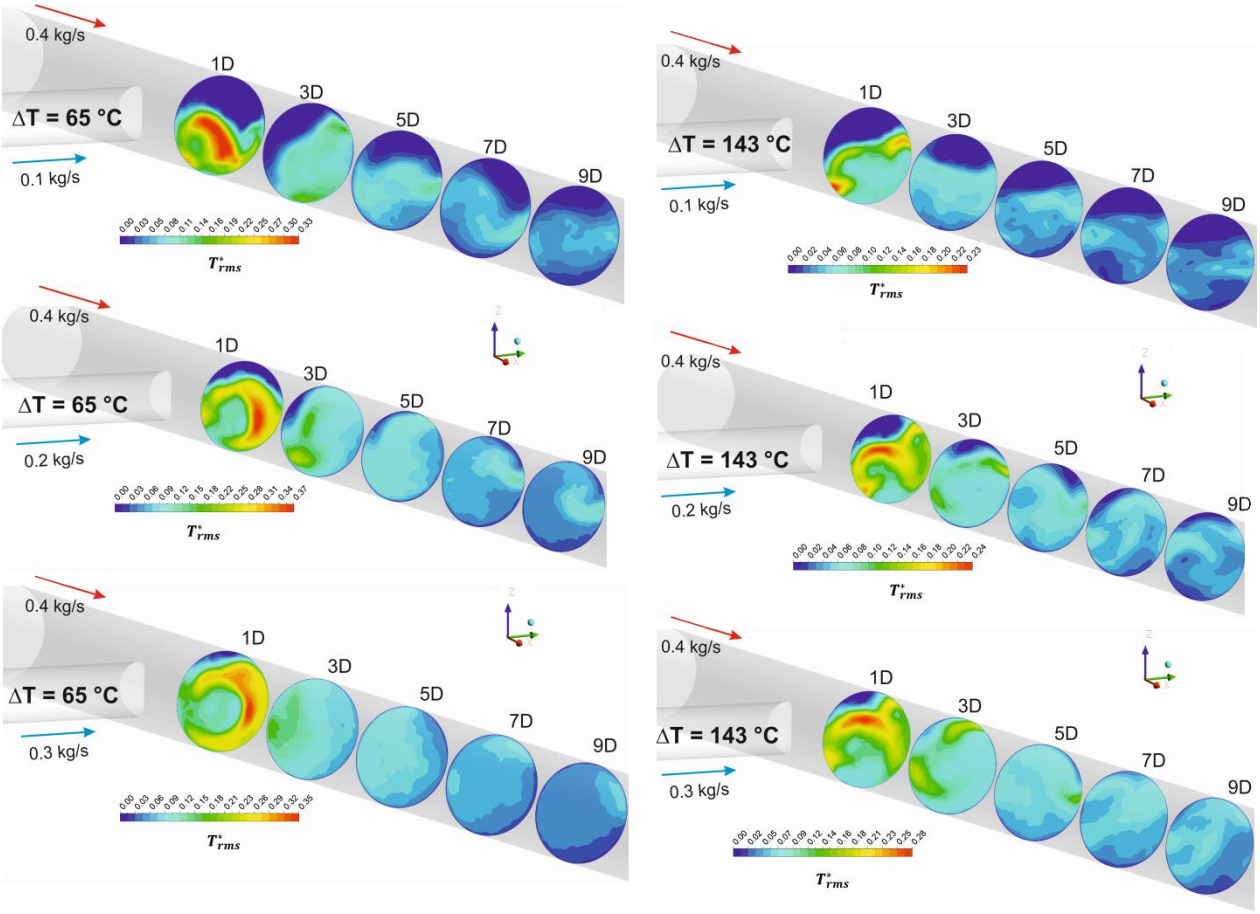

Fig. 71 Cross-sectional thermal fluctuations (T^*_{rms}) with increase in branch flow rates at ΔT = 65 °C (left) and ΔT = 143 °C (right)

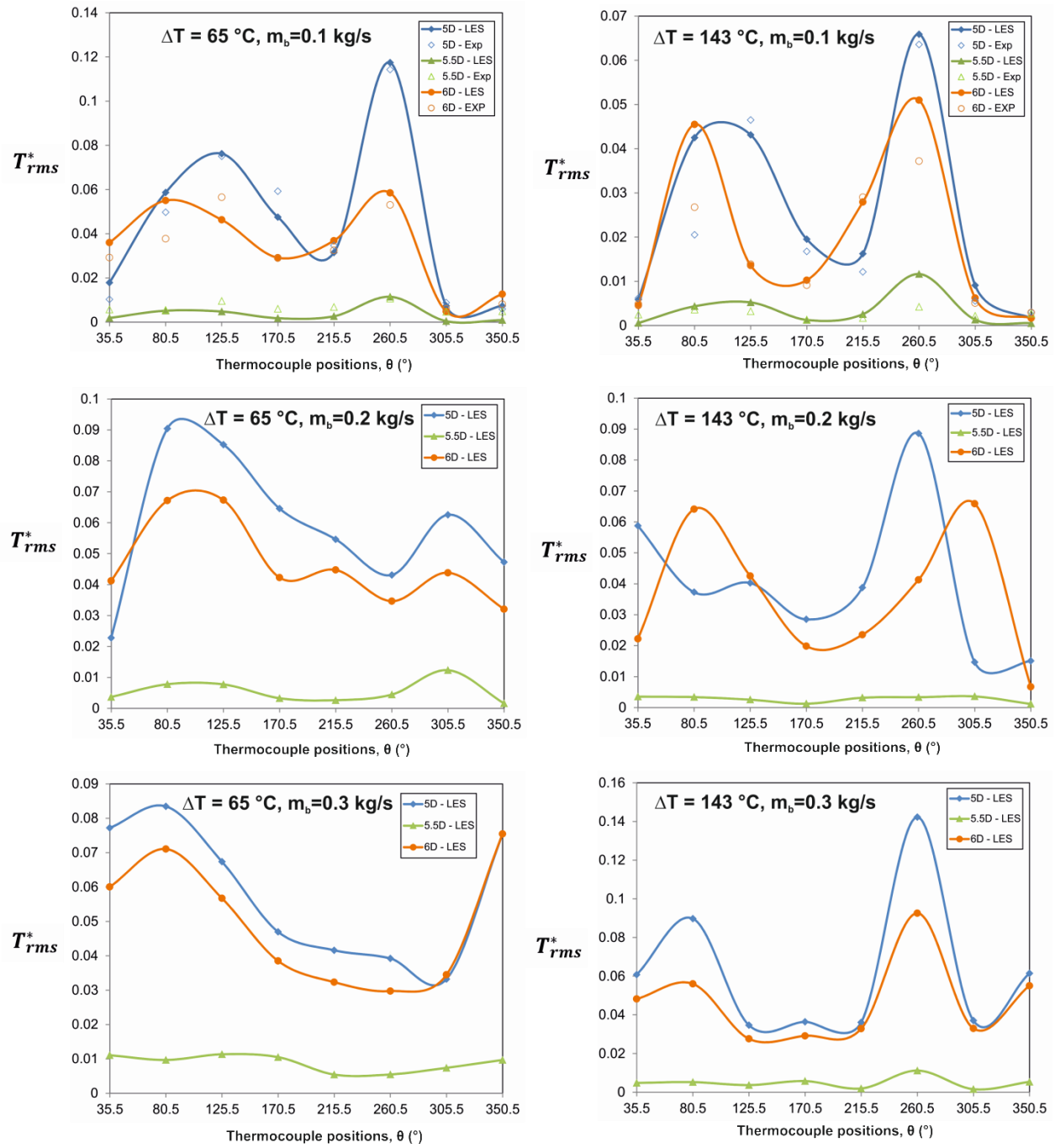

Fig. 72 Thermal fluctuations (T^*_{rms}) at in-flow and in-structure thermocouple positions

Fig. 72 shows the change in T^*_{rms} amplitudes along the circumferential thermocouple positions in response to increase in branch flow rates. T^*_{rms} amplitudes near the top and its vicinity (θ = 35.5 °, 305.5 ° and 350.5 °) are seen to considerably increase with flow rates at ΔT = 65 °C and 143 °C. Angular positions of peak T^*_{rms} have changed as follows: at ΔT = 65

°C, highest magnitude T^*_{rms} (8 – 9 % of ΔT) occurs at θ = 80.5 ° in cases 1a and 1b while it occurred at θ = 260.5 ° in case 1. The possibility of identifying peak T^*_{rms} positions close to the stratification layer becomes non-existent at higher $\dot{m}_b$. At the same time, the oscillation of the stratification layer with rising branch flow rates at ΔT = 143 °C causes rise of T^*_{rms} amplitudes at each angular thermocouple position. While the location of the peak T^*_{rms} with each rise in $\dot{m}_b$ (case 4, 4a, 4b) remains unchanged at θ = 260.5 °, the magnitudes show steady increase with $\dot{m}_b$ from 6.4 % of ΔT (case 4) to 8.8 % of ΔT (case 4a) and reaching the highest amplitude of 14.2 % of ΔT (case 4b). Also to be noted is the similar dampening of T^*_{rms} amplitudes regardless of rising branch flow rates inside the solid (x = 5.5D) which is summarized in Table 13.

Table 13. Fluid and solid thermal fluctuations as recorded from the measurements

ΔT (°C), $\dot{m}_b$ (kg/s)	Peak T^*_{rms} (as % of ΔT) along the		T^*_{rms} (as % of ΔT) inside solid	
	stratification layer to the left wall	stratification layer to the right wall	Peak amplitude	Attenuation from peak fluid level
65, 0.1	7.5 (θ = 125.5 °)	11.4 (θ = 260.5 °)	1.1 (θ = 260.5 °)	90 %
65, 0.2	9.1 (θ = 80.5 °)	6.3 (θ = 305.5 °)	1.23 (θ = 305.5 °)	86.5 %
65, 0.3	8.3 (θ = 80.5 °)	7.5 (θ = 350.5 °)	1.13 (θ = 125.5 °)	86.4 %
143, 0.1	4.6 (θ = 125.5 °)	6.4 (θ = 260.5 °)	0.42 (θ = 260.5 °)	93.4 %
143, 0.2	5.8 (θ = 35.5 °)	8.8 (θ = 260.5 °)	0.36 (θ = 305.5 °)	95.9 %
143, 0.3	8.9 (θ = 80.5 °)	14.2 (θ = 260.5 °)	1.1 (θ = 260.5 °)	92.3 %

Fluid T^*_{rms} along the near-wall region (2 mm into the flow) predicted by LES at the four corners of the cross-section are shown in Fig. 73. Peak T^*_{rms} in all the cases are observed along the left near-wall region (θ = 90 °) at the T-junction where the cold and hot coolant streams meet with amplitudes ranging between 30 – 42 % of ΔT. Near the top (θ = 0°) where the lowest T^*_{rms} usually occurs, a rising trend in T^*_{rms} amplitudes is observed with increase in branch flow rates. T^*_{rms} amplitudes at increased $\dot{m}_b$ (cases 1a, 1b, 4a, 4b) range between 3 – 17 % of ΔT (see the red curve in Fig. 73), a substantial rise in comparison with

the less than 1.5 % of ΔT observed in cases 1 and 4. Reduction in cold flow penetration upstream into the main pipe at ΔT = 143 °C is quantitatively confirmed in Fig. 73. While thermocouple instrumentation is placed in the FSI test facility starting at x = 5D, LES predictions indicate the occurrence of higher amplitude T^*_{rms} to occur within x = 0D to 5D in the mixing zone. This is a valuable insight whereby additional thermocouple instrumentation could be placed much closer to the T-junction in the near-wall region when upgrading the FSI facility to operate at higher branch flow rates. This might reveal some additional information that have gone unnoticed during previous measurements due to the unavailability of thermocouples at those locations.

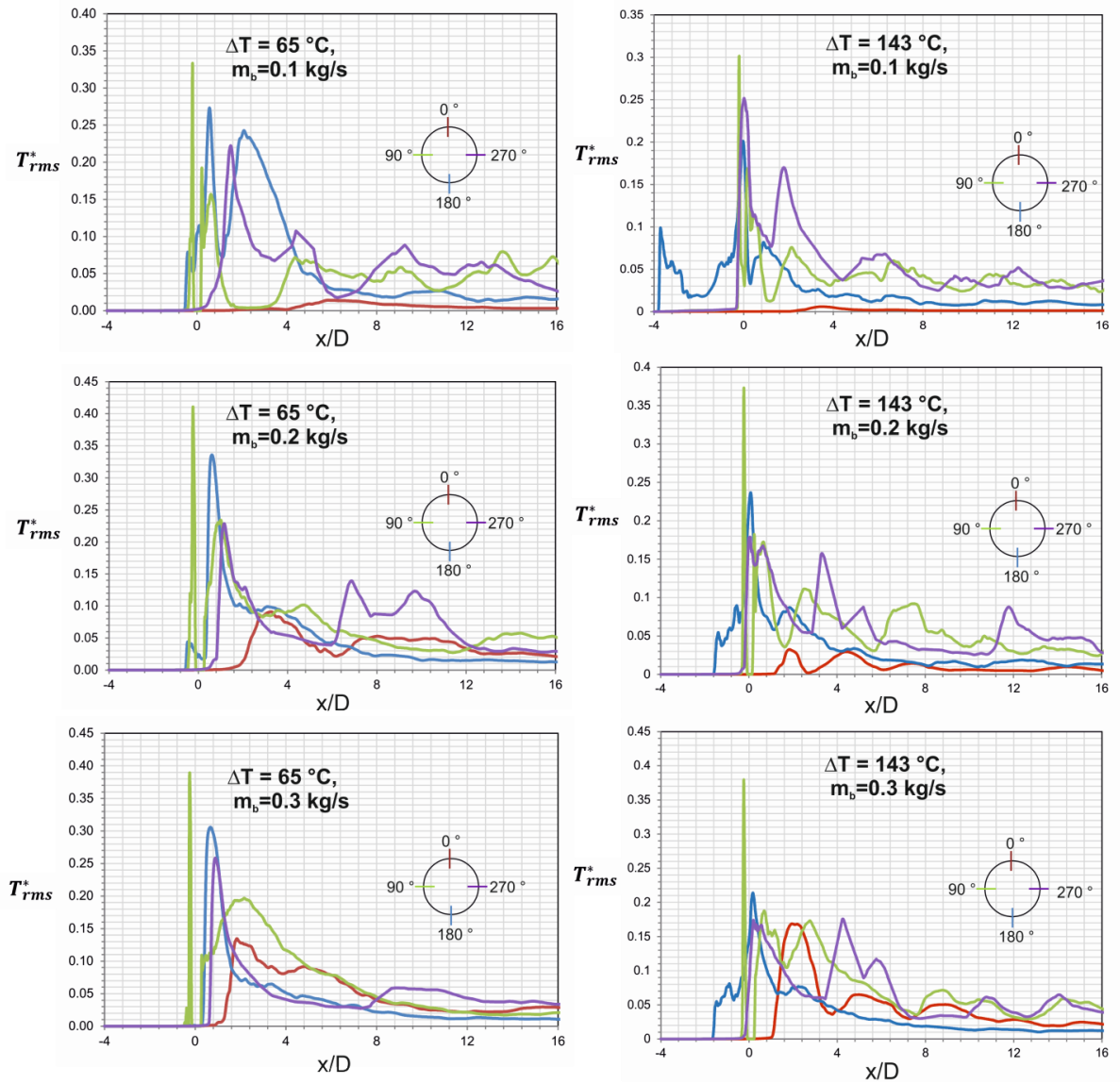

Fig. 73 LES predictions of fluid T^*_{rms} (2 mm in the flow) at θ = 0 °, 90 °, 180 ° and 270 °

4.3.2.3 Frequency spectrum of temperature fluctuations

Fig. 74 shows the PSD of peak fluid thermal fluctuations. The shape of the spectra illustrates the cascading phenomenon and the rise in $\dot{m}_b$ results in higher energy of the high frequency eddies at ΔT = 65 °C and 143 °C, respectively.

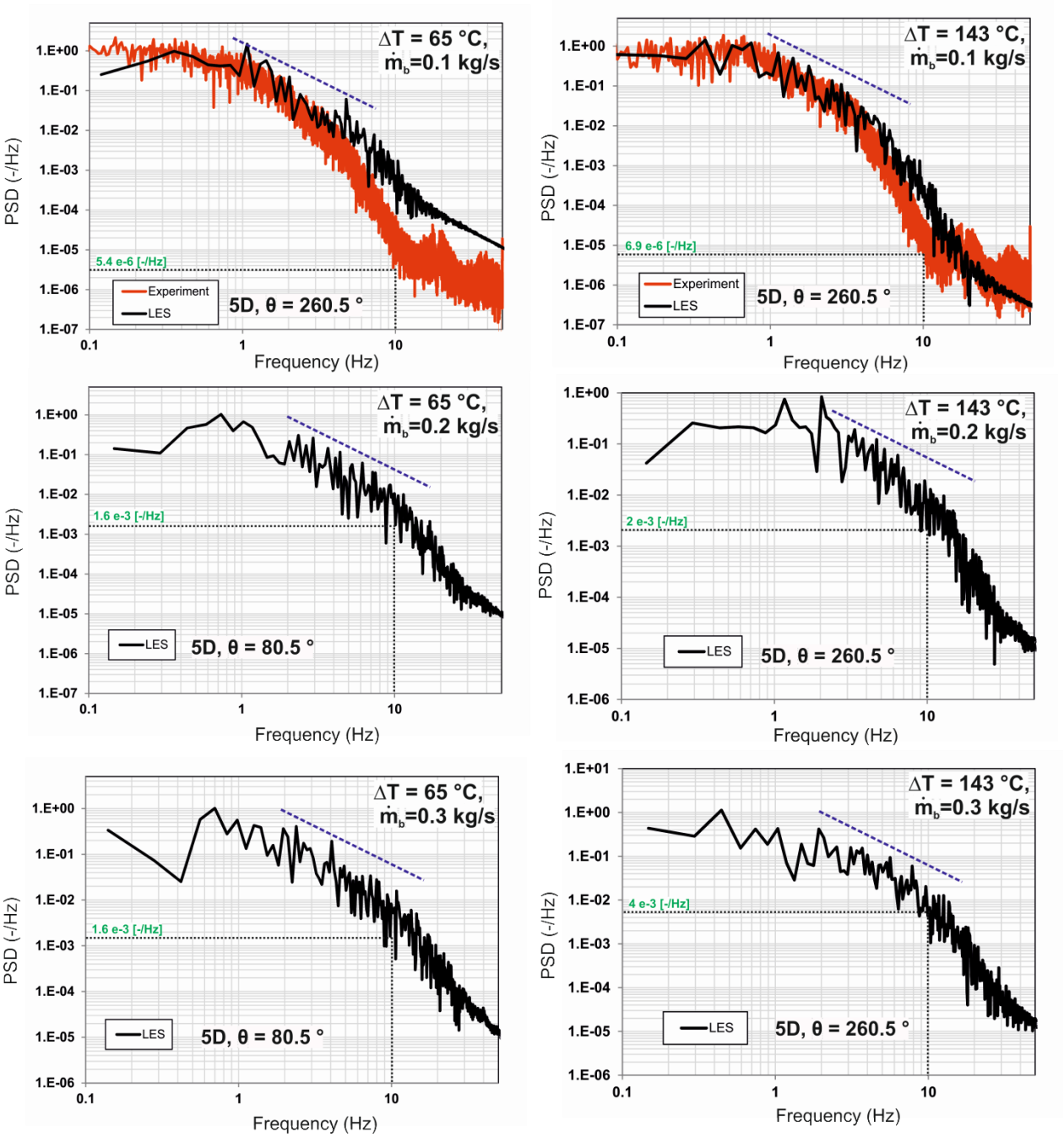

Fig. 74 PSD of peak fluid thermal fluctuations. Dotted lines show the -5/3 trend line in the inertial sub-range of the power spectrum

Energy content of the temperature fluctuations remains fairly stable (0.1 - 1 [-/Hz] at increased $\dot{m}_b$ in cases 1a, 1b, 4a, and 4b) until the frequency of 3 Hz. Beyond this, a linear type of decline in the energy content of fluctuations is noticed at elevated $\dot{m}_b$. At 10 Hz, the energy of fluid thermal fluctuations at increased $\dot{m}_b$ is considerably higher than at $\dot{m}_b$ = 0.1 kg/s at ΔT = 65 °C and 143 °C, respectively.

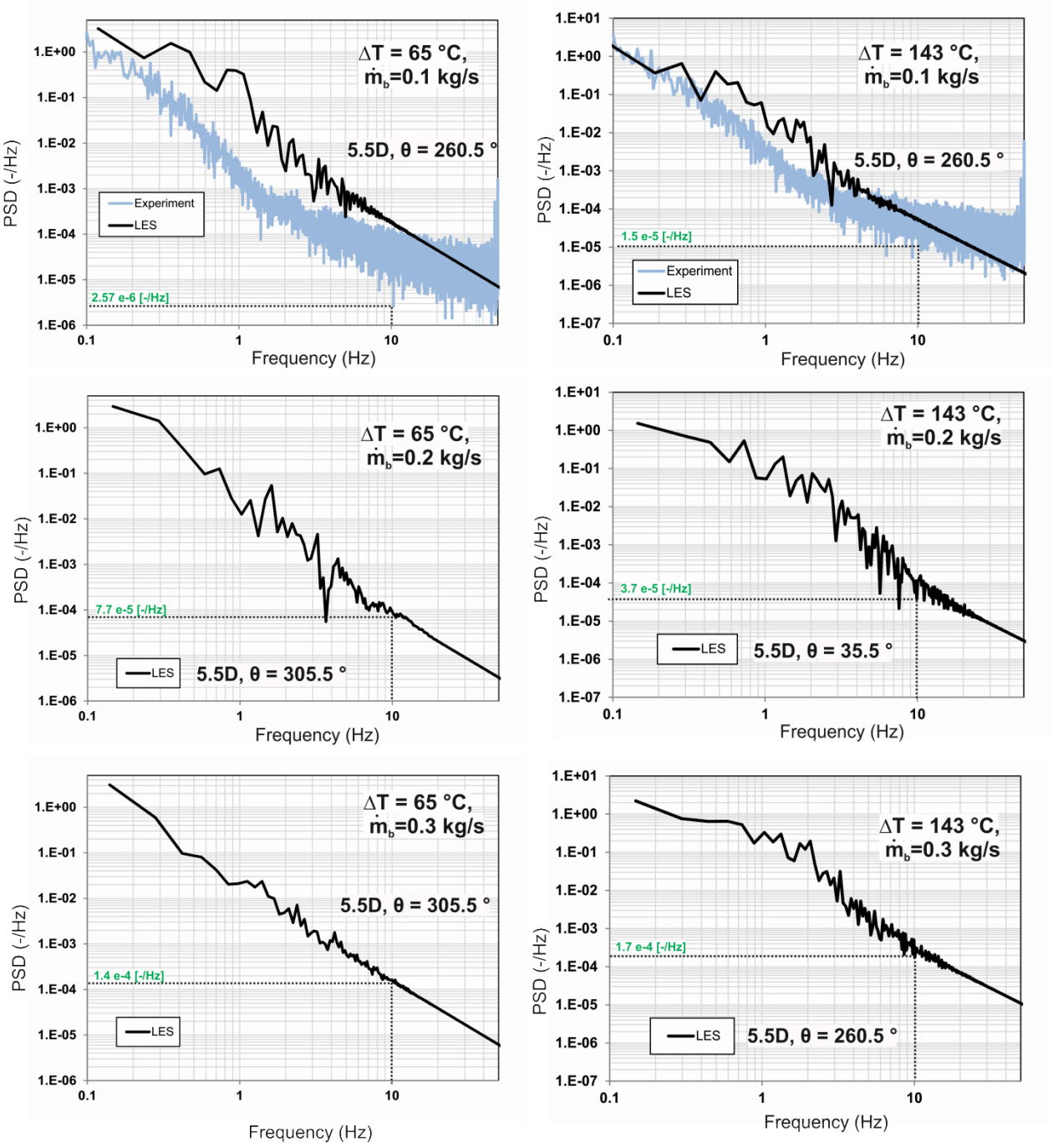

Fig. 75 PSD of peak solid thermal fluctuations

No distinct peak in the power content of fluctuations was observed in the 0.1 – 1 Hz range indicating that the relevance for thermal fatigue is not obvious from the in-flow monitor points.

PSD of thermal fluctuations within the solid is shown in Fig. 75. The trend in the decline of the energy content of thermal fluctuations is linear from 0.1 till 10 Hz at $\dot{m}_b$ = 0.1 kg/s while it continues to be linear beyond 10 Hz at $\dot{m}_b$ = 0.2 kg/s and 0.3 kg/s at ΔT = 65 °C and 143 °C, respectively. Within this interval the power content of solid thermal fluctuations are comparatively lower than the fluid fluctuations discussed in Fig. 75. Rise in $\dot{m}_b$ increases the energy content of thermal fluctuations within the solid at both ΔT = 65 °C and 143 °C as shown in Fig. 74. No distinct peak in the energy content of solid thermal fluctuations was observed.

Aside from the flow phenomenon discussed for the various inflow conditions in sections 4.1, 4.2 and 4.3, investigations at the FSI test facility related to various other inflow temperatures and velocities within the scope of this study have also been published in the existing literature [61, 62, 117, 118, 119, 120, 121, 122, and 123].

SUMMARY AND OUTLOOK

Thermal mixing characteristics of flows in a horizontal T-junction piping system with ΔT between fluids ranging from 65 °C – 235 °C has been experimentally investigated at the Fluid-Structure Interaction (FSI) test facility at the University of Stuttgart. Numerical studies at the aforementioned ΔT range have also been performed using large-eddy simulation turbulence model to gain more insights into the mixing behavior and to validate the data against measurements. Hot fluid flow in the main pipe is turbulent (Reynolds number: 15000 – 72000) while the cold flow is transitional (Reynolds number: 3100 – 3600) due to the operational limits of the booster pump used in the FSI test facility. The traits of the mixed flow downstream of the T-junction could be summarized as follows:

- Flow mixing is observed to be incomplete in all the investigated cases due to the low Reynolds number flow from the branch pipe being insufficient to cause complete mixing of fluids. Thus a thermally stratified flow pattern emerges after the mixing between fluids at the T-junction.
- The nature of the thermally stratified flow illustrates the difference caused by ΔT between the mixing fluids. An unstable stratified flow being subjected to extreme oscillations is seen at low ΔT (e.g. 65 °C) whereas the opposite case of stable stratification is observed at higher ΔT (> 140 °C) between flows. This could be attributed to the significant increase in buoyancy forces that is brought about by the substantial increase in ΔT between fluids.
- Strong turbulent penetration of hot fluid into branch pipe and vice versa was observed at ΔT > 140 °C. Stable stratification also gives rise to strong thermal gradients between the top and bottom of the pipe leading to bending of the structure at ΔT beyond 140 °C. Mean temperature predictions by LES showed good agreement with measurement data.
- Thermal fluctuations are seen to have the highest amplitudes near the stratification layer as seen from both LES and measurement data. Comparison between measurement and LES data exhibit reasonable agreement with one another with the exception of a few positions where LES predictions either over- or understate measurement data.
- Power spectral density (PSD) analysis of thermal fluctuations showed no dominant frequency in the fatigue relevant range of 0.1 – 10 Hz and the energy of fluctuations are

contained mainly in the 0.1 – 1 Hz range. Comparison of PSD between measurement and LES data exhibited good agreement with one another.

Beyond design LES analysis was also performed whereby thermal mixing of flows at increased branch velocities (Reynolds number: 3100 – 11000) was performed at ΔT = 65 °C and 143 °C, respectively. A transition from unstable thermal stratification to complete mixing of fluids is observed at ΔT = 65 °C. Correspondingly, a similar transition from stable stratification to unstable stratification in the flow marked by extreme oscillations was observed at ΔT = 143 °C. These characteristics were confirmed by the mean and fluctuation temperature distribution around the angular thermocouple positions in the mixing zone. PSD of fluctuations still do not register a peak at increased flow velocities in the branch pipe and the energy of fluctuations are contained mainly in the 0.1 – 3 Hz range. Thus thermal mixing experiments have been performed in this study at realistic ΔT between fluids and the thermocouples instrumentation in the vicinity of the T-junction provided valuable data in identifying the nature of flow mixing behavior in response to changes in inflow conditions. This was further reinforced by the application of high-fidelity CFD calculations using the LES turbulence model to studying the flow mixing behavior which provided a wealth of information that could not be otherwise obtained using instrumentation.

The results discussed above pertain to measurements in the FSI test facility where the branch flow is not turbulent (Reynolds number: 3100 – 3600) due to its operating limitations. The next level of advancement will be the upgradation of the facility to enable turbulent flow conditions in the branch pipe (Reynolds number > 6000). The addition of weld seams in the piping might reveal useful information on the influence of weld seams in propagating the cracks in the mixing zone which is a realistic scenario encountered in power plants. Leakage flow measurements for certain defined crack sizes in the piping structure following the T-junction under different inflow conditions is another ongoing research area which is an attempt to answer questions regarding the leakage following the through-wall cracks in the structure.

BIBLIOGRAPHY

1. Abib, E., Bergholz, S., Rudolph, J. German experiences in local fatigue monitoring. International Journal for Nuclear Power, vol. 58, pp. 284 – 289 (2013).
2. Addad, Y., Gaitonde, U., Laurence, D., Rolfo, S. Optimal unstructured meshing for large eddy simulations. ERCOFTAC Series, Quality and Reliability of Large-Eddy Simulations, vol. 12, Springer, pp. 93–103 (2008).
3. Ancelet, O., Chapuliot, S., Henaff, G. Comparative analysis of three thermal fatigue experiments. *Fatigue and Fracture of Engineering Materials and Structures,* vol. 31, pp. 788 – 802 (2008).
4. Angele, K. MOTHER: Modelling T-junction heat transfer – A project in the NULIFE framework portfolio. CONSORTIUM AGREEMENT–Number 8610 – AAP – 5910083925. Vattenfall R&D, EDF, PSI, NRG, TU-D, Onsala, SPG, CEA, E-ON and AREVA (2013). http://s538600174.onlinehome.fr/nugenia/wp-content/uploads/2014/02/NUGENIA_MOTHER1.pdf
5. ANSYS CFX-Solver Modeling Guide (2011).
6. ANSYS CFX-Solver Theory Guide (2011).
7. ANSYS, Best Practice: Scale-Resolving Simulations in ANSYS CFD (2015).
8. Aufort, P., Bimont, G., Chau, T. H., Fournier, I., Morilhat, P., Souchois, T., Codrdier, G. On Line Fatiguemeter: a Large Experiment in French Nuclear Plants, *Nuclear Engineering and Design,* vol. 129, pp. 177-184 (1991).
9. Aulery, F., Toutant, A., Monod, R., Brillant, G., Bataille, F. Numerical simulations of sodium mixing in a T-junction. *Applied Thermal Engineering* 37, pp. 38-43 (2012).
10. Ayhan, H., Sökmen, C.N., 2012. CFD modeling of thermal mixing in a T-junction geometry using LES model. *Nuclear Engineering and Design,* vol. 253, pp. 183 – 191 (2012).
11. Barth, T.J., and Jesperson, D.C. The Design and Application of Upwind Schemes on Unstructured Meshes, AIAA Paper 89-0366 (1989). http://arc.aiaa.org/doi/pdf/10.2514/6.1989-366
12. Beaufils, R., Courtin. Analysis of the Father Experiment with an Engineering Method Devoted to High Cycle Thermal Fatigue. In: Proceedings of the ASME 2011 Pressure Vessels & Piping Conference (PVP 2011), Baltimore, Maryland, USA, July 17-21, 2011.

13. Blanchard, J.N., Brunet, Y., Merlen, A. Influence of a counter rotating vortex pair on the stability of a jet in a cross flow: an experimental study by flowvisualizations. *Experiments in Fluids,* vol. 26, pp. 63–74 (1999).
14. Braillard, O., Edelin, D. Advanced experimental tools designed for the assessment of the thermal load applied to the mixing tee and nozzle geometries in the PWR plant. In: Advancements in Nuclear Instrumentation, Measurement Methods and their Applications, ANIMMA 2009, Marseille, France, June 7–10, 2009.
15. Brunnings, J.E. LMFBR Thermal-Striping Evaluation, EPRI NP-2672, Project 1704-11, Interim Report (1982). http://www.osti.gov/scitech/servlets/purl/6887039
16. Chapuliot, S., Gourdin, C., Payen, T., Magnaud, J.P., Monavon, A. Hydro-thermal-mechanical analysis of thermal fatigue in a mixing tee. *Nuclear Engineering and Design,* vol. 235, pp. 575 – 596 (2005).
17. Chen, M.S., Hsieh, H.E., Ferng, Y.M., Pei, B.S. Experimental observations of thermal mixing characteristics in T-junction piping. *Nuclear Engineering and Design,* vol. 276, pp. 107 – 114 (2014).
18. Courtin, S. High Cycle Thermal Fatigue Damage Prediction in Mixing Zones of Nuclear Power Plants: Engineering Issues Illustrated on the FATHER Case. *Procedia Engineering,* vol. 66, pp. 240 – 249 (2013).
19. Courtin, S., Beaufils, R. Engineering Analyses on the High Cycle Thermal Fatigue FATHER Case. In: International Conference on Structural Mechanics in Reactor Technology (SMiRT-21), India, November 6-11, 2011.
20. Courtin, S., Duff, J. A. L., Tacchini, B., Fissolo, A., Vincent, L., Stephan, J. M., Tampigny, R. High Cycle Thermal Fatigue FATHER Experiment: Non Destructive and Metallographic Examinations. In: International Conference on Structural Mechanics in Reactor Technology (SMiRT-21), India, 2011.
21. CSNI Integrity and Ageing Working Group. FAT3D – An OECD/NEA benchmark on thermal fatigue in fluid mixing areas. NEA/CSNI/R(2005)2, 2005.
22. Curtit, F. INTHERPOL thermal fatigue test. In: Proceedings of the third international conference on fatigue of nuclear reactor components, Seville, Spain, October 3 – 6, 2004. NEA/CSNI/R(2004)21.

23. Curtit, F., Stephan, J,M. INTHERPOL thermal fatigue test. In: Proceedings of the ASME Pressure Vessels and Piping Conference (PVP-2005), Denver, Colorado, USA, July 17-21, 2005.
24. Dahlberg, M., Nilsson, K.F., Taylor, N., Faidy, C., Wilke, U., Chapuliot, S., Kalkhof, D.,Bretherton, I., Church, J.M., Solin, J., Catalano, J. Development of a European procedure for assessment of high cycle thermal fatigue in light water reactors. Final Report of the NESC-Thermal Fatigue Project, EUR 22763 EN, ISSN 1018-5593, 2007.
25. Deardorff, A, F., McGill, R. O. Materials Reliability Program: Third International Conference on Fatigue in Reactor Components (MRP-151), EPRI, Palo Alto, CA, 2005.
26. Duff, J. A. L., Tacchini, B., Stephan, J,M., Tampigny, R., Fissolo, A., Vincent, L. High cycle thermal fatigue issues in RHRS mixing tees and thermal fatigue test on a representative 304L mixing zone. In: Proceedings of the ASME Pressure Vessels and Piping Conference (PVP-2011), Baltimore, Maryland, USA, July 17-21, 2011.
27. ELECTRONIC SENSOR GmbH. Common technical data of sheathing thermocouple: http://www.electronic-sensor.com/en/sheathing-thermocouple
28. Emerson Electric Co. Technical details of the micro-motion flow and density meters: http://www2.emersonprocess.com/siteadmincenter/PM%20Micro%20Motion%20Documents/F-Series-PDS-PS-00603.pdf
29. EPRI: Material Reliability Program: Assessment of Residual Heat Removal Mixing Tee Thermal Fatigue in PWR Plants (MRP-192, Revision 2), 1024994, August 2012.
30. Faidy, C. Thermal fatigue in French RHR system. In: Proceedings of International conference on Fatigue of Reactor Components, Napa, California, USA, July 31 - August 2, 2000.
31. Faidy, C. High Cycle Thermal Fatigue: Lessons Learned From Civaux Event. In: Materials Reliability Program: Second International Conference on Fatigue of Reactor Components (MRP-84), Snowbird, Utah, July 29 – August 1, 2002.
32. Fissolo, A., Forestier, A., Chapuliot, S., Gourdin, C., Magnaud, J.P., Ducros, F., Quéméré, P., Emonot, P., Chatelain, A., Dolias, Y., Braillard, O., Vincent, L., Robertson, C., Guilbaud, D., Le Corre, L., Maillot, V., Haddar, N., Amiable, S., Constantinescu, A., Degallaix, G., Degallaix, S. Advances in thermal fatigue investigations performed in CEA for French

PWR piping. In: Materials Reliability Program: Third International Conference on Fatigue in Reactor Components (MRP-151), EPRI, 1011958, Palo Alto, CA, 2005.

33. Frank, Th., Lifante, C., Prasser, H.-M., Menter, F. Simulation of turbulent and thermal mixing in T-junctions using URANS and scale-resolving turbulence models in ANSYS CFX. *Nuclear Engineering and Design,* vol. 240, pp. 2313 – 2328 (2010).
34. Fric, T. F., and Roshko, A. Vortical structure in the wake of a transverse jet. *Journal of Fluid Mechanics,* vol. 279, pp. 1 – 47 (1994).
35. Galpin, J., Simoneau, J.P. Large eddy simulation of a thermal mixing tee in order to assess the thermal fatigue. *International Journal of Heat and Fluid Flow,* vol. 32, pp. 539 – 545 (2011).
36. Gao, K., Wang, P., Lu, T., Song, T. Experimental investigation and numerical simulation for weakening the thermal fluctuations in a T-junction. *Annals of Nuclear Energy,* vol. 78, pp. 180-187 (2015).
37. Gauder, P., Selvam, P.K., Kulenovic, R., Laurien, E. Large eddy simulation studies on the influence of turbulent inlet conditions on the flow behavior in a mixing tee. *Nuclear Engineering and Design,* vol. 298, pp. 51 – 63 (2016).
38. Golembiewski, H.-J and Miksch, M. Fatigue monitoring in German nuclear power plants. *Nuclear Engineering and Design,* vol. 144, pp. 409 – 421 (1993).
39. Golembiewski, H.-J., Kleinöder, W. Monitoring for fatigue-Examples for unexpected component loading. In: International conference on Nuclear Energy in Central Europe, Bled, Slovenia, September 11-14, 2000.
40. Haddar, N., Fissolo, A., Maillot, V. Thermal fatigue crack networks: an computational study. *International Journal of Solids and Structures,* vol. 42, pp. 771-788 (2005).
41. Hannink, M.H.C., Blom, F.J. Numerical methods for the prediction of thermal fatigue due to turbulent mixing. *Nuclear Engineering and Design,* vol. 241, pp. 681 – 687 (2011).
42. Höhne, T. Scale resolved simulations of the OECD/NEA-Vattenfall T-junction benchmark. *Nuclear Engineering and Design,* vol. 269, pp. 149 – 154 (2014).
43. Hosseini, S.M., Yuki, K., Hashizume, H. Classification of turbulent jets in a T-junction area with a 90-deg bend upstream. *International Journal of Heat and Mass Transfer,* vol. 51, pp. 2444 – 2454 (2008).

44. Howard, R.J.A., Serre, E. Large-eddy simulation in a mixing tee junction: High-order turbulent statistics analysis. *International Journal of Heat and Fluid Flow,* vol. 51, pp. 65 – 77 (2015).
45. Hu, L.W., Kazimi, M.S. LES benchmark study of high cycle temperature fluctuations caused by thermal striping in a mixing tee. *International Journal of Heat and Fluid Flow,* vol. 27, pp. 54 – 64 (2006).
46. IAEA. Validation of Fast Reactor Thermomechanical and Thermalhydraulic Codes, Report, TECDOC-1318, International Atomic Energy agency, Vienna, 2002.
47. IAEA. Assessment and Management of Ageing of Major Nuclear Power Plant Components Important to Safety: Primary piping in PWRs. IAEA-TECDOC 1361. Vienna, Austria, 2003.
48. International Atomic Energy Agency (IAEA) Pris Database. www.iaea.org/pris
49. Jayaraju, S.T., Komen, E.M.J., Baglietto, E. Suitability of wall-functions in Large Eddy Simulation for thermal fatigue in a T-junction. *Nuclear Engineering and Design,* vol. 240, pp. 2544 – 2554 (2010).
50. Jhung, M.J. Assessment of thermal fatigue in mixing tee by FSI analysis. *Nuclear Engineering and Technology,* vol. 45, pp. 99 – 106 (2013).
51. Johnson I.D. Method and apparatus for measuring water in crude Oil, United States Patent, No: 4,644,263 (1987).
52. JSME. Guideline for evaluation of high-cycle thermal fatigue of a pipe. In: JSME, S017-2003.
53. Kader, B.A. Temperature and Concentration Profiles in Fully Turbulent Boundary Layers. *International Journal of Heat and Mass Transfer,* vol. 24, pp. 1541 – 1544 (1981).
54. Kamide, H., Igarashi, M., Kawashima, S., Kimura, N., Hayashi, K. Study on mixing behavior in a tee piping and numerical analyses for evaluation of thermal striping *Nuclear Engineering and Design,* vol. 239, pp. 58 – 67 (2009).
55. Kasahara, N., Hasebe, S., Kobaysashi, S., Masanori, A., Kawasaki, N., Morita, H. SPECTRA thermal fatigue tests under frequency controlled fluid temperature variation – Development of test equipment and preliminary tests. In: Proceedings of the Pressure Vessels & Piping Conference (PVP) – Elevated temperature and design analysis,

nonlinear analysis, and plastic components, San Diego, California, USA, July 25 – 29, 2004.

56. Kasahara, N., Kimura, N., Kamide, H. Thermal fatigue evaluation method based on power spectrum density functions against fluid temperature fluctuation. In: Proceedings of the ASME 2005 Pressure Vessels & Piping Conference (PVP 2005), Denver, Colorado, USA, July 17-21, 2005.
57. Kasahara, N., Takasho, H., Yacumpai, A. Structural response function approach for evaluation of thermal striping phenomena. *Nuclear Engineering and Design,* vol. 212, pp. 281 – 292 (2002).
58. Kawamura, T., Shiina, K., Ohtsuka, M. Study on high-cycle fatigue evaluation for thermal striping in mixing tees with hot and cold water. In: 11th Int. Conf. Nuclear Engineering, ICONE-11, Tokyo, Japan, April 20 – 23, 2003.
59. Kickhofel, J. L. Mixing phenomena relevant to thermal fatigue in T-junctions. Doctoral dissertation, No. 22904, ETH Zürich (2015). http://e-collection.library.ethz.ch/eserv/eth:48693/eth-48693-02.pdf
60. Kickhofel, J., and Prasser, H.-M. Grid Sensor Package. European Patent Application EP14198142, ETH-Invention-No. 2014-053, Priority date December 16, 2014.
61. Kickhofel, J., Prasser, H. M., Selvam, P.K., Kulenovic, R., Laurien, E. T-junction cross-flow mixing with thermally driven density stratification. *Nuclear Engineering and Design,* vol. 309, pp. 23 – 39 (2016).
62. Kickhofel, J., Selvam, P.K., Kulenovic, R., Laurien, E., Prasser, H. M., Huber, H. Wire mesh sensor for high temperature high pressure applications. In: Proceedings of the 16th International Topical Meeting on Nuclear Reactor Thermalhydraulics (NURETH-16), Chicago, USA, Paper – 13930, August, 30 – September 4, 2015.
63. Kickhofel, J., Valori, V., Prasser, H.-M. Turbulent penetration in T-junction branch lines with leakage flow. *Nuclear Engineering and Design,* vol. 276, pp. 43–53 (2014).
64. Kimura, K. et al. Thermal striping in mixing tees with hot and cold water (Type A; Characteristics of flow visualization and temperature fluctuations in collision type mixing tees with same pipe diameter), NTHAS3: Third Korea-Japan Symposium on Nuclear Thermal Hydraulics and Safety (NTHAS3), Korea, October 13–16, 2002.

65. Klören, D., and Laurien, E. Coupled Large-Eddy Simulation of thermal mixing in a T-Junction, International Topical Meeting on Nuclear Reactor Thermalhydraulics, NURETH-14, Ontario, Canada, 2011.
66. Klören, D., and Laurien, E. Large-Eddy Simulations of Stratified and Non-stratified T-junction Mixing Flows. High Performance Computing in Science and Engineering '12: Transactions of the High Performance Computing Center, Stuttgart (HLRS), pp. 311-324 (2013).
67. Klören, D., Kuschewski, M., Laurien, E. Large-eddy simulations of stratified flows in pipe configurations influenced by a weld seam. In: Proc. of the CFD for Nuclear Reactor Safety Applications (CFD4NRS) Workshop, Daejon, Korea (2012).
68. KTA 3201.1. Components of the Reactor Coolant Pressure Boundary of Light Water Reactors – Part 1: Materials and Product Forms (1998). http://www.kta-gs.de/e/standards/3200/3201_1_engl_1998_06.pdf
69. KTA 3201.4. Components of the Reactor Coolant Pressure Boundary of Light Water Reactors Part 4: In-service Inspections and Operational Monitoring (1982). http://www.kta-gs.de/e/standards/3200/3201_4_engl_2010_11.pdf
70. Kuczaj, A.K., Komen, E.M.J., Loginov, M.S. Large-eddy simulation study of turbulent mixing in a T-junction. *Nuclear Engineering and Design,* vol. 240, pp. 2116 – 2122 (2010).
71. Kuhn, S., Braillard, O., Ničeno, B., Prasser, H.M. Computational study of conjugate heat transfer in T-junctions. *Nuclear Engineering and Design,* vol. 240, pp. 1548 – 1557 (2010).
72. Kuschewski, M. Entwicklung und Anwendung von Strömungsmessverfahren zur Untersuchung wandnaher Temperaturfelder. Doctoral dissertation, Universität Stuttgart, No: D93, 2015.
73. Kuschewski, M., Kulenovic, R., Laurien, E. Experimental setup for the investigation of fluid-structure interactions in a T-junction. *Nuclear Engineering and Design,* vol. 264, pp. 223 –230 (2013).
74. Kuschewski, M., Kulenovic, R., Laurien, E. Experimental Investigation of Stratified Pipe Flow Mixing in a Horizontal T-Junction. In: Proc. of the CFD for Nuclear Reactor Safety Applications (CFD4NRS) Workshop, Zürich, Switzerland, 2014.

75. Kweon, H. D., Kim, J. S., Lee, K. Y. Fatigue design of nuclear class 1 piping considering thermal stratification. *Nuclear Engineering and Design,* vol. 238, pp. 1265–1274 (2008).
76. Launder, B. E., and Spalding, D. B. The numerical computation of turbulent flows. *Computer Methods in Applied Mechanics and Engineering*, vol. 3, pp. 269 – 289 (1974).
77. Lawn, C. J. The attenuation of temperature oscillations by liquid metal boundary layers. *Nuclear Engineering and Design*, vol. 42, pp. 209 – 222 (1977).
78. Lee, J.I., Hu, L.W., Saha, P., Kazimi, M.S. Numerical analysis of thermal striping induced high cycle thermal fatigue in a mixing tee. *Nuclear Engineering and Design,* vol. 239, pp. 833 – 839 (2009).
79. Lejeail, Y., Kasahara, N. Thermal fatigue evaluation of cylinders and plates subjected to fluid temperature fluctuations. *International Journal of Fatigue,* vol. 27, pp. 768 – 772 (2005).
80. Lin, C. H., Ferng, Y. M. Investigating thermal mixing and reverse flow characteristics in a T-junction using CFD methodology. *Applied Thermal Engineering,* vol. 102, pp. 733 – 741 (2016).
81. Lydell, B., Riznic, J. OPDE – The international pipe failure data exchange project. *Nuclear Engineering and Design,* vol. 238, pp. 2115 – 2123 (2008).
82. Mahaffy, J., Chung, B., Dubois, F., Ducros, F., Graffard, E., Heitsch, M., Henriksson, M., Komen, E., Moretti, F., Morii, T., Mühlbauer, P., Rohde, U., Scheuerer, M., Smith, B. L., Song, C., Watanabe, T., Zigh, G. Best practice guidelines for the use of CFD in nuclear reactor safety applications. NEA/CSNI/R(2007)5, 2007.
83. Mathey, F., Cokljat, D., Bertoglio, J.P., Sergent,E. Assessment of the vortex method for large eddy simulation inlet conditions. *Progress in Computational Fluid Dynamics,* vol. 6, pp. 58 – 67, (2006).
84. McDevitt, M., Childress, T., Hoehn, M., McGill, R. Analysis and impact of recent thermal fatigue operating experience in the USA. In: Proceedings of the fourth international conference on fatigue of nuclear reactor components, Seville, Spain, 28 September – October 1, 2015.
85. Metzner, K.-J., Wilke, U. European THERFAT project—thermal fatigue evaluation of piping system "Tee"-connections. *Nuclear Engineering and Design,* vol. 235, pp. 473–484 (2005).

86. Miyoshi, K., Kamaya, M., Utanohara, Y., Nakamura, A. An investigation of thermal stress characteristics by wall temperature measurements at a mixing tee. *Nuclear Engineering and Design,* vol. 298, pp. 109 – 120 (2016).
87. Miyoshi, K., Nakamura, A., Takenaka, N. Numerical evaluation of wall temperature measurement method developed to estimate thermal stress at T-junction pipe. *Mechanical Engineering Journal* 1 (2), tep0006 (2014).
88. Miyoshi, K., Nakamura, A., Utanohara, Y., Takenaka, N. An investigation of wall temperature characteristics to evaluate thermal fatigue at a T-junction pipe. *Mechanical Engineering Journal* 1 (5), tep0050 (2014).
89. Naik-Nimbalkar, V.S., Patwardhan, A.W., Banerjee, I., Padmakumar, G., Vaidyanathan, G. Thermal mixing in T-junctions. *Chemical Engineering Science,* vol. 65, pp. 5901 – 5911 (2010).
90. Nakamura, A., Oumaya, T., Takenaka, N. Numerical investigation of thermal striping at a mixing tee using detached eddy simulation. In: Proc. of the 13th International Topical Meeting on Nuclear Reactor Thermal Hydraulics (NURETH-13), N13P1074 (2009).
91. Ndombo, J., Howard, R.J.A. Large Eddy Simulation and the effect of the turbulent inlet conditions in the mixing Tee. *Nuclear Engineering and Design,* vol. 241, pp. 2172 – 2183 (2011).
92. NEA. Specialists meeting on experience with thermal fatigue in LWR piping caused by mixing and stratification, NEA/CSNI/R(98)8, OECD Nuclear Energy Agency, Issy-les-Moulineaux, France, 1998.
93. Nicoud, F., Ducros, F. Subgrid-scale modelling based on the square of the velocity gradient tensor. *Flow, Turbulence and Combustion,* vol. 62, pp. 183 – 200 (1999).
94. Nuclear power reactors in the world, May 2016. Reference data series no. 2, International atomic energy agency (IAEA).
95. Nuclear Power: http://www.nuclear-power.net/nuclear-power-plant/
96. Odemark, Y., Green, T.M., Angele, K., Westin, J., Alavyoon, F., Lundström, S. High-cycle thermal fatigue in mixing tees: New Large-Eddy Simulations validated against new data obtained by PIV in Vattenfall experiment. In: ICONE17 Proceedings, July 12–16, 2009, Brussels, Belgium.

97. Ogawa, H., Igarashi, M., Kimura, N., Kamide, H. Experimental study on fluid mixing phenomena in T-pipe junction with upstream elbow. In: Proc. of the 11th International Topical Meeting on Nuclear Reactor Thermal Hydraulics (NURETH-11), Avignon, France, (2005).
98. Paffumi, E., Nilsson, K. F., Szaraz, Z.. Experimental and numerical assessment of thermal fatigue in 316 austenitic steel pipes. *Engineering Failure Analysis,* vol. 47, pp. 312–327 (2015).
99. Paffumi, E., Nilsson, K-F., Taylor, N., Hurst, R., Bache, M.R. Cracks initiation, propagation and arrest in 316L model pipe components under thermal fatigue. *Journal of ASTM International* 2(5), pp. 1 – 18 (2005).
100. Paffumi, E., Nilsson, K-F., Taylor, N.G. Simulation of thermal fatigue damage in a 316L model pipe component. *International Journal of Pressure Vessels and Piping,* vol. 85, pp. 798–813 (2008).
101. Pasutto, T., Péniguel, C., Sakiz, M. Chained computations using an unsteady 3D approach for the determination of thermal fatigue in a T-junction of a PWR nuclear plant. *Nuclear Engineering and Technology,* vol. 38, pp. 147 – 154 (2006).
102. Peña, H.F.V., and Rodriguez, O.M.H. Applications of wire-mesh sensors in multiphase flows. *Flow Measurement and Instrumentation,* vol. 45, pp. 255-273 (2015).
103. Piomelli, U.. An introduction to direct and large-eddy simulations. In: CFD2001, 9th Annual Conference of the CFD Society of Canada, Kitchener, Canada, 2001.
104. Pöckl, C., Kleinöder, W. Developing and implementation of a fatigue monitoring system for the new European pressurized water reactor EPR. International conference on nuclear energy for new Europe, Slovenia, September 10-13, 2007.
105. Pope, S.B. Turbulent Flows. Cambridge University Press, Cambridge, United Kingdom (2000).
106. Prasser, H. –M., Böttger, A., Zschau, J. A new electrode-mesh tomograph for gas–liquid flow. *Flow Measurement and Instrumentation,* vol. 9, pp. 111 – 119 (1998).
107. Prasser, H.-M. Generalized cross-correlation technique for the measurement of time-dependent velocities. In: Proceedings of the 15th international topical meeting on nuclear reactor thermal-hydraulics (NURETH-15), May 12-17, 2013, Pisa, Italy.
108. Reinecke, N., Boddem, M., Petritsch, G., Mewes, D., 1996. Tomographisches Messen

der relativen Phasenanteile in zweiphasigen Stroemungen fluider Phasen, *Chemie Ingenieur Technik,* vol. 68(11), pp. 1404-1412.

109. Riccardella, P. C., Kuo, A. Y., Tang, S. S., Gustin, H. L. FatiguePro: On-Line Fatigue Usage Transient Monitoring System, EPRI NP-5835M, Electric Power Research Institute (1988).

110. Richardson, L. F. Weather prediction by numerical process. Cambridge university press (1922).

111. RICHTER Wärmebehandlungen GmbH. Technical details of the heat treatment unit: http://www.richter-waerme.de/de/gluehanlagen

112. Rosinski, S. Proceedings of the 2000 International Conference on Fatigue of Reactor Components (MRP-46): PWR Materials Reliability Program (PWRMRP), EPRI, Palo Alto, CA, and Organisation for Economic Co-operation and Development (OECD/NEA/CSNI/R[2000] 24), and the U.S. NRC (2001).

113. Rosinski, S. Materials Reliability Program: Second International Conference on Fatigue of Reactor Components (MRP-84), EPRI, Palo Alto, CA, and Organisation for Economic Co-operation and Development (OECD/NEA/CSNI/R[2003] 2), and the U.S. NRC (2003).

114. Sagaut, P. Large Eddy Simulation for Incompressible Flows – An Introduction (Third edition). ISBN 978-3-540-26403-3 (2006), Springer-Verlag. http://www.springer.com/gp/book/9783540263449

115. SAMSOMATIC GmbH. Technical details of Electric Transmitter for pressure and absolute pressure measurement: http://www.samsomatic.de/pdf/t39940050en.pdf

116. Schuler, X., Laurien, E., Herter, K.-H., Moogk, S., Klören, D., Kulenovic, R., Kuschewski, M. Thermal fatigue: Fluid-structure interaction at thermal mixing events, 38th MPA Seminar: "Energieerzeugung und Energieeffizienz - Werkstoffe und Bauteilverhalten", Stuttgart, 2012.

117. Selvam, P.K., Kulenovic, R., Laurien, E. Large Eddy Simulation on Thermal Fluid Mixing in a T-Junction Piping System. *International Journal for Nuclear Power*, Vol. 59, Issue 11, pp. 648-649 (2014).

118. Selvam, P.K., Kulenovic, R., Laurien, E. Large eddy simulation of fluid mixing at high temperature differences in a T-junction piping system. In: Proceedings of the

International Congress on Advances in Nuclear Power Plants (ICAPP), April 6 - 9, 2014, Charlotte, NC, USA.

119. Selvam, P.K., Kulenovic, R., Laurien, E., 2015. Experimental and numerical analyses of turbulent mixing of coolant streams in a mixing tee. In: Proceedings of the Fourth International Conference on Fatigue of Nuclear Reactor Components, Seville, Spain, Paper – 40, September 28 – October 1, 2015.

120. Selvam, P.K., Kulenovic, R., Laurien, E. Experimental Investigation of High Cycle Thermal Fatigue in a T-Junction Piping System. *International Journal for Nuclear Power*, Vol. 60, Issue 10, pp. 606-608 (2015).

121. Selvam, P.K., Kulenovic, R., Laurien, E. Large eddy simulation on thermal mixing of fluids in a T-junction with conjugate heat transfer. *Nuclear Engineering and Design,* vol. 284, pp. 238 – 246 (2015).

122. Selvam, P.K., Kulenovic, R., Laurien, E. Numerical analyses of influence of branch flow on thermal mixing in a T-junction piping system. In: Proceedings of the 16th International Topical Meeting on Nuclear Reactor Thermalhydraulics (NURETH-16), August, 30 – September 4, 2015, Chicago, USA, Paper – 12873.

123. Selvam, P.K., Kulenovic, R., Laurien, E. Experimental and numerical analyses on the effect of increasing inflow temperatures on the flow mixing behavior in a T-junction. *International Journal of Heat and Fluid Flow,* vol. 61, part B, pp. 323 – 342 (2016).

124. Sergent, E. Vers une mthodolgie de couplage entre la simulation des grandes echelles et les modles statistique. Ph.D. thesis, L'ecole centrale de Lyon (2002).

125. Smith, B. L. Identification and Prioritization of Generic Nuclear Safety Problems Requiring CFD Analysis, Paper 75482, Proc. 17th Int. Conf. on Nuclear Engineering (ICONE-17), July 12-16, 2009, Brussels, Belgium.

126. Smith, B. L. Assessment of CFD codes used in nuclear reactor safety simulations. *Nuclear Engineering and Technology,* vol. 42, pp. 339-364 (2010).

127. Smith, B. L., Andreani, M., Bieder, U., Ducros, F., Graffard, E., Heitsch, M., Henrikkson, M., Höhne, T., Houkema, M., Komen, E., Mahaffy, J., Menter, F., Moretti, F., Morii, T., Mühlbauer, P., Rohde, U., Scheuerer, M., Song, C. –H., Watanabe, T., Zigh, G. Assessment of CFD Codes for Nuclear Reactor Safety Problems – revision 2 (OECD/NEA/CSNI/R(2014) 12), 2015.

128. Smith, B. L., Bestion, D., Hassan, Y. Experiments and CFD Code Applications to Nuclear Reactor Safety (XCFD4NRS). Special Issue: *Nuclear Engineering and Design*, vol. 240, pp. 2075-2382 (2010).

129. Smith, B. L., Hassan, Y. CFD4NRS: Benchmarking of CFD Codes for Application to Nuclear Reactor Safety. Special Issue: *Nuclear Engineering and Design,* vol. 238, pp. 443-785 (2008).

130. Smith, B.L., Mahaffy, J.H., Angele, K. A CFD benchmarking exercise based on flow mixing in a T-junction. *Nuclear Engineering and Design,* vol. 264, pp. 80 – 88 (2013).

131. Smith, B.L., Mahaffy, J.H., Angele, K., Westin, J. Report of the OECD/NEA-Vattenfall T-Junction Benchmark exercise (2011).

132. Stephan, J,M., Curtit, F. Mechanical aspects concerning thermal fatigue initiation in the mixing zones of piping. In: International Conference on Structural Mechanics in Reactor Technology (SMiRT-18), China, August 7-12, 2005.

133. Suzuki, S., Tanimoto, K., Kondoh, Y. Prevention of piping high cycle thermal fatigue at design stage. In: Proceedings of the Nuclear Pressure Equipment Expertise and Regulation (NuPEER) symposium, June 22 – 24, 2005, Dijon, France.

134. Tenchine, D. Boundary layer attenuation in turbulent sodium flows. In: IAEA Specialists Meeting on Correlation Between Material Properties and Thermal Hydraulic Conditions in LMFBR, Aix en Provence, France, November 22–24, 1994.

135. Tenchine, D. Some thermal hydraulic challenges in sodium cooled fast reactors. *Nuclear Engineering and Design,* vol. 240, pp. 1195 – 1217 (2010).

136. Timperi, A. Conjugate heat transfer LES of thermal mixing in a T-junction. *Nuclear Engineering and Design,* vol. 273, pp. 483 – 496 (2014).

137. USNRC Bulletin 88-08. Thermal Stresses in Piping Connected to Reactor Coolant Systems. Washington, D.C., U.S.A (1988).

138. USNRC Bulletin 88-08, Supplement 1: Thermal Stresses in Piping Connected to Reactor Coolant Systems, June 24, 1988.

139. USNRC Bulletin 88-08, Supplement 2: Thermal Stresses in Piping Connected to Reactor Coolant Systems, August 4, 1988.

140. USNRC Bulletin 88-08, Supplement 3: Thermal Stresses in Piping Connected to Reactor Coolant Systems, April 11, 1989.

141. USNRC Bulletin 88-08: Thermal Stresses in Piping Connected to Reactor Coolant Systems, June 22, 1988.

142. USNRC Bulletin 88-11: Pressurizer Surge Line Thermal Stratification, December 20, 1988.

143. Vermaut, M., Cranford, E. L., Gray, M. A., Barbier, C. Use of Westinghouse thermal event monitoring system WESTEMS[TM] for on-line transient and fatigue monitoring. In: Proceedings of the PLIM and PLEX conference, Prague, pp. 177 – 184 (1997).

144. Wagner, W., Kruse, A. Properties of water and steam. The industrial standard IAPWS-IF97 for thermodynamic properties and supplementary equations for other properties. Springer-Verlag, Berlin (1998).

145. Wakamatsu, M., Nei, H., Hashiguchi, K. Attenuation of temperature fluctuations in thermal striping. *Journal of Nuclear Science and Technology,* vol. 32, pp. 752 – 762 (1995).

146. Walker, C., Manera, A., Niceno, B., Simiano, M., Prasser, H.-M. Steady-state RANS-simulations of the mixing in a T-junction. *Nuclear Engineering and Design,* vol. 240, pp. 2107 – 2115 (2010).

147. Walker, C., Simiano, M., Zboray, R., Prasser, H.M. Investigations on mixing phenomena in single-phase flow in a T-junction geometry. *Nuclear Engineering and Design,* vol. 239, pp. 116 –126 (2009).

148. Wang, Y., Wang, P., Lu, T. Experimental investigation of the thermal fluctuations in hot and cold fluids mixing in a T-junction filled with spherical particles. *Applied Thermal Engineering*, vol. 71, pp. 310 – 316 (2014).

149. WESTEMS™ Integrated Diagnostics and Monitoring Systems. http://www.westinghousenuclear.com/LinkClick.aspx?fileticket=uo6hKKcuEFw%3d&portalid=0

150. Westin, J., 't Mannetje, C., Alavyoon, F., Veber, P., Andersson, L., Andersson, U., Eriksson, J., Henriksson, M., Andersson, C. High-cycle thermal fatigue in mixing tees. Large-Eddy Simulations compared to a new validation experiment. In: ICONE16 Proceedings, May 11–15, 2008, Orlando, FL, USA.

151. Westinghouse PWR manual www4.ncsu.edu/~doster/NE405/Manuals/PWR_Manual.pdf

152. World Energy Outlook Special Report 2015 on Energy and Climate Change. International Energy Agency www.iea.org/publications/freepublications/publication/WEO2015SpecialReportonEnergyandClimateChange.pdf

153. World nuclear power reactors. http://www.world-nuclear.org/information-library/facts-and-figures/world-nuclear-power-reactors-and-uranium-requireme.aspx

154. Yoo, B. Development of Fatigue Monitoring System in Nuclear Power Plants, KAERI/RR-1307/93, Korea Atomic Energy Research Institute (1994).

155. Zboray, R., Manera, A., Niceno, B., Prasser, H.-M. Investigations on mixing phenomena in single-phase flows in a T-junction geometry. In: Proceedings of the 12th international topical meeting on nuclear reactor thermal-hydraulics (NURETH-15), September 30 – October 4, 2007, Pittsburg, Pennsylvania, USA.

156. Zboray, R., Prasser, H.-M. On the relevance of low side flows for thermal loads in T-junctions. *Nuclear Engineering and Design,* vol. 241, pp. 2881-2888 (2011).

APPENDIX

A.1 NUMERICAL DISCRETIZATION AND ERROR

The discretization approach used in ANSYS CFX is an element-based finite volume method involving the following steps [6]

- Discretization of the spatial domain using a mesh
- Using the mesh to construct finite volumes where relevant quantities such as mass, momentum, and energy are conserved (see Fig. 76).

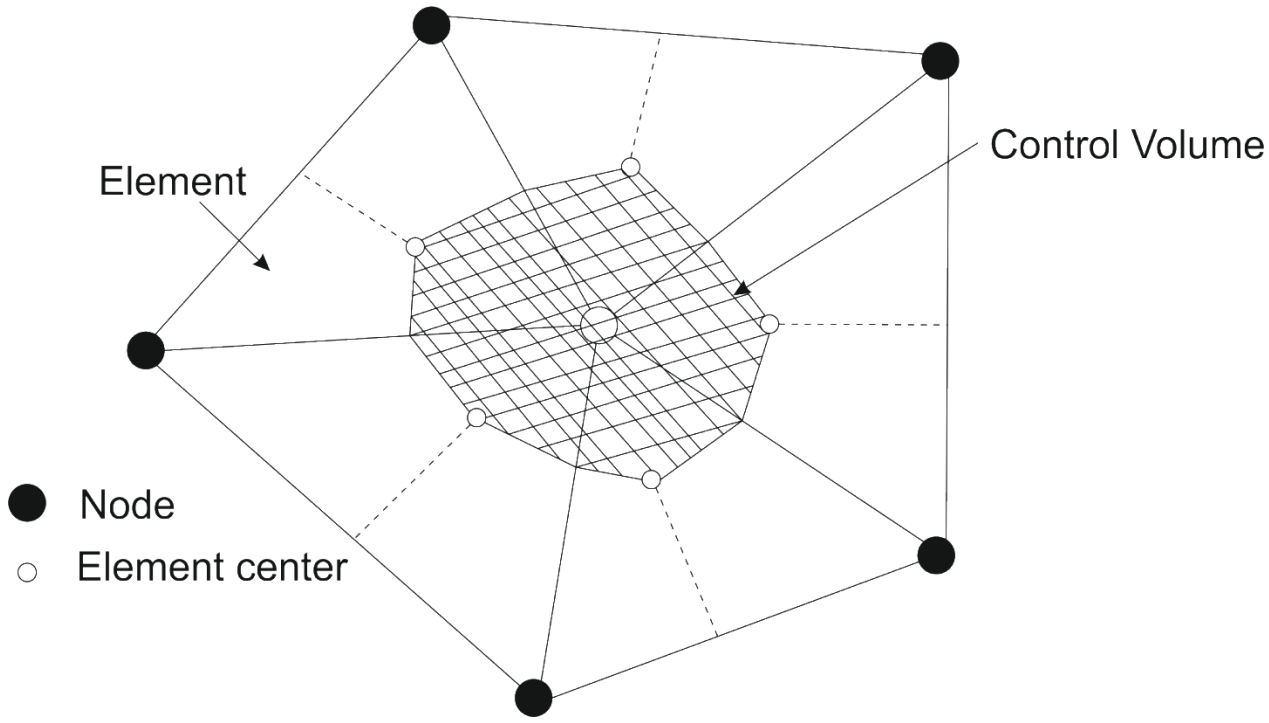

Fig. 76 Control volume as defined in ANSYS CFX [6]

The solution variables and fluid properties are stored at the nodes (mesh vertices). The evaluation of solution field or gradients is approximated at integration points (see Fig. 77). ANSYS CFX uses finite-element based shape functions to perform these approximations. The shape functions describe the variation of a variable φ within an element as follows:

$$\varphi = \sum_{i=1}^{N_{node}} N_i \varphi_i \tag{29}$$

where N_i is the shape function of the node i and φ_i is the value of φ at node i. The summation is performed all over the nodes of an element. The key properties of shape function include

$$\sum_{i=1}^{N_{node}} N_i = 1 \tag{30}$$

At node j, $N_i = \begin{cases} 1, i = j \\ 0, i \neq j \end{cases}$

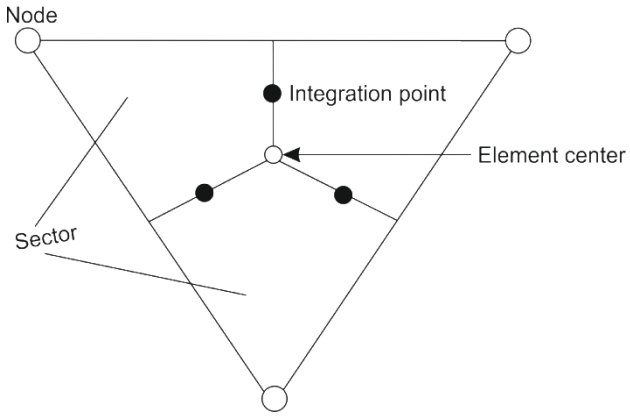

Fig. 77 Mesh element as defined in ANSYS CFX

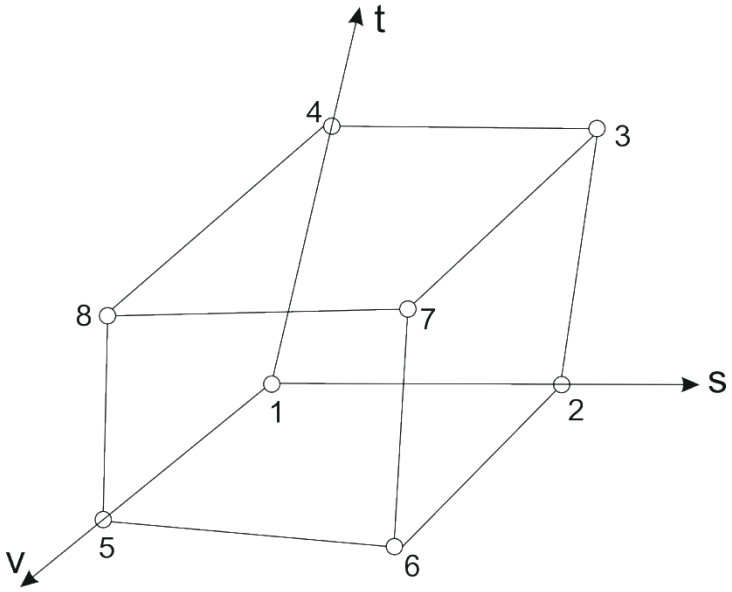

Fig. 78 Description of the hexahedral element used in the T-junction mesh

Shape functions used in ANSYS CFX are linear in terms of parametric coordinates. They are used to calculate various geometric quantities, including integration point coordinates and

surface area vectors. It is possible due to the above equation (31) also hold valid for the coordinates:

$$y = \sum_{i=1}^{N_{node}} N_i y_i \tag{32}$$

The tri-linear shape functions for the hexahedral mesh elements (see Fig. 78) used in this study are given below:

$N_1(s,t,v) = (1-s)(1-t)(1-v)$

$N_2(s,t,v) = s(1-t)(1-v)$

$N_3(s,t,v) = st(1-v)$

$N_4(s,t,v) = (1-s)t(1-v)$

$N_5(s,t,v) = (1-s)(1-t)v$

$N_6(s,t,v) = s(1-t)v$

$N_7(s,t,v) = stv$

$N_8(s,t,v) = (1-s)tv$

The evaluation of gradients might be required in some situations at the nodes and ANSYS CFX uses a formulation of Gauss's divergence theorem to evaluate such gradients which are defined as follows:

$$\nabla\varphi = \frac{1}{V}\sum_{ip}(\varphi\,\Delta\vec{n})_{ip} \tag{33}$$

Where V is the element volume and $\Delta\vec{n}$ is the outward surface vector at the integration point. Thus the above formulation requires φ to be evaluated at integration points using shape-functions.

Also, the advection term requires the integration point values of φ to be approximated in terms of the nodal values of φ, which is implemented in ANSYS CFX as follows

$$\varphi_{ip} = \varphi_{up} + \beta\,\nabla\varphi.\Delta\vec{r} \tag{34}$$

where φ_{up} is the value of φ at the upwind node and $\vec{r}$ is the vector from the upwind node to the integration point. Individual choices of β and $\nabla\varphi$ yield different schemes.

Central Difference Scheme

Here the value of β is set to 1 and $\nabla\varphi$ is set to the local element gradient. Another form of interpretation is that φ_{ip} is evaluated using the tri-linear shape functions:

$$\varphi_{ip} = \sum_{n} N_n(x_{ip}, y_{ip}, z_{ip})\varphi_n \tag{35}$$

Thus the resulting scheme is second-order accurate while an undesirable attribute is that this scheme may suffer from serious decoupling issues.

High-Resolution Scheme

This scheme uses a non-linear recipe for β at each node which is computed to be as close to 1 as possible without introducing new extrema. $\nabla\varphi$ is evaluated using β and $\nabla\varphi$ from the upwind node. The formulation of β is based on the boundedness principles of Barth and Jesperson [11] involving initial computation of φ_{min} and φ_{max} at each node using a stencil involving adjacent nodes and including the node itself. Nextly, each integration point around the node is solver for β to ensure that φ_{min} is not undershot and φ_{max} is not overshot. The equation used is the same as (36).

Nodal value for β is taken to be the minimum value of all integration point values surrounding the node and is not allowed to exceed 1.

Temporal discretization

The discretization of the transient term for the nth time step for control volumes that do not deform in time is given by

$$\frac{\partial}{\partial t}\int_0^V \rho\varphi \, dV \approx V\frac{(\rho\varphi)^{n+\frac{1}{2}} - (\rho\varphi)^{n-\frac{1}{2}}}{\Delta t} \tag{37}$$

Values at the start and end of the time step are assigned the superscripts $n+\frac{1}{2}$ and $n-\frac{1}{2}$, respectively. These time step values for the second order backward Euler scheme used in the present study is defined as

$$(\rho\varphi)^{n-\frac{1}{2}} = (\rho\varphi)^{o} + \frac{1}{2}((\rho\varphi)^{o} - (\rho\varphi)^{oo}) \tag{38}$$

$$(\rho\varphi)^{n+\frac{1}{2}} = \rho\varphi + \frac{1}{2}(\rho\varphi - (\rho\varphi)^{o}) \tag{39}$$

(40) and (41) substituted into (42) yields the resulting discretization as follows

$$\frac{\partial}{\partial t}\int_0^V \rho\varphi \, dV \approx \frac{V}{\Delta t}\left(\frac{3}{2}(\rho\varphi) - 2(\rho\varphi)^o + \frac{1}{2}(\rho\varphi)^{oo}\right) \quad (43)$$

The superscripts o and oo represent the first and second partial derivative, respectively. This scheme is considered robust, implicit, conservative in time, second order accurate and does not have a time step size limitation.

Pressure-Velocity Coupling

ANSYS CFX uses a co-located (non-staggered) grid layout such that the control volumes are identical for all transport equations. More detailed explanation is available in the CFX-solver theory guide [6].

Discretization Errors

Discretization Errors arise due to differences between the exact analytical solution of the modeled differential equations and the fully converged solution of their discrete representations. Like the principal variables being solved for, errors in these values are generated both by localized sources and propagated (i.e. amplified, convected or diffused) throughout the computational domain.

Localized sources of error result from high-order terms that are excluded from the discrete approximations of terms in the modeled equations while error propagation results from the form of terms that are included in the discrete approximations. The current simulations performed using ANSYS CFX are second order accurate in space and time.

A.2 EFFECT OF CHANGE IN THE MAIN FLOW VELOCITIES ON THE FLOW MIXING BEHAVIOR

This section looks into the effects of mass flow rate variations in the main pipe on the flow mixing behavior observed downstream of the T-junction. The results presented in this section follow a pattern similar to what was discussed in section 4.1 and so only pictorial illustrations are used here. The reader is suggested to compare the results presented here to section 4.1 to have an appreciation of the changes in the flow mixing behavior as a function of changes in the mass flow rates in the main pipe.

Table 14: Inflow conditions at the FSI test facility

Case #	ΔT (°C)	T_m* (°C)	$\dot{m}_m$ (kg/s)	u_m (m/s)	T_b* (°C)	$\dot{m}_b$ (kg/s)	u_b (m/s)	u_{mix} (m/s)
8	64	82	0.3	0.076	18	0.1	0.084	0.113
9	104	125	0.3	0.079	21	0.1	0.084	0.115
10	120	141	0.3	0.08	21	0.1	0.084	0.12
11	68	87	0.5	0.127	19	0.1	0.084	0.153
12	112	133	0.5	0.132	21	0.1	0.084	0.156
13	129	150	0.5	0.135	21	0.1	0.084	0.16
14	147	169	0.5	0.14	22	0.1	0.084	0.16
Pressure – 30 bar								

* suffixes m and b denote the main and the branch pipes, respectively

Shown in Table 14 are the inflow conditions in the main and branch pipes, respectively. Two different flow rates in the main pipe – 0.3 kg/s and 0.5 kg/s – are used at ΔT ranging from 64 – 150 °C where the branch flow rate is maintained at a constant value of 0.1 kg/s. Measurements at 0.3 kg/s were limited to a maximum ΔT of 129 °C as higher amounts of cold and hot flow penetrations into the main and branch pipes were observed beyond this ΔT level. The non-dimensional numbers pertaining to the inflow conditions shown in Table 14 are listed in Table 15.

Table 15: Non-dimensional numbers calculated for all the cases

Case #	ΔT (°C)	$\Delta\rho/\bar{\rho}$ (in %)	Re_m	Re_b	Ri	Re_m/Re_b (R)	μ_m/μ_b
8	64	2.8	15340	3100	1.56	4.95	0.33
9	104	6.5	24870	3340	3.43	7.45	0.22
10	120	8.4	28990	3340	4.36	8.68	0.18
11	68	3.2	27150	3220	0.95	8.43	0.32
12	112	6.7	42810	3340	1.94	12.8	0.21
13	129	8.6	49010	3340	2.4	14.7	0.18
14	147	10.7	55940	3420	2.9	16.4	0.16

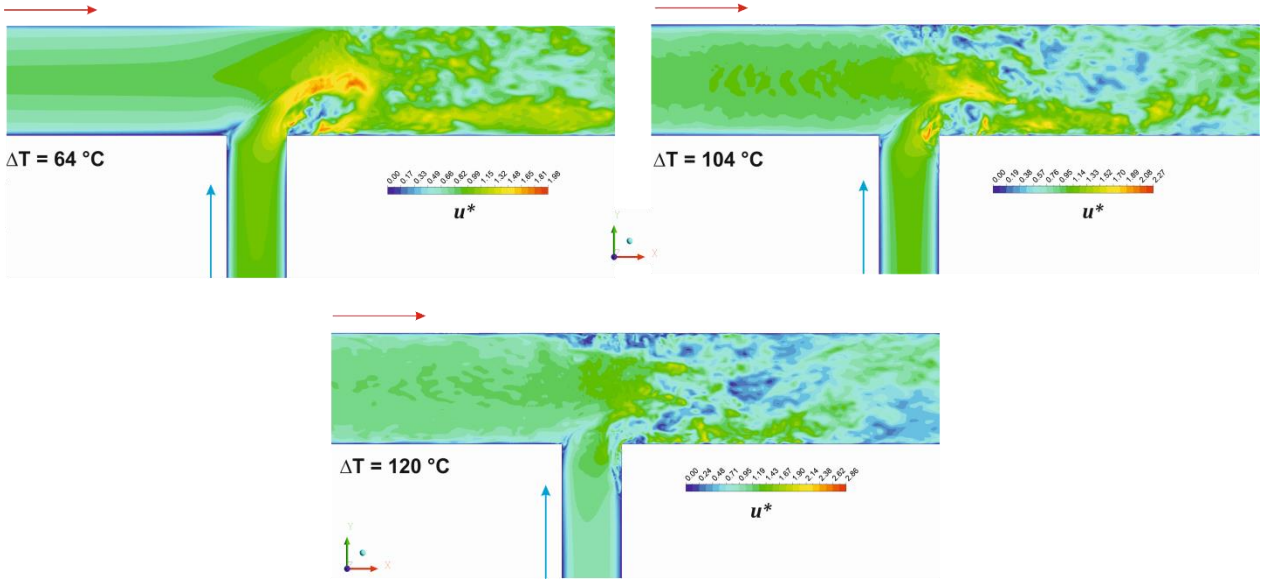

Fig. 79 Instantaneous velocity field at the T-junction with $\dot{m}_m$ = 0.3 kg/s, $\dot{m}_b$ = 0.1 kg/s

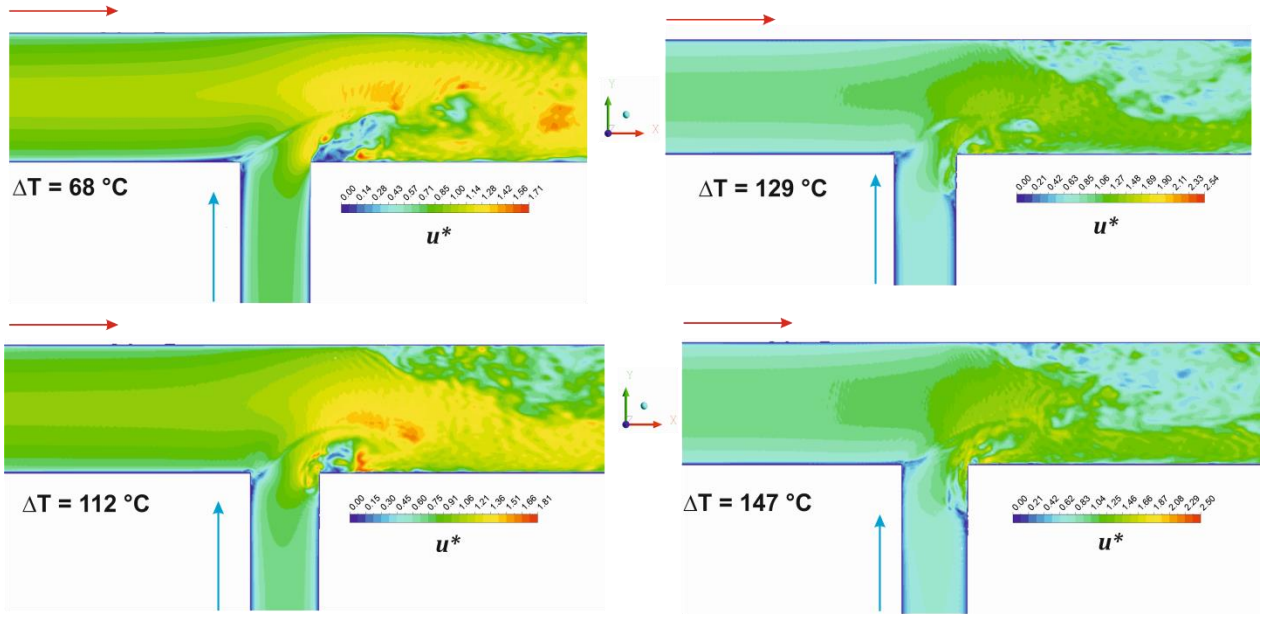

Fig. 80 Instantaneous velocity field at the T-junction with $\dot{m}_m$ = 0.5 kg/s, $\dot{m}_b$ = 0.1 kg/s

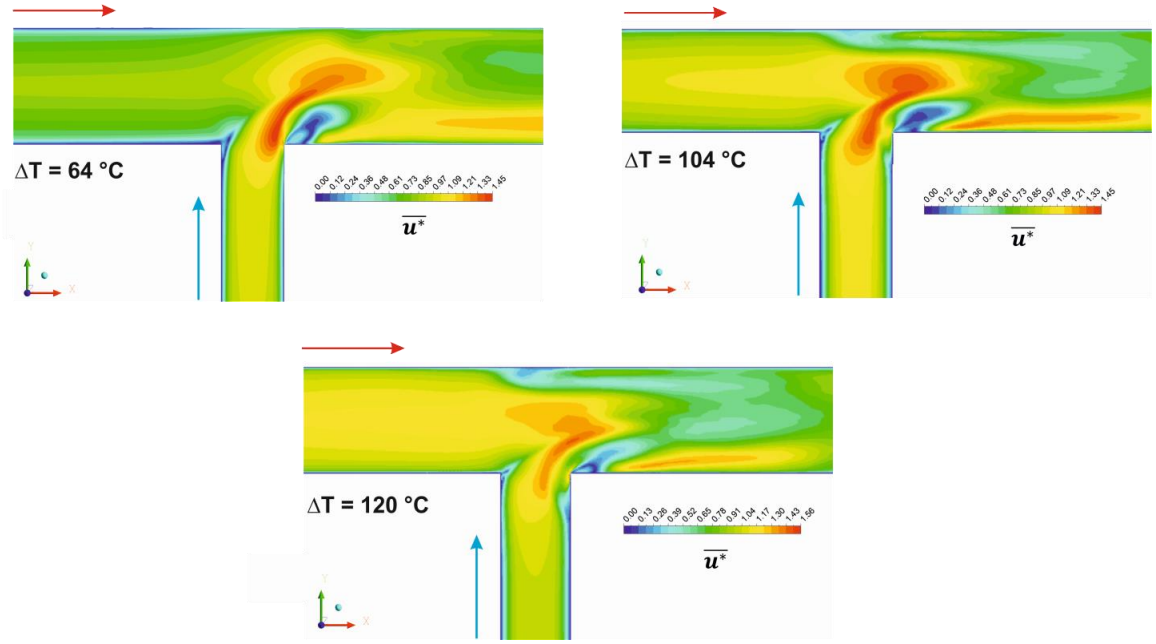

Fig. 81 Mean velocity field at the T-junction with $\dot{m}_m$ = 0.3 kg/s, $\dot{m}_b$ = 0.1 kg/s

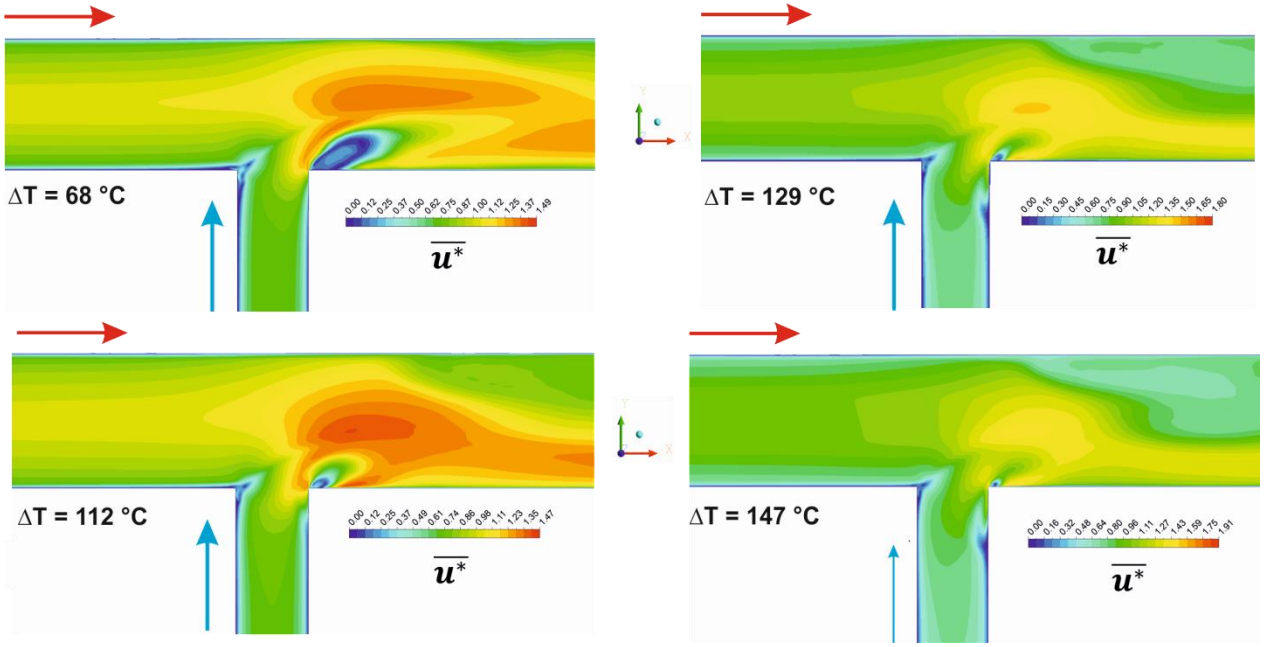

Fig. 82 Mean velocity field at the T-junction with $\dot{m}_m$ = 0.5 kg/s, $\dot{m}_b$ = 0.1 kg/s

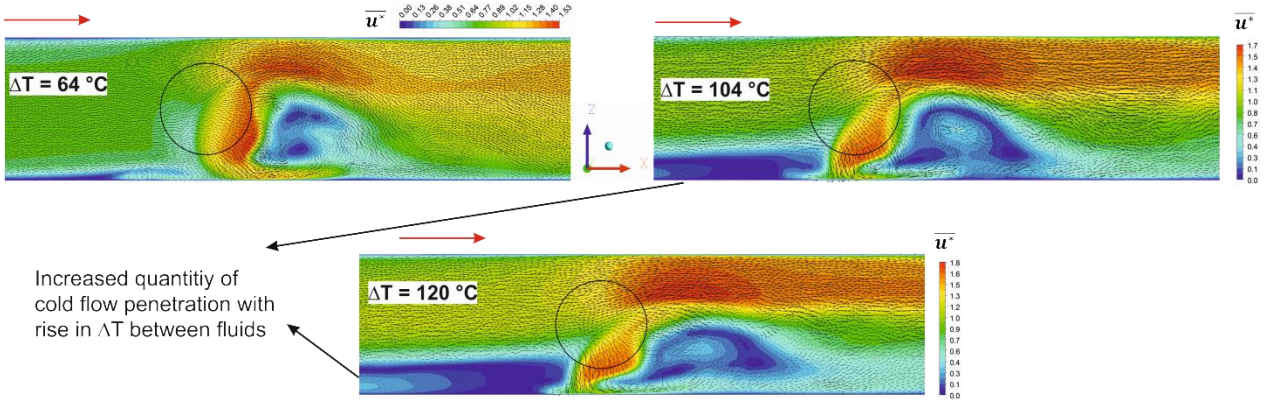

Fig. 83 Mean velocity field illustrating the CVP structurer with $\dot{m}_m$ = 0.3 kg/s, $\dot{m}_b$ = 0.1 kg/s

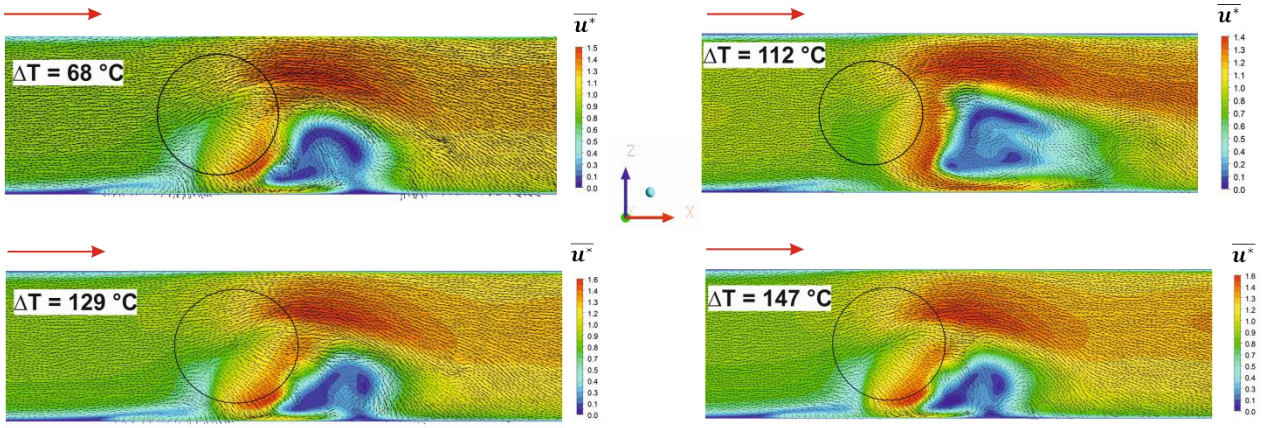

Fig. 84 Mean velocity field illustrating the CVP structurer with $\dot{m}_m$ = 0.5 kg/s, $\dot{m}_b$ = 0.1 kg/s

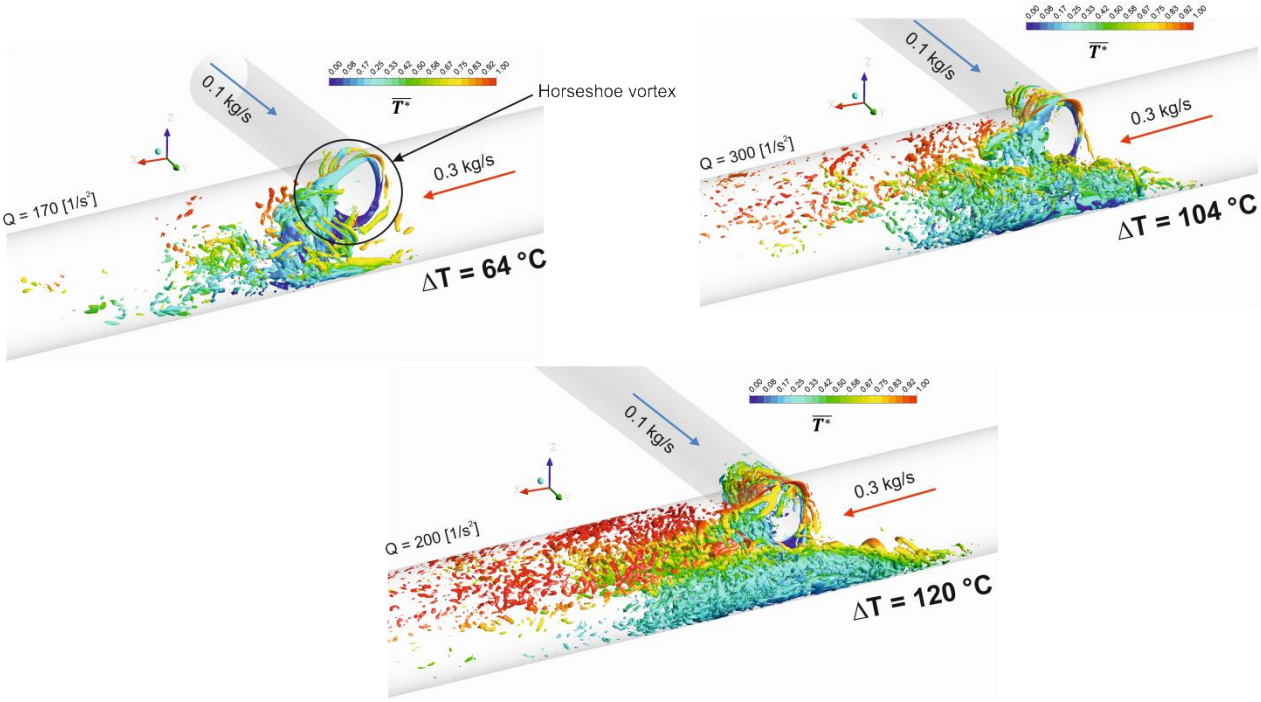

Fig. 85 Vortical structures illustrated using the Q-criterion in the vicinity of the T-junction with $\dot{m}_m$ = 0.3 kg/s, $\dot{m}_b$ = 0.1 kg/s

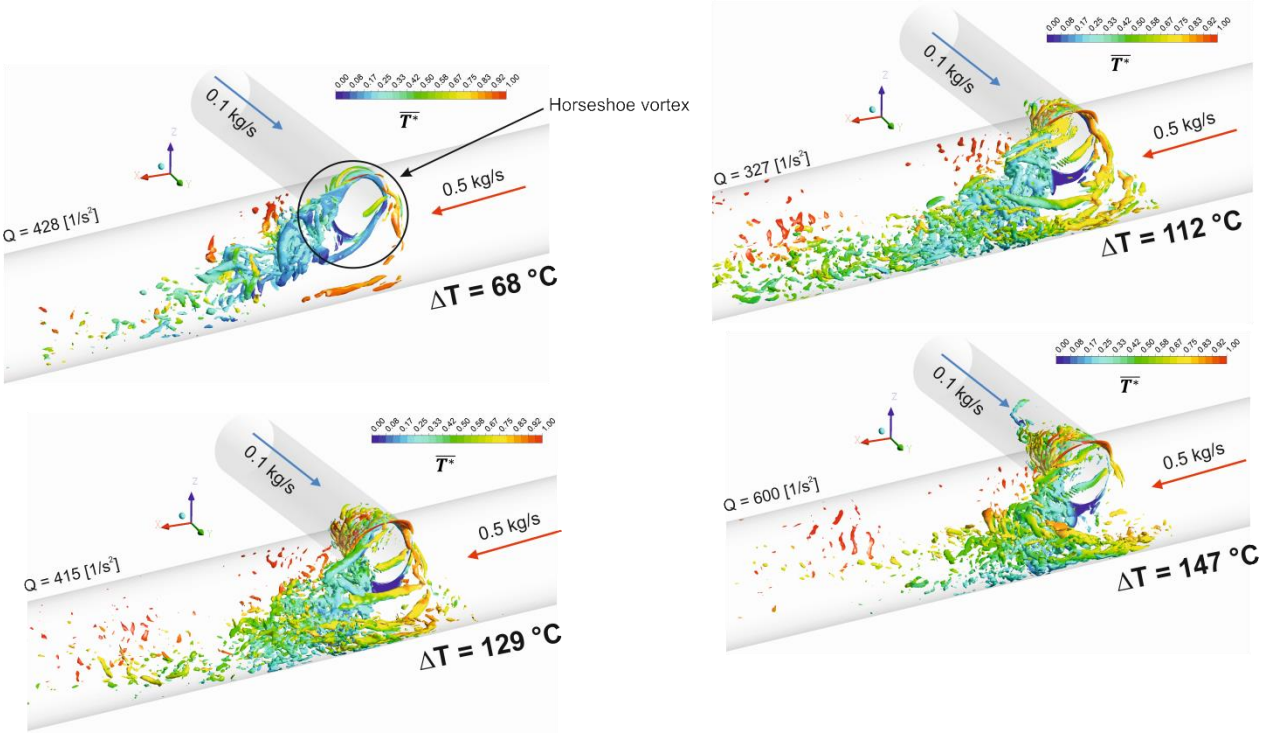

Fig. 86 Vortical structures illustrated using the Q-criterion in the vicinity of the T-junction with $\dot{m}_m$ = 0.5 kg/s, $\dot{m}_b$ = 0.1 kg/s

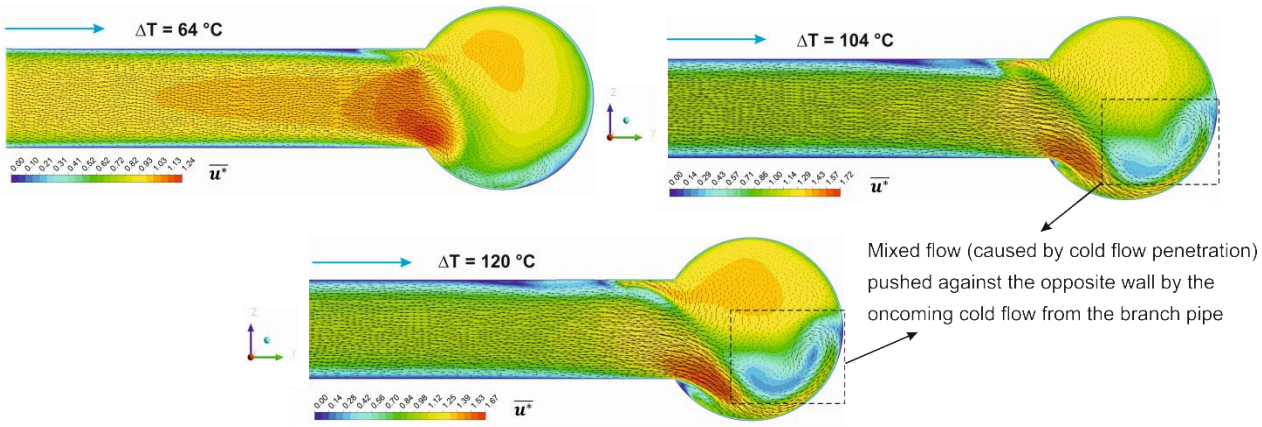

Fig. 87 Mean velocity field illustrating the entry of the cold fluid into the main pipe ($\dot{m}_m$ = 0.3 kg/s, $\dot{m}_b$ = 0.1 kg/s)

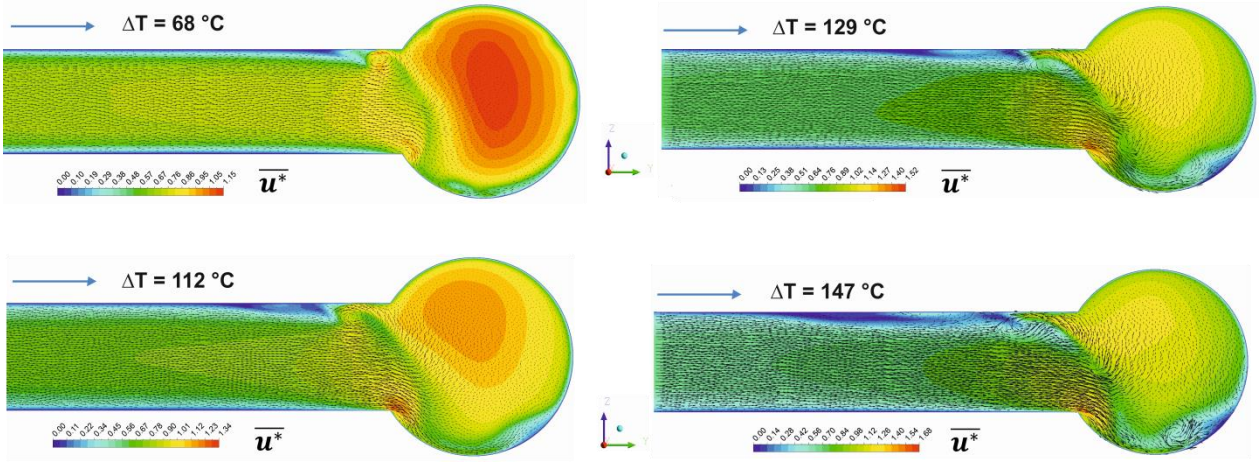

Fig. 88 Mean velocity field illustrating the entry of the cold fluid into the main pipe ($\dot{m}_m$ = 0.5 kg/s, $\dot{m}_b$ = 0.1 kg/s)

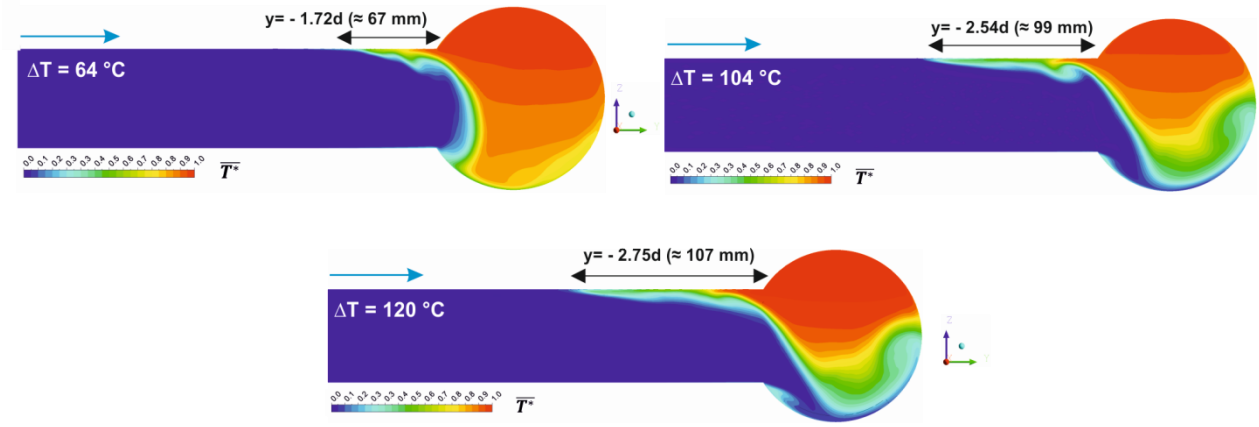

Fig. 89 Hot flow penetration into the branch pipe illustrated using mean temperature field along the y-z axis ($\dot{m}_m$ = 0.3 kg/s, $\dot{m}_b$ = 0.1 kg/s)

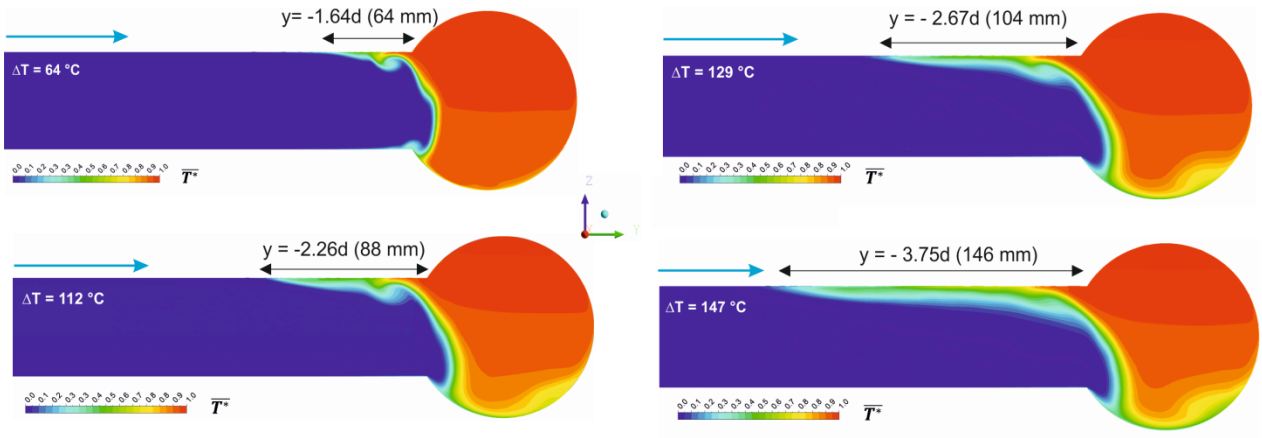

Fig. 90 Hot flow penetration into the branch pipe illustrated using mean temperature field along the y-z axis ($\dot{m}_m$ = 0.5 kg/s, $\dot{m}_b$ = 0.1 kg/s)

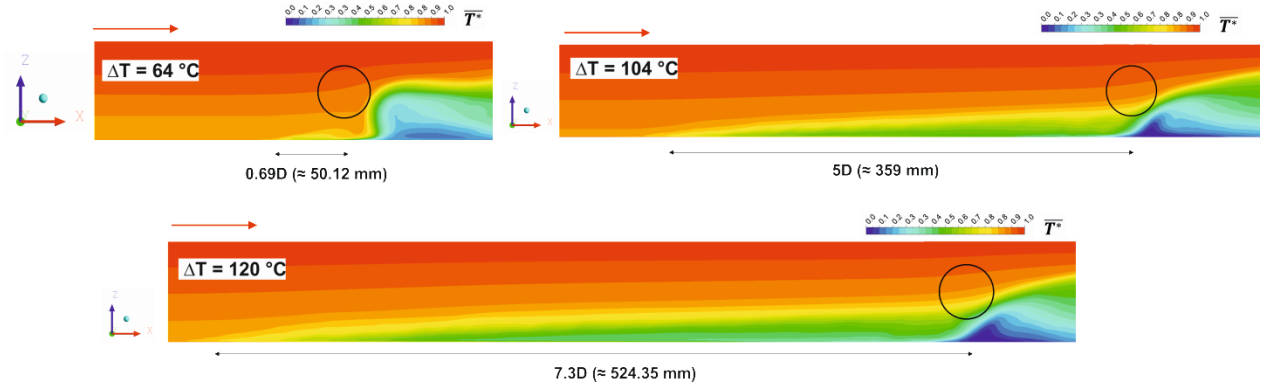

Fig. 91 Cold flow penetration into the main pipe illustrated using mean temperature field along the x-z axis ($\dot{m}_m$ = 0.3 kg/s, $\dot{m}_b$ = 0.1 kg/s)

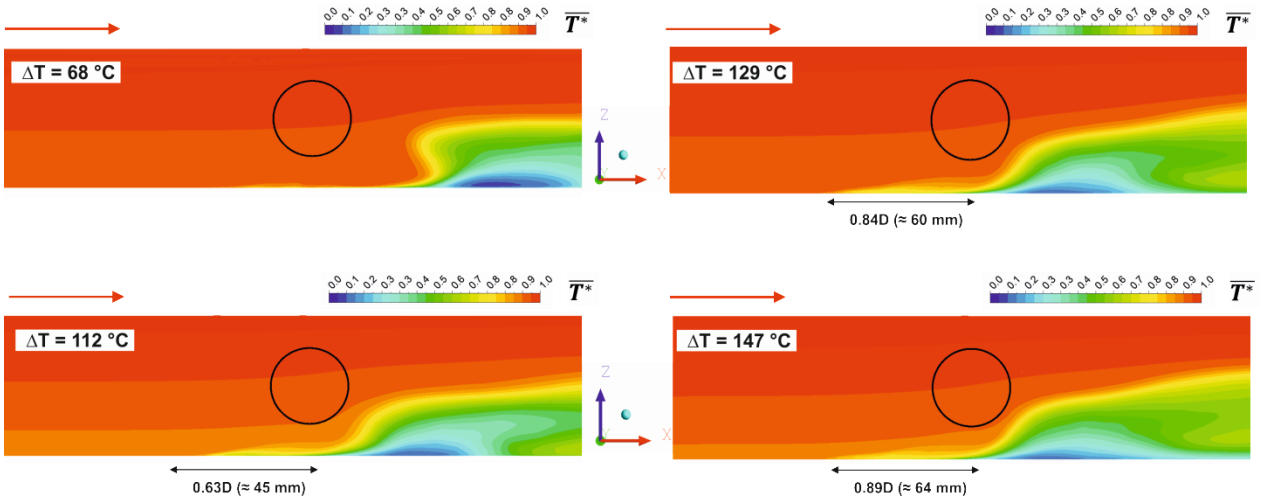

Fig. 92 Cold flow penetration into the main pipe illustrated using mean temperature field along the x-z axis ($\dot{m}_m$ = 0.5 kg/s, $\dot{m}_b$ = 0.1 kg/s)

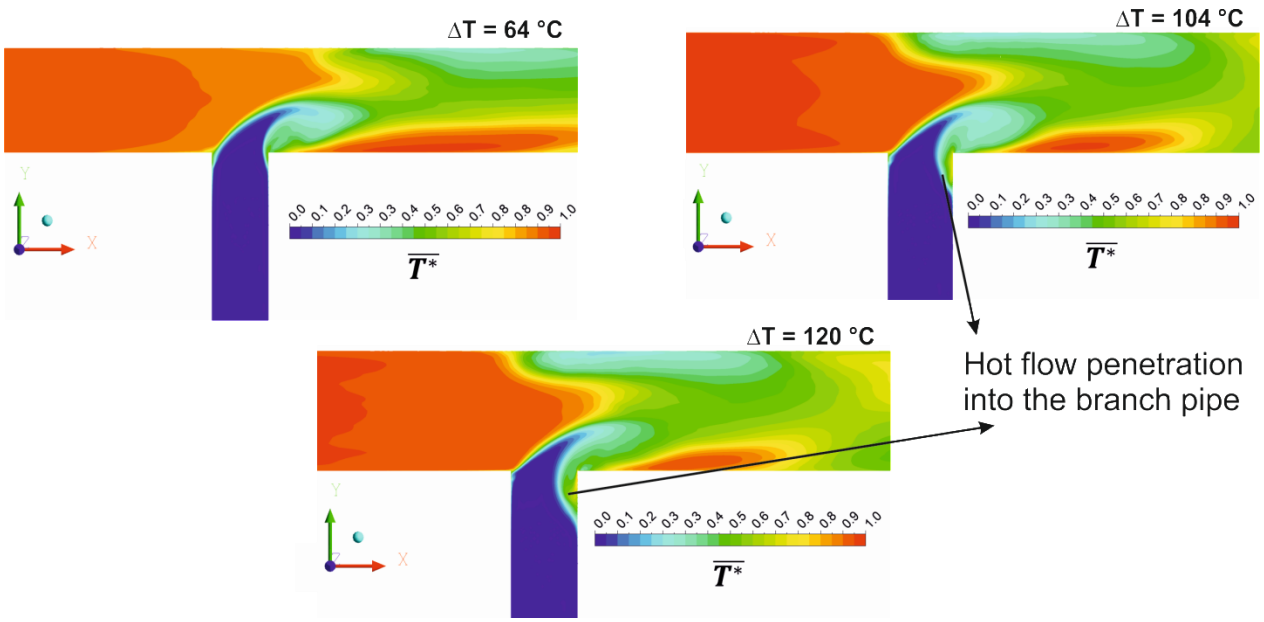

Fig. 93 Mean temperature field at the T-junction along the streamwise direction ($\dot{m}_m$ = 0.3 kg/s, $\dot{m}_b$ = 0.1 kg/s)

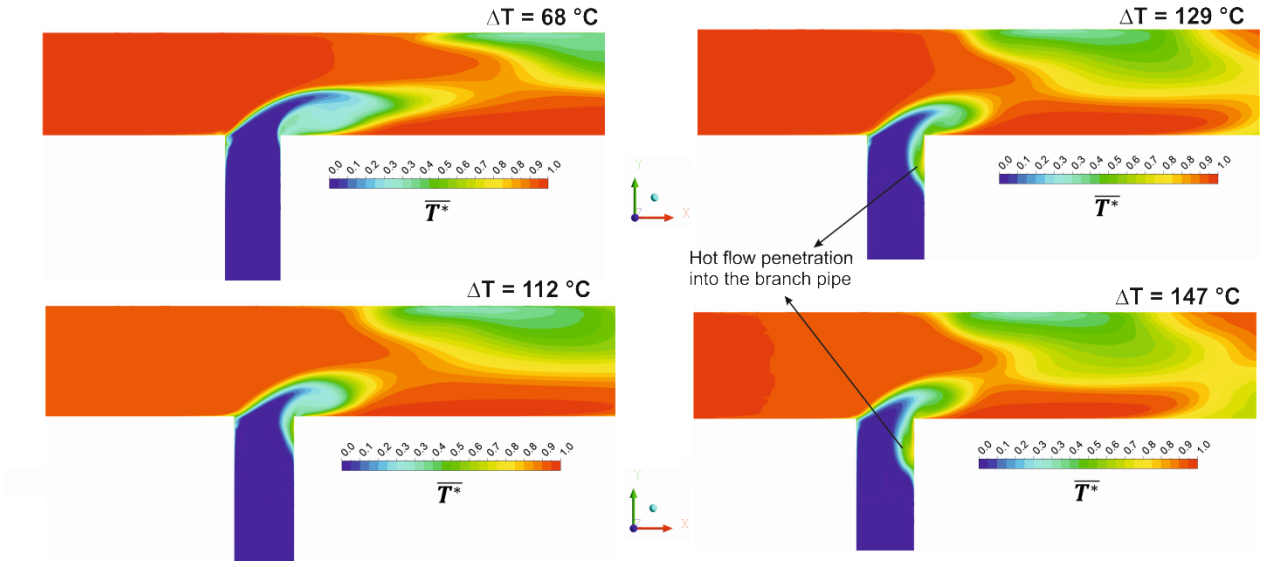

Fig. 94 Mean temperature field at the T-junction along the streamwise direction ($\dot{m}_m$ = 0.5 kg/s, $\dot{m}_b$ = 0.1 kg/s)

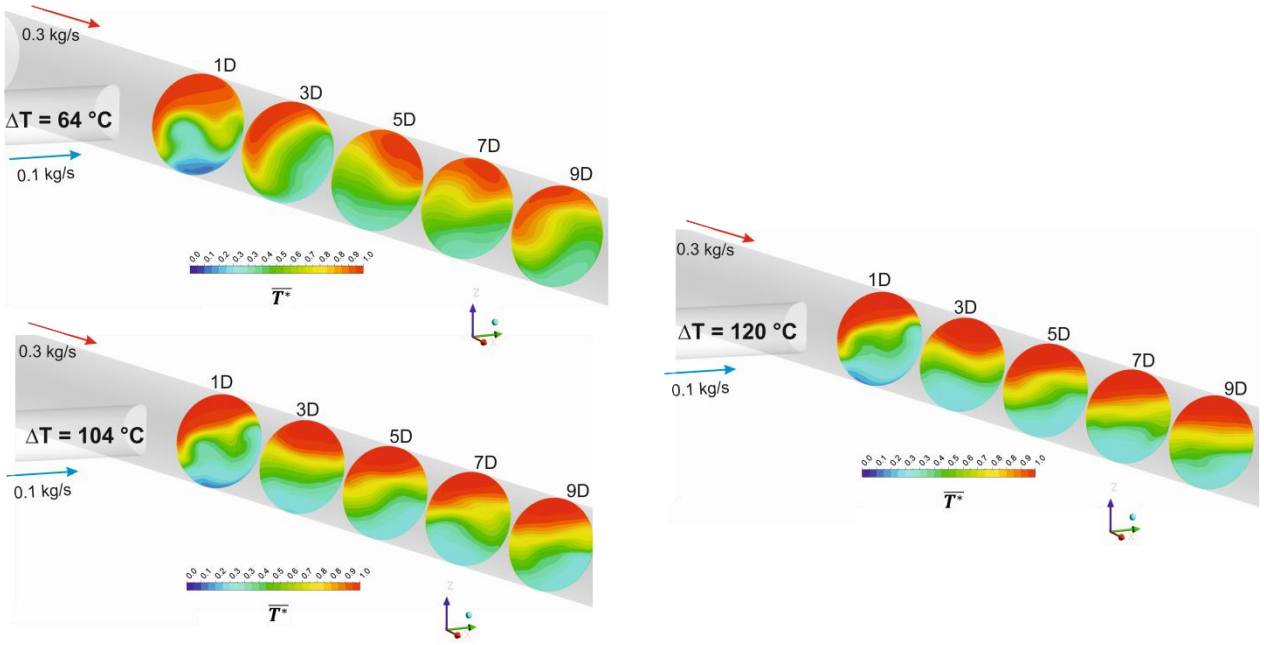

Fig. 95 Mean temperature field along the cross-sectional direction ($\dot{m}_m$ = 0.3 kg/s, $\dot{m}_b$ = 0.1 kg/s)

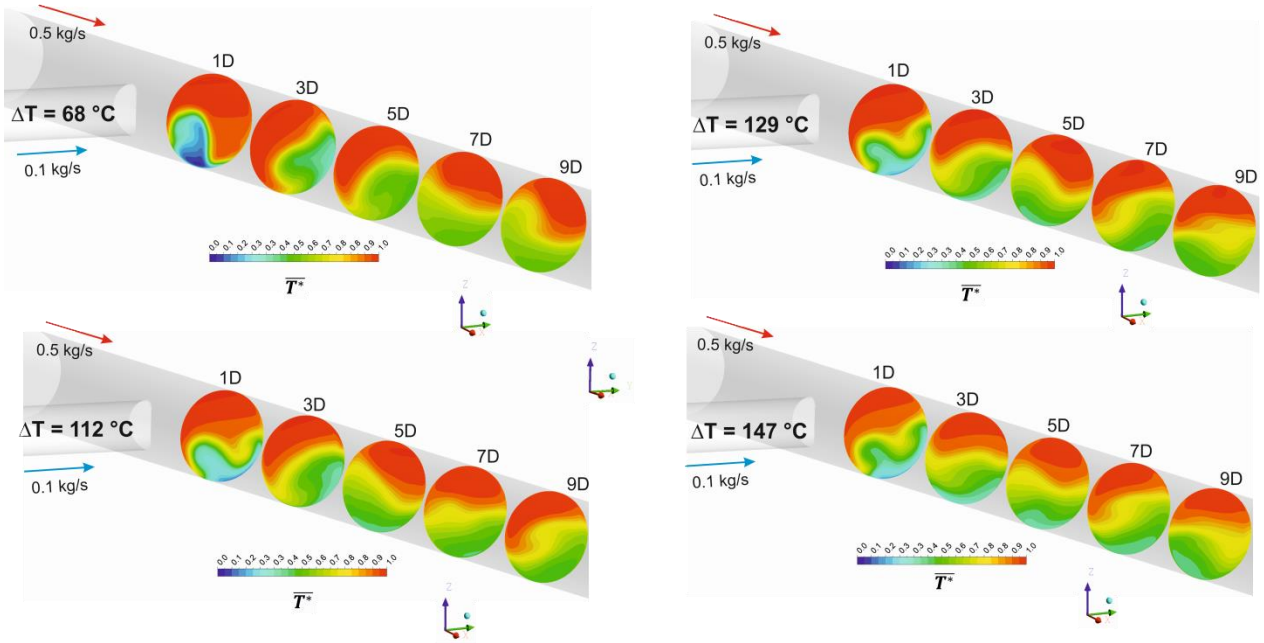

Fig. 96 Mean temperature field along the cross-sectional direction ($\dot{m}_m$ = 0.5 kg/s, $\dot{m}_b$ = 0.1 kg/s)

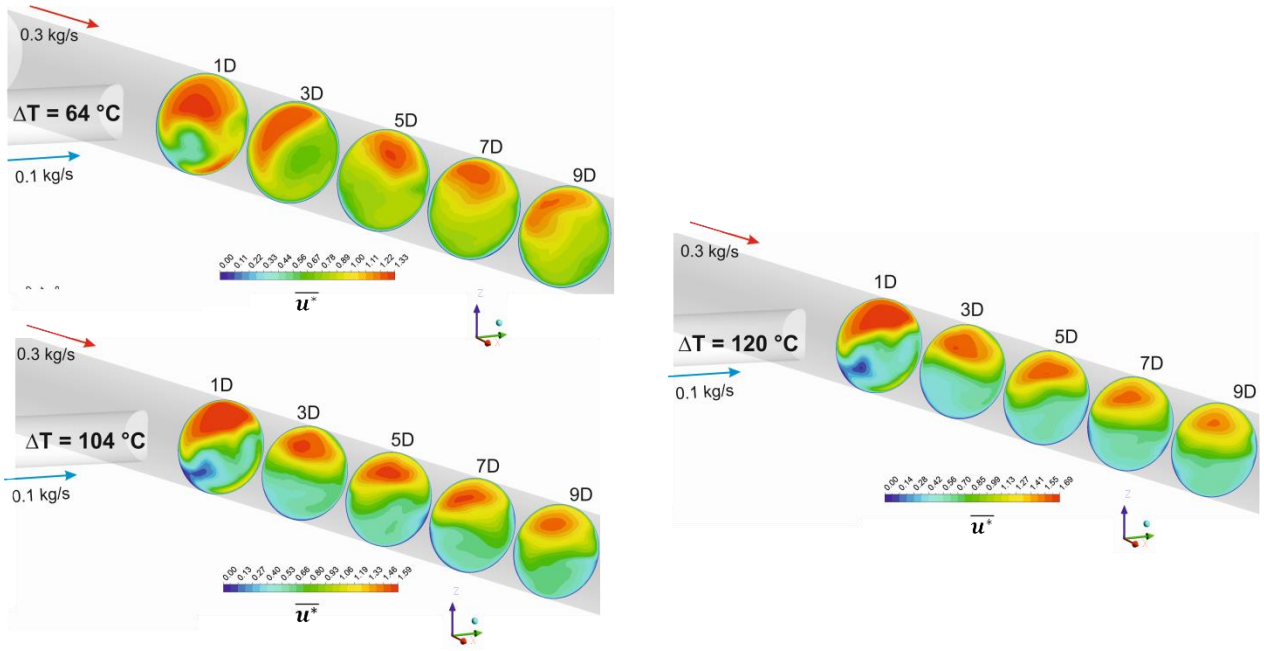

Fig. 97 Mean velocity field along the cross-sectional direction ($\dot{m}_m$ = 0.3 kg/s, $\dot{m}_b$ = 0.1 kg/s)

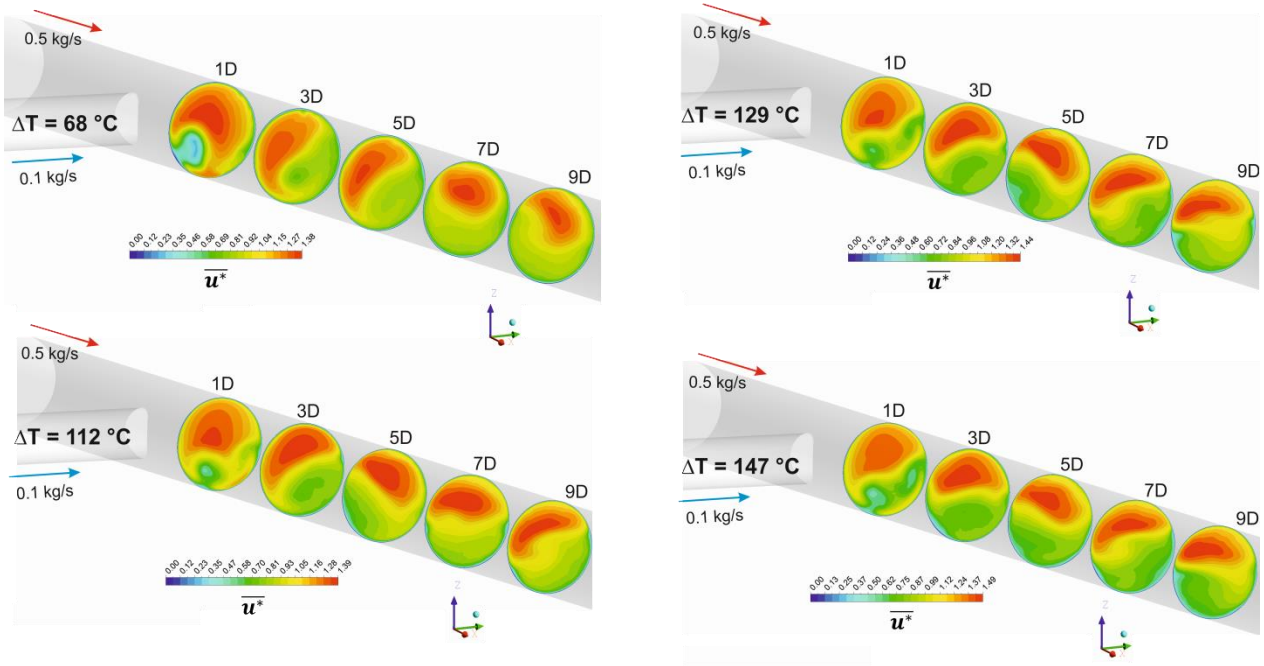

Fig. 98 Mean velocity field along the cross-sectional direction ($\dot{m}_m$ = 0.5 kg/s, $\dot{m}_b$ = 0.1 kg/s)

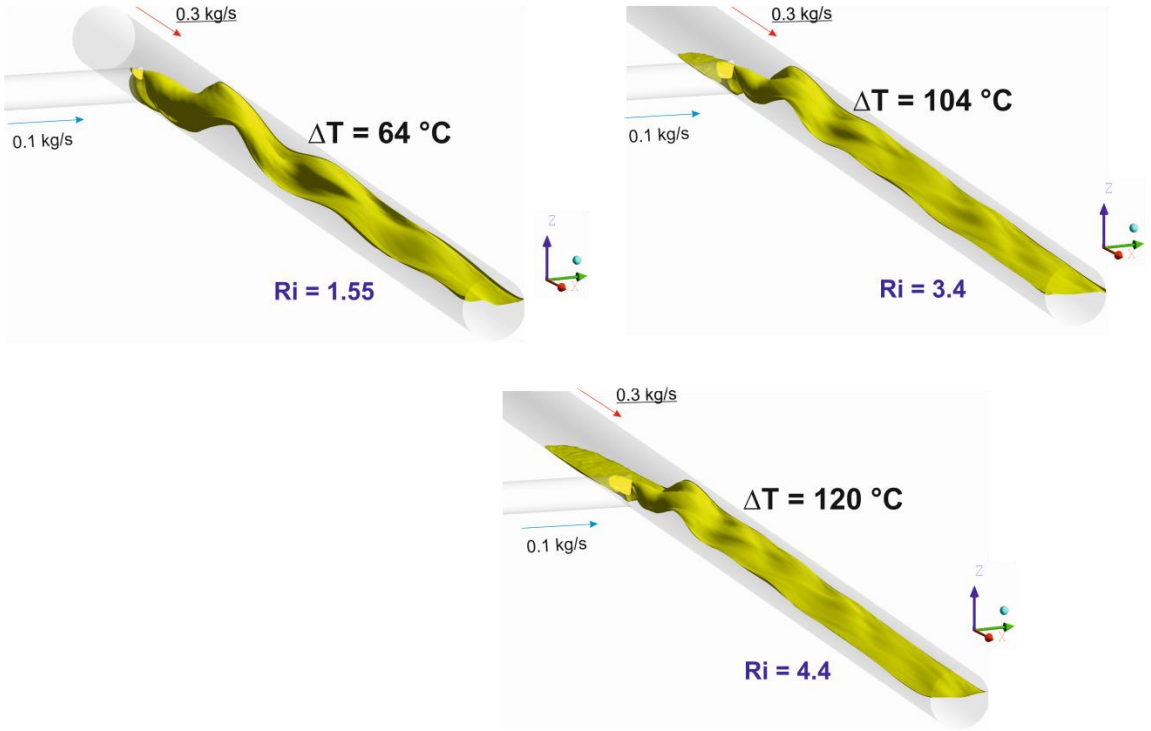

Fig. 99 Isosurfaces of mean temperature at $\overline{T^*}$ = 0.75 ($\dot{m}_m$ = 0.3 kg/s, $\dot{m}_b$ = 0.1 kg/s)

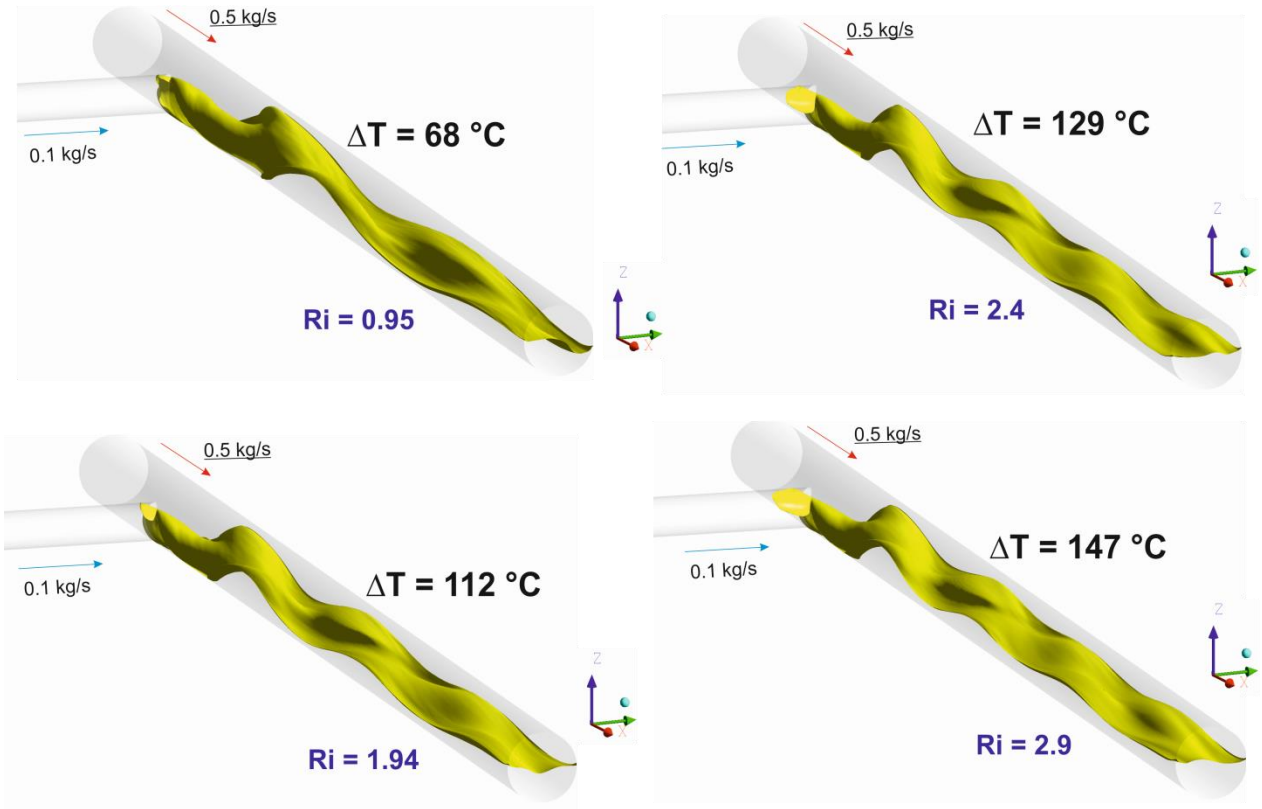

Fig. 100 Isosurfaces of mean temperature at $\overline{T^*}$ = 0.75 ($\dot{m}_m$ = 0.5 kg/s, $\dot{m}_b$ = 0.1 kg/s)

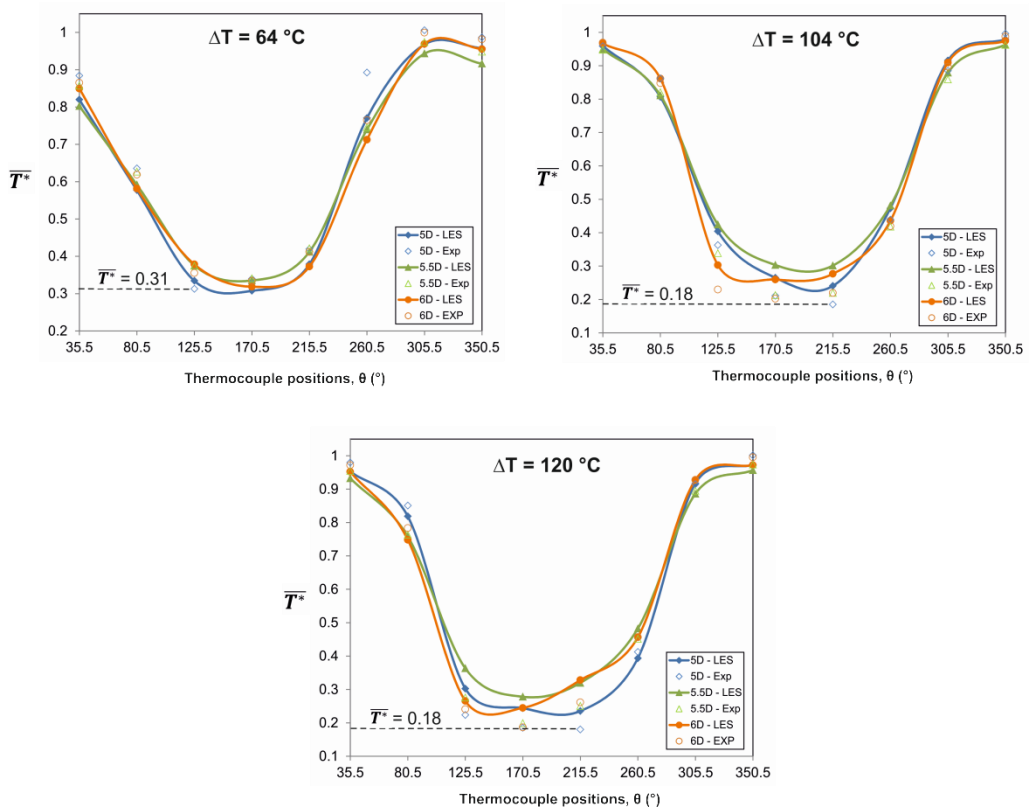

Fig. 101 $\overline{T^*}$ distribution along the angular thermocouple positions ($\dot{m}_m$ = 0.3 kg/s, $\dot{m}_b$ = 0.1 kg/s)

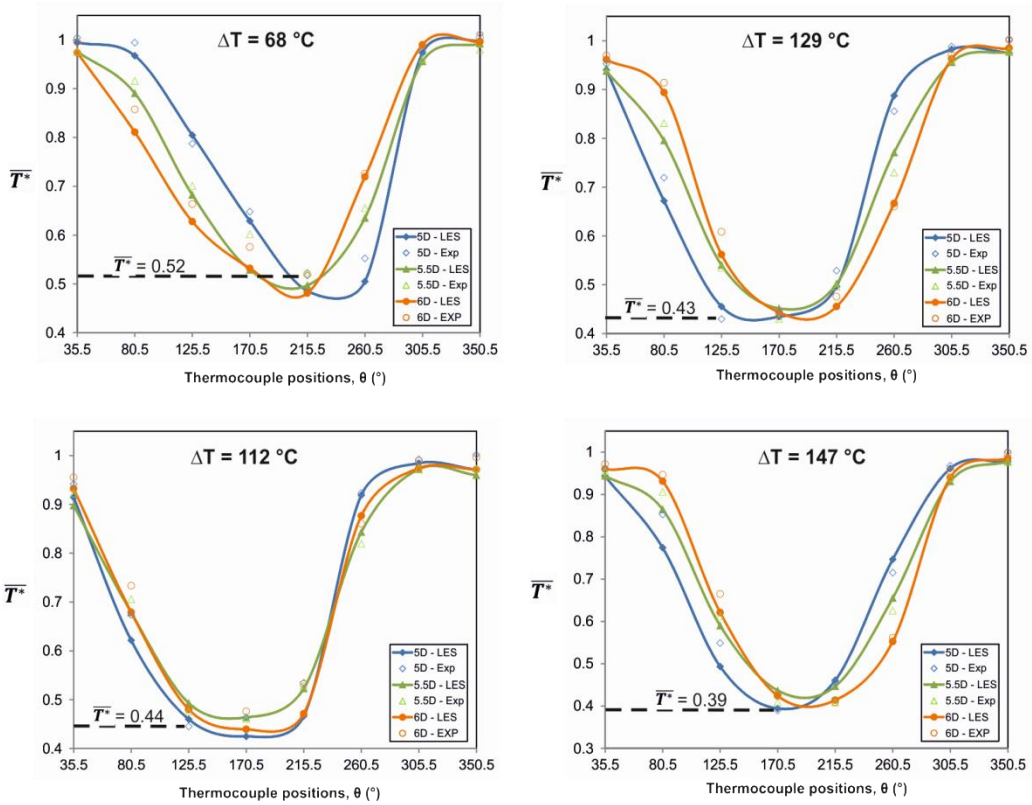

Fig. 102 $\overline{T^*}$ distribution along the angular thermocouple positions ($\dot{m}_m$ = 0.5 kg/s, $\dot{m}_b$ = 0.1 kg/s)

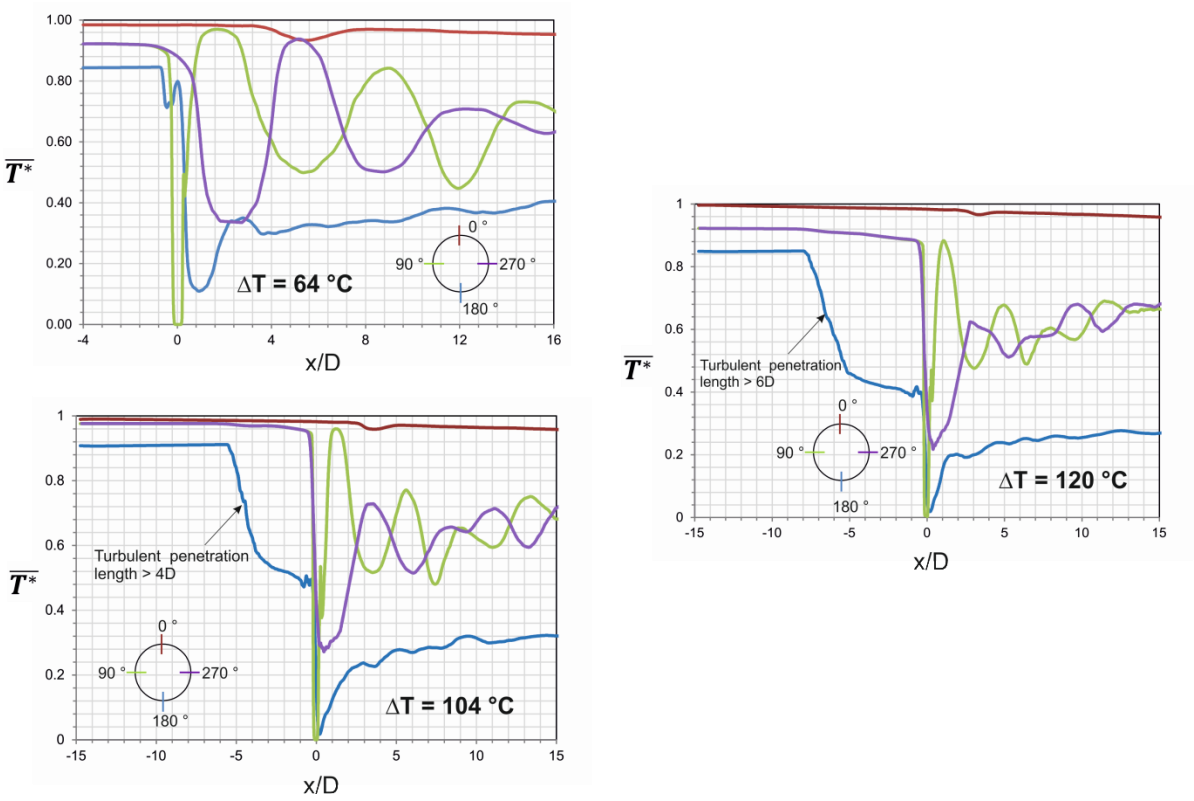

Fig. 103 Axial $\overline{T^*}$ distribution at θ = 0°, 90°, 180° and 270° ($\dot{m}_m$ = 0.3 kg/s, $\dot{m}_b$ = 0.1 kg/s)

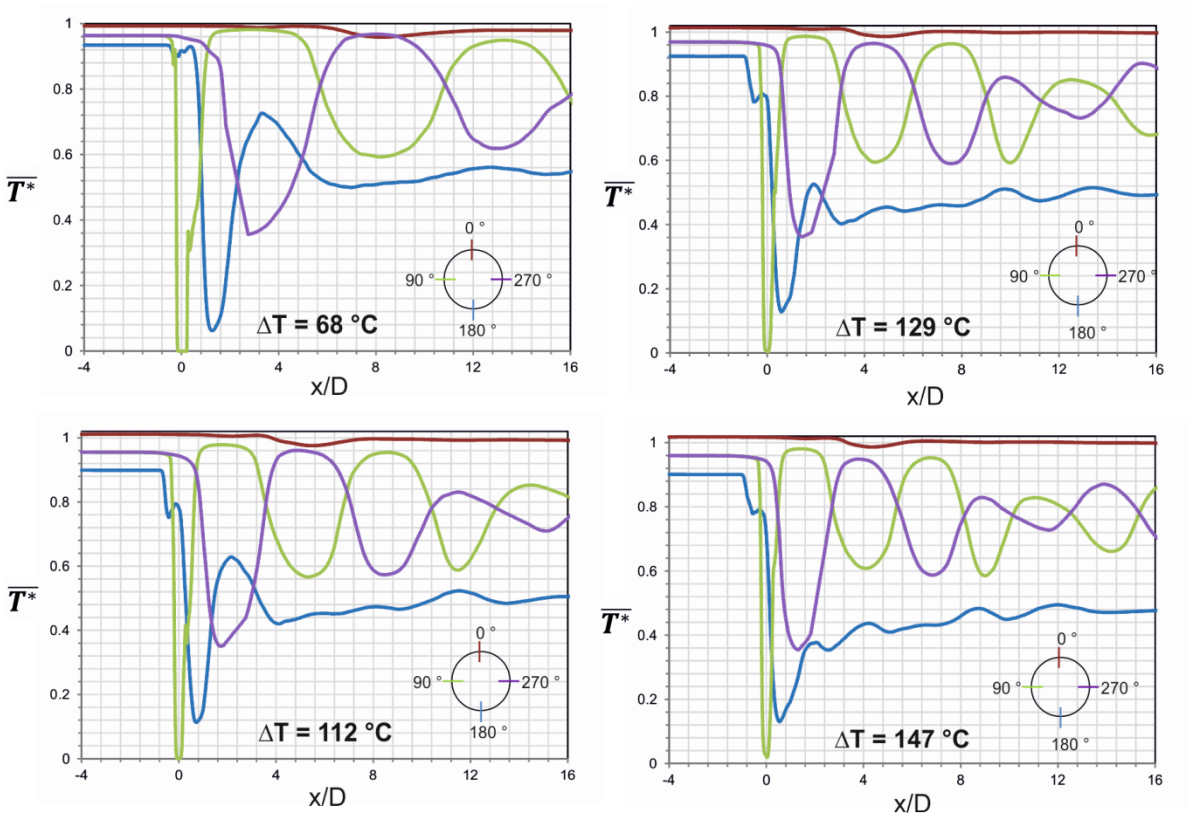

Fig. 104 Axial $\overline{T^*}$ distribution at θ = 0°, 90°, 180° and 270° ($\dot{m}_m$ = 0.5 kg/s, $\dot{m}_b$ = 0.1 kg/s)

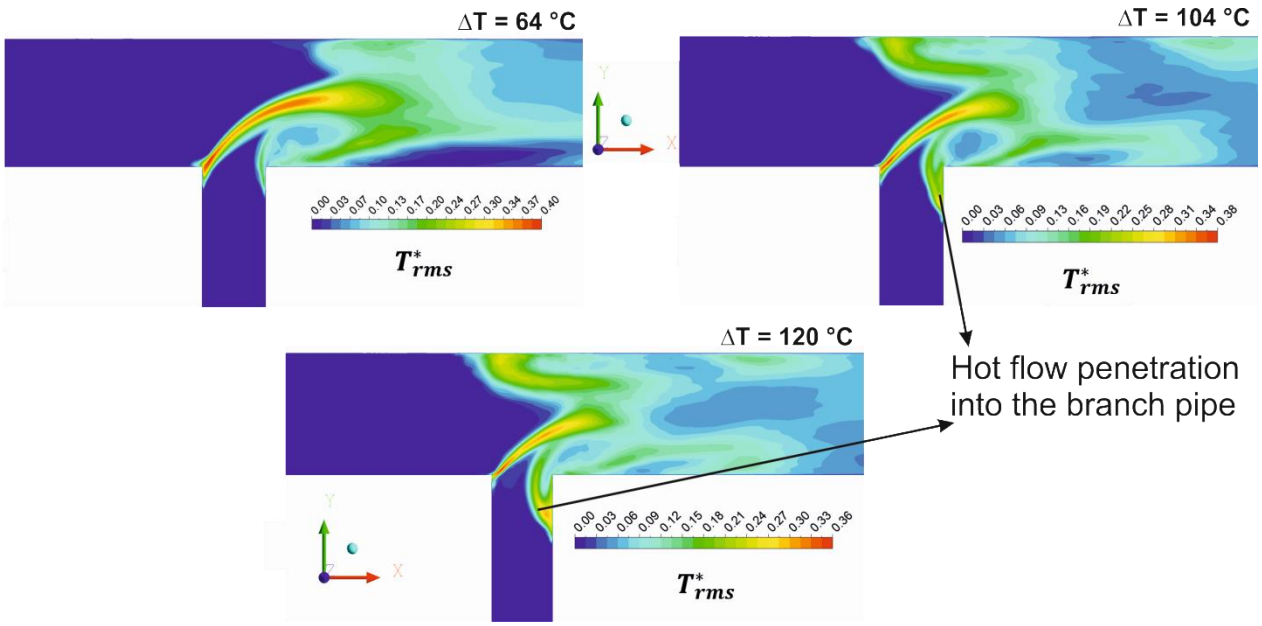

Fig. 105 Temperature fluctuations (T^*_{rms}) at the T-junction along the streamwise direction ($\dot{m}_m$ = 0.3 kg/s, $\dot{m}_b$ = 0.1 kg/s)

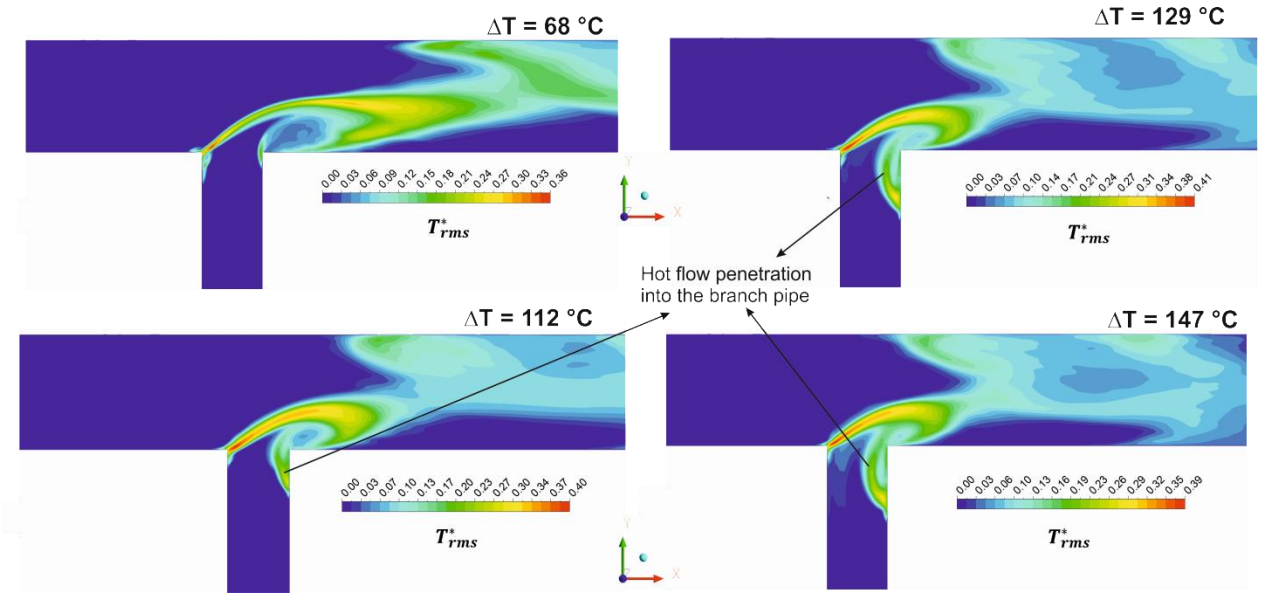

Fig. 106 Temperature fluctuations (T^*_{rms}) at the T-junction along the streamwise direction ($\dot{m}_m$ = 0.5 kg/s, $\dot{m}_b$ = 0.1 kg/s)

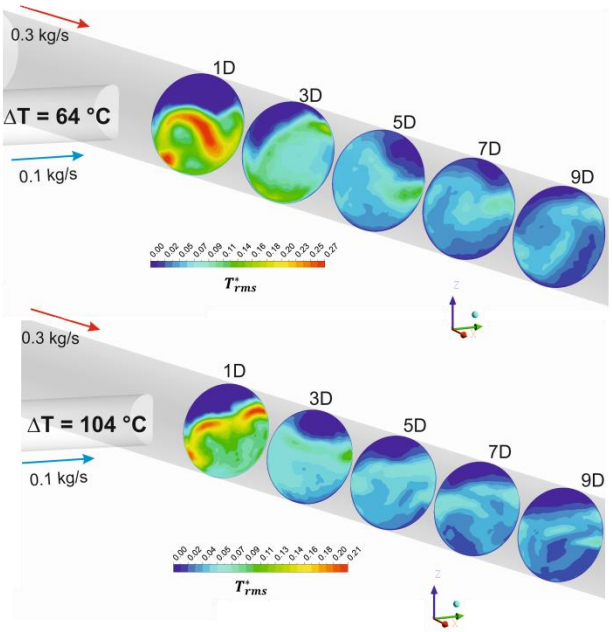

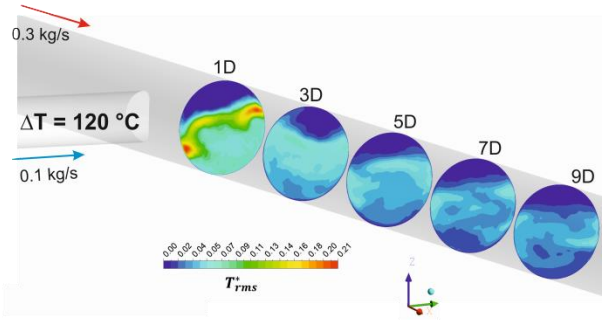

Fig. 107 $\boldsymbol{T^*_{rms}}$ field along the cross-sectional direction ($\dot{\boldsymbol{m}}_{\boldsymbol{m}}$ = 0.3 kg/s, $\dot{\boldsymbol{m}}_{\boldsymbol{b}}$ = 0.1 kg/s)

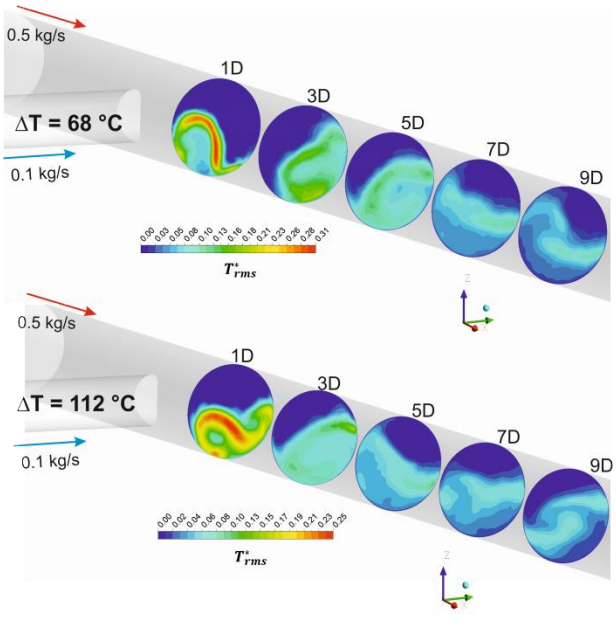

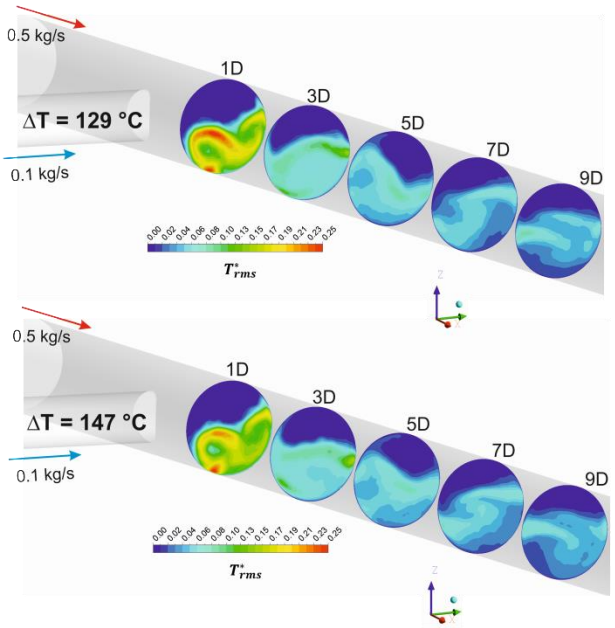

Fig. 108 $\boldsymbol{T^*_{rms}}$ field along the cross-sectional direction ($\dot{\boldsymbol{m}}_{\boldsymbol{m}}$ = 0.5 kg/s, $\dot{\boldsymbol{m}}_{\boldsymbol{b}}$ = 0.1 kg/s)

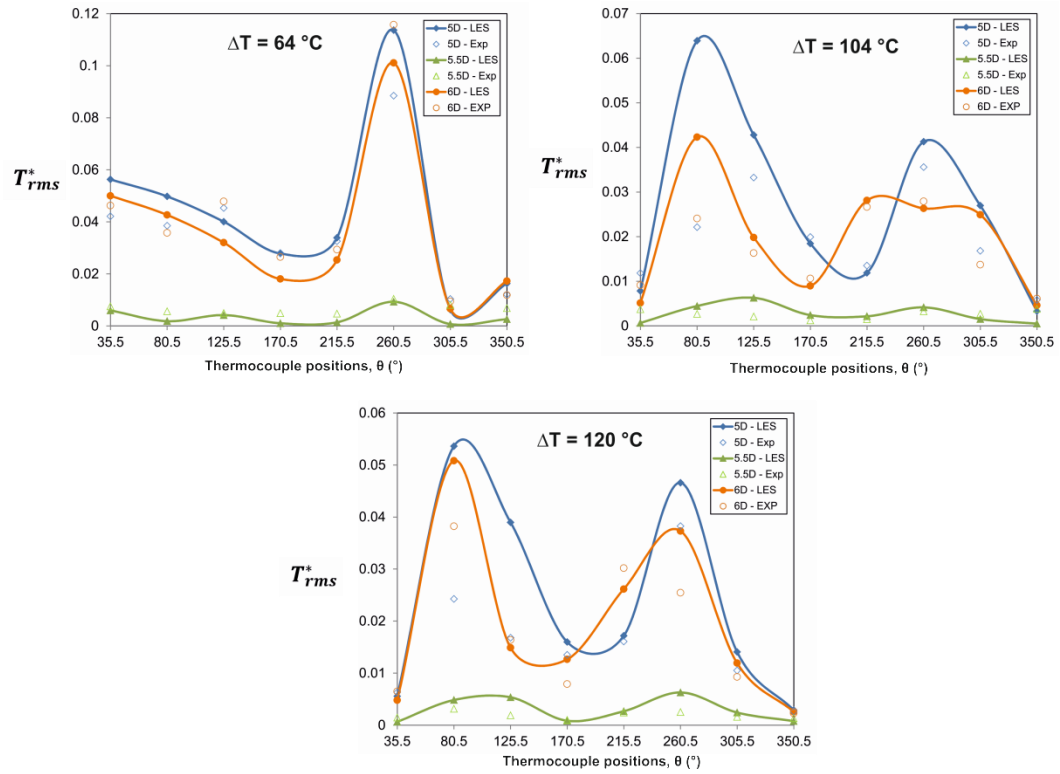

Fig. 109 T^*_{rms} distribution along the thermocouple positions ($\dot{m}_m$ = 0.3 kg/s, $\dot{m}_b$ = 0.1 kg/s)

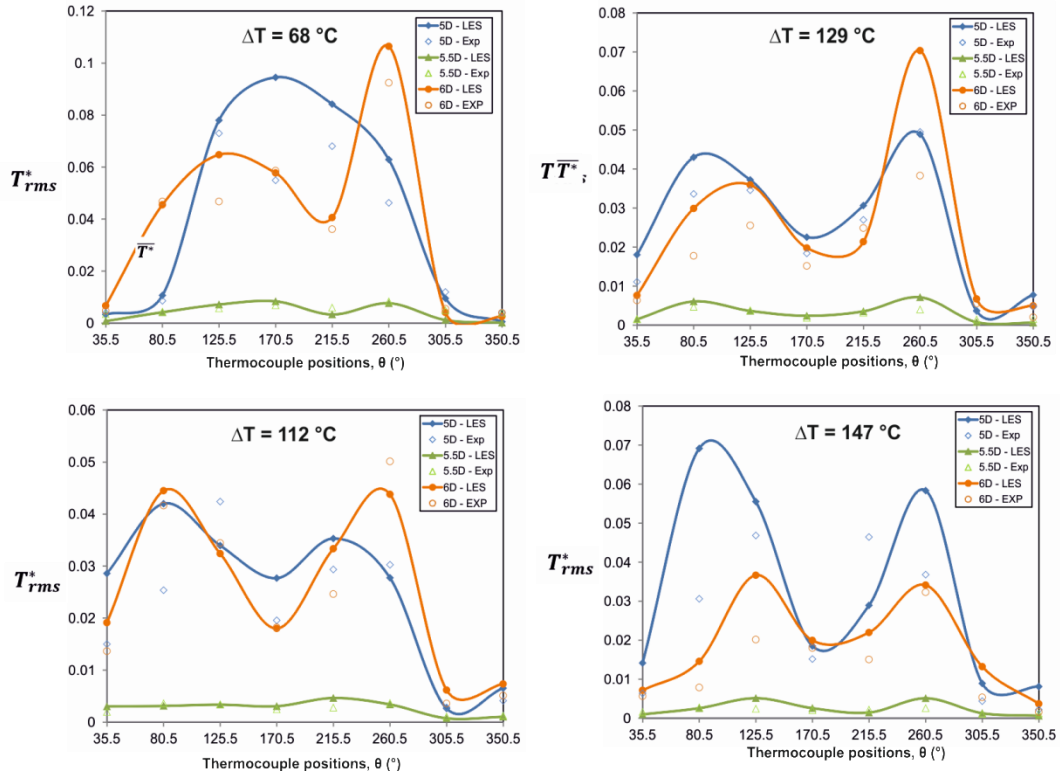

Fig. 110 T^*_{rms} distribution along the thermocouple positions ($\dot{m}_m$ = 0.5 kg/s, $\dot{m}_b$ = 0.1 kg/s)

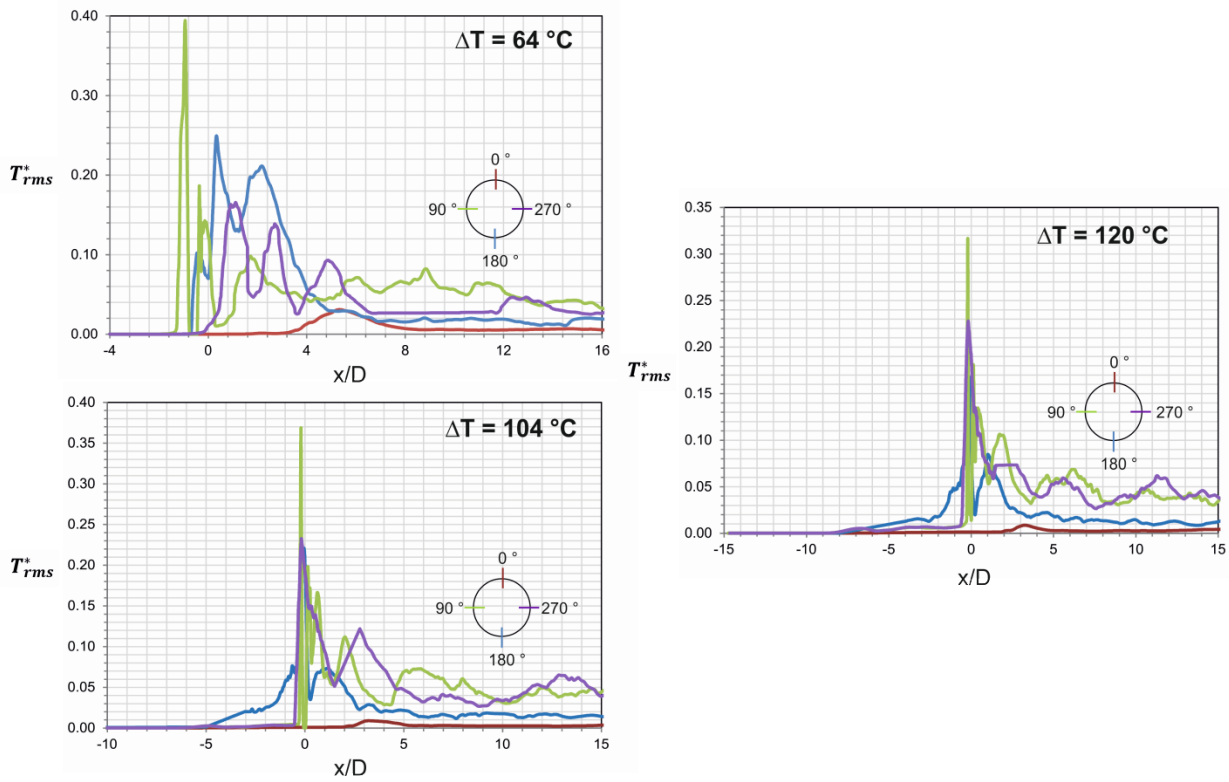

Fig. 111 T^*_{rms} distribution at θ = 0°, 90°, 180° and 270° ($\dot{m}_m$ = 0.3 kg/s, $\dot{m}_b$ = 0.1 kg/s)

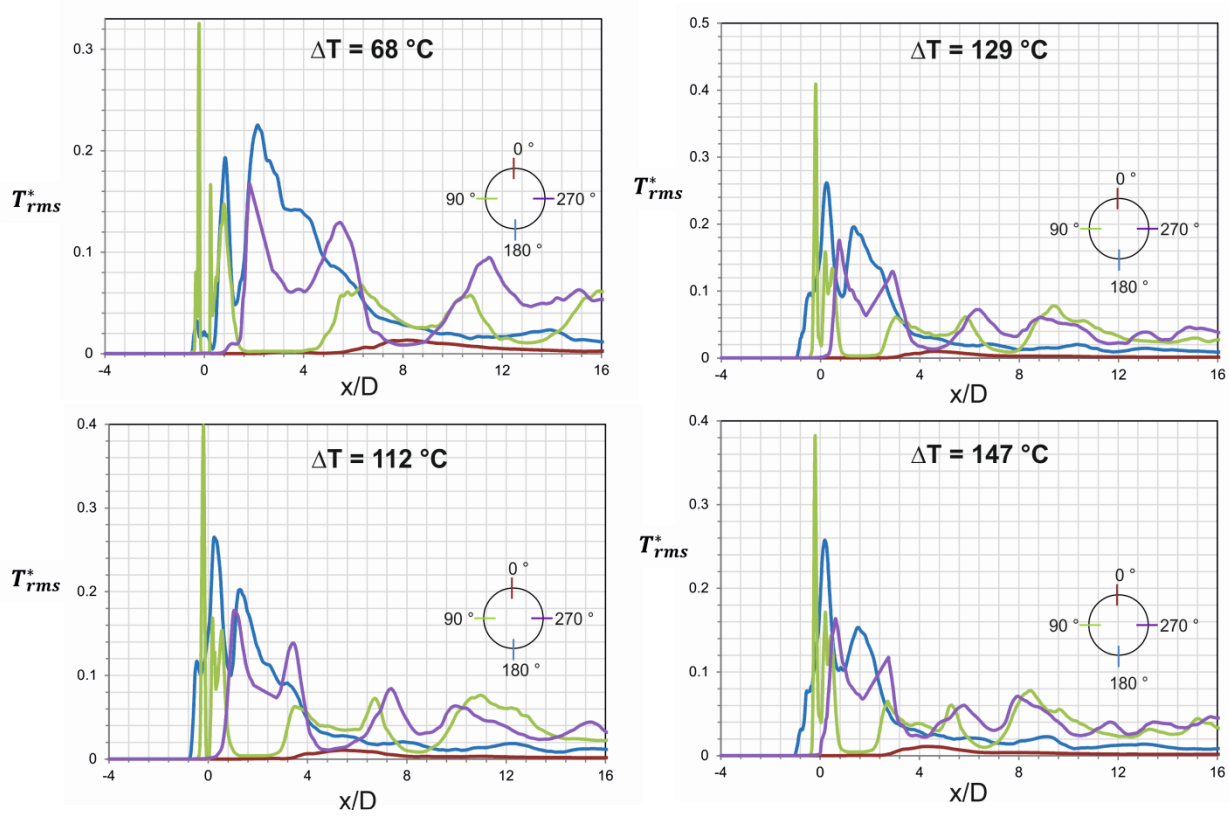

Fig. 112 T^*_{rms} distribution at θ = 0°, 90°, 180° and 270° ($\dot{m}_m$ = 0.5 kg/s, $\dot{m}_b$ = 0.1 kg/s)

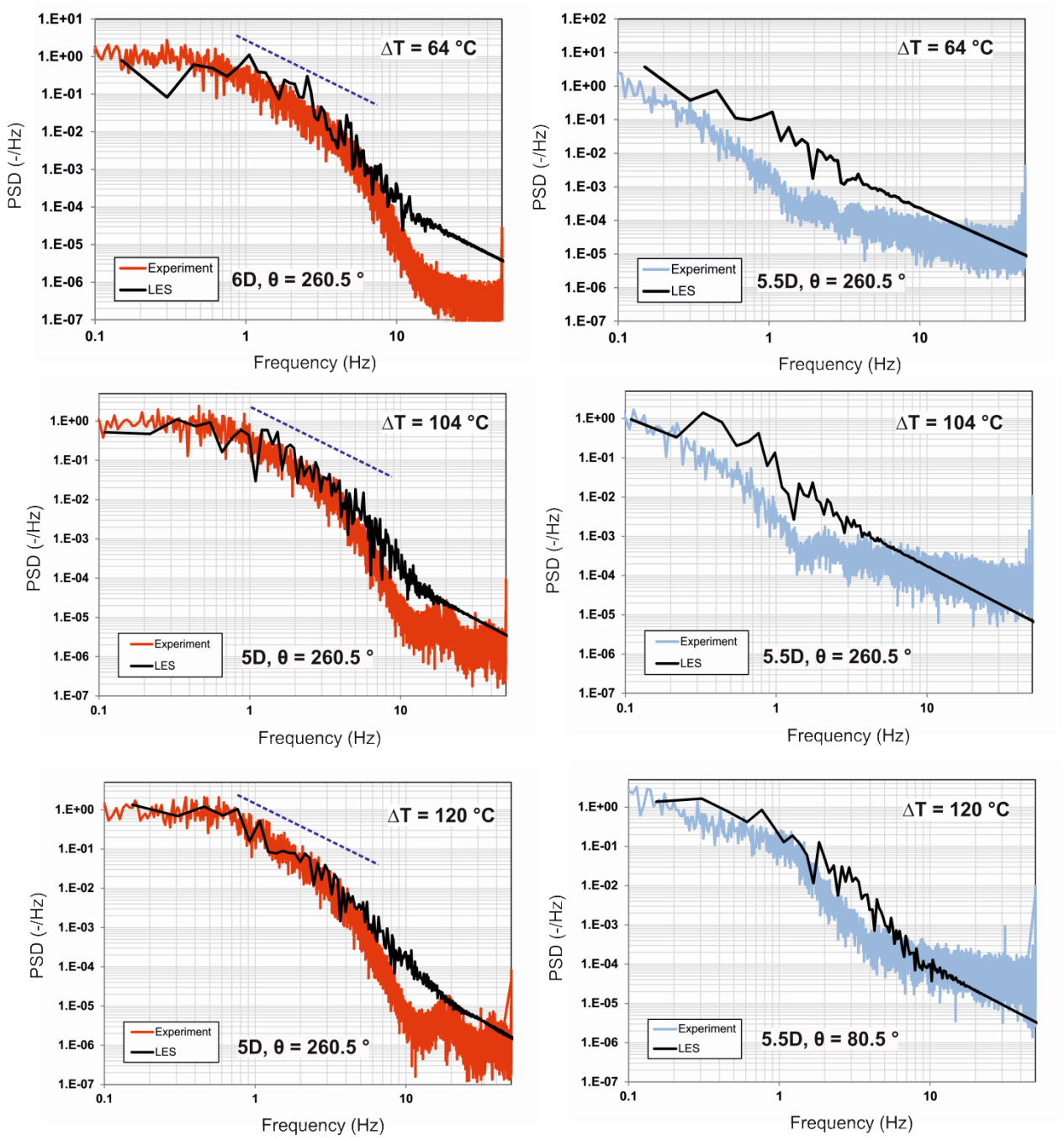

Fig. 113 PSD of peak fluid and solid thermal fluctuations ($\dot{m}_m$ = 0.3 kg/s, $\dot{m}_b$ = 0.1 kg/s)

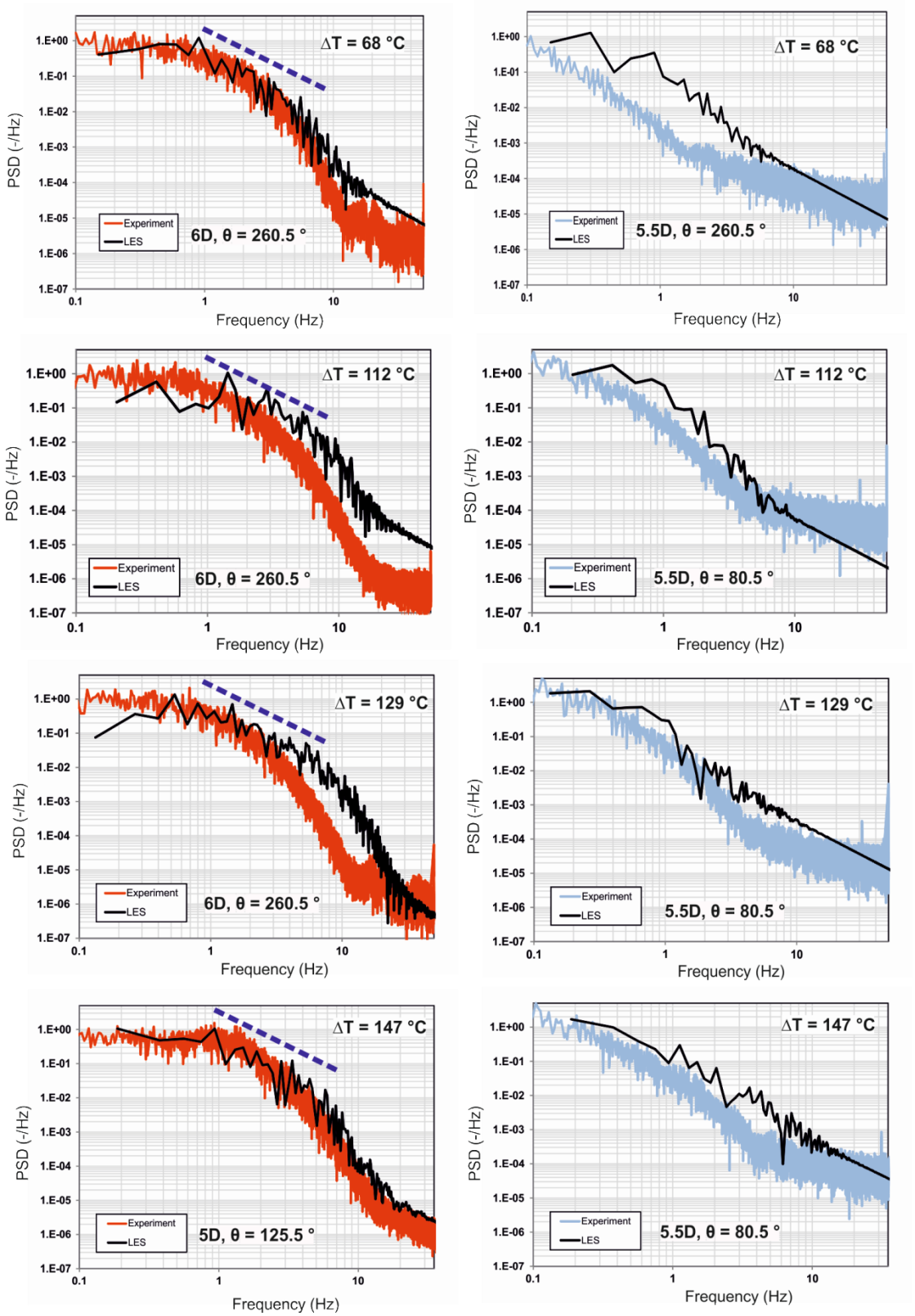

Fig. 114 PSD of peak fluid and solid thermal fluctuations ($\dot{m}_m$ = 0.5 kg/s, $\dot{m}_b$ = 0.1 kg/s)

A.3 MEASUREMENTS USING WIRE MESH SENSOR

The Laboratory of Nuclear Energy Systems at ETH Zürich has developed a conductivity based wire-mesh sensor (WMS) for characterizing single-phase turbulent mixing processes in T-junction piping systems encountered in industrial flows, e.g. piping system in power plants, chemical reactor, combustion chamber. This sensor was successfully tested in the Fluid-Structure Interaction (FSI) T-junction test facility, University of Stuttgart at its highest operating temperature and pressure of 257 °C and 70 bar.

A measurement technique developed to obtain high density of information about the flow with a high time resolution is the wire mesh sensor. The principle of WMS is based on a matrix like arrangement of the measuring points. Two sets of wire electrodes, perpendicular to each other, are stretched along the diameter of the pipe with a small axial separation between them as illustrated in Fig. 115. The transmitter electrodes are activated sequentially while the receiver electrodes are all parallel sampled such that the electrical property of the fluid (conductivity or permittivity) is measured at each crossing point. Processing the data at all the crossing points enables the instantaneous distribution of fluid across the cross-section.

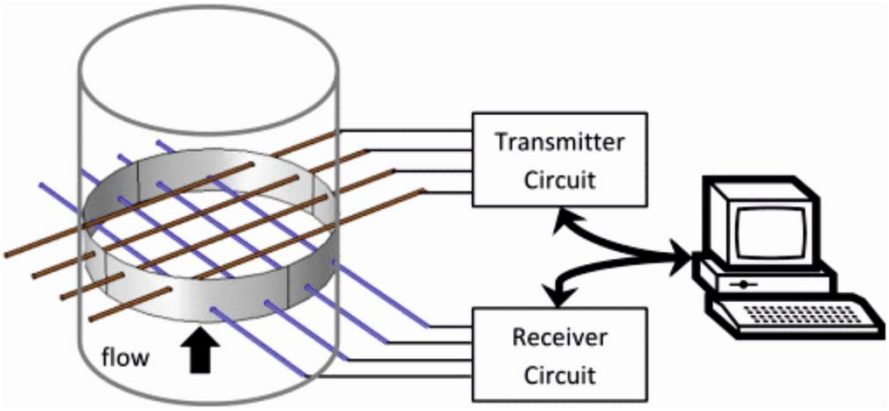

Fig. 115 Schematic view of a typical wire mesh sensor [102]

Wire-mesh sensors are widely used to characterize gas-liquid two-phase flows and single-phase mixing processes. The first concept was patented by Johnson (1987) [51], who proposed it for measuring the volumetric fraction of water in crude oil. The measurement of two-dimensional hold-up profiles was achieved for the first time by Reinecke et al. (1996) [108] by applying tomographic reconstruction techniques. A signal acquisition method allowing a high spatial and temporal resolution without the need of a tomographic

reconstruction was introduced by Prasser et al. (1998) [106] and is currently in use in numerous laboratories worldwide. A comprehensive overview of WMS in multiphase flows is given by Peña and Rodriguez (2015) [102]. The past two decades witnessed successful application of the WMS technology in both single- and multi-phase flows, often with a particular focus on flows encountered during nuclear power generation.

The high-temperature high-pressure wire mesh sensor module (see Fig. 116) used in this study is specifically designed and built to be operated in the FSI test facility. Based on a patented design by Kickhofel and Prasser (2014) [60], the WMS comprises 16 transmitter and 16 receiver electrodes forming a 16 x 16 electrode mesh (see Fig. 116(b)) placed at 90° angle to one another. The electrodes are made of stainless steel (316L) capillaries.

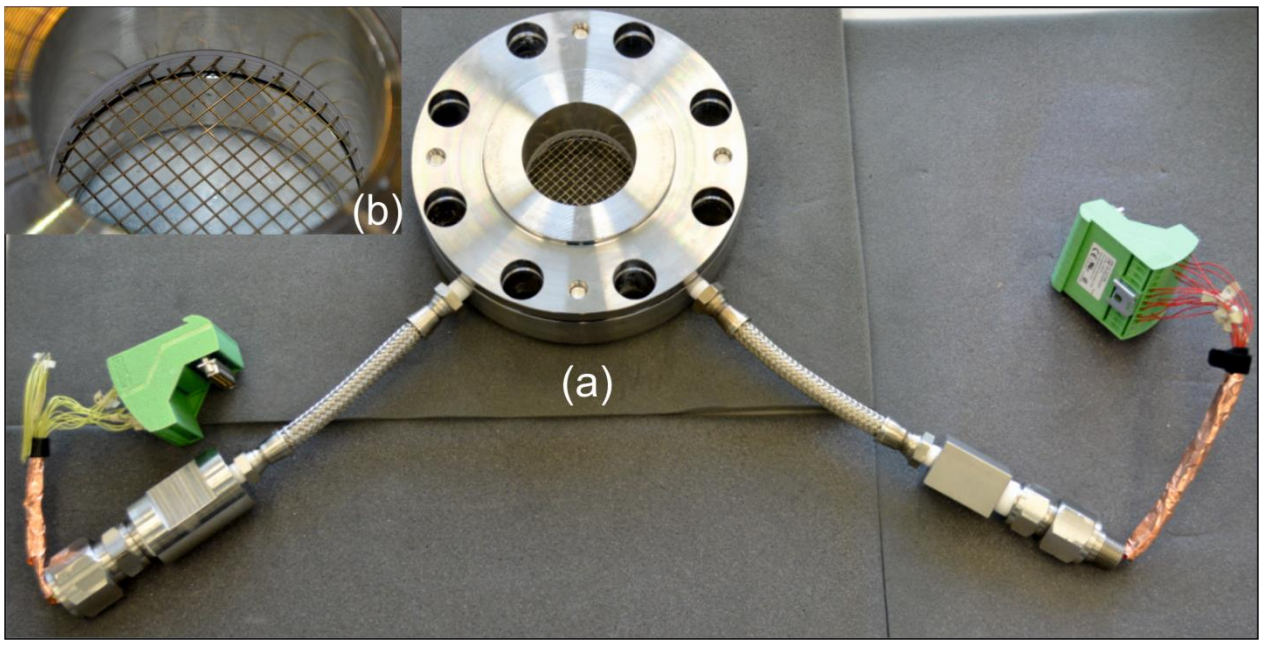

Fig. 116 Wire mesh sensor module (a) and close-up view of the electrode mesh (b)

Two ceramic substrate plates (made of Photoveel II and each 3 mm thick) with grooves and arranged one above the other hold the transmitter and receiver electrodes. The pitch of the electrodes is 4.49 mm and 208 crossing points are exposed to the fluid domain such that the electrical conductivity of the fluid flow between each crossing point can be measured. The WMS along with the substrate plates are placed between two housing flanges (primary flange and lid flange) which surround and secure the sensor. A detailed description of the WMS, the housing flanges, and the calibration methodology are described in Kickhofel (2015) [59].

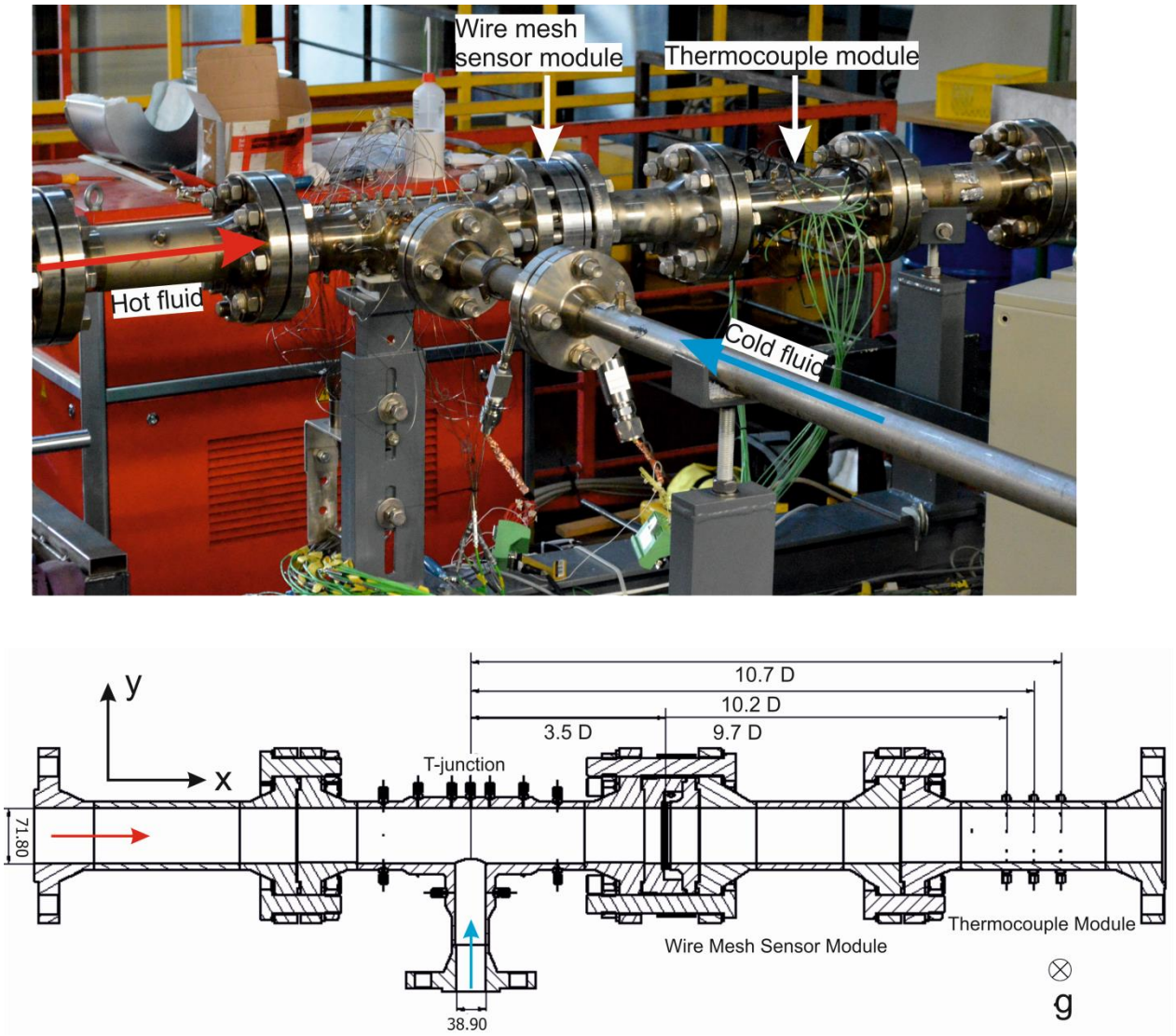

Fig. 117 WMS module positioned adjacent to the T-junction (top) during thermal mixing experiments and the corresponding schematic view (bottom)

A.3.1 Measurement details

Measurements were conducted using two different positional arrangements of the WMS module in the vicinity of the T-junction. During the first trial, the WMS module was placed downstream of the T-junction module (see Fig. 117) with the sensor positioned at a distance of 3.5D (D = 71.8 mm) in the mixing zone. During the second trial, the WMS was placed immediately upstream of the T-junction in the main pipe for calibration purposes as explained in Kickhofel (2015) [59]. Within the pipe, the WMS electrodes are tilted by an angle of 22.5 ° (see Fig. 118). By keeping constant mass flow rates in the main (0.4 kg/s)

and branch (0.1 kg/s) pipes, flow mixing behavior under different ΔTs were measured as shown in Table 16.

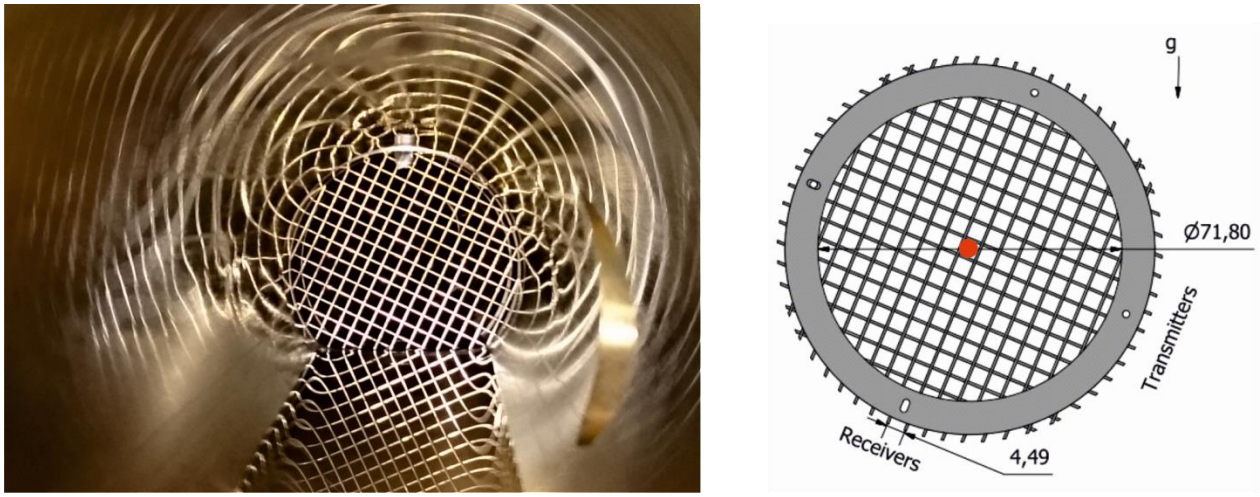

Fig. 118 View of the WMS (tilted by 22.5 °) placed in the FSI test facility (left) and its schematic view describing the transmitter and receiver electrodes

Table 16: Inflow conditions at the FSI test facility

Case #	ΔT (°C)	T_m* (°C)	$\dot{m}_m$ (kg/s)	u_m (m/s)	T_b* (°C)	$\dot{m}_b$ (kg/s)	u_b (m/s)	u_{mix} (m/s)
1	65	85	0.4	0.101	20	0.1	0.084	0.132
4	143	165	0.4	0.109	22	0.1	0.084	0.138
5	159	181	0.4	0.112	22	0.1	0.084	0.14
6	178	201	0.4	0.115	23	0.1	0.084	0.142
7	233	257	0.4	0.13	24	0.1	0.084	0.153
Pressure –70 bar								

A.3.2 Results

With the exception of case 7 (for reasons mentioned in section 4.2), LES calculations were performed for all the other cases and their predictions could be compared against the WMS data. The cross-sectional temperature distribution described below is viewed away from the T-junction.

Figs. 119, 120, 121, 122 and 123 depicts the cross-sectional mean temperature distribution as seen from WMS data and the corresponding LES predictions at X = 3.5D. Mixed flow is seen to exhibit extreme oscillation in case 1 (ΔT = 65 °C) while the flow is seen to exhibit stable stratification in cases 4 5, 6, and 7. LES predictions also reflect this shift in flow behavior brought about by rising ΔT between the fluids. Another interesting aspect to be noted is the reducing area occupied by the mixed flow along the cross-section with rise in ΔT between the fluids which culminates with lowest area occupied by the mixed flow being observed at ΔT = 233 °C.

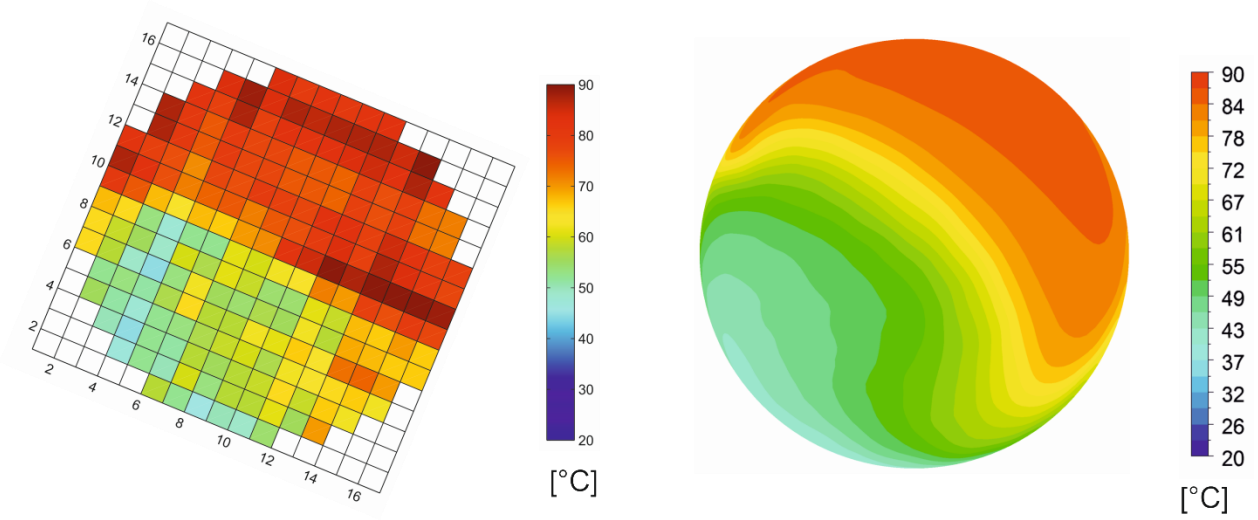

Fig. 119 Mean thermal field –WMS (left) and LES (right) at ΔT = 65 °C

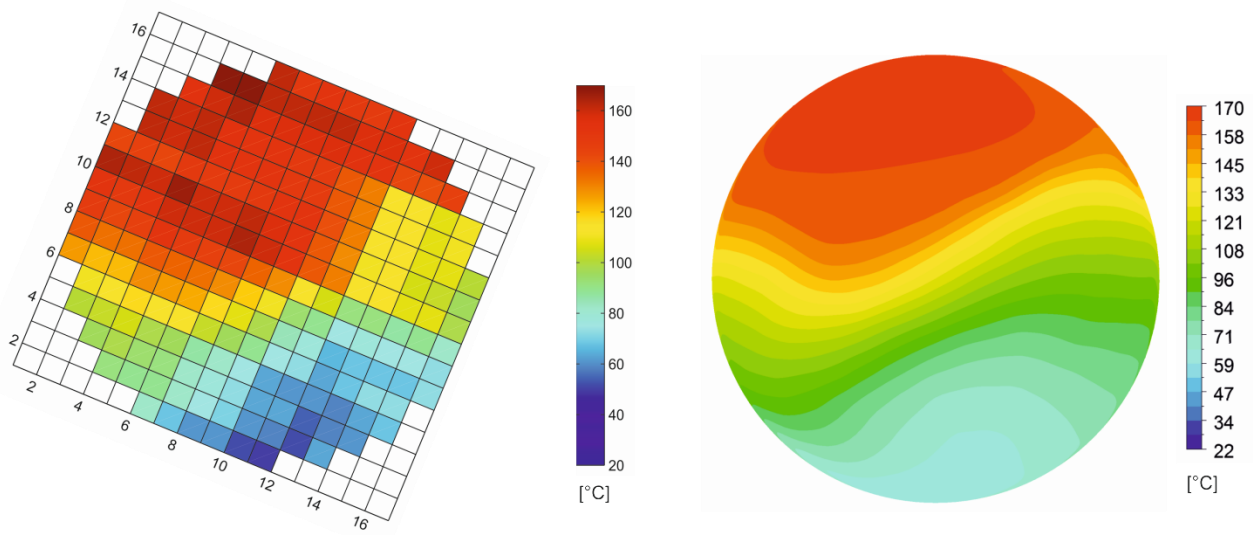

Fig. 120 Mean thermal field –WMS (left) and LES (right) at ΔT = 143 °C

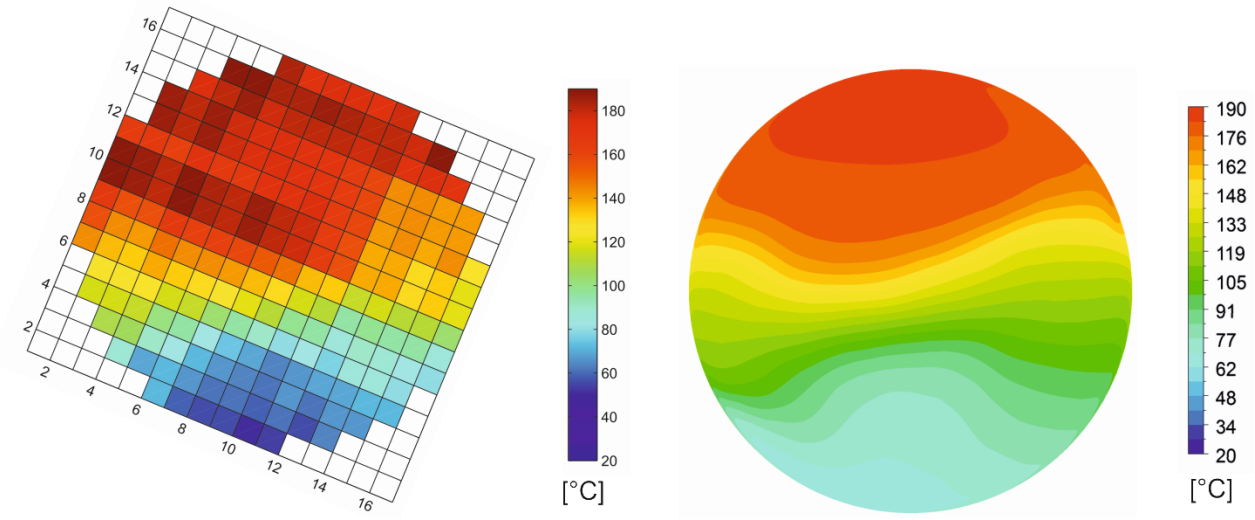

Fig. 121 Mean thermal field –WMS (left) and LES (right) at ΔT = 159 °C

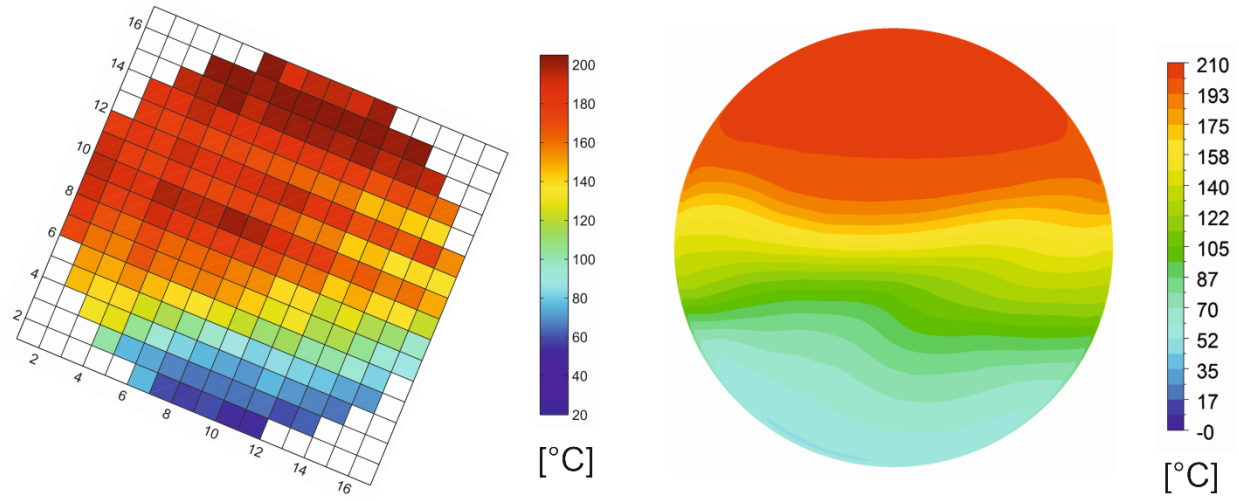

Fig. 122 Mean thermal field –WMS (left) and LES (right) at ΔT = 178 °C

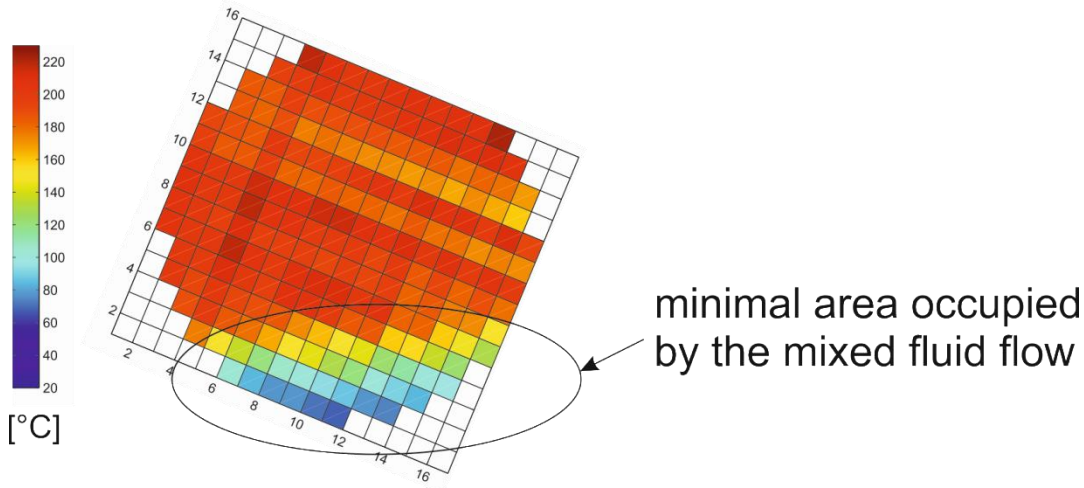

Fig. 123 Mean thermal field from WMS data at ΔT = 233 °C

The primary reason behind this phenomenon is the bending effect displayed by the piping with the T-junction as its vertex as ΔT begins to rise beyond 150 °C (discussed in sections 4.1 and 4.2). Such a scenario results in rising volume of cold fluid traveling upstream into the main pipe which is also correctly predicted by the LES calculations as shown in Fig. 42. Since the LES calculations were performed without incorporating the bending effects observed in the piping, the volume of mixed flow in the downstream region remains unchanged.

Figs. 124, 125, 126, 127, and 128 depict the cross-sectional distribution of temperature fluctuations obtained from WMS data and the corresponding LES predictions at X = 3.5D.

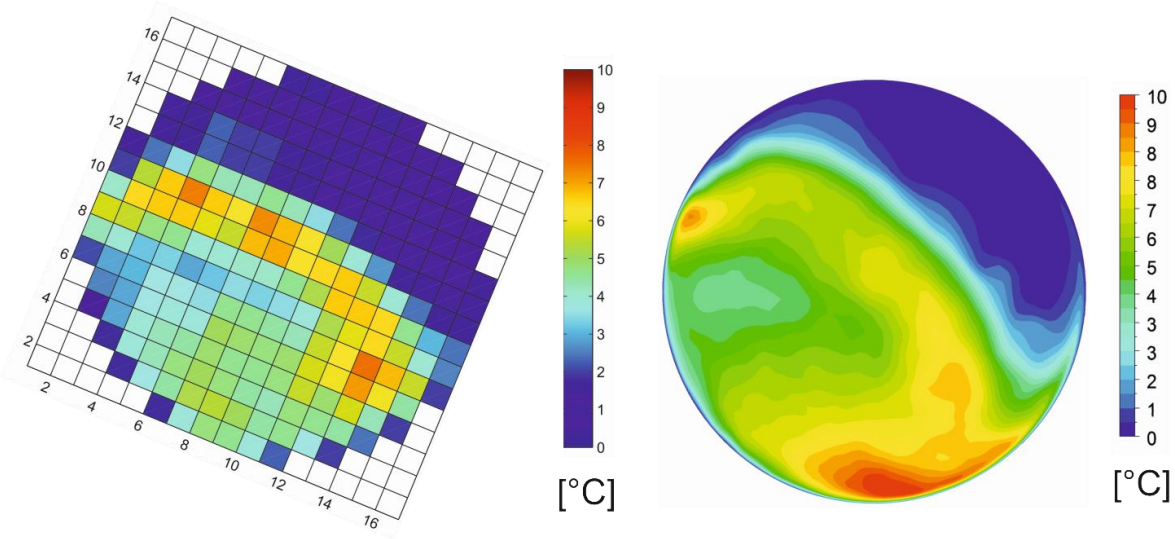

Fig. 124 RMS thermal fluctuations –WMS (left) and LES (right) at ΔT = 65 °C

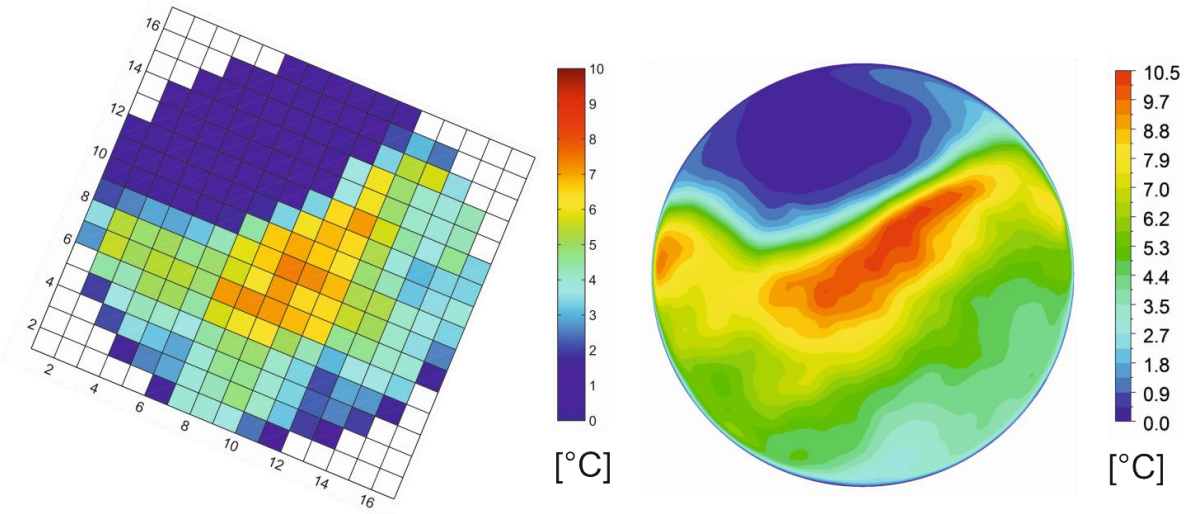

Fig. 125 RMS thermal fluctuations –WMS (left) and LES (right) at ΔT = 143 °C

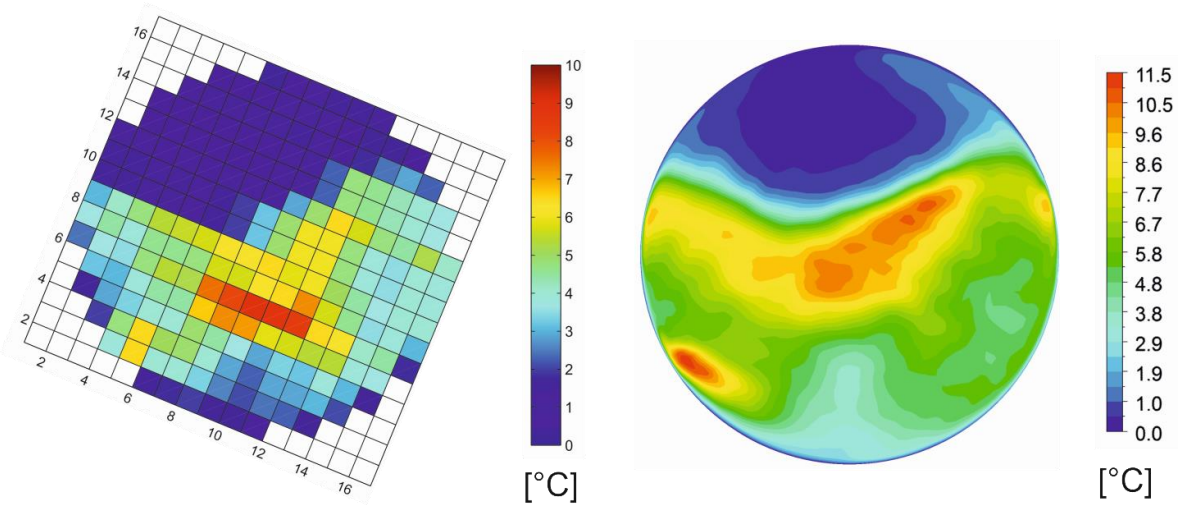

Fig. 126 RMS thermal fluctuations –WMS (left) and LES (right) at ΔT = 159 °C

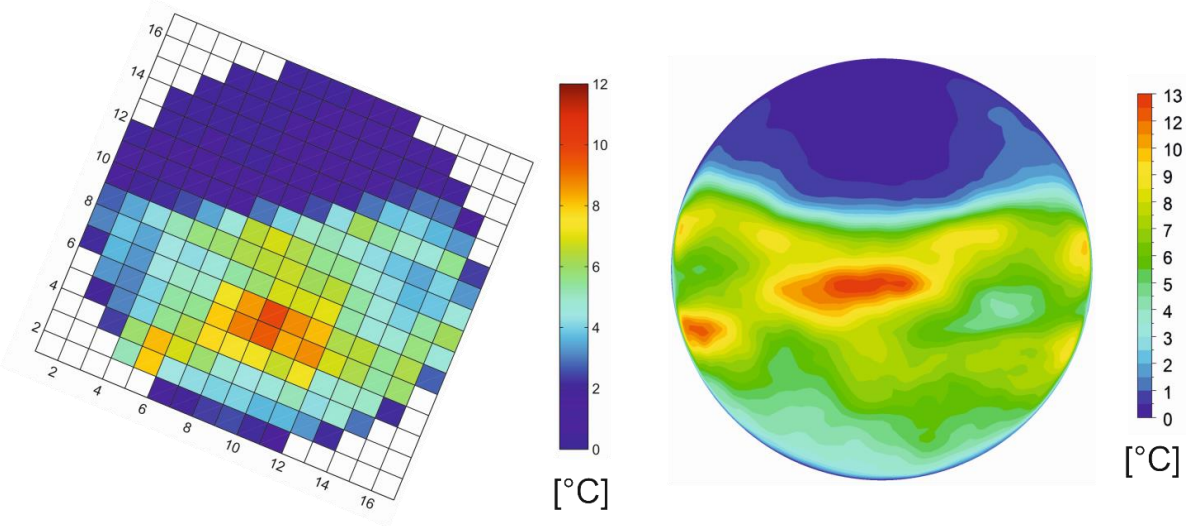

Fig. 127 RMS thermal fluctuations –WMS (left) and LES (right) at ΔT = 178 °C

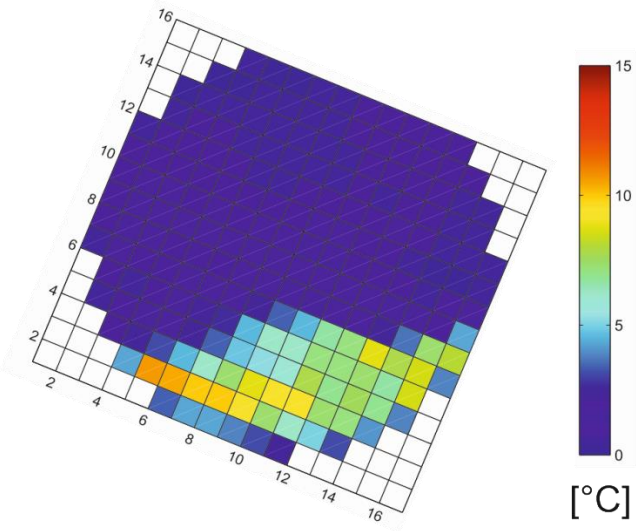

Fig. 128 RMS thermal fluctuations from WMS data at ΔT = 233 °C

Initial observations point out that the orientation of the mixed flow as recorded by the WMS and the corresponding LES predictions show good agreement with one another. Lowest amplitude fluctuations are observed near the top region while the highest amplitudes are seen to occur in the vicinity of the stratification layer. One thing that is clearly noticeable is the discrepancy in amplitudes between the WMS and LES data. While the LES predictions show higher fluctuation amplitudes, corresponding data from WMS exhibits attenuation in fluctuations (compare the WMS and LES predictions in Figs. 124, 125, 126, and 127).

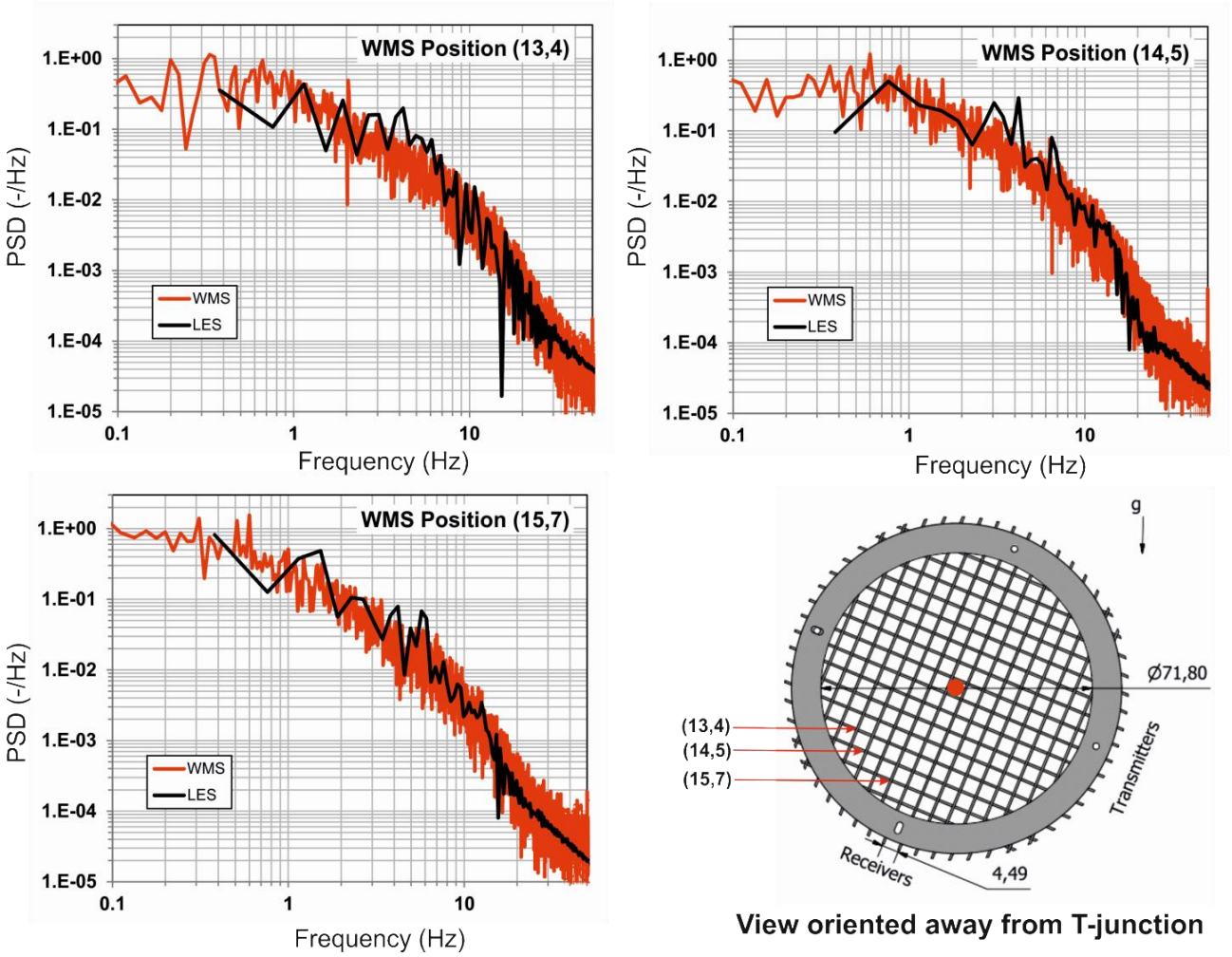

Fig. 129 Comparison of PSD between WMS and LES predictions at ΔT = 143 °C

This could be attributed to the operating principle of the WMS, which in essence is the volume averaging that occurs between the transmitter and receiver electrodes at each crossing point that is exposed to the flow. Electric current passes between the volume of

water occupied by the electrodes and it is possible to discern only a single value regardless of the range of high or low conductivity regions that exist between the electrodes.

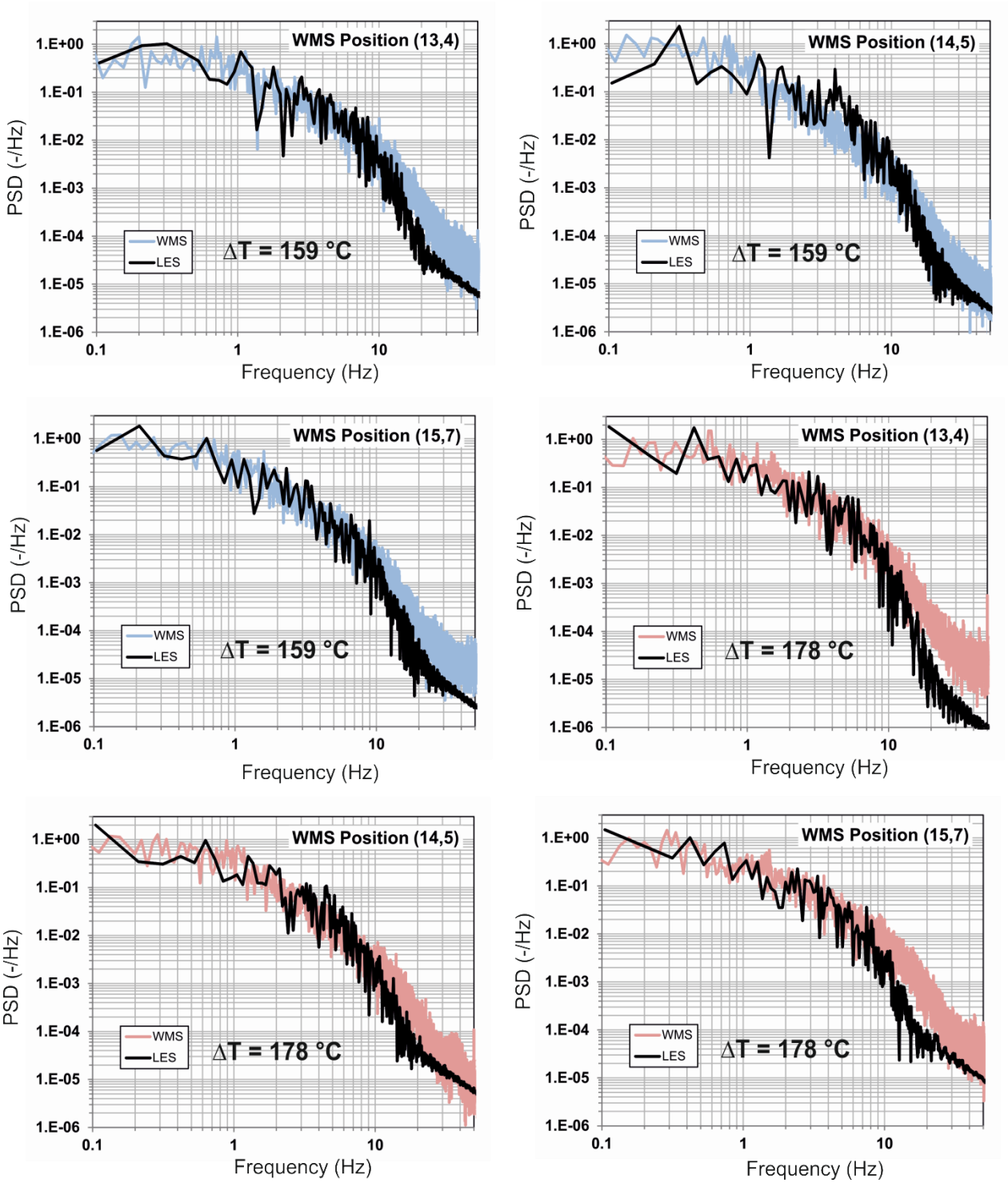

Fig. 130 Comparison of PSD between WMS and LES data at ΔT = 158 °C and 178 °C

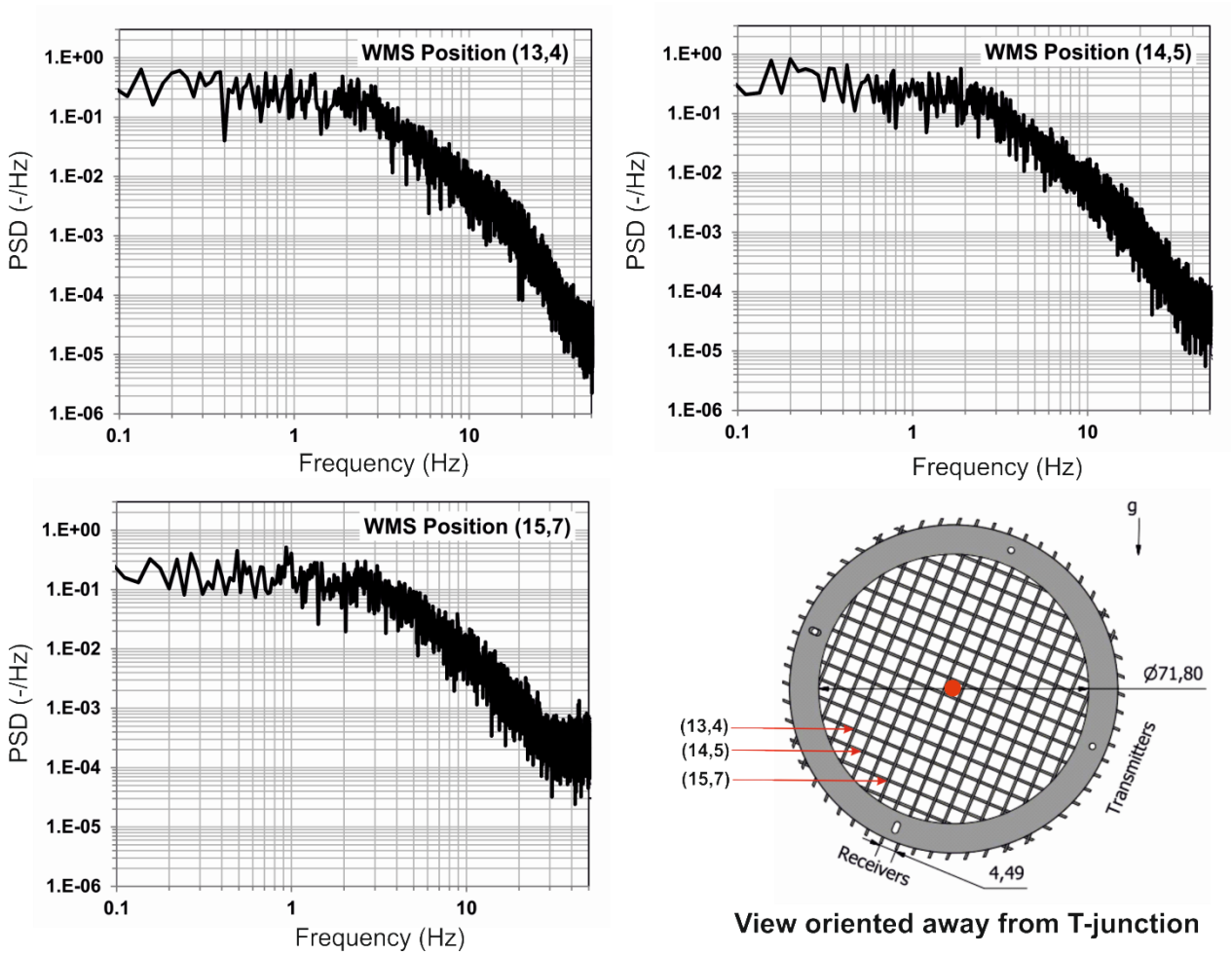

Fig. 131 PSD of WMS data at ΔT = 233 °C

Figs. 129, 130, and 131 shows the PSD of thermal fluctuations from the WMS data and the corresponding LES predictions for all the cases except case 1. Since no LES calculations were performed for case 7 (for reasons explained in section 4.2), only the PSD of thermal fluctuations estimated from the WMS data are shown. Three WMS crossing points are chosen in the mixing region for this exercise as shown in Fig. 129. These crossing points, unlike the near-wall thermocouples, are located slightly away from the wall and this is reflected in the energy of thermal fluctuations. No spectral peaks are observed at all the ΔT levels in the frequency range of 0.1 – 10 Hz and the energy content exhibits a gradual decline with increase in frequency. At frequencies greater than 10 Hz, the energy content remains fairly higher than what was observed from the near-wall thermocouple PSD data in Fig. 47. LES predictions exhibit a close agreement with the WMS data.